The Influence of Velocity Shear on Magnetic Buoyancy Instabilities

Jordan Alexander Bowker

Submitted in accordance with the requirements for the degree of Doctor of Philosophy

The University of Leeds

Department of Applied Mathematics

September 2016

The candidate confirms that the work submitted is his own, except where work which has formed part of jointly authored publications has been included. The contribution of the candidate and the other authors to this work has been explicitly indicated below. The candidate confirms that appropriate credit has been given within the thesis where reference has been made to the work of others.

The work in Chapter 3 is based on work from a jointly-authored publication. The details of this publication are:

Bowker, J. A., Hughes, D. W. & Kersalé, E. (2014). *Incorporating velocity shear into the magneto-Boussinesq approximation*, Geophys. Astrophys. Fluid Dyn. **108**, 553–567.

The co-authors provided ideas and guidance surrounding this work and aided with the writing of the paper. All mathematical and scientific research contained in this work was undertaken by the candidate himself.

Abstract

Most dynamo models agree that large-scale, weak poloidal magnetic field is wound up into strong toroidal field through differential rotation. Therefore, the strong radial gradients of angular velocity present in the solar tachocline are extremely likely to play a crucial role in the solar dynamo. Motivated by this, we focus on the instability mechanism thought to be responsible for the break up of a horizontal field in a stably stratified layer, namely magnetic buoyancy instability, and the effect a velocity shear has upon said instability.

To study this interaction, we derive a new set of equations incorporating velocity shear and magnetic buoyancy into the Boussinesq approximation. These equations not only provide us with the ability to study the effects of a velocity shear on magnetic buoyancy instability, but also allow us to study magnetic buoyancy instability in the presence of a magnetic field varying on a short $O(d)$ length scale, compared to the equations of Spiegel & Weiss (1982), which are restricted to field variations on a longer $O(H_p)$ scale. Stability criteria for this new system is obtained through a linear analysis on the ideal (diffusionless) system.

Motivated by the work of Mizerski et al. (2013) we use the newly derived equations to study the short-wavelength linear magnetic buoyancy instability. We first study this problem in the absence of a velocity shear and dissipation, deriving asymptotic results analogous to Mizerski et al.. The governing set of equations are then solved numerically to verify the asymptotic results. A velocity shear is then added into the analysis; we derive new asymptotic results and use them to comment on the influence the velocity shear has on the instability. Upholding the short-wavelength limit, we individually introduce each diffusive parameter into the analysis, observing the role each has on the instability.

Finally, we solve the newly derived system of linearised equations numerically, whilst including all diffusive parameters. We comment on the role of the diffusive parameters and investigate how they influence the instability.

Acknowledgements

I would first like to thank my supervisors Prof. David Hughes and Dr. Evy Kersalé, without whom this thesis would not be in the state it is today. The guidance and insight they provided over the last four years was invaluable and I am extremely grateful for all their patience and support. In addition I would like to thank my examiners, Prof. Chris Jones and Dr Paul Bushby, for their many helpful comments.

I would also like to thank my family and friends for their continued encouragement and support during my studies. Finally, a special thanks goes to Kate for putting your life on hold whilst I completed this thesis. Your love, friendship and determination has helped me more than you know.

Contents

List of figures

List of tables

Chapter 1

Introduction

1.1   Solar observations

With around 1 billion trillion stars in the observable universe, astrophysically speaking our Sun may be regarded as just another star in the sky. However, being our closest star the Sun is naturally an object of great interest. It is this 'close' proximity that has given astronomers the opportunity to make detailed observations of the Sun for centuries, to the point where now our knowledge of the Sun far outweighs that of any other star in the universe.

The Sun was formed close to 4.6 billion years ago and is classified as a middle aged G-type main-sequence star, with a mass of around 2×10^{30}kg and surface temperature of $5,778$K. The internal structure of the Sun is split into three regions as shown in Figure 1.1: the core, the radiative zone, and the convection zone. Like all G-type stars energy is produced in the core by converting hydrogen to helium through nuclear fusion; at the centre the temperature exceeds 10^7K and the density is approximately $150\,\mathrm{g cm^{-3}}$. The core extends to around $0.25\,R_\odot$, where $R_\odot$ denotes the solar radius ($R_\odot \approx 7 \times 10^8$m).

The radiative zone extends between $0.25\,R_\odot$ and $0.7\,R_\odot$. Across this region the temperature drops from 7×10^6K to 2×10^6K. This decrease in temperature is less than the adiabatic temperature gradient, resulting in an atmosphere that is stable to convection. The primary means of energy transfer is by thermal radiation — energy
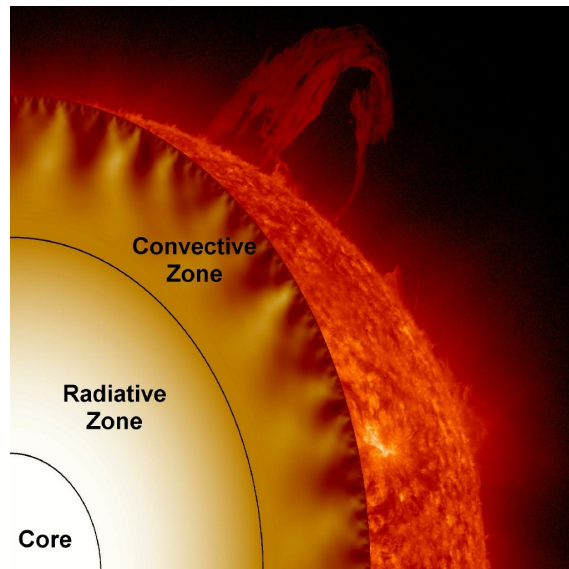
Figure 1.1: The solar interior. Image source: solarscience.msfc.nasa.gov.

travels radially outwards in the form of photons emitted by ions of hydrogen and helium; these photons only travel a brief distance before being reabsorbed by other ions. At $0.7\,R_\odot$ the density has dropped to $0.2\,\mathrm{g\,cm^{-3}}$, nearly three orders of magnitude lower than it is at the core. The region from $0.7\,R_\odot$ to the surface is known as the convection zone; here the temperature gradient is sufficiently large that convection can drive the motion. The convection process can be explained through a parcel argument. A parcel of plasma heated at the base of the convection zone is less dense than its surroundings and begins to 'rise' towards the surface. As the parcel moves up through the convection zone to the colder surface it naturally begins to cool. However, due to the steep temperature gradient the parcel remains warmer, and therefore less dense than its surrounds, thus it continues to rise to the surface. Although this is a simple concept of how plasma moves through the convection zone, it is worth noting that the plasma is not at all viscous and as such fluid motion is likely very turbulent. The surface of the Sun is called the photosphere and is visible with the naked eye. Once the parcel reaches the surface it spreads out, cools and sinks back down into the convection zone. As a result of this overturning motion at the surface, granules can be observed across the entire Sun. Each individual granule has a diameter on the order of 1000km, with a short lifespan of up to 20 minutes before being replaced with a new granule. Also visible on the photosphere are sunspots; regions on

(a)

(b)
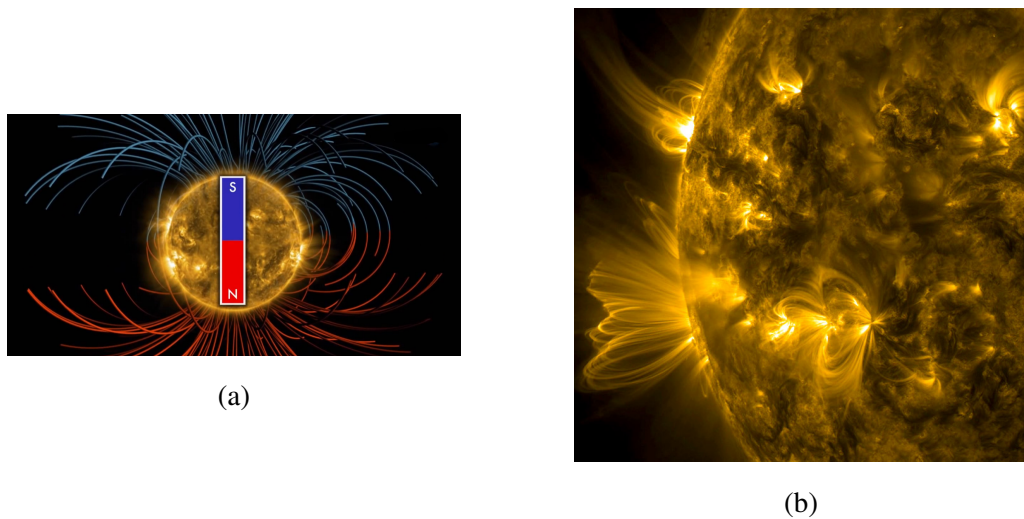
Figure 1.2: Visualisation of solar magnetic field on a variety of scales; The large-scale global dipolar magnetic field (left), and coronal loops (right). Image sources: www.nasa.gov (left) and sdo.gsfc.nasa.gov (right).

the surface where the plasma is colder than the surrounding area. These sunspots appear as dark spots on the surface of the sun and can be up to $150,000$km in diameter. Above the photosphere is the solar atmosphere, which can be split into two distinct layers; the chromosphere and the corona. These outer regions are observed using telescopes that filter light outside the visible wavelength range. The temperature of the chromosphere increases throughout the layer with increasing height, from around 6000K to 35000K. The chromosphere is the location of many solar features, such as filaments and spicules. Above the chromosphere is the corona, which extends millions of kilometres into space and is visible to the naked eye during a total solar eclipse. Coronal features include solar flares, polar plumes and coronal loops.

Measurable by the means of the Zeeman effect, it is thought that most stars are associated with a magnetic field, and our Sun is no different. The solar magnetic field is very complex and acts on a variety of scales, as shown in Figure 1.2. Emerging from each pole is a large-scale global field of opposite polarities. This dipolar field has a typical strength of 1-2 Gauss, and can be carried by the solar wind to form the interplanetary magnetic field, extending through the whole solar system. Smaller-scale coherent structures of the

DAILY SUNSPOT AREA AVERAGED OVER INDIVIDUAL SOLAR ROTATIONS
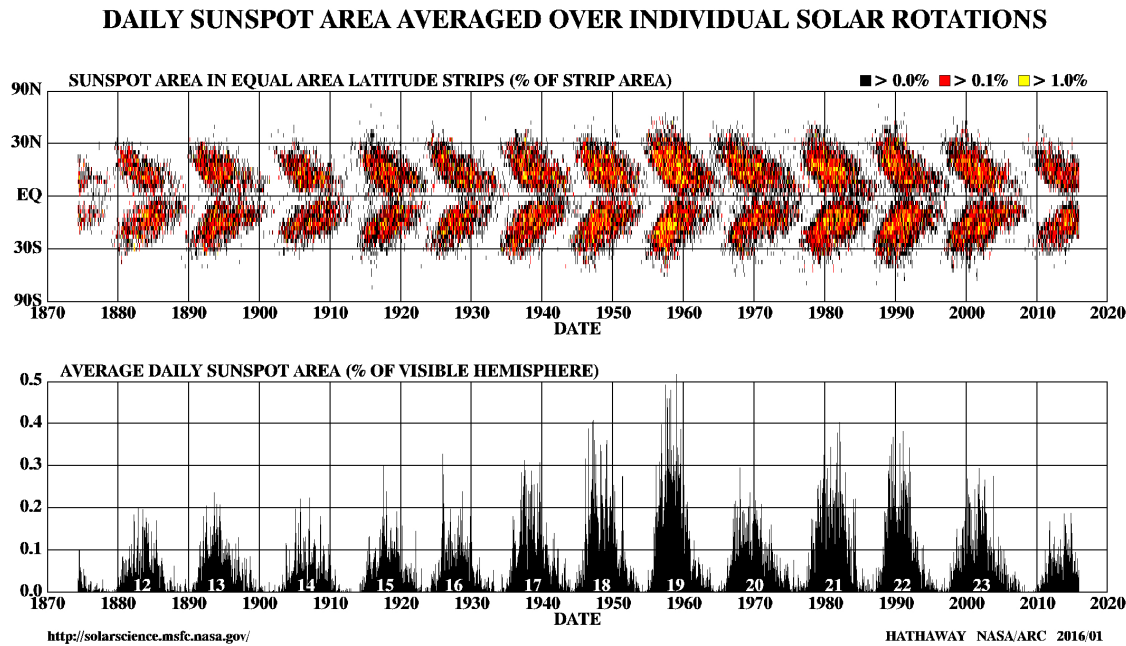
Figure 1.3: Butterfly diagram showing sunspot migration over time (top) and the average area of sunspot coverage versus time (bottom). Image source: solarscience.msfc.nasa.gov.

magnetic field are observable in the atmosphere in the form of coronal loops. These arch-like structures are created by magnetic field emerging from the solar interior as a loop, and have been observed to extend high into the corona. The magnetic field at the base of these coronal loops is significantly stronger than the global field, measuring up to $4,000$ Gauss. This strong field inhibits convection near the surface, acting as a barrier to hot gas rising; as a result the area is colder than its surroundings. The relative difference between this area and its surroundings leads to a visibly darker patch on the surface known as a sunspot. These sunspots often appear in pairs, with each pair having an opposite magnetic polarity. Disruption to these surface features can cause energetic explosions on the Sun such as solar flares and Coronal Mass Ejections, where plasma is thrown out of the Sun into the atmosphere.

Although it has only been known since Hale (1908) that sunspots are associated with magnetic field, sunspot activity, and therefore indirectly the magnetic field, has been recorded since the beginning of the 17th century. In 1612 Galileo famously sketched
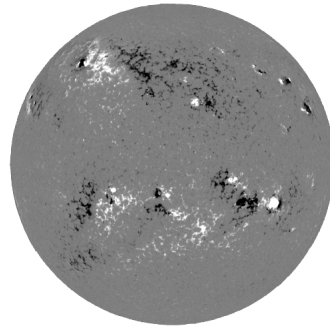
Figure 1.4: Magnetogram displaying the surface distribution and polarity of the Sun's magnetic fields. Image source: solar-center.stanford.edu.

the Sun at the same time every day over a period of several weeks, and observed large-scale dark spots moving across the surface. Since then, detailed records of the temporal evolution of sunspot activity have revealed that despite the complex nature of the solar magnetic field, sunspot behaviour is in fact somewhat organised. Plotting of the area of sunspot coverage at a given latitude over time reveals a distinct cyclic pattern (Figure 1.3). At the start of the cycle, sunspots appear around $30°$ to $40°$ north and south of the equator. As the cycle progresses more sunspots appear at latitudes closer to the solar equator (Spörer's law) and the overall sunspot pattern migrates toward the equator, where individual sunspots maintain their position until they decay.

Individual sunspots can have a life span of anywhere between a few days to a few months, and the overall migration cycle lasts approximately eleven years. Also shown in Figure 1.3 is the area of sunspot coverage versus time. Coinciding with the start of each cycle is a minimum of sunspot coverage. Sunspot areas peak during the middle of the cycle before returning back to the minimum at the end. The fact that sunspots are directly linked to strong magnetic field tells us a lot about the magnetic intensity of the Sun during a sunspot cycle. Specifically that a maximum in sunspots activity results in a maximum in solar magnetic activity, and vice versa. During times of maximum solar activity, features such as flares and coronal mass ejections are more frequent.

During the sunspot cycle all the leading (easternmost) spots of a pair in the northern hemisphere have the same polarity, while its corresponding following (westernmost) spot
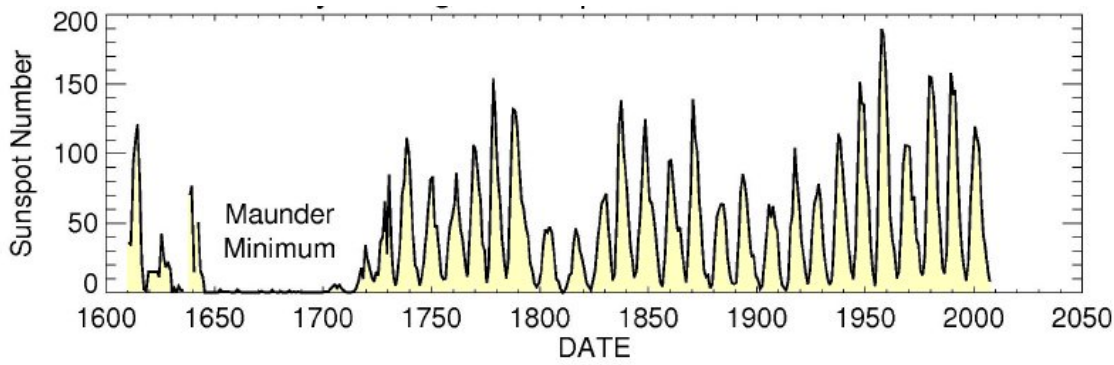
Figure 1.5: The average number of observable sunspots over time. Image source: science.nasa.gov.

has the opposite polarity. The effect is exactly reversed in the southern hemisphere as seen in Figure 1.4, and is known as Hale's polarity law. Hale found this behaviour to be true for the whole eleven year cycle; however he observed that in the following cycle the polarities in both hemispheres reverse. Aligned with the start of each eleven year cycle the polarity of the Sun's global dipolar magnetic field switches. Therefore, although the visual cycle of sunspots has a period of approximately eleven years, the full magnetic cycle is twice as long. Also evident in Figure 1.4 is Joy's law; sunspots appear to be 'angled' relative to the equator, with the leading spot closer to the equator than the following spots.

Figure 1.5 shows the average number of sunspots observed per year plotted over time, in which we see clear evidence of the elven year sunspot cycle. Of interest is the extended period of low sunspot numbers from around 1645 to 1715, known as the Maunder Minimum. It is not known what triggered this disruption to the sunspot cycle or indeed how the cycle rebooted again in the early 18th century. During this time period there was no 'visible' evidence of a magnetic cycle in the Sun. However proxy measurements of beryllium-10 and carbon-14 cosmogenic isotope abundance can be used to study long-term solar activity. The results indicate that the twenty-two year magnetic cycle was still present during this time and suggests that sunspots are actually a symptom of the magnetic cycle, and not a cause. Proxy measurements also reveal that periods of low magnetic activity have their own cycle of approximately 200 years. Since the time of Galileo it has been known that the Sun rotates, and through observations of magnetic features it
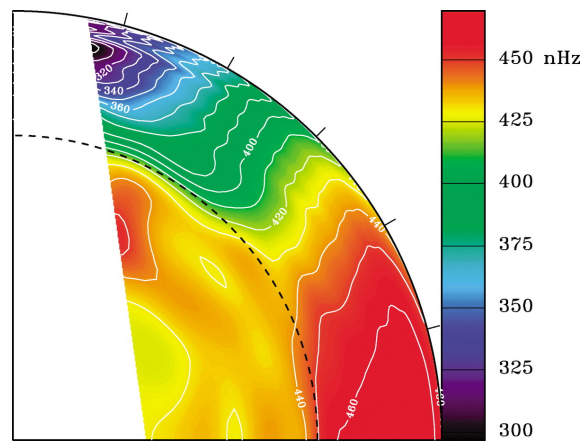
Figure 1.6: The internal rotation profile of the Sun inferred from helioseismology. A rotation rate of $450\,\mathrm{nHz}$ corresponds to a rotation period of 26 days and $325\,\mathrm{nHz}$ corresponds to 36 days. Image source: www2.hao.ucar.edu.

is clear that the Sun's surface rotates differentially. Specifically, the fluid at the equator rotates faster (25 day period) than that at the poles (34 day period). Until the emergence of helioseismology, one could only speculate as to how this surface differential rotation profile is distributed through the Sun. Helioseismology works by measuring the changes in oscillating pressure waves through the Sun and is used to build up a detailed profile of the solar interior. Thus allowing scientists to in a sense 'observe' the internal structure, and rotation rate of the Sun. Figure 1.6 shows a contour plot of angular rotation speeds for the solar interior, with red corresponding to faster rotation speeds and blue slower. Here we see that through the convection zone, angular velocity is roughly constant along radial lines. Therefore the differential rotation profile observable on the surface continues throughout the convective envelope. An interesting result from helioseismology is that this rotation profile does not persist throughout the solar interior; instead the radiative zone rotates more like a solid body, with constant angular velocity. This led to the discovery of a relatively thin ($0.02 - 0.05\,R_{\odot}$) transition region between the two distinct rotation profiles. Termed the tachocline by Spiegel & Zahn (1992), this interface region is located at roughly $0.69 - 0.71\,R_{\odot}$ and naturally consists of a very strong angular velocity gradient. The tachocline is thought to play a very impactful role in how the Sun maintains and transports its magnetic field, a process discussed in §1.2 in more detail. Table 1.1

Definition	Symbol	Quantity
Density	ρ	$0.21\,\mathrm{g\,cm^{-3}}$
Pressure	p	$6.7 \times 10^{13}\ \mathrm{g\,cm^{-2}\,s^{-2}}$
Temperature	T	$2.3 \times 10^6\,\mathrm{K}$
Sound speed	c	$2.3 \times 10^7\,\mathrm{cm\,s^{-1}}$
Gravitational acc.	g	$5.4 \times 10^4\,\mathrm{cm\,s^{-2}}$
Buoyancy Frequency	N	$8 \times 10^{-4}\,\mathrm{s^{-1}}$
Magnetic diffusivity	η	$4.1 \times 10^2\,\mathrm{cm^2\,s^{-1}}$
Kinematic diffusivity	ν	$2.7 \times 10^1\,\mathrm{cm^2\,s^{-1}}$
Thermal diffusivity	κ	$1.4 \times 10^7\,\mathrm{cm^2\,s^{-1}}$

Table 1.1: Estimates of parameter values of the tachocline at $r = 0.7\,R_\odot$, taken from Gough (2007).

shows estimated parameter values for the tachocline, taken from Gough (2007). These will be used to estimate the magnitude of certain non-dimensional parameters used in numerical work throughout the thesis.

Helioseismology allows the detection of temporal variations in the solar rotation profile over a solar cycle. As of yet there is no indication of variations to the rotation profile deep in the solar interior; however, temporal variations on the time-scale of the solar cycle have been detected in the convection zone. Near the surface there exists alternating bands that rotate faster and slower than the average rotation rate, termed torsional oscillations (Howard & Labonte, 1980). At mid to low latitudes, these bands propagate toward the equator and have been measured down to $0.92\,R_\odot$ (Howe et al., 2000). These mid latitude bands coincide with the migrating bands of magnetic activity, suggesting a strong link between torsional oscillations and the solar magnetic field. At higher latitudes the bands propagate towards the poles and are thought to penetrate deeper into the convection zone, possibly down to the base (Vorontsov et al., 2002).

1.2   The solar dynamo

The time-scale for Ohmic diffusion in the Sun is around 10^{10} years, comparable with the age of the Sun. Therefore, it is possible that the magnetic field we observe on the surface has been around since the Sun's formation, held within the solar interior and is slowly diffusing away. However, as discussed in §1.1, the solar magnetic field displays cyclic behaviour; observations of surface magnetic activity suggests a twenty-two year magnetic cycle. Since this cyclic pattern appears on a considerably shorter time-scale than the Sun's life span, it is much more feasible that the magnetic field we observe through surface activity is somehow continually self-generated in the interior of the Sun. Exactly how the solar dynamo works is not currently known, and therefore is a much debated and very active area of research. As we have seen, the solar magnetic field acts on a wide range of length scales and is linked with a variety of solar features such as, the eleven year sunspot cycle, sunspot migration and polar field polarity switching, to name a few. Therefore, a successful dynamo model would not only have to explain how magnetic field is self-generated, but also account for these observable features. Although many contradicting dynamo models exists (see §1.2.2), most models agree that large-scale weak poloidal magnetic field is wound up into strong toroidal field through differential rotation. This toroidal field is stored within the solar interior before it rises to the surface, resulting in the observed magnetic activity. To close the loop, the magnetic field that does not escape must somehow be converted back into poloidal field, for the process to start over. As a region with a strong angular velocity gradient, many believe that the newly discovered tachocline would be an ideal location for the magnetic field to be wound up and stored. In this section we give a mathematical overview of dynamo loop, that is at the heart of the dynamo process. We then go on to discuss some current popular solar dynamo models.

1.2.1   The dynamo loop

Alfvén's theorem states that for a fluid with infinite magnetic conductivity, magnetic field is in a sense *frozen-in* to the fluid and moves with it. Although not at infinite conductivity,

the fluid in the solar interior is highly conductive and it is not unrealistic to assume a similar process takes place. As such, the differential rotation profile of the solar interior is expected to have a very influential effect on the solar magnetic field. Derived from Maxwell's equations and Ohm's Law, the induction equation models the time evolution of the magnetic field $\boldsymbol{B}$ for a gas or fluid with velocity $\boldsymbol{u}$,

$$\frac{\partial \boldsymbol{B}}{\partial t} = \boldsymbol{\nabla} \times (\boldsymbol{u} \times \boldsymbol{B}) - \boldsymbol{\nabla} \times (\eta \boldsymbol{\nabla} \times \boldsymbol{B}). \tag{1.1}$$

Throughout this thesis the magnetic diffusivity $\eta = (\mu_0 \sigma)^{-1}$, where μ_0 is the vacuum permeability and σ is the conductivity, is taken as constant. With this, the induction equation reduces to

$$\frac{\partial \boldsymbol{B}}{\partial t} = \boldsymbol{\nabla} \times (\boldsymbol{u} \times \boldsymbol{B}) + \eta \nabla^2 \boldsymbol{B}. \tag{1.2}$$

Physically this equation tells us that the evolution of the magnetic field in time is dependent on two things: the advection of the field with the flow, and its diffusion through the flow. As we can see from (1.2), in the absence of a flow $\boldsymbol{u} = 0$, the magnetic field would just diffuse away. Therefore dynamo theory requires a process to generate $\boldsymbol{u}$ and in order for the magnetic field to be maintained. Since the magnetic field is solenoidal by nature, in the axisymmetric case a large-scale field can be expressed as the sum its poloidal and toroidal parts; $\boldsymbol{B} = \boldsymbol{B_P} + \boldsymbol{B_T}$, where in cylindrical polar coordinates (r, ϕ, z), $\boldsymbol{B_P} = \boldsymbol{\nabla} \times A\boldsymbol{e_\phi}$ and $\boldsymbol{B_T} = B_\phi \boldsymbol{e_\phi}$. Writing the magnetic field in this form, the evolution of the toroidal field from (1.2) is

$$\frac{\partial}{\partial t}\left(\frac{B_\phi}{r}\right) = \boldsymbol{B_P} \cdot \boldsymbol{\nabla}\Omega - \boldsymbol{\nabla} \cdot \left(\frac{B_\phi}{r}\boldsymbol{u_m}\right) + \left(\frac{\eta}{r}\right)\left(\nabla^2 - \frac{1}{r^2}\right)B_\phi, \tag{1.3}$$

where the velocity is expressed in terms of the axisymmetric meridional flow $\boldsymbol{u_m}$ and angular velocity is the $\Omega(r, z)$, such that $\boldsymbol{u} = \boldsymbol{u_m} + r\Omega\boldsymbol{e_\phi}$. Expressing the equation like this shows how toroidal field is generated from poloidal field by differential rotation, and transported by meridional flow through the advection term. This is what is thought to happen in the solar interior by a process is known as the ω-effect; weak poloidal field in the solar interior is stretched and wound up by differential rotation, to form a strong toroidal field shown in Figure 1.7a. The ω-effect is an important mechanism that is present in many current dynamo models.

(a)   (b)
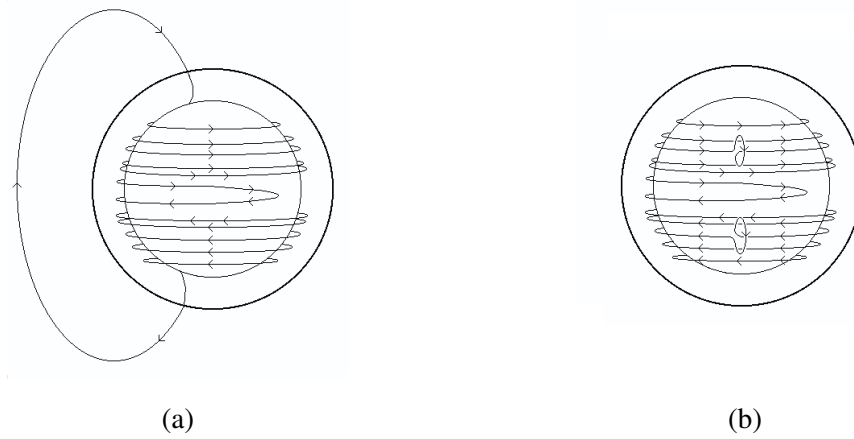
Figure 1.7: Visualisations of (a) the ω-effect and (b) the α-effect.

We know that for the magnetic field to be self-generating there must be a mechanism that in a sense 'closes the loop', by turning toroidal field back to poloidal field. By the same process the evolution of poloidal field can be expressed from (1.2) by

$$\frac{\partial}{\partial t}\left(rA\right) = -\boldsymbol{u_m} \cdot \boldsymbol{\nabla}\left(rA\right) + r\eta\left(\nabla^2 - \frac{1}{r^2}\right)A. \tag{1.4}$$

Here we notice there is no source term to generate the poloidal field and the field will just decay. As a result an axisymmetric magnetic field cannot be created by a self-generating dynamo (Cowling's Theorem). To maintain a field and close the loop a source term needs to be introduced in to equation (1.4). This can be achieved through the study of mean-field electrodynamics, and involves small scale non-axisymmetric motions (usually brought on by turbulence), coming together to generate large-scale poloidal field. This process is known as the α-effect, Figure 1.7b. A more detailed discussion on how the source term is derived can be found in Tobias & Weiss (2007).

1.2.2 Possible dynamo scenarios

It is generally accepted in most dynamo models that the ω-effect is a result of differential rotation. Therefore, the strong radial gradients of angular velocity present in the tachocline are extremely likely to play a crucial role in generating toroidal magnetic field. However, different models have a very different way of invoking the α-effect and

essentially closing the loop. This section outlines three main dynamo models used today, with comments on the positives and negative of each model. A more in depth discussion of these models can be found in Tobias & Weiss (2007).

The distributed dynamo, often known as the classic $\alpha\omega$-dynamo, relies on cyclonic eddies created by the Coriolis force to produce the turbulence required to generate an α-effect and thus poloidal field. Toroidal field is created either by local latitudinal differential rotation in the convection zone or by radial shear, either near the surface or possibly at the tachocline. The advantage of such a model is that it can be applied to any rotating star with a convection zone, even those that are fully convective without a tachocline. However, with this model it will be hard to generate large-scale magnetic field, as small-scale field will rise to the surface too fast before it has a chance to be amplified, especially if the dynamo is situated near the surface.

Another possibility is the flux transport dynamo. In this model poloidal field is wound up by differential rotation at the tachocline to form 'ropes' of toroidal field. This toroidal field rises to the surface, twisting due to the Coriolis force and emerges as active regions. Due to the twisting nature the active regions are of the form of sunspots and obey Joy's law. The field spreads in latitude and the two spots migrate. The proceeding spot migrates toward the equator, where it merges with the field from the other hemisphere and the fields cancel each other out. The following spot moves to higher latitudes and eventually reverses the polar field. The field at the poles is then transported down to the tachocline where it is sheared back into toroidal field and the process starts over. This dynamo was first envisioned by Babcock (1961) who tried to link Hale's law with the observed reversal of the polar fields. As such this model relies heavily on surface activity for a dynamo to exist. This leads to problems during periods when there is no surface activity such as the Maunder Minimum. As we have seen the magnetic cycle still exists during these low active periods, and there is no evidence to suggest that the dynamo shuts off during these times.

By estimating the rise times of strong magnetic flux tubes through the convection zone, Parker (1975) argued that the location of the solar dynamo is likely to be in the 'lowest levels of the convection zone'. In the same paper, Parker showed that strong magnetic

field could in fact be retained for a long time in the sub-adiabatic stratified radiative zone. This led to the possibility of an interface, or deep seated dynamo (Parker, 1993). From helioseismology results it seems logical that poloidal field is sheared out by the strong differential rotation to form toroidal field that is stored in the lower parts of the tachocline, where the atmosphere is convectively stable. The field can remain here until it becomes destabilised, possibly by magnetic buoyancy (see §2) and rises towards the surface. Field that does not reach the surface is thought to experience an α-effect, possibly through turbulence, in the convection zone. The weak poloidal field is then convectively pumped back down to the tachocline, where it is sheared back to toroidal field. This dynamo has the advantage of storing field down in the tachocline where it can be sufficiently amplified by shear without experiencing the any turbulent α-effects. However the exact nature of the α-effect and the process that transports poloidal field back down to the tachocline is still up for debate.

The work in this thesis relies heavily on the interaction between magnetic field and a velocity shear in a convectively stable environment, conditions similar what we expect at the tachocline. As such the exact location of the ω-effect and the resulting α-effect is not crucial to this work. Most models can agree that the tachocline is likely to play an important role in storing toroidal field, so that is can be sufficiently amplified by the inherently strong velocity shear. For the magnetic field to be displaced and rise into the convection zone and ultimately to the surface, it must undergo some sort of instability mechanism, which we believe to be magnetic buoyancy instability. The next chapter contains an overview of the magnetic buoyancy instability, describing the physical mechanism and past work.

Chapter 2

Magnetic buoyancy instability

2.1 Magnetic buoyancy

Somewhat confusingly in astrophysics the term *magnetic buoyancy* can be used to describe three related, but different mechanisms. The overarching idea of magnetic buoyancy was introduced by Parker (1955), and coincidentally, by Jensen (1955). Parker considered an isolated horizontal magnetic flux tube in pressure equilibrium with non-magnetic surroundings. Like him we denote p_i and p_e as the internal and external gas pressures, and define the magnetic pressure is terms of a field of strength B. Balancing total internal and external pressures, gives

$$p_i + \frac{B^2}{2\mu_o} = p_e. \tag{2.1}$$

The presence of magnetic pressure inside the tube therefore leads to a difference in internal and external gas pressure, with $p_i < p_e$. If we suppose the tube is in thermal equilibrium with its surroundings then it follows from the perfect gas law that $\rho_i < \rho_e$. Thus the tube is lighter than its surroundings and will rise under the influence of gravity. More a lack of equilibrium in the system than a true instability, Parker's example outlines the basic physics of the magnetic buoyancy.

Another example of the term magnetic buoyancy is used to describe an instability mechanism that advances on Parker's argument. It can be shown that in general magnetic

flux tubes are not in equilibrium with a non-magnetic surrounding fluid. Therefore, in order for an equilibrium state to be met, there must be a specific temperature difference between the tube and the atmosphere; the flux tube must be cooler than the surrounding fluid so that the internal and external densities are equal. From here the stability of such a tube can be addressed (Spruit & van Ballegooijen, 1982), and any instability found is a result of *magnetic buoyancy*.

The final use of the term is of particular interest for this thesis and is used to describe a convective type of instability resulting from a stratified magnetic field in a convectively stable, magnetised atmosphere. This instability allows a convectively stable atmosphere, such as that found at the tachocline, to become destabilised to a certain magnetic field configuration. In this chapter we focus on this definition of the term of magnetic buoyancy instability, presenting an overview of previous work, building up complexity as we proceed. An in-depth review on magnetic buoyancy instabilities, covering topics not discussed in this chapter, can be found in Hughes (2007).

2.1.1 The instability mechanism

The magnetic buoyancy instability mechanism can be understood through a simple parcel argument (Acheson, 1979). Consider an atmosphere in equilibrium in the presence of a horizontal magnetic field (in the x-direction) varying with height z. The relationship between pressure, density and the magnetic field can be expressed through the magnetohydrostatic equilibrium condition,

$$\frac{\mathrm{d}}{\mathrm{d}z}\left(p + \frac{B^2}{2\mu_0}\right) = -\rho g. \tag{2.2}$$

Throughout this thesis we will define gravity as $\mathbf{g} = -g\hat{\mathbf{z}}$. Suppose we take a 'parcel' of gas at height z in the layer and raise it, without bending magnetic field lines, to a new height $z + \mathrm{d}z$. This corresponds to what is known as an interchange instability, where the horizontal wave number is zero, $k_x = 0$. We denote the variables outside the gas parcel at height $z + \mathrm{d}z$ as $B + \mathrm{d}B$ for the field, $p + \mathrm{d}p$ for the gas pressure and $\rho + \mathrm{d}\rho$ for the density. Variables inside the parcel at this changed height we denote with a δ, such that

the field at this changed height is $B + \delta B$, etc. Since the mass and magnetic flux of the tube are conserved during the move, so is B/ρ and hence

$$\frac{B}{\rho} = \frac{B + \delta B}{\rho + \delta \rho} \quad \Rightarrow \quad \frac{\delta B}{B} = \frac{\delta \rho}{\rho}. \tag{2.3}$$

If we assume that the parcel moves adiabatically, then its specific entropy ($p\rho^{-\gamma}$) is conserved and to first order

$$\frac{p}{\rho^\gamma} = \frac{p + \delta p}{(\rho + \delta \rho)^\gamma} \quad \Rightarrow \quad \frac{\delta p}{p} = \gamma \frac{\delta \rho}{\rho}. \tag{2.4}$$

Finally we suppose the parcel moves slowly enough to maintain total pressure equilibrium with its surroundings, so that

$$p + \mathrm{d}p + \frac{(B + \mathrm{d}B)^2}{2\mu_0} = p + \delta p + \frac{(B + \delta B)^2}{2\mu_0}, \tag{2.5}$$

which to first order simplifies to

$$\mathrm{d}p + \frac{B\mathrm{d}B}{\mu_0} = \delta p + \frac{B\delta B}{\mu_0}. \tag{2.6}$$

Combining (2.3) and (2.4) with equation (2.6) leads to

$$\delta \rho \left(c^2 + a^2 \right) = \mathrm{d}p + \frac{B\mathrm{d}B}{\mu_0}, \tag{2.7}$$

where c is the adiabatic sound speed and a is the Alfvén speed, defined as

$$c^2 = \frac{\gamma p}{\rho}, \quad a^2 = \frac{B^2}{\rho \mu_0}. \tag{2.8}$$

Instability is guaranteed if the parcel is lighter than its surroundings, i.e. $\delta \rho < \mathrm{d}\rho$. Thus with some algebraic manipulation, equation (2.7) can be transformed into a criterion for instability, that states instability is guaranteed provided

$$\frac{-ga^2}{c^2} \frac{\mathrm{d}}{\mathrm{d}z} \ln \left(\frac{B}{\rho} \right) > N^2, \tag{2.9}$$

where N is the Brunt-Väisälä (or buoyancy) frequency, defined as

$$N^2 = \frac{g}{\gamma} \frac{\mathrm{d}}{\mathrm{d}z} \ln \left(p\rho^{-\gamma} \right). \tag{2.10}$$

The inequality (2.9) tells us that a horizontal magnetic field that decreases 'sufficiently' with height can destabilise a convectively stable atmosphere ($N^2 > 0$). As discussed

in §1.1, the tachocline has a sub-adiabatically stratified atmosphere; therefore magnetic buoyancy is a perfectly feasible instability for breaking up the strong toroidal field stored there.

Equation (2.9) was also derived more formally by Newcomb (1961), using the energy principle of Bernstein et al. (1958). Studying an ideal gas in the presence of a stratified horizontal field, Newcomb showed that for modes that do not bend field lines (interchange modes), instability occurs when (2.9) is satisfied somewhere in the fluid. He expressed the instability criteria as

$$\frac{\mathrm{d}\rho}{\mathrm{d}z} > -\frac{\rho g}{c^2 + a^2}. \tag{2.11}$$

This resembles a magnetic extension to Schwarzschild criterion for convection, although when written in this form the influence of the magnetic field gradient is not obvious. It can be shown using the magnetohydrostatic balance condition (2.2), that (2.9) and (2.11) are in fact equivalent.

Although doing a good job of outlining the basic mechanism involved in magnetic buoyancy instability, the above calculations are gross simplifications to the full problem. The obvious extension to this work would be to consider fully three-dimensional perturbations, capable of bending the magnetic field lines (undular modes). Instinctively one might assume that doing work against magnetic tension, by bending field line would inhibit the instability. However, Newcomb (1961) went on to show the somewhat surprising result that three-dimensional perturbations with $k_x \to 0$, are in fact more readily destabilised than interchange modes. These types of modes are unstable if somewhere in the fluid,

$$\frac{\mathrm{d}\rho}{\mathrm{d}z} > -\frac{\rho g}{c^2}. \tag{2.12}$$

Again at first sight this may be viewed as the non-magnetic Schwarzschild criterion. However, as addressed by Thomas & Nye (1975), the role played by the magnetic field can again be made explicit by using the magnetohydrostatic balance (2.2), and writing (2.12) as

$$\frac{-ga^2}{c^2}\frac{\mathrm{d}}{\mathrm{d}z}\ln B > N^2. \tag{2.13}$$

By analysing (2.9) and (2.13), we see that the interchange modes require a sufficient decrease of B/ρ in height for instability, whereas the undular modes require only a

decrease in B, much less of a constraint on the magnetic field. For two-dimensional perturbations, (2.13) is a necessary but not sufficient condition for instability. As such there exist magnetostatic equilibria such that interchange modes are stable and undular modes are unstable.

As addressed by Hughes & Cattaneo (1987) the physical mechanism related to the interchange instability when $k_x = 0$, is very different to the mechanism for the undular mode instability when $k_x \to 0$. We can summarise their findings by again considering a parcel of fluid raised through the atmosphere. Interchange modes do not bend field lines, so moving the parcel will either bring field lines further apart or closer together. As a result the perturbed gas pressure is in a sense 'coupled' with the magnetic pressure perturbation, and one cannot be altered without having to alter the other. For undular modes this restriction no longer applies; by allowing the bending of field lines, compressive motions move along the magnetic field lines and thus do no work against magnetic pressure. Therefore when considering undular modes, gas and magnetic pressure perturbations is no longer coupled. Naturally three-dimensional perturbations do bring a stabilising factor through magnetic tension, however this is minimised when $k_x \to 0$.

2.1.2 The influence of diffusion

Up to this point, all discussion in this chapter has considered only ideal (diffusionless) instabilities. To advance and bring things into a more physical context, it is beneficial to extent the analysis to include the effects of diffusion. Acheson (1979) gives the instability criteria for non zero thermal and magnetic diffusion, in the absence of viscosity as

$$\frac{-ga^2}{c^2} \frac{\mathrm{d}}{\mathrm{d}z} \ln \left(\frac{B}{\rho} \right) > \frac{\eta}{\kappa} N^2, \tag{2.14}$$

for $k_x = 0$ (interchange) modes, and

$$\frac{-ga^2}{c^2} \frac{\mathrm{d}}{\mathrm{d}z} \ln B > a^2 k_x^2 \left(1 + \frac{k_z}{k_y} \right) + \frac{\eta}{\kappa} N^2, \tag{2.15}$$

for $k_x \neq 0$ (undular) modes. Here the magnetic diffusivity η and thermal diffusivity κ are taken as constant, with k_y and k_z denoting the y and z wave numbers respectively. These

criteria are valid provided that $\eta \ll \kappa$ for finite η and κ, a physically realistic parameter region for the solar interior. In this astrophysical limit the dependence on the buoyancy frequency N^2 in the equations is reduced. Hence, it is possible to have instabilities in the presence of diffusivities, where for the same field and atmospheric configuration, instability criteria (2.9) and (2.13) are not satisfied and the ideal system is stable.

Gilman (1970) considered modes with a short transverse wavenumber ($k_y \to 0$), that consequently would be able to rapidly exchange heat with their surrounds ($\kappa \to 0$) and maintain their magnetic buoyancy. Gilman's criteria can be recovered from equations (2.14) and (2.15) by applying $\eta/\kappa \to 0$ and taking the $k_y \gg k_z$ limit.

It can be shown that in the presence of thermal and magnetic diffusion, convection incorporating magnetic buoyancy is indeed a double diffusive system; Spiegel & Weiss (1982) transformed the equations for interchange instabilities to a form identical to that describing two-dimensional thermosolutal convection, a highly studied system (see Turner, 1973). This transformation is not in what may be thought of as the 'obvious fashion' (thermal gradient mapped to entropy gradient, and salinity gradient mapped to magnetic field), but instead maps thermal gradient to a linear combination of both entropy and magnetic field gradient and salinity gradient mapped directly to magnetic field. Therefore direct comparisons are hard to make.

In the absence of diffusion it is only possible to have direct modes of instability - a purely real growth rate. With the analogue to thermosolutal convection, it is of no surprise that the fully diffusive system also supports oscillatory instability (overstability), where the growth rate has a non-zero frequency. Hughes (1985a) derived an instability criteria for oscillatory interchange modes, given by

$$\frac{-ga^2}{c^2}(\eta + \nu - \kappa(\gamma - 1))\frac{\mathrm{d}}{\mathrm{d}z}\ln\left(\frac{B}{\rho}\right)$$
$$> (\kappa + \nu)(\kappa + \eta)(\nu + \eta)\frac{(k_x + k_z)^6}{k_x^2} + (\kappa + \nu)N^2, \qquad (2.16)$$

for constant kinematic viscosity ν. Hughes identified the important role of the coefficient $\eta + \nu - \kappa(\gamma - 1)$ multiplying the gradient terms. Specifically that when $\eta + \nu < \kappa(\gamma - 1)$, overstability of a convectively stable atmosphere ($N^2 > 0$) could occur in the presence of a bottom heavy field gradients (B/ρ increasing with height).

This is a somewhat counter-intuitive result, especially when making comparisons to thermosolutal convection, where instability is not possible when both the thermal and salinity gradients are stabilising.

When considering the influence of diffusion on three-dimensional undular modes, Hughes (1985a) noted that it is possible to stabilise certain unstable top heavy field gradients (B decreasing with height), by making them more top heavy. This is another somewhat unexpected result, especially when we consider what we observed in the diffusionless criteria, equation (2.13). For all modes of instability the viscosity plays a purely stabilising role, with the interesting behaviour resulting from a competition between magnetic and thermal diffusivities. For further reading on the physical mechanism of the diffusive instabilities we refer the reader to Hughes (1985a) and Hughes & Proctor (1988).

2.1.3   The influence of a velocity shear flow

As discussed in §1.2.2 many dynamo models suggest the tachocline is an ideal location for the storage of the bulk toroidal field, before it undergoes magnetic buoyancy instability. Due to the strong radial shear that exists at the tachocline, it is only natural to study the interaction between shear flows and magnetic buoyancy instability. Tobias & Hughes (2004) extended the work of Adam (1978), and considered the linear stability of a stratified magnetic field $\boldsymbol{B} = B(z)\hat{\boldsymbol{x}}$ and an aligned shear flow $\boldsymbol{U} = U(z)\hat{\boldsymbol{x}}$, under the assumptions of ideal (diffusionless), fully compressible MHD. Starting from the energy principle of Bernstein et al. (1958) they derived they derived two stability criteria. The first is that stability is guaranteed if there exists a constant U_0, such that everywhere both

$$(U - U_0)^2 = \widetilde{U}^2 < c_T^2, \tag{2.17}$$

and

$$\widetilde{U}^2 \leq \frac{a^2(c^2\rho' + \rho g)}{(a^2 + c^2)\rho' + \rho g}, \tag{2.18}$$

are satisfied. In above equations the prime notation denotes a derivative with respect to height z, and c_T is the tube speed, defined by

$$c_T^2 = \frac{a^2 c^2}{a^2 + c^2}. \tag{2.19}$$

The second stability criteria involves the derivative of $\widetilde{U}$ and is a little more complicated: stability is assured if, everywhere, (2.17) is satisfied and

$$
\frac{d}{\mathrm{d}z}\left(\frac{\rho g k_x^2 \widetilde{U}^2 (a^2 - \widetilde{U}^2)}{(k_x^2 + k_y^2)(a^2 + c^2)(c_T^2 - \widetilde{U}^2) + k_x^2 \widetilde{U}^4}\right)
$$
$$
\leq -g\frac{d\rho}{\mathrm{d}z} + \rho k_x^2 (a^2 - \widetilde{U}^2) - \frac{\rho g^2 (k_x^2 + k_y^2)(a^2 - \widetilde{U}^2)}{(k_x^2 + k_y^2)(a^2 + c^2)(c_T^2 - \widetilde{U}^2) + k_x^2 \widetilde{U}^4}. \tag{2.20}
$$

In the absence of shear, this criteria becomes equation (2.11) when $k_x = 0$ and equation (2.12) when $k_x \to 0$. The interesting result to come out of equation (2.20), is that for the same k_x and k_y, an atmosphere that is stable to magnetic buoyancy instabilities remains stable when an aligned shear is introduced.

The above criteria are all conditions to guarantee stability and unfortunately tell us nothing about the influence of shear on unstable modes. To proceed we are required to adopt numerical techniques to solve the linear eigenvalue problem. As one might physically expect, it can be shown that a shear flow aligned with the magnetic field has no influence on the interchange ($k = 0$) instability. Therefore of more interest is the influence of a shear flow on the full three-dimensional undular mode. Tobias & Hughes (2004) investigated this by adding a shear flow to an undular mode that was already unstable in the absence of shear. They found that although for some undular modes a weak shear was slightly destabilising, ultimately the shear had a stabilising effect. Along with this they found that increasing the magnitude of the shear had an axisymmetric effect - the preferred mode of instability moved to a lower k_x value as shear strength increased. The stabilisation effect was maximized by introducing a shear flow that is localised at the some height z_c, where z_c is defined as the peak in the eigenfunction solution for the same atmosphere in the absence of shear. The localisation of the shear also has a dramatic effect of the resulting eigenfunctions. The eigenfunctions in the absence of shear are either completely real or imaginary, with a fairly simple z dependency. When velocity shear is added the eigenfunctions become complex, with real and imaginary parts, and have a much more complicated structure to the z dependency of the eigenfunction.

2.1.4 The influence of rotation

Although not revisited in the thesis, for completeness we touch upon the influence of rotation. From Newcomb (1961) one can express the order of magnitude for the growth rate (s) of an interchange mode under the influence of magnetic buoyancy as

$$s^2 \sim \frac{gB^2}{\gamma\mu_0 p} \frac{\mathrm{d}}{\mathrm{d}z} \ln\left(\frac{B}{\rho}\right). \tag{2.21}$$

Approximating $\mathrm{d}_z B$ by $1/d$, Hughes (2007) gave a simple estimate of the order of magnitude for the growth time (T) of a direct magnetic buoyancy instability

$$T \sim \frac{c}{a}\left(\frac{d}{g}\right)^{1/2}. \tag{2.22}$$

At the tachocline a typical value for the plasma beta (the ratio between gas pressure and magnetic pressure, $\beta = 2c^2/(\gamma a^2)$ in our notation) is around $\beta = 10^8$. Adopting this value for β along with $d = 0.03R_\odot$ and g from Table 1.1 gives a growth time of approximately of $T \approx 28$ days. As this magnitude is comparable to the solar rotation period, we expect rotation to have an influential role on magnetic buoyancy instability. A comprehensive study of the influence of differential rotation on magnetic buoyancy instability can be found in Acheson (1978). This is a very complex problem where analytic progress is not possible without certain approximations to simplify the problem. The simplest of such would be the interchange mode in the absence of diffusion, for which modes are unstable providing

$$\frac{-ga^2}{c^2} \frac{\mathrm{d}}{\mathrm{d}z} \ln\left(\frac{B}{\rho}\right) > 4\Omega^2 + N^2, \tag{2.23}$$

where Ω denotes a uniform angular velocity. Here the angular velocity has a purely stabilising role and is of little interest. By adding more complexity to the system the role of rotation becomes more interesting. When considering undular modes in a double diffusive (magnetic and thermal) rapidly rotating system Acheson (1978) showed a somewhat surprising result, that increasing the stable stratification N^2, could have a destabilising affect. It is worth noting that for large enough N^2 the overall effect is still stabilising. Hughes (1985b) and Schmitt & Rosner (1983) both studied the dispersion relation of the system and solved it numerically. When focusing on parameter values that

resemble that of the tachocline, Schmitt & Rosner (1983) found both the high and low frequency undular modes are unstable. Interestingly for both the high and low frequency instability the growth rates are comparable, however the meridional wave numbers are very different. Hughes (1985b) derived stability boundaries for the different types of present modes. Hughes found that unlike the non-rotating system, where viscosity played a purely stabilising role, the inclusion of rotation allows viscosity to destabilise certain modes. As shown through these few examples, even the simple case of including a uniform rotation, introduces considerable complexity to the system.

2.1.5 Non-linear evolution

Of course, up to this point, all studies of magnetic buoyancy discussed in this chapter have been strictly linear. Since perturbations cannot grow exponentially forever, the linear study can only describe the initial evolution of the instability, after which non-linear effects must play a role. If the magnetic field we observe as surface features is indeed linked to the toroidal field destabilised by magnetic buoyancy at the tachocline, then it must have undergone non-linear interactions. Therefore, the question is whether or not the non-linear evolution can give rise to isolated regions of strong field (flux tubes), similar to what we observe at the surface. Cattaneo & Hughes (1988) considered the non-linear evolution of the interchange instability of a uniform magnetic field, surrounded by a non-magnetic atmosphere. The presence of the magnetic field allows the convectively stable atmosphere to hold more mass, creating an interface layer in the fluid susceptible to a Rayleigh–Taylor type of instability. Once the Rayleigh–Taylor instability has taken a hold it gives rise to a local shear, thereby exciting secondary Kelvin–Helmholtz instabilities. This instability wraps up the fluid into regions of strong vorticity, at which point the evolution is then dominated by the interaction of neighbouring vortices. This interaction can lead to downward motion of the fluid despite the inherent buoyancy properties. Therefore, even though the field is wound up into concentrated regions, the resulting 'flux tubes' are not transported to the surface.

Cattaneo et al. (1990) considered a similar model (interchange modes in a non-magnetic atmosphere), in the the presence of a weakly sheared magnetic field $\mathbf{B} = (B_x, B_y, 0)$,

with $B_x > B_y$. The problem is set up such that there exists a 'resonant layer', defined as a point in the layer at which the B_y vanishes. As with the previous model, a Rayleigh–Taylor type of instability is present at the interface of the field. If the resonant layer is close to this interface the non-linear instability produces small-scale flux, this resulting flux only affects a small proportion of the overall field and the fluid remains stable. However, if the resonant layer is situated deep in the magnetic region, the instability affects the whole field, resulting in coherent structures that are maintained as they rise.

The models discussed above describe the evolution of interchange (axisymmetric) modes, however it is without doubt that the field we observe at the surface must have experienced some sort of undulatory (non-axisymmetric) instability. Matthews et al. (1995) studied the fully three-dimensional, non-linear evolution of the magnetic buoyancy instability for a uniform field in a non-magnetic atmosphere. The initial evolution is very similar to that described in Cattaneo & Hughes (1988); the fluid initially experiences a two-dimensional, Rayleigh–Taylor type of instability and is then wrapped in coherent vortices by a secondary Kelvin–Helmholtz instability. The vortices are now susceptible to a three-dimensional instability, which causes the associated magnetic field to become arched. The resulting field resembles a 'kinked' flux tube, which one can envision bursting through the photosphere, creating a bipolar sunspot pair.

Chapter 3

Incorporating velocity shear into the magneto-Boussinesq approximation

Instabilities driven by magnetic buoyancy are by nature compressible, with magnetic pressure playing a crucial role in reducing the local density of the gas. Therefore, as a result, studies of magnetic buoyancy instabilities often opt to investigate a fully compressible system. However, just as the Boussinesq approximation for thermal convection can simplify the equations of a non-magnetic compressible system to that of an incompressible system (Spiegel & Veronis, 1960), a similar process can be applied to simplify the equations of magnetic buoyancy instability (the magneto-Boussinesq approximation Spiegel & Weiss, 1982). These simplifications to the governing equations aid us both analytically and numerically.

Section 3.1 provides a more detailed review of the aforementioned approximations, providing the appropriate foundation for the work in §3.2, which contains the main results of the chapter. The main results of this chapter can also be found in Bowker et al. (2014). Before we advance, it is convenient to introduce the governing equations used throughout this chapter. In standard notation the magnetohydrodynamic (MHD) equations for a

perfect gas are:

$$\partial_t \rho + \boldsymbol{\nabla} \cdot (\rho \boldsymbol{u}) = 0, \tag{3.1a}$$

$$\rho \left(\partial_t + \boldsymbol{u} \cdot \boldsymbol{\nabla} \right) \boldsymbol{u} = -\boldsymbol{\nabla} \Pi - g \rho \hat{\boldsymbol{z}} + \mu_0^{-1} \boldsymbol{B} \cdot \boldsymbol{\nabla} \boldsymbol{B} + \boldsymbol{F} + \boldsymbol{\nabla} \cdot \boldsymbol{\tau}, \tag{3.1b}$$

$$\left(\partial_t + \boldsymbol{u} \cdot \boldsymbol{\nabla} \right) \boldsymbol{B} = \boldsymbol{B} \cdot \boldsymbol{\nabla} \boldsymbol{u} - \boldsymbol{B} (\boldsymbol{\nabla} \cdot \boldsymbol{u}) + \eta \nabla^2 \boldsymbol{B}, \tag{3.1c}$$

$$\boldsymbol{\nabla} \cdot \boldsymbol{B} = 0, \tag{3.1d}$$

$$\rho C_p \left(\partial_t + \boldsymbol{u} \cdot \boldsymbol{\nabla} \right) T - \left(\partial_t + \boldsymbol{u} \cdot \boldsymbol{\nabla} \right) p = K \nabla^2 T + \eta \mu_0^{-1} (\boldsymbol{\nabla} \times \boldsymbol{B})^2 + \Phi, \tag{3.1e}$$

$$p = R \rho T, \tag{3.1f}$$

where $\hat{\boldsymbol{z}}$ is the unit vector in the vertical direction, Π is the total pressure, consisting of the sum of the gas pressure p and the magnetic pressure $p_m = B^2/2\mu_0$, $\boldsymbol{F}$ is a body force and the viscous heating terms Φ are defined in terms of the stress tensor τ_{ij} as

$$\Phi = \tau_{ij} \partial_i u_j, \quad \text{where} \quad \tau_{ij} = \mu \left(\partial_i u_j + \partial_j u_i - \tfrac{2}{3} \delta_{ij} \partial_k u_k \right). \tag{3.2}$$

The specific heat at constant pressure C_p, the permeability μ_0, the magnetic diffusivity η, the thermal conductivity K, the gas constant R and the dynamic viscosity μ are all taken as constant. Although we shall assume a perfect gas throughout, the main ideas of this chapter still hold for a more general equation of state.

3.1 Boussinesq approximations

Spiegel & Veronis (1960) derived the hydrodynamic equations of the Boussinesq approximation for a compressible fluid, when considering the problem of thermal convection in a layer $0 < z < d$. Under two important assumptions discussed below Spiegel & Veronis were able drastically simplify the governing equations ((3.1) with $\boldsymbol{B} = 0$). As a result the fluid can be treated as incompressible, with density perturbations ignored everywhere except where they are coupled to the gravitational acceleration in the buoyancy force. Furthermore, fluctuations in gas pressure are deemed small, and thus density variations are directly proportional to variations in temperature. Since sound waves move via pressure variations this approximation has the physical effect of filtering out sound waves from the governing equations. The simplified equations are used to

model a variety of flows that appear both in nature and industry, and prove to be a very accurate approximation.

To examine the assumptions used by Spiegel & Veronis (1960) mathematically we express variables of density ρ, temperature T, and pressure p as

$$f(\boldsymbol{x}, t) = f_* + f_0(z) + f'(\boldsymbol{x}, t), \tag{3.3}$$

where f_* is the (constant) averaged value of f; f_0 is the basic state variations in the absence of motion; and f' is the fluctuation as a result of motion. Using this notation, the magnitude of scale heights of H_ρ, H_T and H_p are defined by

$$H_f = \left| \frac{1}{f_*} \frac{\mathrm{d}f_0}{\mathrm{d}z} \right|^{-1}. \tag{3.4}$$

The first assumption made in the classic Boussinesq approximation is that layer depth d, is much smaller than the smallest scale height $(H_f)_{\mathrm{min}}$. For consistency with Spiegel & Veronis (1960), we say that this condition holds for all the thermodynamic quantities, thus in particular the first assumption leads to

$$\frac{d}{H_\rho} \ll 1. \tag{3.5}$$

Upon integrating this condition over the layer and defining $\Delta f = f_0(d) - f_0(0)$ to be the variation of f_0 across the layer, Spiegel & Veronis (1960) introduce a small quantity ϵ denoted by

$$\epsilon = \frac{\Delta \rho_0}{\rho_*} \ll 1. \tag{3.6}$$

This is merely a statement regarding the basic state, derived from the assumption that density varies on a very long scale relative to the size of the layer under study.

The second assumption comes from a restriction on the induced fluctuations. Specifically, it says that the motion-induced perturbations do not exceed the magnitude of their static variations, i.e.

$$\left| \frac{\rho'}{\rho_*} \right| \leq \mathrm{O}\left(\epsilon \right). \tag{3.7}$$

This condition guarantees that non-linear terms do not dominate linear terms in the equations, and must be verified *a posteriori* from solutions of the problem. By substituting

the thermal quantities of the form (3.3) into the governing equations (3.1) and making the use of the two assumptions (3.5) and (3.7), Spiegel & Veronis (1960) were able to derive a set of leading order equations known as the Boussinesq equations. Upon dropping the $'$ notation of (3.3), the approximated equations are:

$$\boldsymbol{\nabla} \cdot \boldsymbol{u} = 0, \tag{3.8a}$$

$$(\partial_t + \boldsymbol{u} \cdot \boldsymbol{\nabla}) \boldsymbol{u} = -\frac{1}{\rho_*} \nabla p - \frac{g}{\rho_*} \rho \hat{\boldsymbol{z}} + \nu \nabla^2 \boldsymbol{u}, \tag{3.8b}$$

$$(\partial_t + \boldsymbol{u} \cdot \boldsymbol{\nabla}) T + \left(\frac{\partial T_0}{\partial z} + \frac{g}{C_p} \right) w = \kappa \nabla^2 T, \tag{3.8c}$$

$$\frac{\rho}{\rho_*} = -\frac{T}{T_*}, \tag{3.8d}$$

where the kinematic viscosity and the thermal diffusivity are defined as $\nu = \mu/\rho_*$ and $\kappa = K/\rho_* C_p$ respectively. As a result of the assumptions (3.5) and (3.7) all density variations terms in the mass conservation equation (3.8a) are formally $\mathrm{O}(\epsilon)$ smaller than that of $\boldsymbol{\nabla} \cdot \boldsymbol{u}$ and hence neglected from the equation. Since the focus is on a buoyancy driven flow we cannot neglect the variation in density everywhere; it is important that the buoyancy term in the momentum equation is of equal magnitude to the characteristic acceleration. This is enforced through the scaling

$$\frac{\partial w}{\partial t} \sim g \frac{\rho}{\rho_*}, \tag{3.9}$$

where w is the vertical fluid motion. Here $\sim$ is the notation used to indicate similar magnitudes and is used throughout the thesis. With this ordering it can be shown that the flow remains highly subsonic throughout, i.e. $\boldsymbol{u}^2 \ll p_*/\rho_*$. To ensure pressure perturbations also remain relevant in the momentum equation it is required that p' is $\mathrm{O}\left(d/H_p\right)$ smaller than the perturbation of density. Consequently pressure perturbations are neglected in the equation of state (3.8d). To conclude, provided that both conditions (3.5) and (3.7) are met, a compressible hydrodynamic fluid can in a sense be treated as incompressible, with density perturbations only appearing through the buoyancy term in the momentum equation.

With their focus on magneto-convection, Proctor & Weiss (1982) added a constant magnetic field into the Boussinesq equations in a fairly straight forward manner. As

one would expect the field enters the equations via the induction equation (3.1c) and through the Lorentz force $\boldsymbol{B} \cdot \boldsymbol{\nabla} \boldsymbol{B}$ in the momentum equation (3.1b). Magnetic pressure is assumed to be small, in that it has no influence on the density fluctuations. However, to include the effects of magnetic buoyancy, a stratified magnetic field is required, and a more subtle approach is needed. Spiegel & Weiss (1982) considered this problem and implemented a horizontal, stratified magnetic field, with scale height H_B. They assumed that H_B was comparable to the pressure scale height H_p (which itself was comparable to the scale heights of the other thermodynamic quantities), and hence much larger than the height of the layer d. They also assumed that this magnetic field was sufficiently weak, such that the Alfvén speed was small compared with the sound speed, $B^2/\mu_0\rho_* \ll p_*/\rho_*$. The crucial ordering they adopted is that the fluctuations in total pressure $(p + p'_m)$ are small. As a result, variations in magnetic pressure, density and temperature are comparable, and magnetic pressure now enters into both the momentum and energy equation. This is formally shown in more detail in §3.2.4, specifically equations (3.34), (3.35) and (3.36).

A final feature of the approximation introduced by Spiegel & Weiss (1982), is that magnetic buoyancy instability is only relevant for certain modes, namely where the horizontal length scale, L, in the direction of the imposed field is large and of the same order as the pressure scale height, $L \sim H_p$. The effects of this assumption can be seen when considering the solenoidal condition. Suppose we split the nabla operator into two components, one aligned with the basic state field $\boldsymbol{\nabla}_\parallel$ and the other perpendicular to the field, $\boldsymbol{\nabla}_\perp$, such that $\boldsymbol{\nabla} = \boldsymbol{\nabla}_\parallel + \boldsymbol{\nabla}_\perp$. The magnitude of $\boldsymbol{\nabla} \cdot \boldsymbol{u}$ can then be split into two parts,

$$\boldsymbol{\nabla}_\parallel \cdot \boldsymbol{u} \sim \frac{u}{H_p} \quad \text{and} \quad \boldsymbol{\nabla}_\perp \cdot \boldsymbol{u} \sim \frac{u}{d}. \tag{3.10}$$

In the orderings (3.10), we have made the subtle assumption that the magnitude of all the components of the velocity perturbation are equal. Consequently to leading order the flow is not fully solenoidal; instead the mass equation (3.1a) becomes

$$\boldsymbol{\nabla}_\perp \cdot \boldsymbol{u} = 0, \tag{3.11}$$

and the full solenoidal condition is satisfied only to $\mathrm{O}\,(d/H_p)$. Similar logic can be applied to the solenoidal condition for the magnetic field; thus at leading order,

equation (3.1d) becomes

$$\boldsymbol{\nabla}_{\perp} \cdot \boldsymbol{b} = 0, \tag{3.12}$$

where $\boldsymbol{b}$ represents the perturbation of the magnetic field. Defining the basic state horizontal field as $\boldsymbol{B} = B_0(z)\hat{\boldsymbol{x}}$ and sticking with previously introduced notation, the leading order magneto-Boussinesq equations are:

$$\boldsymbol{\nabla}_{\perp} \cdot \boldsymbol{u} = 0, \tag{3.13a}$$

$$\rho_* \left(\partial_t + \boldsymbol{u} \cdot \boldsymbol{\nabla}_{\perp}\right)\boldsymbol{u} = -\boldsymbol{\nabla}_{\perp}\Pi - g\rho\hat{\boldsymbol{z}} + \frac{1}{\mu_0}\left(\boldsymbol{B}_0 \cdot \boldsymbol{\nabla}_{\parallel} + \boldsymbol{b} \cdot \boldsymbol{\nabla}_{\perp}\right)\boldsymbol{b}$$

$$+ \frac{1}{\mu_0}\boldsymbol{B}_0'b_z + \rho_*\nu\nabla_{\perp}^2\boldsymbol{u}, \tag{3.13b}$$

$$(\partial_t + \boldsymbol{u} \cdot \boldsymbol{\nabla}_{\perp})\boldsymbol{b} + \boldsymbol{B}_0'w = \left(\boldsymbol{B}_0 \cdot \boldsymbol{\nabla}_{\parallel} + \boldsymbol{b} \cdot \boldsymbol{\nabla}_{\perp}\right)\boldsymbol{u}$$

$$- \frac{w}{H_\rho}\boldsymbol{B}_0 + \eta\nabla_{\perp}^2\boldsymbol{b}, \tag{3.13c}$$

$$\boldsymbol{\nabla}_{\perp} \cdot \boldsymbol{b} = 0, \tag{3.13d}$$

$$(\partial_t + \boldsymbol{u} \cdot \boldsymbol{\nabla}_{\perp})\left(T + \frac{1}{\rho_* C_p}p_m\right) + \left(T_0' + \frac{g}{C_p}\right)w = \kappa\nabla_{\perp}^2 T, \tag{3.13e}$$

$$\frac{\rho}{\rho_*} = -\frac{p_m}{p_*} - \frac{T}{T_*}, \tag{3.13f}$$

where $'$ denotes the derivative of basic state variables with respect to z. As note by Corfield (1984), for asymptotic consistency this approximation requires the resulting magnetic perturbations $\boldsymbol{b}$ to be $\mathrm{O}\left(d/H_p\right)$ smaller than basic state field. Together with the fact that $\boldsymbol{\nabla} \cdot \boldsymbol{u} = 0$ is not fully satisfied, this feature of the approximation has an interesting knock-on effect. Specifically, that the next order correction to $\boldsymbol{\nabla} \cdot \boldsymbol{u}$ is required when dealing with $\boldsymbol{B}(\boldsymbol{\nabla} \cdot \boldsymbol{u})$ in the induction equation. Including higher order terms in the mass conservation equation, we can express the next order correction as

$$\boldsymbol{\nabla} \cdot \boldsymbol{u} \approx \frac{w}{H_\rho}. \tag{3.14}$$

It is then this approximation for $\boldsymbol{\nabla} \cdot \boldsymbol{u}$ that appears in leading order induction equation (3.13c). This result is formally shown in §3.3.2. The magneto-Boussinesq equations (3.13) of Spiegel & Weiss (1982) were later re-derived by Corfield (1984) through an asymptotic scaling analysis.

3.2 Incorporating velocity shear into the magneto-Boussinesq approximation

This section builds upon the work of Spiegel & Weiss (1982) to introduce the effects of velocity shear into the magneto-Boussinesq approximation, in such a way that the influence of velocity shear is comparable to that of the magnetic buoyancy instability. As we shall see in §3.2.1, this is not as straightforward as one might imagine and consequently it becomes necessary to take a more in-depth look at the orderings involved in the magneto-Boussinesq equations. This is tackled in §3.2.2 where, in a similar fashion to Corfield (1984), we derive the scalings inherent to the magneto-Boussinesq equations in the absence of shear. However unlike previous derivations that assumed the magnetic field scale height H_B to be the same size as H_p from the onset, we make no prior assumption on the size of H_B. This, in turn, allows us to derive a set of equations that are consistent with the Boussinesq approximation but with a smaller magnetic field scale height. As addressed by Hughes (1985a), this ordering is not possible straight from the equations of Spiegel and Weiss.

Section 3.2.3 introduces a horizontal velocity shear flow, that depends on height z, with scale height H_u. By striking the appropriate balances between terms introduced with the shear and those present from §3.2.2, we derive the necessary scalings for the field and flow, such that both the effects of magnetic buoyancy and the velocity shear are accounted for in the final equations. The resulting scalings allow us to derive asymptotically consistent magneto-Boussinesq equations that incorporate the effects of an influential velocity shear (§3.2.4).

The crucial differences between the magneto-Boussinesq equations of Spiegel & Weiss (1982) and these new equations are then discussed in §3.3. Finally, by making no prior assumption on the size of H_B and H_U we are able to produce a set of mixed-order equations that allow us to make a transition between six possible systems, depending on the choice of certain parameters (§3.3.2).

3.2.1 Naïvely adding shear

If one were to naïvely introduce an arbitrary velocity shear into the magneto-Boussinesq equations of Spiegel & Weiss (1982) (equations (3.13)), one would do so in a manner such that the velocity shear is of the same size as the resulting velocity perturbations. Here we show that when applying a shear in this 'obvious' manner, it has no effect on the linear stability of the diffusionless system.

Suppose that we consider a basic state magnetic field of the form

$$\boldsymbol{B}_0 = B_* \left(1 - \frac{\zeta z}{d} \right) \hat{\boldsymbol{x}}, \tag{3.15}$$

where $\zeta = \mathrm{O}(d/H_p)$. In addition, we consider an aligned basic state velocity shear $\boldsymbol{U}_0 = U_0(z)\hat{\boldsymbol{x}}$, i.e. an arbitrary function of z with scale height H_U. We shall consider separately the two cases of $H_U = \mathrm{O}(d)$ and $H_U = \mathrm{O}(H_p)$.

(i) $H_U \sim d$

As a consequence of the ordering of $\partial_x \sim 1/H_B \sim 1/H_p$, the advective term, $\boldsymbol{U} \cdot \nabla \boldsymbol{u}$, is $\mathrm{O}(d/H_p)$ smaller than the shear term $\boldsymbol{u} \cdot \nabla \boldsymbol{U}$, and hence is neglected. On following Spiegel & Weiss (1982) by linearising the governing equations, ignoring all diffusivities, and adopting d as the unit of length and the Alfvén period d/c_A as the unit of time, we obtain the dimensionless equations,

$$\partial_t \boldsymbol{u} + \boldsymbol{U}_0' w = -\boldsymbol{\nabla}_\perp \Pi + \varepsilon_1 b_x \hat{\boldsymbol{z}} + \partial_x \boldsymbol{b} - \zeta b_z \hat{\boldsymbol{x}}, \tag{3.16}$$

$$\partial_t \boldsymbol{b} - \zeta w \hat{\boldsymbol{x}} = \partial_x \boldsymbol{u} + \boldsymbol{U}_0' b_z - \varepsilon_1 w \hat{\boldsymbol{x}}, \tag{3.17}$$

where $\varepsilon_1 = d/H_p$ and $'$ denotes the derivative with respect to z. For simplicity we have taken an adiabatic atmosphere ($T_0' = -g/C_p$) and made the substitution $T = -p_m/(C_p \rho_*)$ from equation (3.13e). Since $\boldsymbol{\nabla}_\perp \cdot \boldsymbol{u} = 0$ and $\boldsymbol{\nabla}_\perp \cdot \boldsymbol{b} = 0$, we may introduce stream and flux functions, ψ and χ, such that

$$\boldsymbol{u} = \left(u, -\frac{\partial \psi}{\partial z}, \frac{\partial \psi}{\partial y} \right), \quad \boldsymbol{b} = \left(b_x, -\frac{\partial \chi}{\partial z}, \frac{\partial \chi}{\partial y} \right), \tag{3.18}$$

where

$$u(x, y, z, t) = \hat{u}(z) \exp(ikx + ily + pt), \text{ etc.} \tag{3.19}$$

Substituting expressions (3.19) into the x-component of the momentum equation (3.16) and its curl gives, after dropping the hats,

$$pu + ilU_0'\psi = ikb_x - il\zeta\chi, \tag{3.20}$$

$$p\left(-l^2\psi + \psi''\right) = il\varepsilon_1 b_x + ik\left(-l^2\chi + \chi''\right). \tag{3.21}$$

In a similar manner, the induction equation (3.17) gives

$$pb_x - il\zeta\psi = iku + ilU_0'\chi - il\varepsilon_1\psi, \tag{3.22}$$

$$ip\chi = -k\psi. \tag{3.23}$$

On eliminating u between equations (3.20) and (3.22), we obtain

$$\left(p^2 + k^2\right)b_x = klU_0'\psi + il(\lambda - \varepsilon_1)p\psi + kl\lambda\chi + ilpU_0'\chi, \tag{3.24}$$

which, after substituting for χ from (3.23), becomes

$$p\left(p^2 + k^2\right)b_x = il(\lambda - \varepsilon_1)p^2\psi + ik^2 l\lambda\psi. \tag{3.25}$$

Equation (3.21), after substituting for χ from (3.23), and equation (3.25) form an eigenvalue problem for p involving only the functions ψ and b_x. The crucial point to note is that U_0' does not appear in these expressions; hence the shear has no influence on the growth rate p.

(ii) $H_U \sim H_p$

If the scale height H_U is comparable with H_p and H_B then the major change to equations (3.16) and (3.17) is that the shear term is now also to be neglected, as both the advection and shear term are $O(d/H_p)$ smaller than the leading order time derivative term,

$$\partial_t \boldsymbol{u} = -\boldsymbol{\nabla}_\perp \Pi + \varepsilon_1 b_x \hat{\boldsymbol{z}} + \partial_x \boldsymbol{b} - \zeta b_z \hat{\boldsymbol{x}}, \tag{3.26}$$

$$\partial_t \boldsymbol{b} - \zeta w \hat{\boldsymbol{x}} = \partial_x \boldsymbol{u} - \varepsilon_1 w \hat{\boldsymbol{x}}, \tag{3.27}$$

Thus, with the ordering $H_U \sim H_p \sim H_B$, the imposed shear once again has no bearing on the linear stability problem.

Another maybe less 'obvious' attempt to incorporate a velocity shear is to consider a basic state velocity shear that is of a different magnitude to the resulting velocity perturbations. In Corfield (1984) the basic state magnetic field was incorporated in this manner, specifically the basic state field was $O(\varepsilon_1^{-1})$ larger than the magnetic perturbations. Suppose we implement a similar ordering for the shear, such that

$$U_0 \sim \varepsilon_1^{-1} u. \tag{3.28}$$

We shall see in §3.2.2 that to ensure the flow is driven by buoyancy, it is important that the largest term in the non-linear momentum equation is of the order $(\boldsymbol{u} \cdot \boldsymbol{\nabla}_\perp)\boldsymbol{u}$. With the above ordering, $(\boldsymbol{U}_0 \cdot \boldsymbol{\nabla})\boldsymbol{u}$ and $(\boldsymbol{u} \cdot \boldsymbol{\nabla}_\perp)\boldsymbol{u}$ have the same magnitude; as such $U_0 \partial_x \boldsymbol{u}$ will enter the equations at leading order. When considering the size of H_U, it is crucial that the shear term in the momentum equation does not become too large and dominate. Thus for a buoyancy driven flow we require

$$
\begin{aligned}
(\boldsymbol{u} \cdot \boldsymbol{\nabla}_\perp)\boldsymbol{u} &\geq (\boldsymbol{u} \cdot \boldsymbol{\nabla}_\perp)\boldsymbol{U}_0, \\
\Rightarrow \quad H_U &\geq H_p,
\end{aligned}
\tag{3.29}
$$

Therefore for asymptotic consistency we can not consider the case of $H_U < H_p$. Unfortunately for any choice of $H_U \geq H_p$, to first approximation the advective term $(\boldsymbol{U}_0 \cdot \boldsymbol{\nabla})$ just represents advection by a uniform flow. As such, a Galilean transformation can be made and we revert to equations (3.16) and (3.17) when $H_U \sim H_p$, or equations (3.26) and (3.27) when $H_U > H_p$. As already shown, in either of these cases the velocity shear has no effect on the linear diffusionless system. Thereofe, just enforcing (3.28) is not enough to introduce a velocity shear that influences the linear instability.

3.2.2 The magneto-Boussinesq approximation

Since adding velocity shear in what might be thought of as an 'obvious' manner has no effect on the linear stability of the diffusionless system, it is beneficial to take a closer look at the magnitudes of both the imposed magnetic field and velocity shear, together with their gradients, as well as the size of the resulting perturbations and their horizontal length scale. With this information we shall be able to produce a set of simplified equations

containing the features of magnetic buoyancy instability in which the velocity shear enters in an influential manner.

An important point to make is that our analysis proceeds via three distinct stages. First we consider a purely hydrostatic, z-dependent *reference state* (denoted by $\hat{\ }$). This is then perturbed by the inclusion of a horizontal magnetic field and aligned shear flow, both z-dependent, leading to a z-dependent MHD *basic state* (subscript zero). Finally we consider three-dimensional, time-dependent perturbations of this basic state (denoted by δ). Therefore in our notation a variable f will be expressed as

$$f(\boldsymbol{x}, t) = \hat{f}(z) + f_0(z) + \delta f(\boldsymbol{x}, t). \tag{3.30}$$

Throughout this analysis it is necessary to distinguish the difference between the vector variables aligned with, and those perpendicular to, the basic state magnetic field. Therefore it is convenient to introduce the notation $\boldsymbol{f}_\parallel$ and $\boldsymbol{f}_\perp$, corresponding to the magnitudes of the components of the fluctuations parallel and perpendicular to the basic state field. Following Spiegel & Veronis (1960) we define $\Delta f = f_0(d) - f_0(0)$ as the change in f_0 across the layer, and make the assumption that the size of the time-dependent perturbations do not exceed that of the jump across the layer, i.e. $\delta f \leq \mathrm{O}(\Delta f)$.

In the absence of any basic state (i.e. no magnetic field and no flow), the reference state consists of a vertically stratified layer of gas in hydrostatic balance in the region $0 < z < d$, governed by the equation

$$\frac{\mathrm{d}\hat{p}}{\mathrm{d}z} = -g\hat{\rho}. \tag{3.31}$$

For any field variable f we define the inverse scale height of a reference state $\hat{f}(z)$ by $H_f^{-1} = \mathrm{d}(\ln \hat{f})/\mathrm{d}z\big|_{z=0}$ and take $f_* = \hat{f}(0)$ to be a characteristic value of the variable. As addressed in §3.1, the physical idea of the Boussinesq approximation is that the depth of the layer d is considered small in comparison with the pressure scale height, $H_p = c_s^2/g$, where the isothermal sound speed c_s is defined by $c_s^2 = p_*/\rho_*$; note, from the equation of state (3.1f), that the density and temperature scale heights have the same magnitude as H_p and so it follows that $d \ll H_\rho, H_T$. The reference state is modified by the introduction of a steady, horizontal magnetic field and an aligned steady shear flow. The field takes the form $\boldsymbol{B}_0 = B_0(z)\hat{\boldsymbol{x}}$, where, for non-zero magnetic diffusivity, $B_0(z)$ is a linear function

of height z; the flow $\boldsymbol{U}_0 = U_0(z)\hat{\boldsymbol{x}}$ results from the (arbitrary) body force $\boldsymbol{F}$. These, in turn, introduce a perturbation of the reference state to form a *basic state*. Analogous to the hats denoting reference state quantities, we shall use a subscript zero to denote the perturbations away from the reference state that result from the imposed magnetic field and shear flow. We define the scale heights H_B and H_U in terms of B_0 and U_0; at this stage we stipulate only that $d \lesssim H_B \lesssim H_p$ and $d \lesssim H_U \lesssim H_p$. As the representative value for the magnetic field, we may take B_* to be the rms value of $B_0(z)$ over the layer. For the velocity field, the physics is of course unchanged by the addition of a constant flow to $U_0(z)$; thus we define U_* as the rms value of a shear flow in a frame of reference chosen such that the flow has zero mean. We make the assumption, as in Spiegel & Weiss (1982), that the Alfvén speed $c_A = B_*/\sqrt{\mu_0 \rho_*}$ is small in comparison with the sound speed c_s; this guarantees that the difference between the reference and basic states is small. On subtracting off the reference state, the '0' variables satisfy the equations

$$\frac{\mathrm{d}\Pi_0}{\mathrm{d}z} = -g\rho_0, \tag{3.32a}$$

$$\frac{\mathrm{d}^2 B_0}{\mathrm{d}z^2} = 0, \tag{3.32b}$$

$$K \frac{\mathrm{d}^2 T_0}{\mathrm{d}z^2} = -\frac{\eta}{\mu_0} \left(\frac{\mathrm{d}B_0}{\mathrm{d}z} \right)^2 - \mu \left(\frac{\mathrm{d}U_0}{\mathrm{d}z} \right)^2. \tag{3.32c}$$

Here we remind the reader that Π_0 represents the total pressure, such that $\Pi_0 = p_0 + p_{m0}$. Turning our attention to the resulting perturbations that arise from the introduction of this basic state, we proceed in a similar fashion to Corfield (1984) by finding appropriate magnitudes for the perturbations in terms of the basic state quantities. The aim of this work is to focus on buoyancy-driven instabilities; therefore an appropriate ordering is that the kinetic energy of the transverse flow results from buoyancy perturbations, i.e.

$$\rho_* \delta u_\perp^2 \sim \delta\rho\, gd. \tag{3.33}$$

In the hydrodynamic Boussinesq approximation (Spiegel & Veronis, 1960), fluctuations in gas pressure are small, and therefore the predominant balance in the equation of state is between temperature and density fluctuations. The idea underlying magnetic buoyancy is that it is fluctuations in *total* pressure that are considered small, with fluctuations in gas pressure therefore being comparable with those of magnetic pressure; thus gas pressure

variations are retained in the perturbed equation of state. With this in mind, we adopt the same scaling for total pressure fluctuations as Spiegel & Weiss (1982), namely

$$\delta\Pi \sim \delta\rho\, gd \sim \frac{\delta\rho}{\rho_*}\frac{d}{H_p}p_*, \tag{3.34}$$

from which it follows that

$$\frac{\delta p}{p_*} = -\frac{\delta p_m}{p_*} + \mathrm{O}\left(\frac{\delta\rho}{\rho_*}\frac{d}{H_p}\right). \tag{3.35}$$

Thus, using the equation of state, the density perturbation may be expressed in terms of temperature and magnetic pressure perturbations as

$$\frac{\delta\rho}{\rho_*} = -\left(\frac{\delta T}{T_*} + \frac{\delta p_m}{p_*}\right)\left(1 + \mathrm{O}\left(\frac{d}{H_p}\right)\right). \tag{3.36}$$

On the assumption that the magnitude of the magnetic field fluctuations does not exceed that of the imposed field, $\delta B_\parallel \le B_*$, the largest resulting term in the magnetic pressure perturbation may be written as

$$\delta p_m \approx \frac{B_* \delta B_\parallel}{\mu_0} \sim \frac{\delta\rho}{\rho_*}p_*. \tag{3.37}$$

Balancing the two terms of the parallel component of $\boldsymbol{u}\cdot\boldsymbol{\nabla}\boldsymbol{B}$ provides the following crucial ordering:

$$\frac{\delta u_\perp\, \delta B_\parallel}{d} \sim \frac{\delta u_\perp\, B_*}{H_B}, \quad \text{implying} \quad \delta B_\parallel \sim \frac{d}{H_B}B_*. \tag{3.38}$$

Hence, using (3.37) and (3.38), we obtain a relation between the magnitude of the density perturbations and that of the basic state magnetic field,

$$\frac{\delta\rho}{\rho_*}\frac{H_B}{d}p_* \sim \frac{B_*^2}{\mu_0}. \tag{3.39}$$

Combining the orderings (3.33) and (3.39) then provides the consistent scaling of the magnitude of the perpendicular velocity in terms of the basic state magnetic field,

$$\frac{\delta u_\perp^2}{c_A^2} \sim \frac{d}{H_B}\frac{d}{H_p}. \tag{3.40}$$

As shown by Spiegel & Weiss (1982) and Corfield (1984), a significant difference between the standard Boussinesq equations and the magneto-Boussinesq equations is

that the latter necessarily impose a restriction on the perturbation length scale L in the direction of the imposed magnetic field. With no prior assumption on the size of L, we arrive at an appropriate magnitude for L by balancing relevant terms in the equations.

We expect advection and stretching of the magnetic field to be of comparable importance; from the perpendicular and parallel components of the induction equation this gives the scalings

$$\frac{\delta u_\perp \, \delta B_\perp}{d} \sim \frac{B_* \, \delta u_\perp}{L} \quad \text{and} \quad \frac{\delta u_\perp \, \delta B_\parallel}{d} \sim \frac{B_* \, \delta u_\parallel}{L}, \tag{3.41}$$

leading, after the use of (3.38), to

$$\delta B_\perp \sim \frac{H_B}{L} \delta B_\parallel \quad \text{and} \quad \delta u_\perp \sim \frac{H_B}{L} \delta u_\parallel. \tag{3.42}$$

Finally, we use the fact that it is physically important to include the effects of magnetic tension. Balancing inertia against magnetic tension in the momentum equation leads to the ordering

$$\rho_* \frac{\delta u_\perp^2}{d} \sim \frac{B_*}{\mu_0} \frac{\delta B_\perp}{L}, \tag{3.43}$$

and hence, using (3.42), to

$$\frac{\delta u_\perp^2}{c_A^2} \sim \frac{d^2}{L^2}. \tag{3.44}$$

In deriving (3.43) we have used the perpendicular component of the momentum equation directly; balancing the terms in the parallel component and using the expressions (3.38) and (3.42) for $\delta B_\parallel$ and $\delta u_\parallel$ respectively leads to the same result. Finally, combining the scalings (3.40) and (3.44) provides an important constraint on the horizontal length scale, namely

$$L^2 \sim H_p H_B. \tag{3.45}$$

The above scalings have been derived solely by consideration of the basic ideas of magnetic buoyancy, without any reference as yet to the shear flow $U_0(z)$. Their derivation follows a rather different line of argument to that of Corfield (1984), and allows for a range of magnetic scale heights $d \lesssim H_B \lesssim H_p$. In the case of $H_B \sim H_p$, they are entirely consistent with those of Corfield. As we shall see, for our future exposition involving the introduction of velocity shear, it is important that we make no *a priori* assumption about the magnitude of H_B.

3.2.3   Incorporating velocity shear

As seen in §3.2.1, when considering the linear stability analysis of the basic state formed by the imposition of a shear flow into the magneto-Boussinesq equations of Corfield (1984), i.e. with $L \sim H_B \sim H_p$, the flow is assumed to have scale height $H_U \sim d$ and a characteristic velocity comparable in magnitude with that of the velocity fluctuations. As such, $(\boldsymbol{U}_0 \cdot \boldsymbol{\nabla})$ is neglected in favour of $(\boldsymbol{u}_\perp \cdot \boldsymbol{\nabla})$ in the advective terms, although the shear (through $\boldsymbol{U}_0'$) does appear in both the momentum and induction equations ((3.16) and (3.17)). However, somewhat surprisingly, it plays no role in the resulting eigenvalue problem. Similarly, on taking a longer scale length $H_u \sim L \sim H_B \sim H_p$, the shear never enters the system.

On demanding that the velocity shear enters the momentum equation in a significant manner, a balance between inertia and magnetic tension gives

$$\rho_* \frac{\delta u_\perp \, U_*}{H_U} \sim \frac{1}{\mu_0} \frac{B_* \, \delta B_\parallel}{L}. \tag{3.46}$$

Similarly, from the induction equation, a balance between advection and stretching of magnetic field leads to

$$\frac{\delta u_\perp \, B_*}{H_B} \sim \frac{\delta B_\perp \, U_*}{H_U}. \tag{3.47}$$

Equating these two expressions for $\delta u_\perp$, and making use of the orderings (3.38) and (3.42) for the relative sizes of the magnetic field perturbations, yields the important result,

$$\frac{U_*^2}{c_A^2} \sim \frac{H_U^2}{H_B^2}. \tag{3.48}$$

In order to involve the velocity shear in a meaningful manner we require two crucial orderings are met. The first is that the imposed flow is 'significant' in the advective terms; this requires that $(\boldsymbol{U}_0 \cdot \boldsymbol{\nabla})$ and $(\boldsymbol{u}_\perp \cdot \boldsymbol{\nabla})$ be of comparable magnitude, thus forcing a balance between the basic state velocity and the perpendicular velocity perturbation,

$$\frac{U_*}{L} \sim \frac{\delta u_\perp}{d}. \tag{3.49}$$

Secondly we require a condition on the velocity scale height. Suppose that we take a long scale height $H_U \sim H_p$; then to first approximation the advective term $(\boldsymbol{U}_0 \cdot \boldsymbol{\nabla})$ just

represents advection by a uniform flow. As such, a Galilean transformation can be made and we revert back to equations (3.16) and (3.17), in which the velocity shear has no effect on the linear diffusionless system. To avoid this problem we require

$$H_U \sim d. \tag{3.50}$$

Henceforth, we shall refer to a shear flow that satisfies both (3.49) and (3.50) as being *influential*. Combining the two expressions for $\delta u_\perp$, (3.44) and (3.49), provides the following important ordering for the magnitude of the shear flow in terms of the Alfvén velocity of the imposed magnetic field,

$$U_*^2 \sim c_A^2. \tag{3.51}$$

Unlike Corfield (1984), we made no prior assumption for the magnitude of the magnetic scale height. As such, all the orderings in §3.2.2 are valid for a range of magnetic scale heights $d \lesssim H_B \lesssim H_p$. By introducing a velocity shear that influences the magnetic buoyancy instability, it in turn restricts the size of H_B. Scalings (3.48), (3.50) and (3.51) lead to the crucial result that

$$H_B \sim H_U \sim d. \tag{3.52}$$

3.2.4 Derivation of the magneto-Boussinesq velocity shear equations

Sections 3.2.2 and 3.2.3 provide the framework required to introduce velocity shear into the magneto-Boussinesq approximation. We shall now incorporate these ideas into the derivation of an asymptotically consistent set of governing equations. We focus on an influential shear flow, with $H_U \sim H_B \sim d$, and define two small parameters,

$$\varepsilon_1 = \frac{d}{H_p} \quad \text{and} \quad \varepsilon_2 = \frac{c_A^2}{c_s^2}, \tag{3.53}$$

where $\varepsilon_1, \varepsilon_2 \ll 1$. Physically, ε_1 is a measure of the inverse pressure scale height of the hydrostatic reference state, whereas ε_2, through (3.39), provides a measure of the amplitude of the fluctuations driven by magnetic buoyancy. (We note that our ε_2 is of the same order of magnitude as the ε_2 of Corfield (1984), defined as $\delta\rho/\rho$.) It follows from (3.51) that

$$U_*^2 \sim \varepsilon_2 c_s^2. \tag{3.54}$$

Using expression (3.45), we may rewrite the horizontal length scale in terms of ε_1,

$$\frac{d}{L} \sim \varepsilon_1^{1/2}. \tag{3.55}$$

We non-dimensionalise T by T_*, p by p_*, ρ by ρ_*, p_m by p_*, lengths with d and times with the sound crossing time across the layer. The condition that motion-induced fluctuations do not exceed, in order of magnitude, static variations across the layer translates to the requirement that $\varepsilon_2 \lesssim \varepsilon_1$. Following Corfield (1984), we express all variables in terms of the two small parameters, with non-dimensional variables of order unity denoted by a tilde. Based on the scalings derived in §3.2.2, the thermodynamic quantities are expressed as

$$T\left(\mathbf{x}, t\right) = T_* \left(1 + \varepsilon_1 \frac{H_p}{H_T} \frac{z}{d} + \varepsilon_2 \widetilde{T}_0 + \varepsilon_2 \delta \widetilde{T}\left(\mathbf{x}, t\right) + \ldots \right), \tag{3.56a}$$

$$p\left(\mathbf{x}, t\right) = p_* \left(1 + \varepsilon_1 \frac{z}{d} + \varepsilon_2 \widetilde{p}_0 + \varepsilon_2 \delta \widetilde{p}\left(\mathbf{x}, t\right) + \ldots \right), \tag{3.56b}$$

$$\rho\left(\mathbf{x}, t\right) = \rho_* \left(1 + \varepsilon_1 \frac{H_p}{H_\rho} \frac{z}{d} + \varepsilon_2 \widetilde{\rho}_0 + \varepsilon_2 \delta \widetilde{\rho}\left(\mathbf{x}, t\right) + \ldots \right), \tag{3.56c}$$

where we have linearised the reference state. The magnetic and total pressure are expanded as

$$p_m(\mathbf{x}, t) = \varepsilon_2 p_* (\widetilde{p}_{m0} + \delta \widetilde{p}_m(\mathbf{x}, t) + \ldots), \tag{3.57a}$$

$$\Pi(\mathbf{x}, t) = \varepsilon_1 \varepsilon_2 p_* (\widetilde{\Pi}_0 + \delta \widetilde{\Pi}(\mathbf{x}, t) + \ldots), \tag{3.57b}$$

where equation (3.32a) and expression (3.34) respectively have been used for the ordering of $\widetilde{\Pi}_0$ and $\delta\widetilde{\Pi}$. It is worth noting a small typographical error in equation (31b) in Bowker et al. (2014) (31b), corresponding to a missing ε_1 coefficient in front of Π_0

It is convenient to split the velocity and magnetic field into their parallel and perpendicular components; from expressions (3.42), (3.54) and (3.55) these become

$$\boldsymbol{u} = \varepsilon_2^{1/2} c_s \left(\widetilde{\boldsymbol{U}}_0 + \delta \widetilde{\boldsymbol{u}}_\parallel + \varepsilon_1^{1/2} \delta \widetilde{\boldsymbol{u}}_\perp \right), \tag{3.58a}$$

$$\boldsymbol{B} = (\varepsilon_2 \mu_0 p_*)^{1/2} \left(\widetilde{\boldsymbol{B}}_0 + \delta \widetilde{\boldsymbol{B}}_\parallel + \varepsilon_1^{1/2} \delta \widetilde{\boldsymbol{B}}_\perp \right). \tag{3.58b}$$

Based on (3.55), we write

$$\boldsymbol{\nabla}_\parallel = \frac{\varepsilon_1^{1/2}}{d} \widetilde{\boldsymbol{\nabla}}_\parallel, \qquad \boldsymbol{\nabla}_\perp = \frac{1}{d} \widetilde{\boldsymbol{\nabla}}_\perp. \tag{3.59}$$

The time scale is determined by the conventional Boussinesq approach of balancing the vertical acceleration against the buoyancy. Using the scalings for $\delta\rho$ and $\delta u_\perp$, this gives

$$\partial_t = (\varepsilon_1\varepsilon_2)^{1/2} \frac{c_s}{d} \partial_{\tilde{t}}. \tag{3.60}$$

The various expansions (3.56)–(3.60) are then substituted into the MHD equations (3.1). To simplify the notation, we drop the tildes, write $\delta\boldsymbol{B} = \boldsymbol{b}$ and drop the δ from the other terms. After substituting for δp and $\delta\rho$ from equations (3.35) and (3.36), and removing terms that arise from the basic state, the governing equations at leading order become:

$$\left(\partial_t + (\boldsymbol{U}_0 + \boldsymbol{u}) \cdot \boldsymbol{\nabla}\right)\boldsymbol{u} + \boldsymbol{U}_0' w = -\boldsymbol{\nabla}_\perp \Pi + (T + p_m)\,\hat{\boldsymbol{z}}$$
$$+ (\boldsymbol{B}_0 + \boldsymbol{b}) \cdot \boldsymbol{\nabla}\boldsymbol{b} + \boldsymbol{B}_0' b_z + Re^{-1}\nabla_\perp^2 \boldsymbol{u}, \tag{3.61a}$$

$$\boldsymbol{\nabla} \cdot \boldsymbol{u} = 0, \tag{3.61b}$$

$$\left(\partial_t + (\boldsymbol{U}_0 + \boldsymbol{u}) \cdot \boldsymbol{\nabla}\right)\boldsymbol{b} + \boldsymbol{B}_0' w = (\boldsymbol{B}_0 + \boldsymbol{b}) \cdot \boldsymbol{\nabla}\boldsymbol{u}$$
$$+ \boldsymbol{U}_0' b_z + Rm^{-1}\nabla_\perp^2 \boldsymbol{b}, \tag{3.61c}$$

$$\boldsymbol{\nabla} \cdot \boldsymbol{b} = 0, \tag{3.61d}$$

$$\left(\partial_t + (\boldsymbol{U}_0 + \boldsymbol{u}) \cdot \boldsymbol{\nabla}\right)\Big((T_0 + T) + D(p_{m0} + p_m)\Big) + w\hat{\beta}$$
$$= Pe^{-1}\nabla_\perp^2 T$$
$$+ DRm^{-1}\Big((\partial_y b_\|)^2 + (\partial_z b_\|)^2 + 2B_0'\partial_z b_\|\Big)$$
$$+ DRe^{-1}\Big((\partial_y u_\|)^2 + (\partial_z u_\|)^2 + 2U_0'\partial_z u_\|\Big), \tag{3.61e}$$

where the vertical components of the velocity and magnetic field perturbations are denoted by w and b_z respectively and $'$ denotes the derivative of a basic state variable with respect to z. It is worth noting that from the scaling (3.59), p_m in equations (3.61) is given by $p_m = B_0 b_\| + b_\|^2/2$. Using similar reasoning to that which led to (3.35) we are able to say at leading order $p_{m0} = -p_0$, which we have used in (3.61e). The operator $\boldsymbol{\nabla}$ is defined as

$$\boldsymbol{\nabla} = \tilde{\boldsymbol{\nabla}}_\| + \tilde{\boldsymbol{\nabla}}_\perp. \tag{3.62}$$

To be consistent with the rest of the thesis we have used the following non-dimensional numbers, defined as:

$$Re = \frac{\varepsilon_1^{1/2} U_* d}{\nu}, \quad Rm = \frac{\varepsilon_1^{1/2} U_* d}{\eta}, \quad Pe = \frac{\varepsilon_1^{1/2} U_* d}{\kappa}, \quad D = \frac{\gamma - 1}{\gamma}, \tag{3.63}$$

where γ is the conventional ratio of specific heats; Re is a modified Reynolds number, Rm is a modified magnetic Reynolds number and Pe a modified Péclet number. Here U_* can be written in terms of ε_2 from equation (3.54). These parameters are equivalent to the parameters given in Bowker et al. (2014) equation (37a-d) through the transformations

$$Re = \left(\frac{Ra}{\sigma}\right)^{1/2}, \quad Rm = \sigma_m \left(\frac{Ra}{\sigma}\right)^{1/2}, \quad Pe = (Ra\,\sigma)^{1/2}, \qquad (3.64)$$

where Ra, σ and σ_m are the Rayleigh, Prandtl and mangetic Prandtl numbers respectively. To ensure that the diffusion terms do not dominate we impose the restriction that Re^{-1}, Rm^{-1} and Pe^{-1} are all at most O(1). For asymptotic consistency, the non-dimensional subadiabatic temperature gradient $\hat{\beta}$ in equation (3.61e) must be O(ε_2), and so we have defined

$$\frac{1}{\gamma}\frac{\mathrm{d}}{\mathrm{d}z}\ln\left(\frac{\hat{p}}{\hat{\rho}^{\gamma}}\right) = \varepsilon_2\hat{\beta}. \qquad (3.65)$$

Equations (3.61) are derived only under the assumption that $\varepsilon_2 \lesssim \varepsilon_1$. If ε_1 and ε_2 are comparable, then the subadiabatic gradient is O(ε_1), comparable in magnitude with its component gradients of pressure and density. However, if $\varepsilon_2 \ll \varepsilon_1$ then the subadiabatic gradient, being O(ε_2), is formally smaller than the pressure and density gradients, and therefore, in this case, equations (3.61) hold only for atmospheres that are close to adiabatic.

3.3 Comparison with the equations of Spiegel & Weiss (1982) and Corfield (1984)

There are significant differences between the new system of equations (3.61) and the equations derived by Spiegel & Weiss (1982) and Corfield (1984). In order to introduce a shear flow that can interact with the magnetic buoyancy instability, the magnetic field scale height H_B has to be O(d), considerably smaller than that adopted in Corfield (1984), namely $H_B \sim H_p$. As the scalings derived in §3.2.2 and §3.2.3 are clearly dependent on H_B, this change has a knock-on effect on the magnitudes of both perturbation and basic state quantities.

It can be seen from (3.45) that adopting the Corfield (1984) ordering of $H_B \sim H_p$ forces $L \sim H_p$; in turn, from (3.42), this implies that the perpendicular and parallel components of both the flow and field perturbations have the same magnitude. This is in marked contrast to our system, in which, although the perpendicular components of the flow and field scale as in Corfield (1984), namely

$$\delta u_\perp^2 \sim \varepsilon_1 \varepsilon_2 c_s^2 \qquad \text{and} \qquad \frac{\delta B_\perp^2}{\mu_0} \sim \varepsilon_1 \varepsilon_2 p_*, \tag{3.66}$$

the parallel components are $\mathrm{O}\left(\varepsilon_1^{-1/2}\right)$ greater. Furthermore, from (3.41), the characteristic strength of the basic state magnetic field B_* is given by

$$\frac{B_*^2}{\mu_0} \sim \frac{L^2}{d^2} \frac{\delta B_\perp^2}{\mu_0} \sim \frac{L^2}{d^2} \varepsilon_1 \varepsilon_2 p_*, \tag{3.67}$$

thus highlighting a further important difference between the two systems: for our equations, governed by the scaling $L^2 \sim dH_p$, expression (3.67) becomes

$$\frac{B_*^2}{\mu_0} \sim \varepsilon_2 p_*, \tag{3.68}$$

whereas for Corfield (1984) the characteristic field strength B_* is $\mathrm{O}\left(\varepsilon_1^{-1/2}\right)$ greater. Hence the condition that an imposed shear flow be influential requires an $\mathrm{O}\left(\varepsilon_1^{1/2}\right)$ reduction in the strength of the basic state magnetic field.

Unlike the equations of Spiegel & Weiss (1982), equations (3.61) now satisfy, at leading order, both the full solenoidal condition on the velocity (3.61b) and the magnetic field (3.61d). Consequently, since the new system is fully incompressible, there is no longer a next-order correction of $\nabla \cdot \boldsymbol{u}$ introduced into the induction equation, thus the induction equation now conserves $\nabla \cdot \boldsymbol{b}$. Note also that, in contrast to the standard Boussinesq approximation, both ohmic and viscous heating terms are included in the energy equation (3.61e), these terms arising as a consequence of having increased the magnitude of both the parallel velocity and parallel magnetic field perturbations.

3.3.1 Temperature gradient

To be consistent with the equations of Spiegel & Weiss (1982), it is important to address their definition of the subadiabatic temperature gradient and how it relates to ours. In our

detailed derivations we define a purely hydrodynamic reference state that is separate from the basic state variables that are introduced with the magnetic field. As a result, we can separate the temperature gradient into two parts, the reference state $\hat{\beta}$ defined in (3.65) and a basic state

$$\beta_0 = \frac{\mathrm{d}}{\mathrm{d}z}T_0 + D\frac{\mathrm{d}}{\mathrm{d}z}p_{m0}. \tag{3.69}$$

In their derivation, Spiegel & Weiss (1982) (and Corfield (1984)) defined their reference state and basic state as just one global 'background state'. Thus their temperature gradient consisted of both what we would call reference state and basic state terms. In our notation this would be defined as

$$\beta = \frac{1}{\varepsilon_2\gamma}\frac{\mathrm{d}}{\mathrm{d}z}\ln\left(\frac{\hat{p} + \varepsilon_2 p_0}{(\hat{\rho} + \varepsilon_2\rho_0)^\gamma}\right). \tag{3.70}$$

Separating the above expression into reference state and basic state terms, it can be shown that at leading order the temperature gradient used in Spiegel & Weiss (1982) is the same as the combination of $\hat{\beta}$ and β_0 used our derivations. Proceeding in this manner leads to

$$\beta = \frac{1}{\varepsilon_2\gamma}\frac{\mathrm{d}}{\mathrm{d}z}\ln\left(\frac{\hat{p}}{\hat{\rho}^\gamma}\right) + \frac{1}{\gamma}\frac{\mathrm{d}}{\mathrm{d}z}p_0 - \frac{\mathrm{d}}{\mathrm{d}z}\rho_0. \tag{3.71}$$

From the equation of state (3.1f)

$$\frac{1}{T_0}\frac{\mathrm{d}}{\mathrm{d}z}T_0 = \frac{1}{p_0}\frac{\mathrm{d}}{\mathrm{d}z}p_0 - \frac{1}{\rho_0}\frac{\mathrm{d}}{\mathrm{d}z}\rho_0. \tag{3.72}$$

Substituting (3.72) into (3.71) and making use of $p_0 = -p_m$ at leading order, gives

$$\beta = \frac{1}{\varepsilon_2\gamma}\frac{\mathrm{d}}{\mathrm{d}z}\ln\left(\frac{\hat{p}}{\hat{\rho}^\gamma}\right) + \frac{\mathrm{d}}{\mathrm{d}z}T_0 + D\frac{\mathrm{d}}{\mathrm{d}z}p_{m0}. \tag{3.73}$$

Finally, with the use of (3.65) and (3.69), we can express the definition of the temperature gradient in Spiegel & Weiss (1982) in terms of our reference state and basic state definitions as

$$\beta = \hat{\beta} + \beta_0. \tag{3.74}$$

3.3.2   Linking the magneto-Boussinesq systems

The previous section presented a new set of equations describing the combined effects of magnetic buoyancy instability and an influential shear flow, consistent within the magneto-Boussinesq approximation. As discussed, there are a number of significant differences between these equations and those of Spiegel & Weiss (1982). It is therefore of interest to examine how a connection may be made between the two systems. To achieve this we can introduce two control parameters q and r, defined by

$$\frac{H_B}{H_p} = \varepsilon_1^q, \quad \frac{H_U}{H_p} = \varepsilon_1^r, \tag{3.75}$$

where both q and r satisfy $0 \leq q, r \leq 1$. These parameters measure the size of the scale height of magnetic field (for q) and the velocity shear (for r), relative to the pressure scale height. Doing this from the onset allows us to derive a set of mixed order equations, dependent on q and r, that can be used to switch easily between the new set of equations in §3.2.4 ($q = 1, r = 1$) and the equations of Spiegel & Weiss (1982), Corfield (1984) ($q = 0$). As shown in §3.2.1, when $q = 0$ it is irrelevant what choice of r we pick as the shear will not enter the equations in an influential manner.

It can be seen from §3.2.2 that the size of all perturbations and the basic state variables depend on H_B and therefore on q. In order to keep the magnitudes of the density fluctuations constant as the parameter q varies, using (3.39) we express the magnitude of the basic state magnetic fields as

$$\frac{B_*^2}{\mu_0 p*} = \frac{H_B}{d}\varepsilon_2 \quad \Rightarrow \quad \frac{B_*^2}{\mu_0 \rho_*} = \varepsilon_1^{q-1}\varepsilon_2 c_s^2. \tag{3.76}$$

The assumption that the Alfvén speed is much smaller than the sound speed leads to the inequality $\varepsilon_2 \ll \varepsilon_1^{1-q}$. To ensure we scale the magnitude of the basic state velocity shear consistently, we fix U_* to be of the same size as the velocity perturbation parallel to the field $\delta u_\parallel$. Therefore, following the ideas of §3.2.2, we can express the required strength of the velocity shear and horizontal length scale in terms of the parameter q as

$$U_*^2 \sim \varepsilon_1^{1-q}\varepsilon_2 c_s^2, \quad \frac{d}{L} \sim \varepsilon_1^{1-q/2}. \tag{3.77}$$

Although more complicated than the $q = 1$ expressions of §3.2.4, we can nonetheless proceed in a similar manner and express the variables in terms of non-dimensional

expansions. The scalar variables are independent of q and are therefore scaled as in (3.56a) – (3.57b). The vector quantities may be expanded as

$$\boldsymbol{u} = (\varepsilon_1\varepsilon_2)^{1/2} c_s \left(\varepsilon_1^{-q/2} \widetilde{\boldsymbol{U}}_0 + \varepsilon_1^{-q/2} \delta\widetilde{\boldsymbol{u}}_\| + \delta\widetilde{\boldsymbol{u}}_\perp \right), \tag{3.78a}$$

$$\boldsymbol{B} = (\varepsilon_1\varepsilon_2\mu_0 p_*)^{1/2} \left(\varepsilon_1^{q/2-1} \widetilde{\boldsymbol{B}}_0 + \varepsilon_1^{-q/2} \delta\widetilde{\boldsymbol{b}}_\| + \delta\widetilde{\boldsymbol{b}}_\perp \right). \tag{3.78b}$$

Writing the expansions like this confirms what we know from equation (3.66), namely that the perpendicular fluctuations are independent of q and hence are the same size for both the new equations and those of Spiegel & Weiss (1982). The operators $\boldsymbol{\nabla}_\|$ and $\boldsymbol{\nabla}_\perp$ are scaled as

$$\boldsymbol{\nabla}_\| = \frac{\varepsilon_1^{1-q/2}}{d} \widetilde{\boldsymbol{\nabla}}_\|, \qquad \boldsymbol{\nabla}_\perp = \frac{1}{d} \widetilde{\boldsymbol{\nabla}}_\perp, \tag{3.79}$$

and we adopt the same q-independent time scale as in (3.60),

$$\partial_t = (\varepsilon_1\varepsilon_2)^{1/2} \frac{c_s}{d} \partial_{\widetilde{t}}. \tag{3.80}$$

Performing the same sequence of operations that leads to equations (3.61), leads to the following q and r-dependent mixed-order system of equations:

$$\left(\partial_t + \varepsilon_1^{1-q} \left(\boldsymbol{U}_0 + \boldsymbol{u} \right) \cdot \boldsymbol{\nabla}_\| + \boldsymbol{u} \cdot \boldsymbol{\nabla}_\perp \right) \boldsymbol{u} + \varepsilon_1^{1-r} U_0' w$$

$$= - \boldsymbol{\nabla}_\perp \Pi + \left(T + p_m \right) \hat{\boldsymbol{z}} + \left(\boldsymbol{B}_0 \cdot \boldsymbol{\nabla}_\| + \varepsilon_1^{1-q} \boldsymbol{b} \cdot \boldsymbol{\nabla}_\| + \boldsymbol{b} \cdot \boldsymbol{\nabla}_\perp \right) \boldsymbol{b}$$

$$+ B_0' b_z + Re^{-1} \nabla_\perp^2 \boldsymbol{u}, \tag{3.81a}$$

$$- \varepsilon_1 \frac{w}{H_\rho} + \varepsilon_1^{1-q} \boldsymbol{\nabla}_\| \cdot \boldsymbol{u} + \boldsymbol{\nabla}_\perp \cdot \boldsymbol{u} = 0, \tag{3.81b}$$

$$\left(\partial_t + \varepsilon_1^{1-q} \left(\boldsymbol{U}_0 + \boldsymbol{u} \right) \cdot \boldsymbol{\nabla}_\| + \boldsymbol{u} \cdot \boldsymbol{\nabla}_\perp \right) \boldsymbol{b} + B_0' w$$

$$= \left(\boldsymbol{B}_0 \cdot \boldsymbol{\nabla}_\| + \varepsilon_1^{1-q} \boldsymbol{b} \cdot \boldsymbol{\nabla}_\| + \boldsymbol{b} \cdot \boldsymbol{\nabla}_\perp \right) \boldsymbol{u} + \varepsilon_1^{1-r} U_0' b_z$$

$$- \boldsymbol{B}_0 \left(\boldsymbol{\nabla}_\| \cdot \boldsymbol{u} + \varepsilon_1^{q-1} \boldsymbol{\nabla}_\perp \cdot \boldsymbol{u} \right) + Rm^{-1} \nabla_\perp^2 \boldsymbol{b}, \tag{3.81c}$$

$$\varepsilon_1^{1-q} \boldsymbol{\nabla}_\| \cdot \boldsymbol{b} + \boldsymbol{\nabla}_\perp \cdot \boldsymbol{b} = 0, \tag{3.81d}$$

$$\left(\partial_t + \varepsilon_1^{1-q} \left(\boldsymbol{U}_0 + \boldsymbol{u} \right) \cdot \boldsymbol{\nabla}_\| + \boldsymbol{u} \cdot \boldsymbol{\nabla}_\perp \right) \left((T_0 + T) + D(p_{m0} + p_m) \right)$$

$$+ w\hat{\beta} = Pe^{-1} \nabla_\perp^2 T$$

$$+ \varepsilon_1^{1-q} D Rm^{-1} \left((\partial_y b_\|)^2 + (\partial_z b_\|)^2 + 2B_0' \partial_z b_\| \right)$$

$$+ \varepsilon_1^{1-q} D Re^{-1} \left((\partial_y u_\|)^2 + (\partial_z u_\|)^2 + 2\varepsilon_1^{1-r} U_0' \partial_z u_\| \right), \tag{3.81e}$$

In the above equations the non-dimensional numbers are defined as

$$Re = \frac{\varepsilon_1^{q/2} U_* d}{\nu}, \quad Rm = \frac{\varepsilon_1^{q/2} U_* d}{\eta}, \quad Pe = \frac{\varepsilon_1^{q/2} U_* d}{\kappa}, \tag{3.82}$$

and $'$ denotes the derivative of a basic state variable with respect to z. Although not obvious, with the use of equation (3.77) it can be shown that these non-dimensional parameters do not actually depend on q and therefore, as required, their numerical values remain the same as we switch between systems. Note that the leading order term arising from $\boldsymbol{B}(\boldsymbol{\nabla} \cdot \boldsymbol{u})$ in the induction equation,

$$\boldsymbol{B}_0 \left(\boldsymbol{\nabla}_{\parallel} \cdot \boldsymbol{u} + \varepsilon_1^{q-1} \boldsymbol{\nabla}_{\perp} \cdot \boldsymbol{u} \right), \tag{3.83}$$

can be written with the use of (3.81b) into the same form used by Corfield (1984)

$$\varepsilon_1^q \boldsymbol{B}_0 \frac{w}{H_\rho}. \tag{3.84}$$

Writing (3.83) in this form it becomes clear that this term enters into the leading order equations only when $q = 0$, and is formally smaller than all other terms for every other value of q. Equations (3.81) allow us to identify six different systems, depending on the choice of q and r. For $q = 0$ the system reverts to the magneto-Boussinesq equations of Spiegel & Weiss (1982), for which, regardless of the choice of r, the inclusion of a shear flow has no influence on the onset of instability. Either $r = 1$ and we revert to equations (3.16) – (3.17), in that the shear terms drop out, or $0 \leq r < 1$ and we have a equations (3.26) – (3.27) where velocity shear never enters. For $0 < q < 1$ the resulting two systems are very similar to those produced when $q = 0$, thus the velocity shear has no 'influential' effect. The final two systems come from taking $q = 1$. When $r = 1$, we recover the system of equations (3.61), in which velocity shear can influence magnetic buoyancy. For $0 \leq r < 1$, the advection terms associated with U_0 just represent uniform flow, and, as before, with a Galilean transformation we can move into the frame of the flow and lose all basic state shear terms. This system does have some merit however. It represents a system of equations that can be used to model magnetic buoyancy instability in the absence of shear for an $\mathrm{O}\,(1)$ magnetic field gradient, something that, as addressed by Hughes (1985a), is not possible working straight from the equations of Spiegel & Weiss (1982).

3.4   Discussion

In §3.2.1 we showed how naïvely incorporating velocity shear in the equations of Spiegel & Weiss (1982) and Corfield (1984), has no influence on the linear stability problem. To combat this and to introduce a shear flow that assumes a non-trivial role on the magnetic buoyancy instability, we had to take a closer look at the asymptotic orderings used to derive the magneto-Boussinesq equations (3.13). This is done in §3.2.2, where we were able to reproduce these orderings, without specific reference to incorporating a shear flow. Unlike Corfield (1984) however, we make no assumption about the magnetic field scale height; as a result, all the orderings are valid for $d \lesssim H_B \lesssim H_p$.

As shown in §3.2.3, to incorporate shear in an influential manner, two conditions must be met; that H_U is $\mathrm{O}(d)$ and that $U_*^2 \sim c_A^2$. For consistency with the scalings determined in §3.2.2, it follows that H_B must also be $\mathrm{O}(d)$. The various required orderings are applied to the full MHD governing equations (3.1) in §3.2.4 to yield the leading order equations (3.61) that involve both the effects of velocity shear and magnetic buoyancy. As discussed above, equations (3.61) also allow us to examine the effects of magnetic buoyancy for a magnetic field with an $\mathrm{O}(d)$ scale height in the absence of velocity shear, a scenario that is excluded from the equations of Corfield (1984), as identified by Hughes (1985a).

In the absence of shear, the transformation between equations (3.61) and those of Spiegel & Weiss (1982) and Corfield (1984) (equations (3.13)) can be effected by increasing the magnetic field scale height from $\mathrm{O}(d)$ to $\mathrm{O}(H_p)$. This is verified in §3.3.2, where we introduce two new parameters, q and r, that control the relative magnitudes of the scale heights of the magnetic field and velocity shear to the pressure scale height. Varying these parameters allows us to switch between six different regimes, each with their own set of equations.

The new equations in this chapter are derived with the intent of being used to study the solar tachocline. Therefore it is logical to investigate how well the assumptions and scalings used relate to conditions at the tachocline. Let us first consider the magnitudes of the two small quantities in our asymptotic expansions, ε_1 and ε_2. From table 1.1

the pressure scale height in the tachocline is approximately $0.08 R_\odot$ (Gough, 2007). Estimates of the vertical extent of the tachocline vary a little, according to how it is defined (see, for example, Miesch, 2005), but lie in the range between $0.02 R_\odot$ and $0.05 R_\odot$. Thus $\varepsilon_1 = d/H_p$ is certainly less than unity, but is not particularly small. Ossendrijver (2003) estimates the small parameter ε_2, as $O\left(10^3/B_*^2\right)$, where B_* is measured in Gauss. The mean toroidal field strength in the tachocline is currently unknown; however theoretical assumptions put it between 10^3G and 10^5G. This certainly makes ε_2 small, in the range $10^{-7} \lesssim \varepsilon_2 \lesssim 10^{-3}$.

Since the magnitudes of ε_1 and ε_2 for the tachocline fall within our assumptions, it suggests that a magneto-Boussinesq approach is appropriate. Finally, we need to validate our assumptions for an influential shear, equations (3.50) and (3.51). Equation (3.50) specifies that $H_U \sim d$; this is true of the tachocline, almost by definition. Expression (3.51) requires that U_* be comparable with the Alfvén speed c_A. Since we have a good estimate of U_* from helioseismic inversions, but no direct knowledge of the magnetic field strength B_*, it makes more sense to look at this from the other perspective and to ask what values of B_* will allow (3.51) to be satisfied. From the helioseismological results of Schou et al. (1998), the jump in the angular velocity across the tachocline (at the equator) is of the order of $20\,$nHz, which translates into $U_* \approx 30$ms^{-1}. Requiring $c_A \sim U_*$ determines the characteristic magnetic field strength as $B_* \approx 10^3$G. Thus everything ties together very nicely, suggesting that equations (3.61) form an appropriate system for the study of magnetic buoyancy instabilities in the tachocline.

Chapter 4

Linear diffusionless theory

In Chapter 3 we derived a new set of equations (3.61) that incorporated a velocity shear into the magneto-Boussinesq equations. In this chapter we focus on the linear evolution of these equations in the diffusionless limit. Thus we assume from the onset that $\nu = \eta = \kappa = 0$. Making these assumptions aids us mathematically in deriving generalised results for this new system.

This chapter is split into three main sections. In §4.1 we set up an eigenvalue problem, manipulating the governing equations to a single, second order ODE. This equation can be solved as a boundary value problem and is used throughout this thesis. As mentioned in Chapter 3, equations (3.61) not only offer the chance to examine the effects of a velocity shear on the magnetic buoyancy instability, but also allow us to study magnetic buoyancy in the presence of a magnetic field that varies on a length scale of $\mathrm{O}(1)$. In §4.2 we derive stability criteria for said case, comparing the results to the previous work on magnetic buoyancy laid out in Chapter 2. Finally, in §4.3 we reintroduce shear back into the equations and obtain semicircle bounds that are then used to derive stability criteria for the full system.

4.1   Eigenvalue problem

For a basic state magnetic field of the form $\boldsymbol{B} = B(z)\hat{\boldsymbol{x}}$, in the absence of diffusion, the linearised version of equations (3.61) are;

$$\nabla \cdot \boldsymbol{u} = 0, \tag{4.1a}$$

$$\nabla \cdot \boldsymbol{b} = 0, \tag{4.1b}$$

$$\left(\frac{\partial}{\partial t} + U\frac{\partial}{\partial x}\right)\boldsymbol{u} + \boldsymbol{U}'w = -\nabla_{\perp}\Pi + \left(T + Bb_x\right)\hat{\boldsymbol{z}} + B\frac{\partial \boldsymbol{b}}{\partial x} + \boldsymbol{B}'b_z, \tag{4.1c}$$

$$\left(\frac{\partial}{\partial t} + U\frac{\partial}{\partial x}\right)\boldsymbol{b} + \boldsymbol{B}'w = B\frac{\partial \boldsymbol{u}}{\partial x} + \boldsymbol{U}'b_z, \tag{4.1d}$$

$$\left(\frac{\partial}{\partial t} + U\frac{\partial}{\partial x}\right)(T + DBb_x) = -\beta w, \tag{4.1e}$$

where $'$ denotes differentiation with respect to z and $D = 1 - 1/\gamma$. For neatness the subadiabatic temperature gradient β is a combination of the reference state and basic state terms defined in (3.74), and the subscript '0' has been dropped from the basic state terms. Since the coefficients of the system of linear PDEs given above are functions only of z, we may assume perturbation variables are of the form

$$\boldsymbol{f}(x, y, z, t) = \hat{\boldsymbol{f}}(z)\exp^{i(kx + ly + \omega t)}. \tag{4.2}$$

We consider a complex ω, defined as $\omega = \omega_r + i\omega_i$; thus a modal solution of this form grows when $\omega_i < 0$. After dropping the hatted notation, equations (4.1) reduce to an eigenvalue problem given by the following system of equations,

$$iku + ilv + w' = 0 \tag{4.3a}$$

$$ikb_x + ilb_y + b'_z = 0 \tag{4.3b}$$

$$i(\omega + kU)u + U'w = ikBb_x + B'b_z, \tag{4.3c}$$

$$i(\omega + kU)v = -il\Pi + ikBb_y, \tag{4.3d}$$

$$i(\omega + kU)w = -\Pi' + (T + Bb_x) + ikBb_z, \tag{4.3e}$$

$$i(\omega + kU)b_x + B'w = ikBu + U'b_z, \tag{4.3f}$$

$$i(\omega + kU)b_y = ikBv, \tag{4.3g}$$

$$i(\omega + kU)b_z = ikBw, \tag{4.3h}$$

$$i\left(\omega + kU\right)\left(T + DBb_x\right) = -\beta w. \tag{4.3i}$$

Provided $l \neq 0$, the equations (4.3) can be reduced to a single governing second order ODE for w

$$\alpha_1(z)w'' + \alpha_2(z)w' + \alpha_3(z)w = 0, \tag{4.4}$$

where

$$\alpha_1(z) = (\omega + kU)^2 - k^2 B^2, \tag{4.5}$$

$$\alpha_2(z) = \frac{2k^3 B^2 U'}{\omega + kU} - 2k^2 BB', \tag{4.6}$$

$$\alpha_3(z) = k^2 l^2 B^2 - l^2(\omega + kU)^2 + l^2\beta + \frac{l^2 BB'}{\gamma}$$

$$+ \frac{2k^3 BB'U'}{\omega + kU} - \frac{2k^4 B^2 U'^2}{(\omega + kU)^2} - k(\omega + kU)U'' + \frac{k^3 B^2 U''}{\omega + kU}. \tag{4.7}$$

A detailed breakdown on how to recover equation (4.4) is given in appendix A. Equation (4.4) can be solved as a boundary value problem, subject to impermeable boundary conditions on the vertical velocity w. Performing a transformation similar to that used by Howard (1961), equation (4.4) can be represented in a more compact form. Writing $w = (\omega + kU)^{1-n/2}\psi$, the eigenvalue equation (4.4) becomes

$$\left(PQ^{-n}\psi'\right)' - l^2\left(P - \beta - \frac{BB'}{\gamma}\right)Q^{-n}\psi$$

$$+ \frac{n}{2}\left[P\left(\frac{(n/2+1)Q'^2}{Q} - Q''\right) - Q'P'\right]Q^{-1-n}\psi = 0, \tag{4.8}$$

where

$$P = (\omega + kU)^2 - k^2 B^2 \quad \text{and} \quad Q = \omega + kU. \tag{4.9}$$

Since ψ is proportional to w, equation (4.8) can also be solved as a boundary value problem, subject to impermeable boundary conditions on ψ. In the absence of magnetic field ($B = 0$) the above n-dependent ODE can be used to produce three important results for hydrodynamic flows: $n = 0$ produces Howard's semicircle theorem, $n = 1$ leads to the Richardson number criteria for stratified flows and $n = 2$ to a generalization of Rayleigh's inflection-point criteria for stratified flows, derived by Synge (1933). We shall focus on the case where $n = 0$; thus equation (4.8) becomes

$$(P\psi')' - l^2\left(P - \beta - \frac{BB'}{\gamma}\right)\psi = 0. \tag{4.10}$$

Note that equation (4.10) remains unchanged under the transformations $l \to -l$, so without loss of generality we will assume $l > 0$, we also make a similar assumption for k ($k \geq 0$). We will solve this in a domain bounded by rigid walls at $z = 0$ and $z = 1$, thus $\psi = 0$ at each boundary. Therefore, for given real wavenumbers k, l, equation (4.10) is an eigenvalue problem for the unknown $\omega = \omega_r + i\omega_i$.

4.2 Magnetic buoyancy stability criteria for an $O(1/d)$ field gradient, in the absence of velocity shear

In the absence of a velocity shear, equations (3.61) allow us to study magnetic buoyancy instability in the presence of a magnetic field varying on a short $O(d)$ length scale, compared to equations of Spiegel & Weiss (1982), which are restricted to field variations on an $O(H_p)$ scale. It is therefore of interest to derive stability criteria for this new system.

Neglecting velocity shear U, the governing ODE (4.10) simplifies to

$$((\omega^2 - k^2 B^2)\psi')' - l^2 \left(\omega^2 - k^2 B^2 - \beta - \frac{BB'}{\gamma}\right)\psi = 0. \qquad (4.11)$$

Multiplying (4.11) by ψ^* (the complex conjugate of ψ), integrating over z and making use of the boundary conditions gives

$$\int_0^1 \omega^2 \Lambda \, dz = l^2 \int_0^1 \left(k^2 B^2 + \beta + \frac{BB'}{\gamma}\right)|\psi|^2 dz + \int_0^1 k^2 B^2 |\psi'| dz, \qquad (4.12)$$

where $\Lambda = |\psi'|^2 + l^2|\psi|^2$. Expressing the ODE in this form allows us to derive sufficient conditions for stability for both the interchange and undular modes. That is, interchange modes are guaranteed to be stable ($\omega_i > 0$) if everywhere in the layer

$$\beta + \frac{BB'}{\gamma} > 0. \qquad (4.13)$$

Similarly undular modes with longitudinal wavenumber k, are guaranteed to be stable if everywhere

$$k^2 B^2 + \beta + \frac{BB'}{\gamma} > 0. \qquad (4.14)$$

Reverting back to dimensional form, the stability criteria for the interchange and undular respectively become

$$-\frac{\gamma g a^2}{c^2}\frac{\mathrm{d}}{\mathrm{d}z}\ln B < \hat{N}^2 + \frac{g}{T_*}\frac{\mathrm{d}}{\mathrm{d}z}T \tag{4.15a}$$

$$\text{and}\quad -\frac{\gamma g a^2}{c^2}\frac{\mathrm{d}}{\mathrm{d}z}\ln B < a^2 k^2 + \hat{N}^2 + \frac{g}{T_*}\frac{\mathrm{d}}{\mathrm{d}z}T, \tag{4.15b}$$

where c is the adiabatic sound speed and a is the Alfvén speed, defined using the characteristic values as

$$c^2 = \frac{\gamma p_*}{\rho_*}, \quad \text{and}\quad a^2 = \frac{B_*^2}{\mu_0 \rho_*}. \tag{4.16}$$

To separate the hydrodynamic and magnetic states, the Brunt-Väisälä frequency used in (4.15) is defined only in terms of reference state variables,

$$\hat{N}^2 = \frac{g}{\gamma}\frac{\mathrm{d}}{\mathrm{d}z}\ln\left(\frac{\hat{p}}{\hat{\rho}^\gamma}\right). \tag{4.17}$$

As addressed in §3.3.1 it is possible to define the temperature gradient in a similar form to that used in Spiegel & Weiss (1982) by combining reference and basic state terms, as in (3.70). Expressing the buoyancy frequency in this form

$$N^2 = \frac{g}{\gamma}\frac{\mathrm{d}}{\mathrm{d}z}\ln\left(\frac{\hat{p}+\varepsilon_2 p_0}{(\hat{\rho}+\varepsilon_2 \rho_0)^\gamma}\right), \tag{4.18}$$

we are able to express the stability criteria (4.15) in a more familiar fashion. Thus interchange modes are guaranteed to be stable if everywhere in the layer

$$-\frac{g a^2}{c^2}\frac{\mathrm{d}}{\mathrm{d}z}\ln B < N^2. \tag{4.19}$$

Likewise undular modes are guaranteed to be stable if everywhere in the layer

$$-\frac{g a^2}{c^2}\frac{\mathrm{d}}{\mathrm{d}z}\ln B < a^2 k^2 + N^2. \tag{4.20}$$

By analysing stability criteria (4.19) and (4.20) we can conclude that if an interchange mode is stable, then for the same atmospheric configuration all undular modes must also be stable. In other words, an undular mode cannot be unstable if the interchange mode is stable. This is unlike the results in §2.1.1 where for an $O(d/H_p)$ field gradient, such a situation was possible. When comparing the interchange criteria (4.19) and (2.9), we see that for an $O(1/d)$ field gradient, stability is no longer dependent on the decrease of B/ρ, but instead just of B. This can be seen through our orderings laid out in Chapter 3, as $\mathrm{d}\hat{\rho}/\mathrm{d}z$ is $O(d/H_p)$ smaller than $\mathrm{d}B/\mathrm{d}z$ and therefore does not enter the equations.

4.3   Semicircle theorems

In this section we reintroduce the effects of a velocity shear into our analysis. For incompressible, hydrodynamic shear flows, Howard (1961) showed that the complex wave speed $c = -\omega/k$ of an unstable mode must lie within a semicircle in the complex plane, the size of which is determined by properties of the basic state flow. A magnetic extension to this was provided by Hughes & Tobias (2001), who studied the incompressible, ideal MHD equations in the presence of a basic state shear flow aligned with the basic state magnetic field. Their aim was to examine the influence of the magnetic field on the shear flow; as such they neglected buoyancy effects. Stability criteria can then be derived from the semicircle bounds. A similar process can be carried out using our new equations to include magnetic buoyancy effects.

As part of their derivation, Hughes & Tobias (2001) made use of a magnetic extension to Squire's theorem (Squire, 1933), where it can be shown that for any unstable three-dimensional (undular) mode, there corresponds a two-dimensional undular mode ($l = 0$) with a larger growth rate. A striking difference between our system and that used by Hughes & Tobias (2001) is the lack of a total pressure term in the x-component of the momentum equation (4.3c). As such we require a non-zero l to eliminate the total pressure terms in our equations and thus there is no analogue of Squire's theorem.

Multiplying (4.10) by ψ^*, integrating over the layer and applying the impermeable boundary conditions gives

$$\int_0^1 P\Lambda\,\mathrm{d}z - l^2 \int_0^1 \left(\beta + \frac{BB'}{\gamma} \right) |\psi|^2 \mathrm{d}z = 0. \tag{4.21}$$

Since the eigenvalue ω is complex this can be split into real and imaginary parts, the imaginary part becoming

$$\omega_i \int_0^1 (\omega_r + kU)\Lambda\,\mathrm{d}z = 0. \tag{4.22}$$

This is Rayleigh's result that states for any unstable mode ($\omega_i < 0$), ω_r lies within a range of negative kU (i.e. $-kU_{\max} \le \omega_r \le -kU_{\min}$). Note that this bound is independent of the basic state magnetic field and temperature gradient.

With the use of (4.22), the real part of (4.21) becomes

$$\int_0^1 \left(\omega_r^2 + \omega_i^2\right) \Lambda \, \mathrm{d}z = k^2 \int_0^1 \left(U^2 - B^2\right) \Lambda \, \mathrm{d}z - l^2 \int_0^1 \left(\beta + \frac{BB'}{\gamma}\right) |\psi|^2 \mathrm{d}z. \quad (4.23)$$

As we do not know the magnitude of $|\psi|^2$, to proceed further we have to restrict our analysis to two cases; $\beta + BB'/\gamma > 0$ everywhere and $\beta + BB'/\gamma < 0$ everywhere. Unfortunately we are not able to conclude anything regarding the case where $\beta + BB'/\gamma$ changes sign over the layer.

If $\beta + BB'/\gamma > 0$ everywhere, equation (4.23) implies

$$0 \leq \left(\omega_r^2 + \omega_i^2\right) \int_0^1 \Lambda \, \mathrm{d}z \leq k^2 \left(U^2 - B^2\right)_{\max} \int_0^1 \Lambda \, \mathrm{d}z. \quad (4.24)$$

This is the same result found by Hughes & Tobias (2001), who went on to derive two semicircle bounds for the eigenvalue. Their results tell us that if $\beta + BB'/\gamma > 0$ everywhere, the eigenvalue ω of an unstable mode must lie within the intersection of the two semicircles defined by

$$\omega_r^2 + \omega_i^2 \leq k^2 \left(U^2 - B^2\right)_{\max}, \quad (4.25)$$

$$\left(\omega_r + \frac{k}{2}(U_{\min} + U_{\max})\right)^2 + \omega_i^2 \leq \frac{k^2}{4}(U_{\min} - U_{\max})^2 - k^2 \left(B^2\right)_{\min}. \quad (4.26)$$

Now suppose $\beta + BB'/\gamma < 0$ everywhere; we can rewrite (4.23) as

$$\int_0^1 \left(\omega_r^2 + \omega_i^2\right) \Lambda \, \mathrm{d}z = \int_0^1 \left[k^2 \left(U^2 - B^2\right) - \left(\beta + \frac{BB'}{\gamma}\right)\right] \Lambda \, \mathrm{d}z$$
$$+ \int_0^1 \left(\beta + \frac{BB'}{\gamma}\right) |\psi'|^2 \mathrm{d}z. \quad (4.27)$$

Thus for an unstable mode, $\omega_r^2 + \omega_i^2$ lies within a semicircle defined by

$$\omega_r^2 + \omega_i^2 \leq k^2 \left(U^2 - B^2\right)_{\max} - \left(\beta + \frac{BB'}{\gamma}\right)_{\min}. \quad (4.28)$$

Another semicircle bound may be obtained using the inequality

$$0 \geq k^2 \int_0^1 \left(U - U_{\min}\right) \left(U - U_{\max}\right) \Lambda \, \mathrm{d}z. \quad (4.29)$$

Making use of (4.22) and (4.27), we can write the above inequality (4.29) as

$$
\begin{aligned}
0 \geq \int_0^1 \bigg[&\left(\omega_r^2 + \omega_i^2\right) + k\left(U_{\min} + U_{\max}\right)\omega_r + k^2 U_{\min} U_{\max} \\
&+ k^2 B^2 + \left(\beta + \frac{BB'}{\gamma}\right) \bigg] \Lambda \, \mathrm{d}z - \int_0^1 \left(\beta + \frac{BB'}{\gamma}\right) |\psi'|^2 \mathrm{d}z.
\end{aligned}
\tag{4.30}
$$

Since $\beta + BB'/\gamma$ is negative everywhere, it follows that

$$
\begin{aligned}
0 \geq &\left(\omega_r^2 + \omega_i^2\right) + k\left(U_{\min} + U_{\max}\right)\omega_r + k^2 U_{\min} U_{\max} \\
&+ k^2 \left(B^2\right)_{\min} + \left(\beta + \frac{BB'}{\gamma}\right)_{\min},
\end{aligned}
\tag{4.31}
$$

or equivalently in semicircle form

$$
\begin{aligned}
\left(\omega_r + \frac{k}{2}\left(U_{\min} + U_{\max}\right)\right)^2 + \omega_i^2 \leq \frac{k^2}{4}\left(U_{\min} - U_{\max}\right)^2 \\
- k^2 \left(B^2\right)_{\min} - \left(\beta + \frac{BB'}{\gamma}\right)_{\min}.
\end{aligned}
\tag{4.32}
$$

Together these results tell us that when $\beta + BB'/\gamma < 0$ everywhere, the eigenvalue ω of an unstable mode must lie within the intersection of the two semicircles defined by equations (4.28) and (4.32).

4.3.1 Stability criteria

As noted by Hughes & Tobias (2001), as well as yielding eigenvalue bounds for unstable modes, the semicircle results allow us to derive sufficient conditions for stability. Since instability requires an overlap of both the semicircles, we can conclude that the flow is stable if either of the semicircle's radius shrinks to zero and hence the semicircle ceases to exists (Figure 4.1c). When $\beta + BB'/\gamma$ is positive throughout the layer we arrive at the same result as Hughes & Tobias (2001); from (4.25) and (4.26), stability is guaranteed when $\beta + BB'/\gamma > 0$ everywhere, if either of these conditions are satisfied:

$$
|B| > |U|,
\tag{4.33a}
$$

everywhere in the fluid, or

$$
|B|_{\min} > \frac{|U_{\min} - U_{\max}|}{2}.
\tag{4.33b}
$$

In the absence of a basic state shear flow ($U = 0$), these conditions are always satisfied. This confirms what we found §4.2; namely that stability is assured in the absence of shear, when $\beta + BB'/\gamma > 0$ everywhere.

Stability is also guaranteed when both semicircles are well defined but are disjoint (Figure 4.1d). Again using (4.25) and (4.26), if $\beta + BB'/\gamma > 0$ everywhere, the flow is stable when

$$\frac{U_{\min} + U_{\max}}{2} - \sqrt{\frac{(U_{\min} - U_{\max})^2}{4} - (B^2)_{\min}} > \sqrt{(U^2 - B^2)_{\max}}. \qquad (4.34)$$

Similar stability criteria can be derived when $\beta + BB'/\gamma$ is negative throughout the layer, from semicircles (4.28) and (4.32). Thus stability is guaranteed when $\beta + BB'/\gamma < 0$ everywhere, if any of the three following criteria are satisfied:

$$k^2 \left(U^2 - B^2\right)_{\max} > \left(\beta + \frac{BB'}{\gamma}\right)_{\min}, \qquad (4.35)$$

$$\frac{k^2}{4} \left(U_{\min} - U_{\max}\right)^2 - k^2 \left(B^2\right)_{\min} > \left(\beta + \frac{BB'}{\gamma}\right)_{\min}, \qquad (4.36)$$

$$\frac{k}{2} \left(U_{\min} + U_{\max}\right) + \sqrt{\frac{k^2 \left(U_{\min} - U_{\max}\right)^2}{4} - k^2 \left(B^2\right)_{\min} - \left(\beta + \frac{BB'}{\gamma}\right)_{\min}}$$

$$> \sqrt{k^2 \left(U^2 - B^2\right)_{\max} - \left(\beta + \frac{BB'}{\gamma}\right)_{\min}}. \qquad (4.37)$$
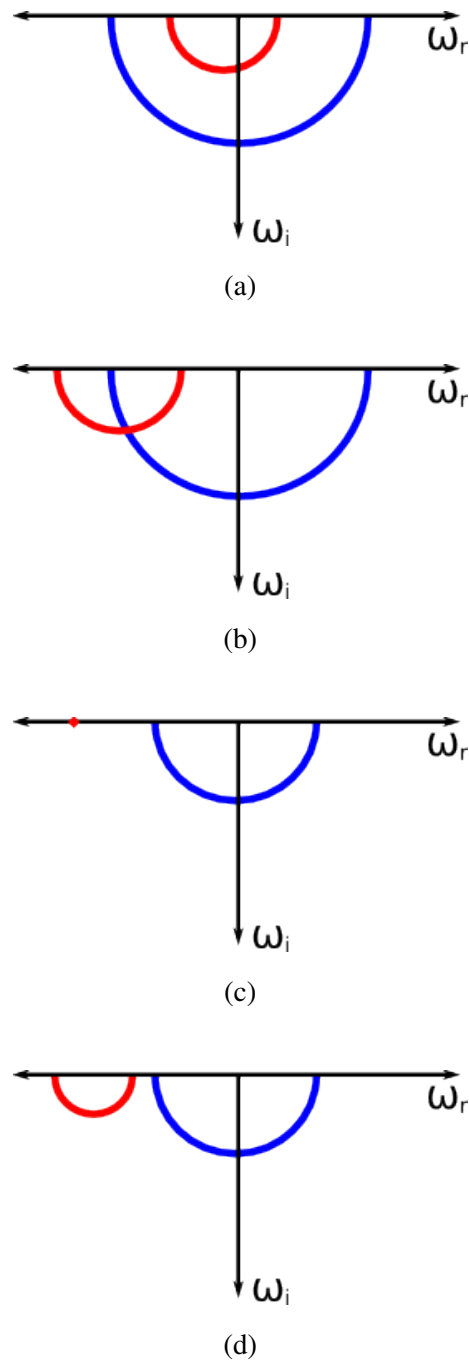
Figure 4.1: Four possible configurations for the semicircles bounds. The bounds could:
(a) fully overlap; (b) partially overlap; (c) have one undefined semicircle; (d) be disjoint.
In configurations (a) and (b) the semicircles overlap and instability is possible, whereas
in (c) and (d) linear stability is guaranteed.

Chapter 5

Short-wavelength magnetic buoyancy instability

5.1 Introduction

The study of magnetic buoyancy instability in the short-wavelength limit was introduced by Gilman (1970), who considered the linear instability of a horizontal stratified magnetic field in a compressible layer. With the extreme parameter values of the solar interior in mind, Gilman considered the case where the thermal diffusivity is large compared to viscosity and the diffusivity of the magnetic field. With these parameter values in place one can represent the set of governing equations as an eigenvalue problem, which can be solved by employing appropriate boundary conditions. Gilman suggested that the fastest growing mode in such a system would be infinitesimally narrow in the horizontal direction perpendicular to the imposed magnetic field. By adopting this short-wavelength limit ($l \to \infty$) and assuming derivatives in height z remain sufficiently small, the governing equations can be drastically simplified. Specifically, all z derivatives in our system vanish, leaving a '*depth-dependent*' dispersion relation for the eigenvalue. Thus the eigenvalue, and therefore the growth rate, can be written in terms of basic state variables that vary in height. This suggests the growth rate can theoretically take different values throughout the layer. As noted by Mizerski et al. (2013), mathematically this raises

an interesting question as to how the boundary conditions play a role in such a system where z derivatives are seemingly irrelevant. Through an asymptotic boundary layer analysis Mizerski et al. (2013) bridged the gap and incorporated the boundary value problem with Gilman's $l \to \infty$ depth-dependent dispersion relation. Their results showed that in the short-wavelength limit, eigenfunctions of the system are localised around a point in the layer and this point corresponds to the height at which the growth rate, given by the depth-dependent dispersion relation, is maximised.

Similar localised results have also been found in a very different contexts. Using similar boundary layer techniques, Griffiths (2008) studied inertial instabilities of a rotating, stratified flow influenced by a horizontal cross-stream shear and found similar results. Griffiths took a small vertical scale that corresponded to a 'near-inertial' limit and found solutions localised in the direction of the horizontal cross-stream direction.

Guided by the work of Mizerski et al. (2013) and Griffiths (2008) we aim to study the short-wavelength magnetic buoyancy instability for our new system of equations (3.61). In §5.2 we look at the instability in the absence of shear. Although this work follows that of Mizerski et al. (2013), it is necessary in order to gain a good understanding of the simplified problem before adding further complexity. In §5.3 we tackle the problem with velocity shear. It would appear at first glance that the shear plays no role on the instability, as the $l \to \infty$ limit suggests that the shear contributes only to the frequency of the mode. Through an asymptotic analysis we shall see that this is not necessarily the case, and that in fact the shear can play a very big role in determining the growth rate and structure of the mode. These influences of the shear on the instability are discussed in detail in §5.4. As well as revealing new results, the work in this chapter lays the foundations for the work in Chapter 6, where the effects of diffusion on the short-wavelength instability are considered.

5.2 Short-wavelength instability with an $\mathrm{O}\left(1/d\right)$ magnetic field gradient, in the absence of velocity shear

This first section on short-wavelength magnetic buoyancy instability will all be studied in the absence of shear and follows closely the work of Mizerski et al. (2013). Mizerski et al. results were obtained using the fully compressible MHD equations. Whereas, as with the rest of this thesis, we use equations (3.61), which are derived under the magneto-Boussinesq approximation, with an $\mathrm{O}\left(1/d\right)$ magnetic field gradient.

As shown in Chapter 4, it is possible to reduce the linear, diffusionless governing equations (4.1) to a second order differential equation (4.10),

$$\left((\omega^2 - k^2 B^2)\psi'\right)' - l^2 \left(\omega^2 - F\right)\psi = 0, \tag{5.1}$$

where $\psi = (\omega + kU)^{-1} w$. For neatness we have introduced the variable F made up of basic state quantities, defined as

$$F(z) = k^2 B^2 + \beta + \frac{BB'}{\gamma}. \tag{5.2}$$

Equation (5.1) can be solved as a boundary value problem subject to impermeable boundary conditions on ψ. It is important at this stage to comment upon our assumptions leading to equation (5.1) and how they differ to the assumptions of Gilman (1970), and consequently Mizerski et al. (2013). With the magnitudes of the solar parameters in mind Gilman considered (as did we) the case of an inviscid, perfectly conducting gas. However, unlike us, he made the assumption that the thermal relaxation was sufficiently fast that the temperature perturbation could be specified at all times, therefore treating the gas as isothermal and ignoring the energy equation in his calculations. To keep the effects of the reference state stratification we have not made this assumption and instead have just neglected thermal diffusion. It is straightforward however to derive an analogue to equation (5.1) for the isothermal case

$$\left((\omega^2 - k^2 B^2)\psi'\right)' - l^2 \left(\omega^2 - k^2 B^2 - BB'\right)\psi = 0. \tag{5.3}$$

We can seamlessly transition between our governing ODE (5.1) and the isothermal analogue (5.3) by implementing both $\hat{\beta} = 0$ and $T_0' = 0$.

When considering the short-wavelength limit, Gilman assumes that perturbations are very narrow in the y direction compared with the scales in x and z, which is enforced through the scaling $l \to \infty$ with $\partial_z \ll l$. Applying this assumption to equation (5.1) we obtain,

$$\left(\omega^2 - F \right) \psi = 0. \tag{5.4}$$

Besides the trivial solution, in which $\psi = 0$ throughout the layer, the only other solution is a discontinuous one; $\psi = 0$ everywhere expect at a point z_c where

$$\omega^2 = F(z_c). \tag{5.5}$$

It is interesting to note that eigenvalues defined in (5.5) vary continuously with height. This could lead to the possibility of a continuum of peaked solutions, all at different heights, each of which corresponding to a different eigenvalue ω and hence a different growth rate. Therefore is it logical to ask which solution is preferred and thus what is the height z_c, at which the eigenfunction is peaked? Mizerski et al. (2013) identified that the physical solution would naturally be the most unstable mode, thus z_c would be the point in the layer at which the '*depth–dependent*' eigenvalue given by

$$\omega(z) = -\sqrt{F(z)} = -\left(k^2 B^2 + \beta + \frac{BB'}{\gamma} \right)^{1/2}, \tag{5.6}$$

takes its most negative imaginary value; i.e. the point in the layer where the growth rate is maximised. The idea behind the $l \to \infty$ limit solution can be visualised in Figure 5.1. Here the depth–dependent imaginary part of the eigenvalue given by equation (5.6) is minimised at $z_c = 0.4$, when $\Im(\omega) = -1$. Thus the corresponding eigenfunction solution is zero everywhere expect at the point $z = 0.4$.

Equation (5.6) also provides us with a criterion for instability. That is, in the short-wavelength limit, instability ($\Im(\omega) < 0$) occurs if somewhere in the layer

$$F(z) = k^2 B^2 + \beta + \frac{BB'}{\gamma} < 0. \tag{5.7}$$
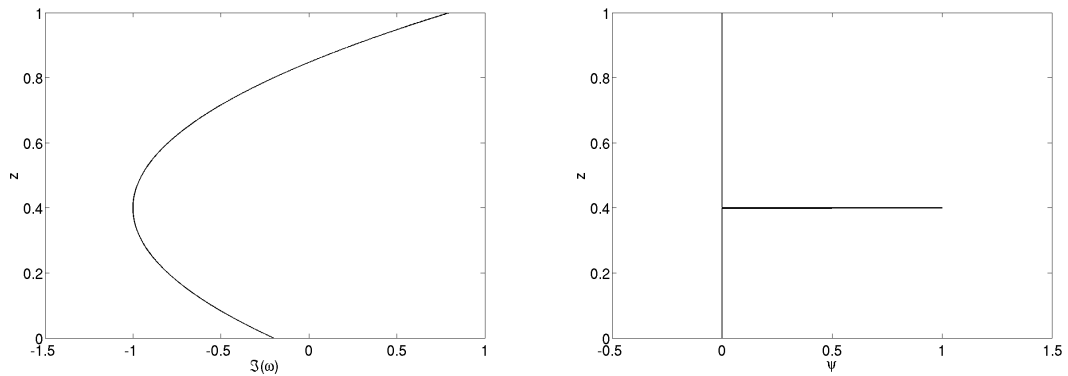
Figure 5.1: An example of the discontinuous problem in the $l \to \infty$ limit, with the depth-dependent $\Im(\omega)$ given by (5.6) (left), and the corresponding discontinuous eigenfunction solution ψ (right).

As done in §4.2, this inequality can be converted back to dimensional form. Thus short-wavelength instability is guaranteed if somewhere in the layer

$$-\frac{ga^2}{c^2}\frac{\mathrm{d}}{\mathrm{d}z}\ln B > a^2 k^2 + N^2, \tag{5.8}$$

where the a, c and N are defined as in (4.16) and (4.18). Written in this form it is clear that instability is more readily achieved for interchange modes (i.e $k = 0$). Thus for a given configuration in the short-wavelength limit, the most unstable mode will always be an interchange mode. The same result was found by Mizerski et al. (2013), who found that, provided $H_b \lesssim 2H_p$, the dominant mode will always be an interchange mode. This is very different to the results of Chapter 2, where for a smaller field gradient ($H_B \sim H_p$) the preferred mode of instability was the undular mode with finite $k \to 0$. If we were only interested in the case without velocity shear it would be logical at this stage to restrict our analysis to just interchange modes. However, we see from our governing equation with velocity shear (4.10) that upon taking $k = 0$, we lose all terms associated with U. Therefore, to examine the effects of velocity shear on the short-wavelength magnetic buoyancy instability it is crucial that $k \neq 0$. With this in mind, we do not neglect k terms in our calculations and hence study the full three-dimensional problem throughout.

In a similar vein, we see that the instability is hindered by increasing the convective

stability of the atmosphere (i.e. increasing N^2). Thus the isothermal limit adopted by Gilman, corresponding to $N^2 = 0$, leads to modes of higher growth rate. This idea is discussed further in Chapter 6 as we introduce diffusivities into the system.

5.2.1 Asymptotic analysis

Upon adopting the $l \to \infty$ limit, our governing equation is transformed from a second order ODE (5.1) with appropriate boundary conditions, to equation (5.4), in which all z derivatives have vanished. Therefore, in this limit, the system seemingly has no dependency on the boundary conditions. Following in the footsteps of Mizerski et al. (2013) we perform a boundary layer analysis on the governing ODE (5.1), in an attempt to link the discontinuous problem outlined above to the full solution of the eigenvalue problem for large finite l. Formally this is achieved by introducing a boundary layer variable

$$\xi_i = \frac{z - z_c}{\delta_i},$$ (5.9)

where $\delta_i(l)$ is a measure of the thickness of the boundary/internal layer. From what we observed in §5.2, we expect δ_i to become small as l becomes large. Therefore, we expand the eigenvalue in powers of δ_i such that $\omega = \omega_0 + \delta_1\omega_1 + \delta_2^2\omega_2 + \dots$, and assume $\omega_0 \sim \mathrm{O}(1)$. By introducing appropriate boundary layers we aim to match the main flow solution $\psi = 0$ to the point z_c, where equation (5.5) is satisfied. By Taylor expanding all functions of z around the point z_c, it is possible to derive asymptotically consistent analytic solutions for the eigenvalue ω and eigenfunction ψ. Like Mizerski et al. (2013), we impose impermeable boundary conditions on ψ, such that $\psi = 0$ at both the top and bottom boundaries.

Considering $i = 0$ with $\omega = \omega_0 + o(1)$, equation (5.1) becomes

$$\left(\omega_0^2 - k^2 B^2\right) \frac{\mathrm{d}^2\psi}{\mathrm{d}\xi_0^2} - \delta_0^2 l^2 \left(\omega_0^2 - F\right) \psi = 0,$$ (5.10)

where all basic state functions of z are evaluated at z_c. It is worth noting that in equation (5.10) we have dropped all terms smaller than $\mathrm{O}(1)$; hence for asymptotic

consistency we require $\delta_0 = l^{-1}$. The only continuous, non-trivial solution to this equation that obeys the boundary conditions is a constant ψ, with

$$\omega_0 = -\sqrt{F(z_c)} = -\left(k^2 B^2 + \beta + \frac{BB'}{\gamma} \right)^{1/2} \Bigg|_{z=z_c}. \tag{5.11}$$

Therefore, in order to match this constant ψ solution to the main flow ($\psi = 0$), we must consider higher-order terms and introduce more internal boundary layers. With our overall focus on the linear instabilities, we take ω_0 to be the negative root of $\omega_0^2 = F$. As addressed in §5.2, z_c is defined as the place in the layer at which $F(z)$ takes its most negative value. Thus, like Mizerski et al. (2013), we have to split our analysis into two cases. In §5.2.2 we consider the case when $F(z)$ has a quadratic minimum in the layer at $z = z_{\max}$, thus $z_c = z_{\max}$ similar to what we saw in Figure 5.1. In §5.2.3 we examine what happens when $F(z)$ has no minimum, or is minimised outside the layer. In this case, z_c is defined on the upper or lower boundary, depending on whether $F(z)$ is a decreasing or increasing function. The final special case in which $F(z)$ is minimised exactly on the boundary is addressed at the end of §5.2.3.

5.2.2 z_c in the layer

In this section we are interested in the case where the growth rate, defined by $-\Im\left(\omega(z)\right)$, is maximised in the layer at $z = z_c$. Suppose we introduce another boundary layer coordinate

$$\xi_1 = \frac{z - z_c}{\delta_1}, \tag{5.12}$$

and look for next order corrections to the eigenvalue $\omega = \omega_0 + \delta_1\omega_1 + o(\delta_1)$. Substituting these expressions into (5.1) and making use of equation (5.11) we obtain, through Taylor expansion,

$$\left(\omega_0^2 - k^2 B^2\right) \frac{\mathrm{d}^2\psi}{\mathrm{d}\xi_1^2} - \delta_1^3 l^2 \left[2\omega_0\omega_1 - \xi_1 \frac{\mathrm{d}F}{\mathrm{d}z} \right] \psi = 0, \tag{5.13}$$

where again all basic state functions of z are evaluated at $z = z_c$. Terms in this equation balance when $\delta_1 = l^{-2/3}$ and all terms smaller than $\mathrm{O}\left(1\right)$ are neglected. By definition, z_c

is the height at which $F(z)$ is minimised and hence

$$\frac{\mathrm{d}F}{\mathrm{d}z}\bigg|_{z=z_c} = \frac{\mathrm{d}}{\mathrm{d}z}\left(k^2 B^2 + \beta + \frac{BB'}{\gamma}\right)\bigg|_{z=z_c} = 0. \tag{5.14}$$

Therefore, equation (5.13) reduces to

$$\left(\omega_0^2 - k^2 B^2\right)\frac{\mathrm{d}^2\psi}{\mathrm{d}\xi_1^2} - 2\omega_0\omega_1\psi = 0. \tag{5.15}$$

The only continuous solution for ψ with a turning point in the layer has $\omega_1 = 0$, and hence provides no new information on the eigenvalue. Thus we are required to introduce a further boundary layer to our expansion. Let

$$\xi_2 = \frac{z - z_c}{\delta_2}, \tag{5.16}$$

and expand the eigenvalue with $\omega_1 = 0$ as $\omega = \omega_0 + \delta_2^2 \omega_2 + o(\delta_2^2)$. When substituted into (5.1) the leading order terms becomes

$$\left(\omega_0^2 - k^2 B^2\right)\frac{\mathrm{d}^2\psi}{\mathrm{d}\xi_2^2} - \delta_2^4 l^2 \left[2\omega_0\omega_2 - \frac{\xi_2^2}{2}\frac{\mathrm{d}^2 F}{\mathrm{d}z^2}\right]\psi = 0. \tag{5.17}$$

There is a balance of terms when $\delta_2 = l^{-1/2}$, with this equation (5.17) can be rewritten in a more compact form as

$$\frac{\mathrm{d}^2\psi}{\mathrm{d}\xi_2^2} - \left[\frac{2\omega_0\omega_2}{\omega_0^2 - k^2 B^2} - \frac{\xi_2^2}{2}\Upsilon\right]\psi = 0, \tag{5.18}$$

where

$$\Upsilon = \frac{1}{\omega_0^2 - k^2 B^2}\frac{\mathrm{d}^2 F}{\mathrm{d}z^2}\bigg|_{z=z_c}. \tag{5.19}$$

By construction, we know that z_c is the minimum of $F(z)$, hence $F''(z_c) > 0$. For instability we require $\omega_0^2 - k^2 B^2 < 0$; therefore in this case Υ is strictly real and negative. Following Mizerski et al. (2013), we introduce two parameter transformations,

$$X = (-2\Upsilon)^{1/4}\xi_2 \quad \text{and} \quad a = \frac{\omega_0\omega_2}{\omega_0^2 - k^2 B^2}\sqrt{-\frac{2}{\Upsilon}}, \tag{5.20}$$

to reduce (5.18) into the standard form of a parabolic cylinder equation

$$\frac{\mathrm{d}^2\psi}{\mathrm{d}X^2} - \left[\frac{1}{4}X^2 + a\right]\psi = 0. \tag{5.21}$$

Under this transformation the impermeable boundary conditions become $\psi = 0$ as $X \to \pm\infty$. The problem is now analogous to that of the quantum harmonic oscillator, with the most general solution written in terms of two linearly independent parabolic cylinder functions D_ν as

$$\psi = C_1 D_\nu(X) + C_2 D_{-\nu-1}(-iX), \tag{5.22}$$

where $\nu = -1/2 - a$. Since this solution has to obey the above mentioned boundary conditions, it is useful to consider the behaviour of the parabolic cylinder function as $X \to \pm\infty$. Taken from Bender & Orszag (1978), for $|\arg(X)| < 3\pi/4$, D_ν can be expressed asymptotically when $X \to \infty$ as

$$D_\nu(X) \sim X^\nu e^{-X^2/4} \left(1 - \frac{\nu(\nu-1)}{2X^2} + \frac{\nu(\nu-1)(\nu-2)(\nu-3)}{8X^4} + \mathrm{O}\left(\frac{1}{X^6}\right) \right). \tag{5.23}$$

With this expression we are able to deduce that as $X \to \infty$, $D_\nu(X) \to 0$ and $D_{-\nu-1}(-iX)$ grow exponentially for all ν. Therefore, to satisfy the boundary condition $\psi = 0$ as $X \to \infty$, we require $C_2 = 0$ in our general solution (5.22). To satisfy the other boundary condition we have to consider the behaviour of D_ν as $X \to -\infty$; For $3\pi/4 < \arg(X) < 5\pi/4$, the parabolic cylinder equation for $X \to \infty$ can be expressed asymptotically as

$$D_\nu(X) \sim -\frac{(2\pi)^{1/2}}{\Gamma(-\nu)} e^{X^2/4} e^{i\pi\nu} X^{-\nu-1} \left(1 + \frac{(\nu+1)(\nu+2)}{2x^2} \right. \tag{5.24}$$

$$\left. + \frac{(\nu+1)(\nu+2)(\nu+3)(\nu+4)}{8X^4} + \mathrm{O}\left(\frac{1}{X^6}\right) \right). \tag{5.25}$$

Thus as $X \to -\infty$, $D_\nu(X)$ grows exponentially except for values of ν for which $\Gamma(-\nu)$ is infinite. By definition, the Gamma function $\Gamma(\bar{x})$ takes infinite values at $\bar{x} = 0$ and all negative integer $\bar{x}$ values. Thus, to ensure the boundary conditions are satisfied and that $D_\nu(X)$ does not grow exponentially as $X \to -\infty$, we are restricted to non-negative values of ν, i.e. for $\nu = 0, 1, 2, \cdots$. This corresponds to the allowable values of a, as $a = -1/2, -3/2, -5/2, \cdots$. Thus, with the use of (5.20) we are able to obtain an analytic solution for ω_2 and therefore the eigenvalue of the system as

$$\omega = \omega_0 \left(1 + l^{-1} \frac{a(\omega_0^2 - k^2 B^2)}{\omega_0^2} \sqrt{-\frac{\Upsilon}{2}} \right) + o(l^{-1}). \tag{5.26}$$
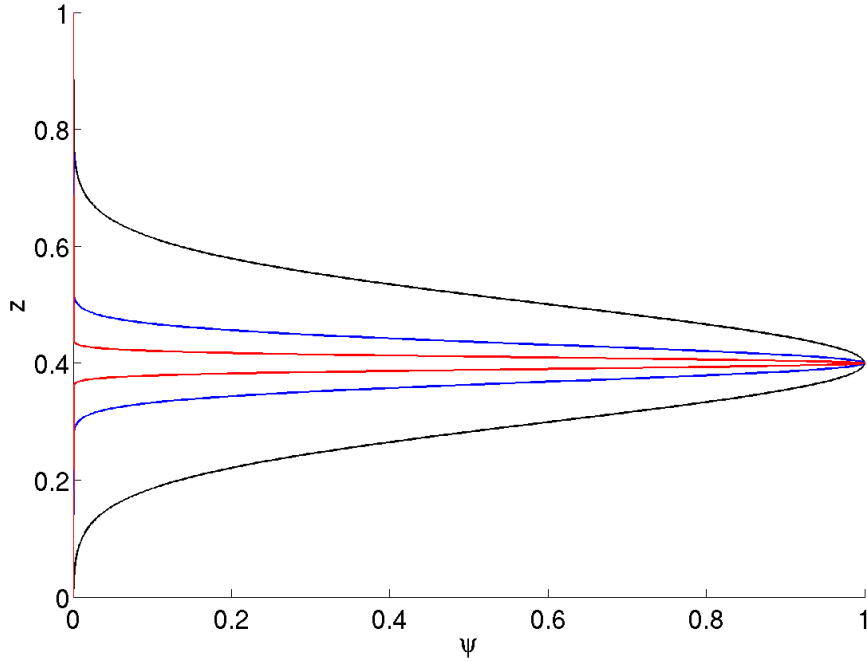
Figure 5.2: Eigenfunction (5.28) with $z_c = 0.4$ and $\Upsilon = -1$, for wavenumbers $l = 50$ (black), $l = 500$ (blue) and $l = 5000$ (red).

For non-negative integer $\nu = n$ values, the parabolic cylinder function can be expressed in terms of a modified n^{th} degree Hermite polynomial $\text{He}_n(X)$, as

$$D_n(X) = e^{-X^2/4}\text{He}_n(X). \tag{5.27}$$

In general the Hermite polynomial $\text{He}_n(X)$ can be written as a polynomial of degree n. Hence a solution for a given n will have $n + 1$ turning points. The first few $\text{He}_n(X)$ are given by $\text{He}_0(X) = 1$, $\text{He}_1(X) = X$, $\text{He}_2(X) = X^2 + 1$ and $\text{He}_3(X) = X^3 - 3X$. Since $\omega_0^2 < 0$, we can conclude from the analytic solution for the eigenvalue (5.26) that the most unstable mode will be the mode with the largest possible value of a. In our case this is when $a = -1/2$, which corresponds to $\nu = n = 0$.

We have shown that when $F(z)$ has a quadratic minimum in the layer at the point $z = z_c$, the most unstable mode in the short-wavelength limit can be written in the form of a parabolic cylinder function. The eigenvalue for such a mode is given by (5.26) (for

$a = -1/2$), with corresponding eigenfunction

$$\psi = C_1 e^{-l\left(\frac{-\Upsilon}{8}\right)^{1/2}(z-z_c)^2},\tag{5.28}$$

where Υ is defined as in equation (5.19). To examine the behaviour of the eigenfunction for increasing l, we introduce a fictional basic state such that $z_c = 0.4$ and $\Upsilon = -1$. Figure 5.2 shows a plot of the eigenfunction (5.28) for this basic state plotted for $l = 50$, $l = 500$, $l = 5000$. As one might expect, by increasing the wavenumber l the mode becomes more localised around the point $z = z_c$. Modes of this type, which are peaked in the layer, will often be referred to as *body modes* throughout the rest of the thesis.

5.2.3 z_c on the boundary

Suppose now that the minimum of the function $F(z)$ lies either outside the layer or that the function has no minimum value. In this case z_c would be defined on either the bottom or top boundary, depending on whether $F(z)$ is an increasing or decreasing function. Following §5.2.2 we are required to introduce an additional boundary layer to match the constant w solution to the $w = 0$ main flow. Defining ξ_1 as in (5.12) and expanding the eigenvalue as $\omega = \omega_0 + \delta_1\omega_1 + o(\delta_1)$, at leading order the governing ODE (5.1) becomes equation (5.13). To balance terms we require $\delta_1 = l^{-2/3}$, which therefore gives

$$\left(\omega_0^2 - k^2B^2\right)\frac{\mathrm{d}^2\psi}{\mathrm{d}\xi_1^2} - \left[2\omega_0\omega_1 - \xi_1\frac{\mathrm{d}F}{\mathrm{d}z}\right]\psi = 0,\tag{5.29}$$

where again all functions of z are evaluated at $z = z_c$. As mentioned, this is just equation (5.13), however unlike the results in §5.2.2; z_c is no longer defined as the point at which $F(z)$ is minimised. Thus equation (5.14) does not hold, and we are able to progress without requiring addition boundary layers. Sticking closely to the notation of Mizerski et al. (2013) it is possible to rewrite (5.29) as

$$\frac{\mathrm{d}^2\psi}{\mathrm{d}\xi_1^2} - \left[\frac{2\omega_0\omega_1}{\omega_0^2 - k^2B^2} - \xi_1\Sigma\right]\psi = 0,\tag{5.30}$$

where,

$$\Sigma = \frac{1}{\omega_0^2 - k^2B^2}\frac{\mathrm{d}F}{\mathrm{d}z}\bigg|_{z=z_c}.\tag{5.31}$$

If we introduce the new variable

$$s = \left(\frac{2\omega_0\omega_1}{\omega_0^2 - k^2 B^2} - \xi_1 \Sigma \right) \Sigma^{-2/3}, \tag{5.32}$$

equation (5.30) can be transformed into Airy's equation

$$\frac{\mathrm{d}^2\psi}{\mathrm{d}s^2} - s\psi = 0. \tag{5.33}$$

Abramowitz & Stegun (1972) show that solutions to this equation can be expressed in terms of the sum of two linearly independent Airy functions $\mathrm{Ai}(s)$ and $\mathrm{Bi}(s)$, i.e. as

$$\psi = C_1\mathrm{Ai}(s) + C_2\mathrm{Bi}(s), \tag{5.34}$$

where C_1 and C_2 are complex constants.

To match this solution to the main flow we must apply the appropriate boundary conditions. Suppose that we assume $F(z)$ is an increasing function that takes its most negative value on the bottom boundary; thus for an unstable mode $z_c = 0$ and $\Sigma < 0$. The solution must then converge to zero as we approach the top boundary; therefore to satisfy the top boundary condition we require $\psi \to 0$ as $\xi_1 \to \infty$. Since $\Sigma < 0$ and the definition of 's' explicitly contains a $\Sigma^{2/3}$ term, it raises the question as to which root of $\Sigma^{2/3}$ is required. Olver (1974) states that there are three sectors in which $\psi(s)$ exists, split up by $|\arg(s)| < \pi/3$, $\pi/3 < \arg(s) < \pi$ and $-\pi < \arg(s) < \pi/3$. Examining the behaviour as $s \to \infty$, it can be shown that the $\mathrm{Ai}(s)$ function decays exponentially in the first sector, and grows exponentially in the other two sectors, whereas $\mathrm{Bi}(s)$ grows exponentially in all three sectors. Thus, in order to satisfy the boundary condition, we require two conditions to be met; The root of $\Sigma^{-2/3}$ is chosen such that $|\arg(s)| < \pi/3$ as $\xi_1 \to \infty$, and $C_2 = 0$. The same conditions are required when considering a decreasing function $F(z)$ that has its most negative value on the top boundary. Therefore, independent of the choice of z_c, the general solution reduces to

$$\psi = C_1\mathrm{Ai}(s) = C_1\mathrm{Ai}\left[\left(\frac{2\omega_0\omega_1}{\omega_0^2 - k^2 B^2} - \xi_1 \Sigma \right) \Sigma^{-2/3} \right]. \tag{5.35}$$

We now have to implement the second boundary condition, $\psi = 0$ when $z = z_c$. With this condition, (5.35) gives

$$\mathrm{Ai}\left[\left(\frac{2\omega_0\omega_1}{\omega_0^2 - k^2 B^2} \right) \Sigma^{-2/3} \right] = 0. \tag{5.36}$$
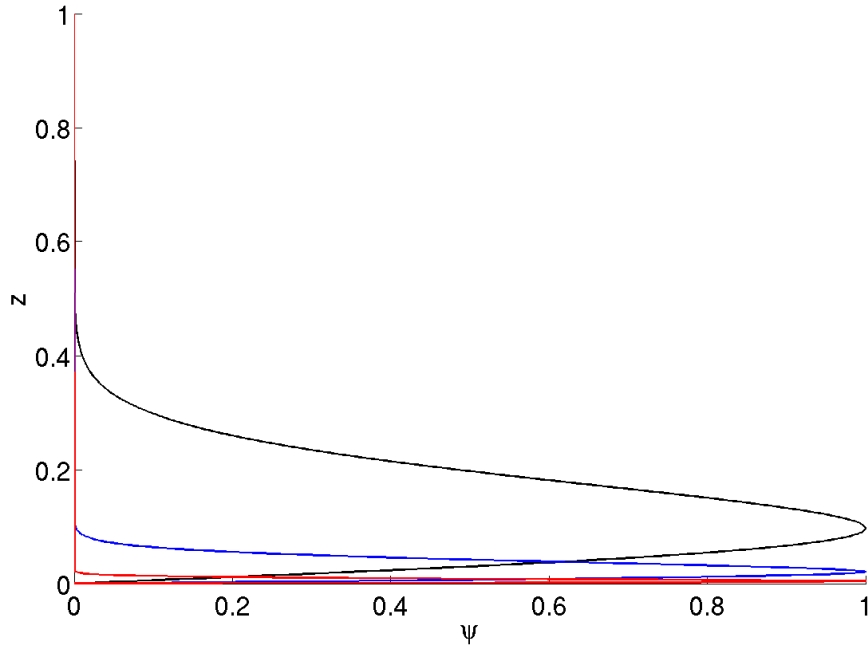
Figure 5.3: Eigenfunction (5.39) with $z_c = 0$ and $\Sigma = -1$, for wavenumbers $l = 50$ (black), $l = 500$ (blue) and $l = 5000$ (red).

Defining χ such that $\mathrm{Ai}(\chi) = 0$ allows us to express ω_1 in terms of basic state variables as

$$\omega_1 = \frac{\chi(\omega_0^2 - k^2 B^2)\Sigma^{2/3}}{2\,\omega_0}. \tag{5.37}$$

It can be shown that when $|\arg(s)| < \pi/3$, all zeros of the Airy function $\mathrm{Ai}(s)$ are real and negative, and therefore $\chi < 0$. With this we can express the full eigenvalue of the system as

$$\omega = \omega_0 \left(1 + l^{-2/3}\frac{\chi(\omega_0^2 - k^2 B^2)\Sigma^{2/3}}{2\,\omega_0^2}\right) + o\left(l^{-2/3}\right). \tag{5.38}$$

Since $\omega_0^2 < 0$, the mode with the highest growth rate occurs when χ takes its largest possible value, which corresponds to $\chi \approx -2.338$.

We have shown that in the case when $F(z)$ either has no minimum or that the minimum is outside the layer, the most unstable mode in the short-wavelength limit has z_c located

at the boundary on which $F(z)$ takes its most negative value. The eigenfunction for such a mode in the large wavelength limit can be expressed by an Airy function as

$$\psi(z) = C_1 \text{Ai} \left[\chi - l^{2/3}(z - z_c)\Sigma^{1/3} \right], \tag{5.39}$$

where Σ is defined as in equation (5.31), with corresponding eigenvalue (5.38). To examine the behaviour of the eigenfunction for this case we suppose that $F(z)$ is minimised below the bottom boundary; thus $z_c = 0$ and we take $\Sigma = -1$. Figure 5.3 shows a plot of the eigenfunction (5.39) for increasing wavenumbers $l = 50$, $l = 500$, $l = 5000$. As before, increasing the wavenumber forces the mode to become more localised. Ideally the system would like to be peaked exactly on the boundary at $z = 0$; however there is a conflict between this desire and the need to satisfy the bottom boundary condition. As such, the localisation approaches $z = 0$ as l is increased.

For completeness we also examine the unique case when $F(z)$ is minimised exactly on the boundary. Specifically we will assume that $F(z)$ is minimised on the bottom boundary, and thus $z_c = 0$ (the same result holds when $z_c = 1$). Analogous to §5.2.2 we introduce a boundary layer through (5.12) and expand the eigenvalue as $\omega = \omega_0 + \delta_1 \omega_1 + o(\delta_1)$. Since z_c is the location at which $F(z)$ is minimised, upon substituting the expansion into the governing ODE, we arrive at equation (5.15). Thus we proceed by taking $\omega_1 = 0$, and seeking another boundary layer, defined by (5.16). Expanding the eigenvalue as $\omega = \omega_0 + \delta_2^2 \omega_2^2 + o(\delta_2^2)$ and fixing $\delta_2 = l^{-1/2}$ we arrive at equation (5.18),

$$\frac{\text{d}^2 \psi}{\text{d}\xi_2^2} - \left[\frac{2\omega_0 \omega_2}{\omega_0^2 - k^2 B^2} - \frac{\xi_2^2}{2}\Upsilon \right] \psi = 0, \tag{5.40}$$

where

$$\Upsilon = \frac{1}{\omega_0^2 - k^2 B^2} \left. \frac{\text{d}^2 F}{\text{d}z^2} \right|_{z=z_c}. \tag{5.41}$$

Through the transformations (5.20), we are able to write equation (5.40) in the form of a parabolic cylinder equation (5.21), which has the general solution

$$\psi = C_1 D_\nu(X). \tag{5.42}$$

Here we have already neglected the second parabolic cylinder function found in (5.22) since it grows exponentially when applying the first boundary condition $\xi \to \infty$. The

second boundary condition is impermeability on the bottom boundary, $\psi = 0$ at $X = 0$, which gives the relation

$$D_\nu(0) = \frac{\sqrt{\pi}}{2^{(2a+1)/4}\Gamma\left(\frac{1}{2} - \frac{\nu}{2}\right)} = 0. \tag{5.43}$$

This is satisfied when the Gamma function takes infinite values and occurs when $(1 - \nu)/2$ equals zero or any negative integer value. Since $\nu = -1/2 - a$, the largest possible value of a (which corresponds to the largest growth rate) corresponds to $\nu = 1$, giving $a = -3/2$. With the use of (5.20) we can express the next order correction to the eigenvalue at this value of a as

$$\omega_2 = -\frac{3(\omega_0^2 - k^2 B^2)}{2\omega_0^2}\sqrt{-\frac{\Upsilon}{2}}. \tag{5.44}$$

Thus the most unstable mode solution to the eigenvalue problem in the case when $F(z)$ is minimised exactly on the boundary, has eigenvalue

$$\omega = \omega_0\left(1 - l^{-1}\frac{3(\omega_0^2 - k^2 B^2)}{2\omega_0^2}\sqrt{-\frac{\Upsilon}{2}}\right) + o(l^{-1}), \tag{5.45}$$

and corresponding eigenfunction

$$\psi(z) = C_1 l\left(-2\Upsilon\right)^{1/4}(z - z_c)e^{-l\left(\frac{-\Upsilon}{8}\right)^{1/2}(z-z_c)^2}. \tag{5.46}$$

This eigenfunction solution behaves in the same way as (5.39), shown in Figure 5.3. Throughout the rest of the thesis, modes peaked near a boundary will often be referred to as *wall modes*.

5.2.4 Boundary value problem

This subsection aims to validate the asymptotic results, by comparing the asymptotic solutions to the numerical solutions of the full boundary value problem. For the boundary value problem, we will solve the governing equation (5.1),

$$\left((\omega^2 - k^2 B^2)\psi'\right)' - l^2\left(\omega^2 - k^2 B^2 - \beta - \frac{BB'}{\gamma}\right)\psi = 0, \tag{5.47}$$
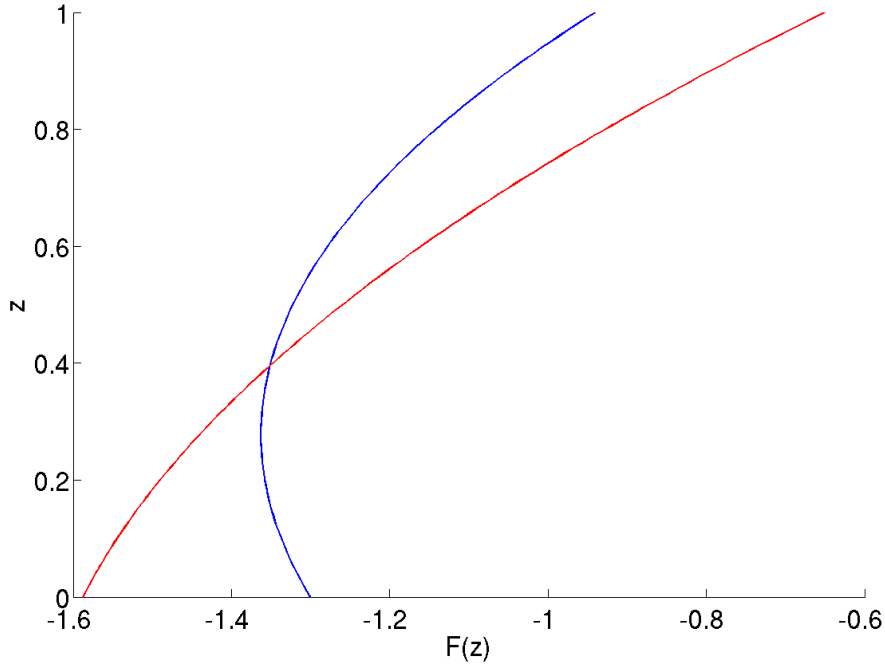
Figure 5.4: Plots of $F(z)$, defined by (5.2), for parameter values P_1 and P_2 given in (5.51).

subject to impermeable boundary conditions $\psi(0) = \psi(1) = 0$ using MATLAB's inbuilt boundary value problem solver BVP4c. Results have been confirmed by solving the same problem using an inverse iteration method described in appendix B.

With our overall intent of studying the full system with the effects of diffusion, we consider a linear basic state magnetic field that satisfies equation (3.32b),

$$B = 1 + \zeta(1 - z). \tag{5.48}$$

We also adopt a linear basic state temperature profile $T = 1 + \alpha z$; the subadiabatic temperature gradient β in our equation thus becomes

$$\beta = \hat{\beta} + \alpha - \frac{\zeta(\gamma - 1)}{\gamma}\left(1 + \zeta(1 - z)\right). \tag{5.49}$$

Using (5.48) and (5.49), we can write our equation for F (5.2) as,

$$F = k^2 B^2 + \hat{\beta} + \alpha + BB'. \tag{5.50}$$

Since our focus is on magnetic buoyancy instability in a stably stratified atmosphere we enforce $\hat{\beta} > 0$ and $\alpha > 0$. Figure 5.4 shows a plot of $F(z)$ (5.50) for two different parameter cases P_1 and P_2,

$$P_1 : \quad \alpha = 0.1, \ \hat{\beta} = 0.1, \ \zeta = 1.5, \ k = 0.6; \tag{5.51a}$$

$$P_2 : \quad \alpha = 0.5, \ \hat{\beta} = 0.1, \ \zeta = 1.5, \ k = 0.5. \tag{5.51b}$$

For parameter values P_1 the growth rate is maximised in the layer with leading order growth rate $-\Im(\omega_0) \approx 1.1673$ (from (5.11)), corresponding to $z_c \approx 0.2776$. We therefore expect that as the wavenumber l is increased, the solution to the boundary value problem will become peaked at this location, with the growth rate tending towards 1.1673. Figure 5.5a shows the solution (ψ) to the boundary value problem (5.47) for parameter values P_1 plotted at three different wavenumber values $l = 50$, $l = 500$, $l = 5000$. The black dots on the same figure are the asymptotic solution (5.28) for $l = 5000$. At this value of l the growth rate obtained from the asymptotic analysis (5.26) (with $a = -1/2$) is $-\Im(\omega) = 1.1671$, which agrees well with the result from the full boundary value problem; clearly the asymptotic analysis provides a good approximation to the full problem. This is confirmed in Figure 5.5b, which plots the growth rate obtained from the boundary value problem for a range of wavenumbers values (red) together with the growth rate obtained from the asymptotic analysis (black). As expected by increasing l, the growth rate of the full solution tends towards the leading order growth rate. Even for relatively low values of l, the asymptotics provides an excellent approximation to the growth rate.

As shown in Figure 5.6, similar results apply when z_c is located at the boundary, as with parameter values P_2. In this case the leading order growth rate from (5.11) is $-\Im(\omega_0) \approx 1.26$ and $z_c = 0$. Again we see that the asymptotic analysis provides an excellent approximation to the full problem.
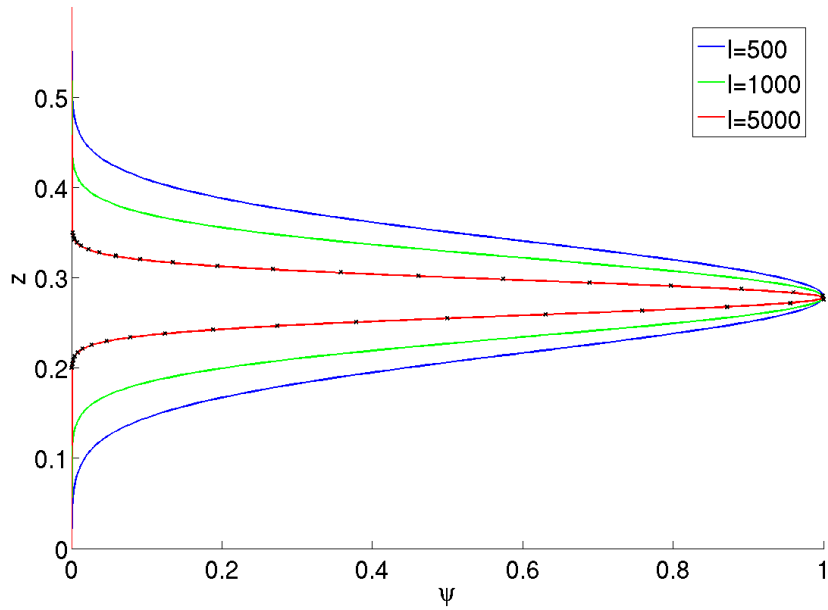
(a)
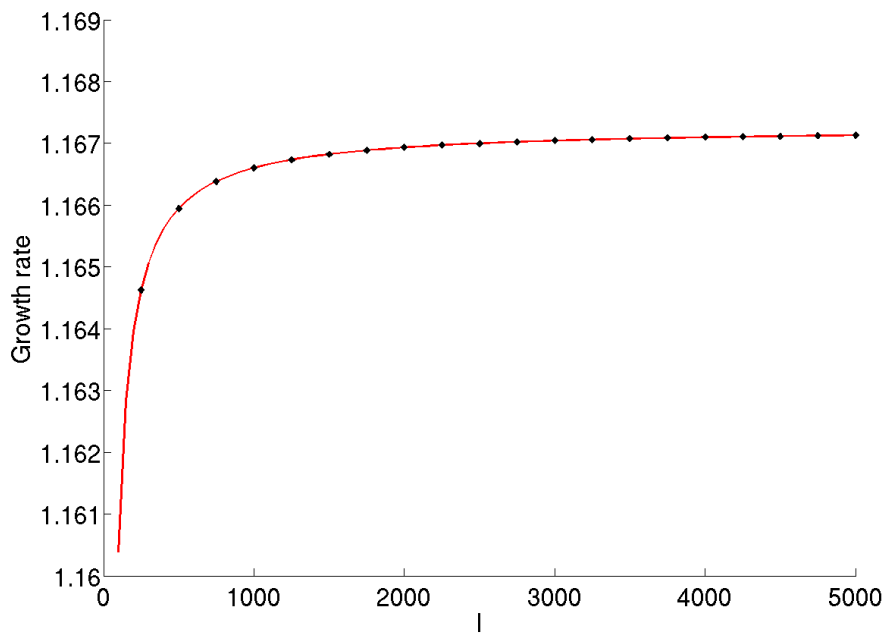
(b)

Figure 5.5: Plots for parameter values P_1 (5.51a), where z_c is located in the layer at $z_c \approx 0.28$. (a): Eigenfunction ψ for the boundary value problem (5.47), plotted at three different wavenumber values $l = 50$, $l = 500$, $l = 5000$. The black dots represent the asymptotic solution (5.28) taken at $l = 5000$. (b): Growth rate $(-\Im(\omega))$ for a range of wavenumbers l. The solid red line represents the full solution to the boundary value problem and the black dots are the asymptotic solution (5.26).
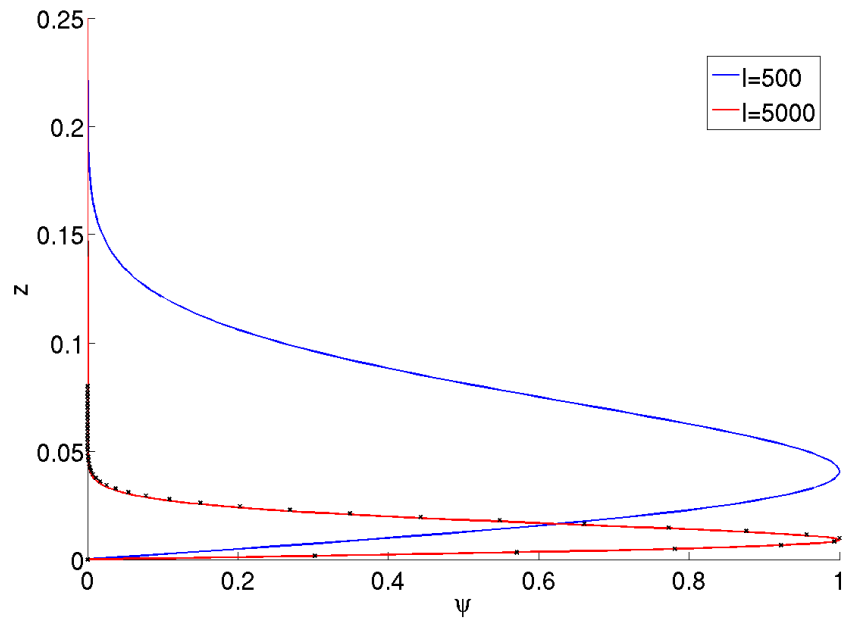
(a)
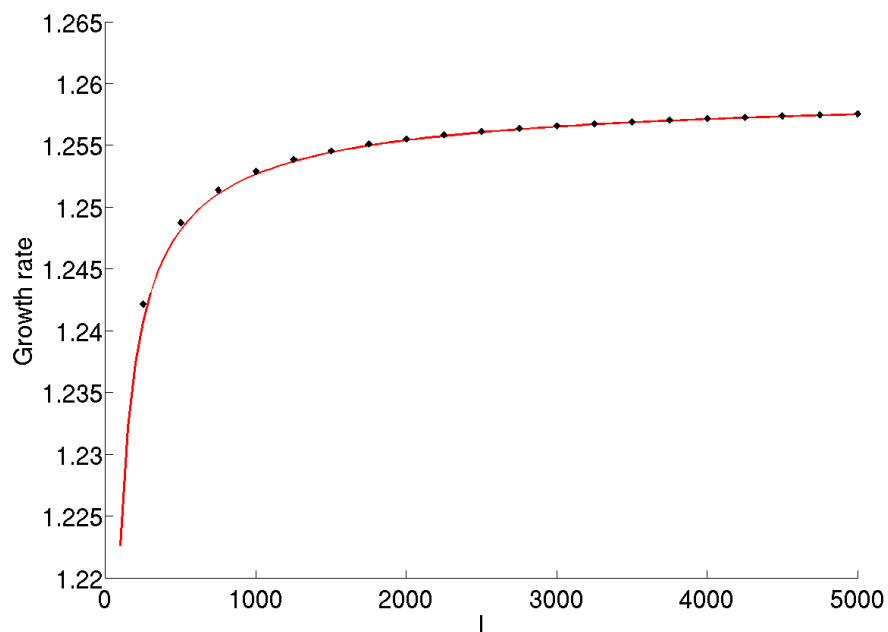
(b)

Figure 5.6: Plots for parameter values P_2 (5.51b), where z_c is located on the bottom boundary. (a): Eigenfunction ψ for the boundary value problem (5.47), plotted at two different wavenumber values $l = 500$ and $l = 5000$. The black dots represent the asymptotic solution (5.39) taken at $l = 5000$. (b): Growth rate $(-\Im(\omega))$ for a range of wavenumbers l. The solid red line represents the full solution to the boundary value problem and the black dots are the asymptotic solution (5.38).

5.3   Introducing velocity shear

Armed with our previous findings we are now in a position to introduce the effects of a basic state velocity shear into our analysis. As derived in Chapter 4, the linear, diffusionless equations can be manipulated into a single second order differential equation for ψ as

$$\left(((\omega + kU)^2 - k^2 B^2)\psi'\right)' - l^2 \left((\omega + kU)^2 - F\right)\psi = 0, \qquad (5.52)$$

where $F(z) = k^2 B^2 + \beta + BB'/\gamma$ is unchanged from its definition in §5.2 and thus independent of U. As with the governing equation in §5.2.4, equation (5.52) can be solved as a boundary value problem subject to impermeable boundary conditions, $\psi(0) = \psi(1) = 0$. Following the work of §5.2 it is possible to derive a depth-dependent eigenvalue in the $l \to \infty$ limit,

$$\omega(z) = -\sqrt{F(z)} - kU(z). \qquad (5.53)$$

We know that in the absence of shear the most unstable mode localises around a point in the layer where the growth rate given by $-\Im\left(\omega(z)\right)$ is maximised, or in other words the point in the layer where $F(z)$ is minimised. At first glance it seems the only contributing factor to the growth rate in equation (5.53) is the function $F(z)$, with the requirement for instability that $F(z) < 0$ somewhere in the layer. This raises the question as to how the shear plays a role in the instability. We might again expect the mode to be localised at the point where $F(z)$ takes its lowest value, and the shear to only contribute to the frequency of the mode.

To examine this further we consider a simple linear shear

$$U(z) = \lambda z, \qquad (5.54)$$

and solve (5.52) as a boundary value problem. Figure 5.7 plots the eigenfunction ψ for the most unstable mode with $\lambda = 5$, $l = 500$ and parameter values P_1 (5.51a). The eigenfunction is now made up of real and imaginary parts and exhibits strong oscillations contained within a peaked envelope. This envelope can be visualised by plotting $|\psi|$, shown by the black dashed lines in Figure 5.7. Interestingly, the localisation has moved
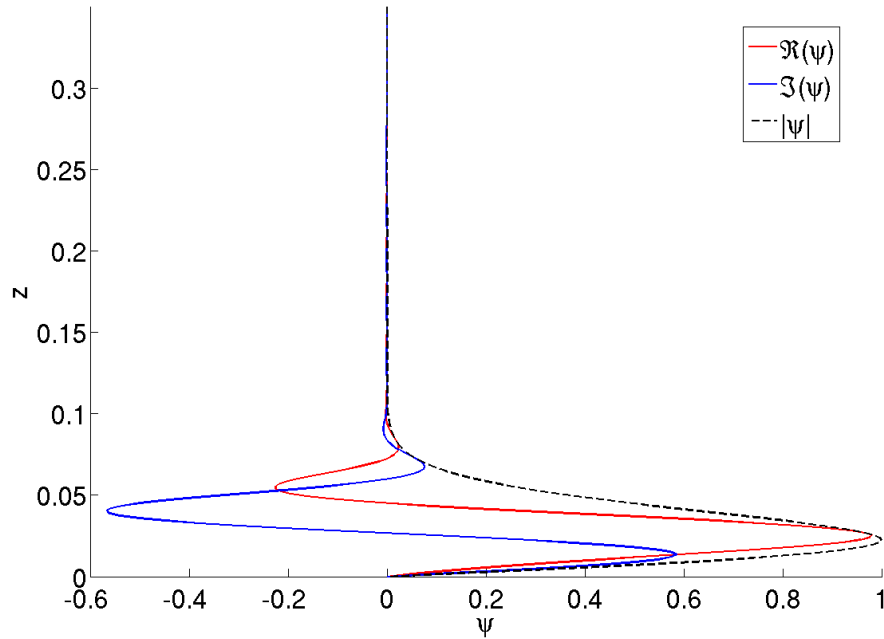
Figure 5.7: Eigenfunction ψ for the boundary value problem (5.52) in the presence of a linear shear (5.54), with parameter values P_1 and $l = 500$.

from $z \approx 0.28$ in the layer, as in Figure 5.5a when no shear was present, to a new position $z \approx 0.02$ near the boundary. From Figure 5.5b we note that the growth rate in the absence of shear for this value of l is approximately $-\Im(\omega) = 1.166$. The eigenvalue for the mode with the linear shear at $\lambda = 5$, is $\omega = -0.08 - 1.09i$, and thus the growth rate has not drastically changed. This slight stabilisation may be a result of higher order terms affecting the growth rate due to the low value of l chosen. Although for this particular shear profile the growth rate remains relatively unchanged, it is clear that the shear has had a huge influence on the structure of the mode. In particular, the idea of the mode being localised at the point in the layer where $F(z)$ is minimised is no longer valid.

5.3.1 Asymptotic analysis – velocity shear

To get to grips with what is happening when shear is introduced we again perform a boundary layer analysis on the governing equation. To do this we define a boundary layer

variable similar to (5.9), namely

$$\xi_i = \frac{z - z_u}{\delta_i}.$$ (5.55)

Here, in order to stress the difference between the two main sections in this chapter we have switched notation from z_c to z_u. In the absence of shear the most unstable mode is located at the point z_c where $F(z)$ takes its most negative value. As we have seen in Figure 5.7, when shear is introduced the point of localisation is no longer z_c and instead is some new location, which we shall denote by z_u, which seems to have some dependency on the shear.

Let us first consider the boundary layer variable associated with $i = 0$. By expanding all functions of z about z_u and the eigenvalue as $\omega = \omega_0 + o(1)$, to leading order the governing ODE (5.52) with $\delta_0 = l^{-1}$ becomes analogous to equation (5.10),

$$\left((\omega_0 + kU)^2 - k^2 B^2\right) \frac{d^2\psi}{d\xi_0^2} - \left((\omega_0 + kU)^2 - F\right)\psi = 0.$$ (5.56)

In equation (5.56) all functions of z are evaluated at $z = z_u$ and the only continuous, non-trivial solution is for a constant ψ with

$$\omega_0 = -\sqrt{F(z_u)} - kU(z_u).$$ (5.57)

Without formally defining z_u at this stage we proceed by following §5.2.1 and split the analysis into two cases, depending whether z_u is located on the boundary or z_u located in the layer.

5.3.2 z_u on the boundary

We start with the simpler case of the two and define z_u to be situated on the boundary, such that $z_u = 0$ or $z_u = 1$. With §5.2.3 as our guide we introduce a further boundary layer

$$\xi_1 = \frac{z - z_u}{\delta_1},$$ (5.58)

and include the next order correction in the eigenvalue, $\omega = \omega_0 + \delta_1\omega_1 + o\left(\delta_1\right)$. With $\delta_1 = l^{-2/3}$ the leading order equation is the shear analogue to (5.29),

$$\left((\omega_0 + kU)^2 - k^2B^2\right)\frac{\mathrm{d}^2\psi}{\mathrm{d}\xi_1^2} - \left[2\omega_1(\omega_0 + kU) - \xi_1\left(F' - 2kU'(\omega_0 + kU)\right)\right]\psi = 0.$$

(5.59)

As always $'$ denotes the derivative with respect to z and all functions of z and the derivatives are evaluated at $z = z_u$. Equation (5.59) can be written in a more compact form as

$$\frac{\mathrm{d}^2\psi}{\mathrm{d}\xi_1^2} - \left[\frac{2\omega_1(\omega_0 + kU)}{(\omega_0 + kU)^2 - k^2B^2} - \xi_1\Sigma\right]\psi = 0,$$

(5.60)

where

$$\Sigma = \frac{F' - 2kU'(\omega_0 + kU)}{(\omega_0 + kU)^2 - k^2B^2}.$$

(5.61)

For instability we require ω_0 to be a complex number; by considering shear we have introduced an ω_0 term into the expression for Σ; consequently Σ is now also complex. Introducing the new variable s denoted by

$$s = \left(\frac{2\omega_1(\omega_0 + kU)}{(\omega_0 + kU)^2 - k^2B^2} - \xi_1\Sigma\right)\Sigma^{-2/3},$$

(5.62)

transforms (5.60) into Airy's equation

$$\frac{\mathrm{d}^2\psi}{\mathrm{d}s^2} - s\psi = 0.$$

(5.63)

As discussed in §5.2.3, the crux of this problem comes down to how we define the root of $\Sigma^{2/3}$ in the s variable. We showed that to satisfy one of the boundary conditions we are required to pick the root such that $|\arg(s)| < \pi/3$ as $\xi_1 \to \infty$. This still holds true for the current case in which Σ is complex. With this we can express the solution to equation (5.63) as

$$\psi = C_1\mathrm{Ai}(s) = C_1\mathrm{Ai}\left[\left(\frac{2\omega_1(\omega_0 + kU)}{(\omega_0 + kU)^2 - k^2B^2} - \xi_1\Sigma\right)\Sigma^{-2/3}\right].$$

(5.64)

Similarly, we satisfy the second boundary condition, $\psi = 0$ at $z = z_c$, by defining ω_1 in terms of a zero of the Airy function Ai , such that

$$\omega_1 = \frac{\chi\left((\omega_0 + kU)^2 - k^2B^2\right)\Sigma^{2/3}}{2(\omega_0 + kU)}.$$

(5.65)
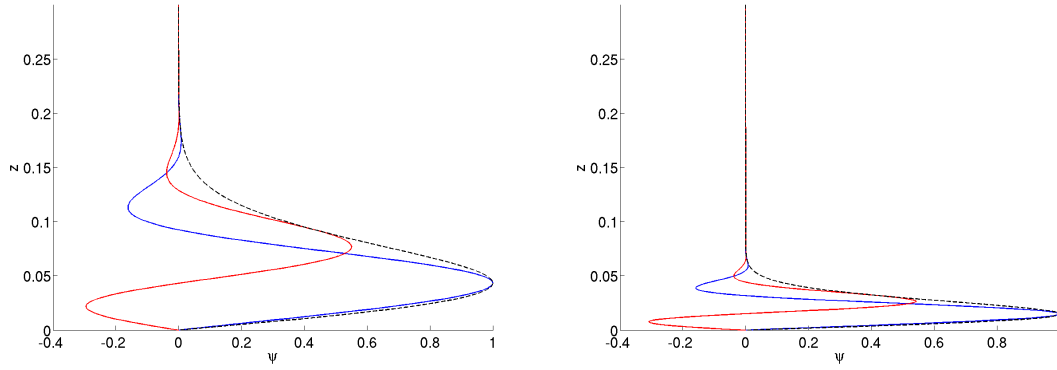
Figure 5.8: Eigenfunction solutions to (5.67) with $z_u = 0$ and $\Sigma = -1 + 5i$ and $l = 100$ (left), $l = 500$ (right). Since all variations in the eigenfunctions occur close to the bottom of the layer, we show only the region $0 < z < 0.3$.

With this, the eigenvalue of the system becomes

$$\omega = \omega_0 \left(1 + l^{-2/3} \frac{\chi \left((\omega_0 + kU)^2 - k^2 B^2 \right) \Sigma^{2/3}}{2\,\omega_0(\omega_0 + kU)} \right) + o\left(l^{-2/3} \right), \tag{5.66}$$

with corresponding eigenfunction

$$\psi(z) = C_1 \mathrm{Ai}\left[\chi - l^{2/3}(z - z_u)\Sigma^{1/3} \right]. \tag{5.67}$$

This is in exactly the same form as the case without shear (5.39), the major difference being that $\Sigma^{1/3}$ is now complex, whereas before it was just a positive real number. To examine how this alteration impacts the eigenfunction, Figure 5.8 shows ψ obtained (5.67) for $z_u = 0$ and $\Sigma = -1 + 5i$. Here we have considered two different wavenumber values $l = 100$ and $l = 500$. We see that both the eigenfunctions are made up of oscillations contained within a peaked envelope. As l is increased the envelope compresses and the localisation of the peak moves towards $z = z_u = 0$.

5.3.3 z_u in the layer

We now turn our attention to the case in which z_u is defined at some point in the layer, $0 < z_u < 1$. Although approached in a slightly different manner, this section has similarities to Griffiths (2008). To match our constant solution to the main flow we again

introduce the boundary layer variable ξ_1 defined in (5.58). Performing the same analysis as in §5.3.2 we arrive at equation (5.59),

$$\left((\omega_0 + kU)^2 - k^2 B^2\right)\frac{\mathrm{d}^2\psi}{\mathrm{d}\xi_1^2} - \left[2\omega_1(\omega_0 + kU)^2 - \xi_1\left(F' - 2k(\omega_0 + kU)\right)U'\right]\psi = 0,$$

(5.68)

which we have shown can be manipulated into Airy's equation. However, since z_u is now located in the layer, the two boundary conditions become $\psi \to 0$ as $\xi_1 \to \pm\infty$. This causes an issue as both Airy functions $\mathrm{Ai}(\xi_1)$ and $\mathrm{Bi}(\xi_1)$ oscillate as $\xi_1 \to -\infty$; therefore we are only able to satisfy one of the boundary conditions. From our previous findings it would be more desirable to cast the governing equation in the form of a parabolic cylinder equation. In §5.2.2 this result came out in the wash, as the coefficient multiplying ξ_1 in equation (5.13) equalled zero, thus forcing us to take $\omega_1 = 0$ and introduce a second boundary layer into the analysis. Now suppose we try and construct the same conditions here by taking

$$F'(z_u) - 2k\left(\omega_0 + kU(z_u)\right)U'(z_u) = 0.$$

(5.69)

With this, equation (5.68) reduces to a form similar to (5.15), where a continuous solution requires $\omega_1 = 0$. We therefore now have to introduce a further boundary layer variable

$$\xi_2 = \frac{z - z_u}{\delta_2}.$$

(5.70)

By expanding the eigenvalue as $\omega = \omega_0 + \delta_2^2 \omega_2 + o(\delta_2^2)$, with $\delta_2 = l^{-1/2}$ and equation (5.69) satisfied, the leading order equation can be written in a similar form to equation (5.18), as

$$\frac{\mathrm{d}^2\psi}{\mathrm{d}\xi_2^2} - \left[\frac{2\omega_2(\omega_0 + kU)}{(\omega_0 + kU)^2 - k^2 B^2} - \frac{\xi_2^2}{2}\Upsilon\right]\psi = 0,$$

(5.71)

where

$$\Upsilon = \left.\frac{F'' - 2k(\omega_0 + kU)U'' - 2k^2 U'^2}{(\omega_0 + kU)^2 - k^2 B^2}\right|_{z=z_u}.$$

(5.72)

Introducing similar variables to (5.20), namely

$$X = (-2\Upsilon)^{1/4}\xi_2 \quad \text{and} \quad a = \frac{\omega_2(\omega_0 + kU)}{(\omega_0 + kU)^2 - k^2 B^2}\sqrt{-\frac{2}{\Upsilon}},$$

(5.73)

equation (5.71) reduces to the standard form of a parabolic cylinder equation

$$\frac{d^2\psi}{dX^2} - \left[\frac{1}{4}X^2 + a\right]\psi = 0. \tag{5.74}$$

Therefore, by enforcing (5.69) and $\omega_1 = 0$, we are able to reduce the governing equation into a form that has solutions capable of satisfying both boundary conditions. Together with (5.57), equation (5.69) provides two simultaneous equations for two unknowns, ω_0 and z_u. Thus by solving (5.57) and (5.69) simultaneously we not only reduce the governing equation to the form of a parabolic cylinder equation, but also obtain the leading order growth rate ω_0 and the height in the layer z_u at which the enveloped solution to ψ is peaked. When solving the simultaneous equations, the resulting value of z_u is in fact a complex number, thus formally we define the point in the layer at which $|\psi|$ is peaked to be $z = \Re(z_u)$.

A similar problem to what we have witnessed is addressed by Yano (1992) and Jones et al. (2000) when finding the critical Rayleigh number for the onset of thermal convection in a rapidly rotating system. Yano (1992) stated that since the zeros of the Airy function are distributed only along the real negative axis, an equation of the form (5.68) can not be bounded as $\xi_1 \to -\infty$. When solving a similar problem to Yano (1992), Jones et al. (2000) transformed their Airy equation to an equation with solutions that decayed as $\xi_1 \to \pm\infty$, by first finding a complex point (z_u in our case) where

$$\frac{d\omega_0}{dz} = 0. \tag{5.75}$$

Upon satisfying (5.75), and one other condition not relevant here, Jones et al. (2000) included higher order corrections into their analysis and arrived at an equation analogous to (5.71). Although derived in different fashion, this is essentially what we have done above; by taking the z derivative of (5.57) and equating it to zero, we receive

$$\frac{d\omega_0}{dz} = -\frac{1}{2}F^{-1/2}F' + kU' = 0. \tag{5.76}$$

If we multiply this equation by $\sqrt{F}$ and use (5.57) to write $-\sqrt{F} = \omega_0 + kU$, we arrive at equation (5.69). With equation (5.69) satisfied for some z_u, we look for next order corrections to our governing equation and arrive at an equation with decaying solutions as ψ approaches the boundaries (5.71).

It is possible that there are several roots found when solving the simultaneous equations (5.57) and (5.69), and hence several different eigenmode solutions, all with different growth rates localised at different heights in the layer. Alternatively, there could be cases in which there are no valid solutions to the equations and therefore no solutions peaked in the layer. These traits are discussed further in §5.3.5. Since we now know that solutions peaked in the layer require complex z_u, it becomes clear from (5.57) how the shear can affect the leading order growth rate and not just the frequency as originally we might have thought when taking the $l \to \infty$ limit.

In §5.2.2 we derived a general solution to the parabolic cylinder function (5.74) that satisfies the appropriate boundary conditions. Thus, provided $|\arg(X)| < \pi/4$, the most unstable mode when $\Re(z_u)$ is located in the layer has $a = -1/2$ and thus eigenvalue

$$\omega = \omega_0 \left(1 - l^{-1} \frac{(\omega_0 + kU)^2 - k^2 B^2}{2\omega_0(\omega_0 + kU)} \sqrt{-\frac{\Upsilon}{2}} \right) + o\left(l^{-1} \right). \tag{5.77}$$

The eigenfunction takes the same form as in the case without shear, namely

$$\psi = C_1 e^{-l\left(\frac{-\Upsilon}{8}\right)^{1/2}(z-z_u)^2}. \tag{5.78}$$

However we stress that Υ and z_u are now both complex numbers. Figure 5.9 demonstrates these differences in the eigenfunction solution for two different wavenumber $l = 100$ and $l = 500$. As with the case when z_u is defined on the boundary, as l increases the oscillatory envelope compresses, with the peak localised at $z = \Re(z_u) = 0.5$.
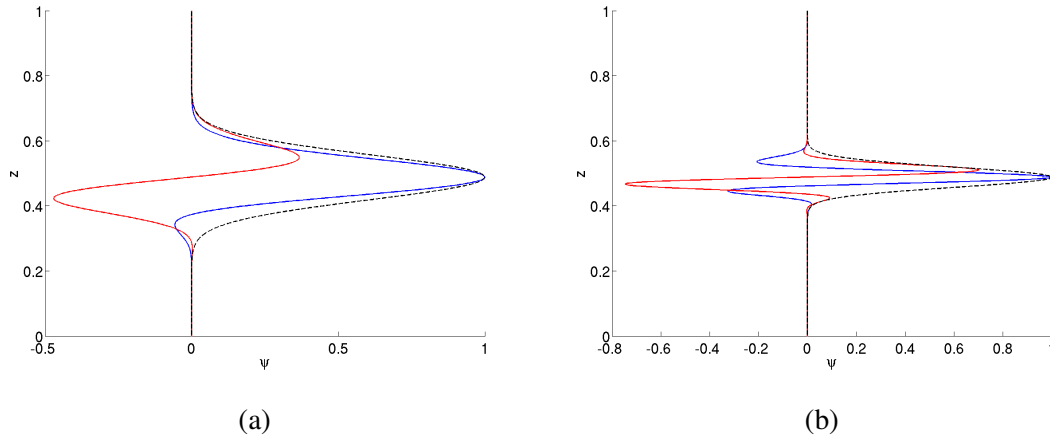
Figure 5.9: Eigenfunction solutions to (5.78) with $z_u = 0.5 + 0.05i$, $\Upsilon = -1 - 0.5i$ and $l = 100$ (left), $l = 500$ (right).

5.3.4 $U'(z_u) = 0$ and $F'(z_u) = 0$ on the boundary

This section covers the unique case when the solution to the simultaneous equations (5.57) and (5.69) results in either $z_u = 0$ or $z_u = 1$. Such a case would only occur when $F(z)$ has a quadratic minimum on the boundary and $U'(z) = 0$ on the same boundary. This is directly analogous to the case when just $F(z)$ is minimised on the boundary in the absence of shear, as considered at the end of §5.2.3. When both the simultaneous equations are satisfied we can follow the work in §5.3.3 and introduce a second boundary layer (5.70) with $\omega_1 = 0$. By expanding the eigenvalue as $\omega = \omega_0 + \delta_2^2 \omega_2 + o(\delta_2^2)$, with $\delta_2 = l^{-1/2}$, we recover equation (5.71),

$$\frac{\mathrm{d}^2 \psi}{\mathrm{d}\xi_2^2} - \left[\frac{2\omega_2(\omega_0 + kU)}{(\omega_0 + kU)^2 - k^2 B^2} - \frac{\xi_2^2}{2}\Upsilon \right]\psi = 0, \qquad (5.79)$$

where

$$\Upsilon = \left. \frac{F'' - 2k(\omega_0 + kU)U'' - 2k^2 U'^2}{(\omega_0 + kU)^2 - k^2 B^2} \right|_{z=z_c}. \qquad (5.80)$$

We have seen that applying the transformations (5.73) an equation of this form can be reduced to the standard form of a parabolic cylinder equation, with general solution

$$\psi = C_1 D_\nu(X) + C_2 D_{-\nu-1}(-iX). \qquad (5.81)$$

In §5.2.3 we saw that after satisfying the boundary conditions the most unstable mode solution has $C_2 = 0$ and $\nu = 1$. Thus the most unstable eigenvalue for this case becomes

$$\omega = \omega_0 \left(1 - l^{-1} \frac{3(\omega_0 + kU)^2 - k^2 B^2}{2\omega_0(\omega_0 + kU)} \sqrt{-\frac{\Upsilon}{2}} \right) + o\left(l^{-1}\right), \tag{5.82}$$

with corresponding eigenfunction

$$\psi = C_1 l(-2\Upsilon)^{1/4}(z - z_u)e^{-l\left(\frac{-\Upsilon}{8}\right)^{1/2}(z - z_u)^2}. \tag{5.83}$$

When plotted, the eigenfunction looks similar to that of an Airy function solution when z_u is on the boundary, as seen in Figure 5.8. However, equation (5.83) shows the solution is slightly different from an Airy function.

5.3.5 The localisation of the eigenfunction

In the absence of shear (see §5.2) it was fairly straightforward to predict where the eigenfunction would be peaked and hence which branch of the asymptotics would be required in order to approximate the full solution. When the function $F(z)$ is minimised in the layer at $z = z_{\max}$, one would take $z_c = z_{\max}$ and proceed with the approximations given in §5.2.2. Similarly, if $F(z)$ had no minimum or it was minimised outside the layer, z_c would be defined on either boundary, depending on whether $F(z)$ was an increasing or decreasing function; one would then use the work in §5.2.3. The introduction of shear has complicated this simple idea. With the exception of the special case described in §5.3.4, it is no longer obvious just from inspection of the structure of $F(z)$, or indeed any combination of basic state values, as to whether $\Re(z_u)$ is located in the layer or on the boundary. Instead we have to consider both cases individually and come to a conclusion based on which branch of the asymptotics leads to the most unstable mode, or, in other words, the case which corresponds to the highest growth rate $-\Im(\omega)$.

We do this first by solving (5.57) and (5.69) simultaneously to obtain the possible values of ω_0 and z_u, with the restriction that $\Re(z_u)$ is located in the layer. As mentioned in §5.3.3, for certain configurations it is possible to have several acceptable ω_0 and z_u that satisfy the simultaneous equations. Since we are only interested in the most unstable

mode, we only consider the $z_u = z_*$ solution that corresponds to the eigenvalue ω with the highest growth rate. Thus the most unstable mode with $\Re(z_u)$ located in the layer has a leading order eigenvalue given by $\omega_0(z_*)$. We then calculate the growth rates for the two cases when z_u is located on the boundary. Only after this procedure will we know which of the z_u values corresponds to the eigenvalue with the highest growth rate. When we have this value of z_u we can then say where the eigenfunction will be localised for large wavenumbers l.

5.3.6 Boundary value problem: shear

The aim of this section is again to confirm the validity of the asymptotic results by comparing them to solutions of the boundary value problem (5.52). We keep the same set up as in §5.2.4, that is a basic state magnetic field (5.48) with temperature gradient (5.49), and consider two different shear profiles,

$$U_1 = \lambda \left(z^2 - z + 1 \right), \tag{5.84a}$$

$$U_2 = \lambda(1 - z). \tag{5.84b}$$

To ensure the asymptotics of both cases ($\Re(z_u)$ in the layer and z_u on the boundary) are tested, we assign parameter values P_1 (5.51a) to shear profile U_1, and P_2 (5.51b) to shear profile U_2. For both profiles we take the shear gradient coefficient to be $\lambda = 10$. Following §5.3.5, we expect the eigenfunction associated with shear profile U_1 to be peaked in the layer with $z_u \approx 0.4992 + 0.013i$ and corresponding $\omega_0 \approx -4.50 - 1.15i$. Similarly, for the parameter values associated with shear profile U_2, we expect the eigenfunction to be peaked at the bottom boundary with $z_u = 0$ and $\omega_0 \approx -4.90 - 1.20i$.

Figure 5.10 shows results from solving both the boundary value problem (5.52) and the corresponding asymptotics (equations (5.77) and (5.78)) for shear profile U_1. As seen in Figure 5.10a, the eigenmode ψ solved at $l = 500$ using the full boundary value problem exhibits an oscillatory structure, enclosed within a peaked envelope. To demonstrate the accuracy of the asymptotics, Figure 5.10b shows a plot of the envelope $|\psi|$ with the black dots corresponding to the asymptotic solution (5.78). Even at this relatively low value of l, the asymptotic results are a very good approximation to the full solution. We have

also included a plot of the growth rate for a range of wavenumber values, with the black dots given by the solution to the asymptotic eigenvalue (5.77). Figure 5.11 shows that similar results hold for shear profile U_2. Again, even for relatively low values of l, the asymptotics are an excellent approximation to the full solution.

(a)

(b)

(c)

Figure 5.10: Solutions to the boundary value problem (5.52) (coloured lines) and corresponding asymptotics (equations (5.77) and (5.78)) (black dots) for shear profile U_1, with $\lambda = 10$, $l = 500$ and parameter values P_1. (a) plots the eigenfunction ψ, (b) the envelope given by $|\psi|$ and (c) the growth rate versus wavenumber l.
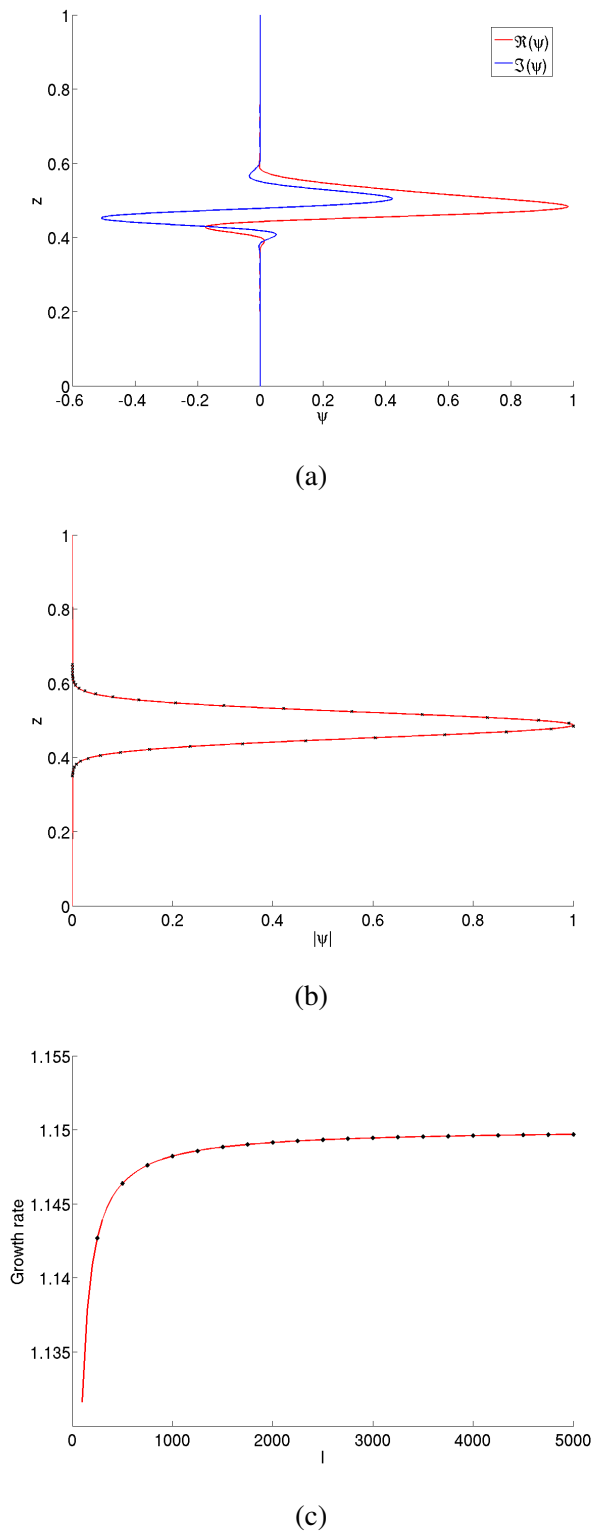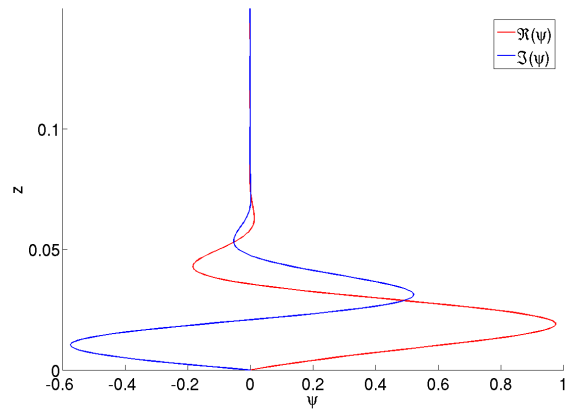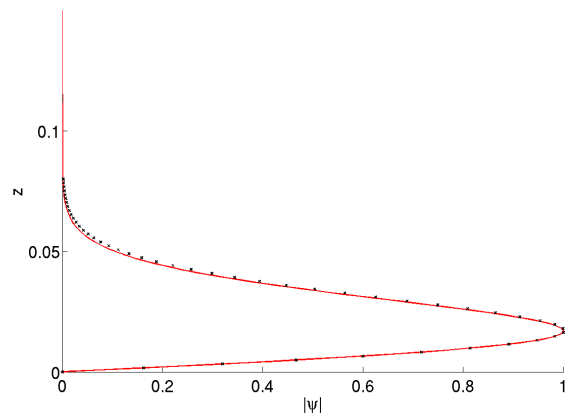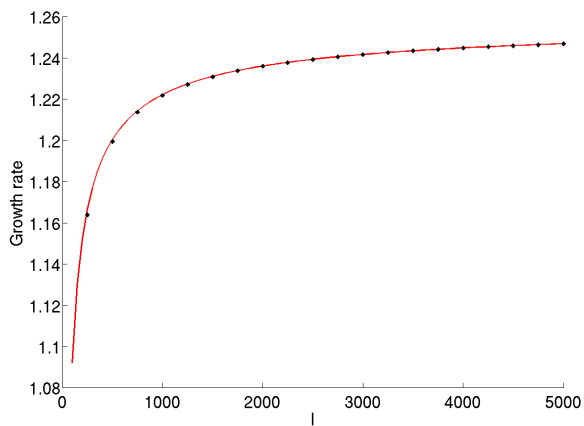
(a)

(b)

(c)

Figure 5.11: Solutions to the boundary value problem (5.52) (coloured lines) and corresponding asymptotics (equations (5.67) and (5.66)) (black dots) for shear profile U_2, with $\lambda = 10$, $l = 500$ and parameter values P_2. (a) plots the eigenfunction ψ, (b) the envelope given by $|\psi|$ and (c) the growth rate versus wavenumber l.

5.4   The influence of velocity shear

In §5.3 we extended the work of Mizerski et al. (2013) by introducing a basic state velocity shear into the analysis of short-wavelength magnetic buoyancy instability. At first glance it seemed as if the shear would have no effect on the instability and instead just alter the frequency of the mode. However, we showed that the shear can play a vital role, not only on the growth rate of the mode, but also its structure. In this section we take a more in-depth look at how altering the profile and magnitude of the shear influences the resulting instability.

As discussed in §5.3.5, with the inclusion of a velocity shear it is no longer obvious as to where in layer the eigenfunction solution will be localised. Instead we have to consider all the cases where $\Re(z_u)$ is peaked inside the layer and on the boundary, in order to determine which corresponds to the eigenvalue ω with the highest growth rate. Only then can we say where the mode will be localised. This leads to a very interesting result, namely that the most unstable mode in the absence of shear can be transformed from a wall (or body) mode into a body (wall) mode by introducing a certain shear configuration. This is demonstrated in Figure 5.12, by plotting the growth rates corresponding to the most unstable wall and body mode for increasing λ. The growth rate values are taken from equation (5.66) for the wall mode, and equation (5.77) for the body mode, both with $l = 500$. In Figure 5.12a we use parameter values P_2, where in the absence of shear the most unstable mode is a wall mode, peaked at the boundary. When considering shear profile U_1 we see that around $\lambda \approx 38$ the most unstable mode transitions from a wall mode into a body mode. The alternative result can be seen in Figure 5.12b with parameter values P_1 and shear profile U_2. Here the most unstable mode switches from a body mode to a wall mode at a much smaller value of λ, namely when $\lambda \approx 0.31$.

Due to the complexity involved in determining the value of z_u it is not possible to produce an analytic expression as to when this mode switching occurs. Fortunately, we can use the numerical solutions to gain a better understanding of this process and hence predict, for a large enough λ, where the most unstable mode will be localised. Figure 5.13 shows the height in the layer $\Re(z_u)$ corresponding to the most unstable mode for a range of λ

(a)　　　　　　　　　　　　　　　　　(b)
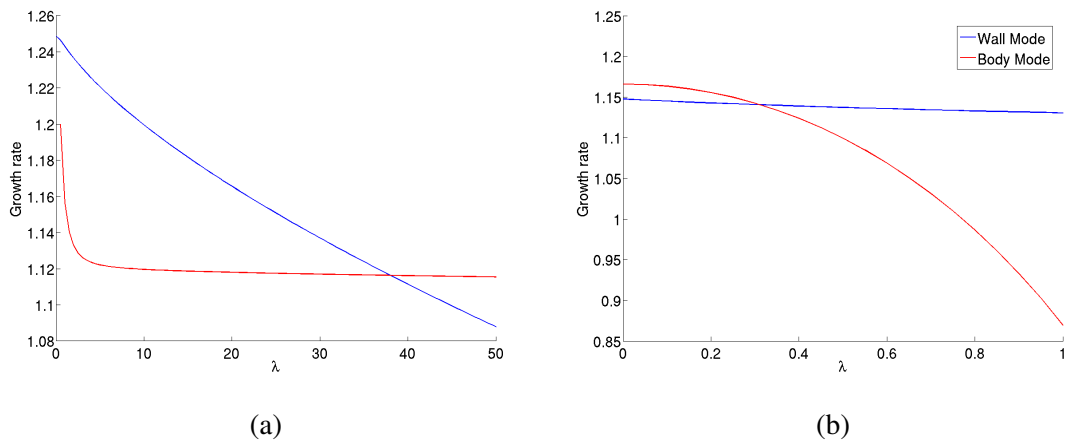
Figure 5.12: Growth rate of the wall and body modes for increasing λ, with $l = 500$. These plots have been derived using parameter values P_2 with shear profile U_1 for (a), and parameter values P_1 with shear profile U_2 for (b).

values. Each coloured branch represents a different quadratic shear profile, all maximised at different places both in and out the layer. We have taken $l = 500$ and used parameter values P_2 such that in the absence of shear the most unstable mode is localised in the layer at $\Re(z_u) \approx 0.27$. Interestingly, for $\lambda > 7$ the most unstable mode of all the branches localises around the point in the layer (or on the boundary) where $\Re(U') = 0$. Thus for 'large enough' λ the basic state shear $U(z)$ plays a similar role to the function $F(z)$ when $U = 0$, in determining where the mode is localised. As we have addressed, since z_u is very dependent on both the type of magnetic field and velocity shear profiles, we cannot predict analytically just how big λ needs to be in order to have the mode localised around the point where $\Re(U') = 0$. It is very likely that there exists a trade off between the apparent magnitude of $F(z)$ and $U(z)$ to determine where the mode will be localised. Figure 5.13 also highlights the unpredictability of where the mode will be localised as λ is increased. We notice that when the shear is peaked in the layer at $z = 0.8$, the most unstable mode with parameter values P_2 transitions from a body mode to a wall mode at $\lambda \approx 0.5$, and then back to a body mode at around $\lambda \approx 7$.

All the numerical examples in this chapter have shown that the addition of a velocity shear only has a stabilising effect on the system for a given k. In §5.2 we showed that short-
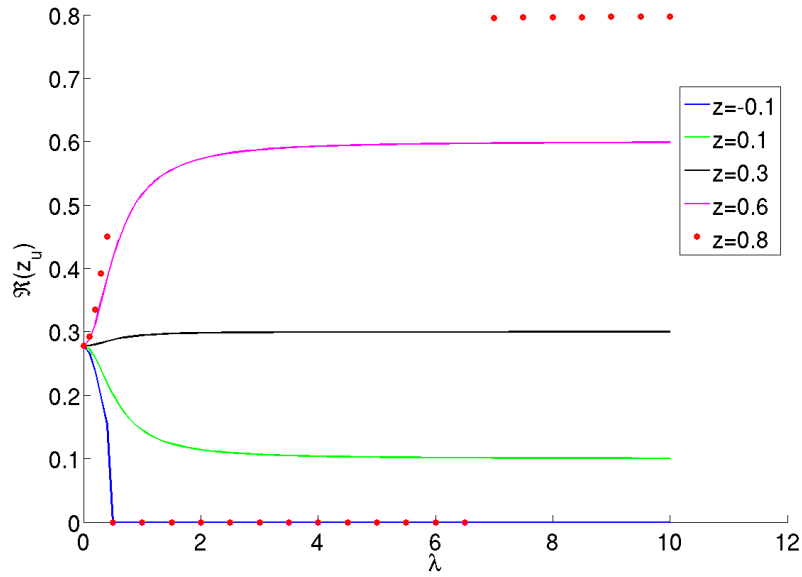
Figure 5.13: The height $\Re(z_u)$ at which the most unstable mode is localised when increasing λ for different quadratic shears of the form $U(z) = \lambda(az^2 + bz + c)$. Each coloured branch represents a different shear, maximised at the values given in the legend.

wavelength instability in the absence of shear is more readily achieved for interchange modes when $k = 0$. This is confirmed in the asymptotics through the leading order eigenvalue (5.11), which takes its highest possible growth rate value when $F(z)$ is most negative ($k = 0$). For a linear magnetic field profile, F can never be minimised in the layer when $k = 0$. Therefore the interchange mode will always be a wall mode. As a velocity shear is introduced it became obvious from our governing equation (5.52) that to study its effect on the instability the wavenumber k had to be non-zero. In this case, the leading order eigenvalue (5.57) is defined as a combination of the basic state variables evaluated at a possibly complex z_u. When considering only the wall modes, z_u is a real number and we revert to the same situation as when $U = 0$. That is, the leading order growth rate is only a function of $F(z)$ and is thus maximised when $k = 0$. Therefore, physically, the most unstable wall mode is an interchange mode, with $F(z)$ taking its most negative value on the boundary and the velocity shear having no influence. However, as we have seen, there is no guarantee that simply because the most unstable mode in the absence of shear is a wall mode, that it will remain the most unstable mode when shear is

added. It is possible that for an arbitrary shear there exists a k such that a body mode is more unstable than the $k = 0$ wall mode. This is due to the fact that when considering a body mode, z_u is complex, and thus the leading order growth rate of the system depends on both the magnetic field and the shear. Since for an arbitrary shear we do not know *a priori* the value of z_u, we cannot say analytically whether or not an interchange will always be the most unstable mode. This unfortunately is an unavoidable trait and has to be addressed case by case. Having said that we have not found a shear profile in which the body mode is more unstable than the $k = 0$ wall mode.

Chapter 6

Short-wavelength magnetic buoyancy instability : the role of diffusion

6.1 Introduction

In the previous chapter we built upon the work of Mizerski et al. (2013) by including the effects of a velocity shear on the short-wavelength magnetic buoyancy instability. In the absence of shear we saw how a given mode in the large l limit could take the form of a wall mode or a body mode, depending on the location at which the function F, defined by basic state variables, was minimised. For a linear magnetic field, F would always take its most negative value when $k = 0$, which results in the most unstable mode of the system being an interchange wall mode. The introduction of a velocity shear into the analysis complicates this simple idea; since the height of the localisation is dependent on both the function F and the velocity shear, it is no longer obvious *a priori* where a given mode will be localised. This leads to the interesting result that a wall (body) mode in the absence of shear could be transformed into a body (wall) mode for a sufficiently large shear strength. How the shear affects the growth rate of the mode is dependent on the mode considered; the leading order growth rate for the wall mode is unaffected by the shear, whereas for a body mode the shear influences the growth rate. Despite the possibility of modes switching, in all cases examined the addition of shear seems only to

have a stabilising effect on the system. Therefore, the most unstable mode of the system is still the interchange wall mode; velocity shear only alters the frequency of the mode at leading order.

The aim of this thesis is to study the influence of velocity shear on the magnetic buoyancy instability using the newly derived equations (3.61), which contain the effects of diffusion. In Chapter 7 we solve these governing equations numerically, providing results for a variety of basic state shear profiles, strengths and parameter values. This chapter is in place to bridge the gap between Chapter 5 and Chapter 7, and aims to provide us with insight into the forthcoming numerical results found in the final chapter that would otherwise be hard to understand. We do this by introducing each of the diffusive quantities, ν, κ and η individually and following the work in the previous chapter in order to derive asymptotically consistent results for the eigenvalue and eigenmodes. Within each section we split our analysis up further, depending on the relative magnitude of the diffusive term to the large wavenumber l. By doing this we can analyse the growth rate and structure of the modes for different regions of l, and therefore predict where the most unstable mode will be located. As we will see in §6.3, when considering just the effects of thermal diffusion, the system reverts back to something similar to that found in Chapter 5. In this case the most unstable mode is the interchange mode, with a large finite l and is unaffected by the shear. However, by including the effects of either just viscosity §6.2, or just magnetic diffusion §6.4, we arrive at a different result. In these cases the leading order growth rate is dependent on the shear gradient, and for certain configurations, the velocity shear can have a destabilising effect on the instability. Therefore, by including either viscosity or magnetic diffusion, the possibility arises that an undular mode becomes the preferred mode of instability.

6.2 Viscous diffusion

When considering only the effects of viscosity, the linear set of governing equations from (3.61) are;

$$\boldsymbol{\nabla} \cdot \boldsymbol{u} = 0, \tag{6.1a}$$

$$\boldsymbol{\nabla} \cdot \boldsymbol{b} = 0, \tag{6.1b}$$

$$\left(\frac{\partial}{\partial t} + U\frac{\partial}{\partial x}\right)\boldsymbol{u} + \boldsymbol{U}'w = -\boldsymbol{\nabla}_\perp \Pi + (T + Bb_x)\,\hat{\boldsymbol{z}}$$

$$+ B\frac{\partial \boldsymbol{b}}{\partial x} + \boldsymbol{B}'b_z + \frac{1}{Re}\nabla_\perp^2 \boldsymbol{u}, \tag{6.1c}$$

$$\left(\frac{\partial}{\partial t} + U\frac{\partial}{\partial x}\right)\boldsymbol{b} + \boldsymbol{B}'w = B\frac{\partial \boldsymbol{u}}{\partial x} + \boldsymbol{U}'b_z, \tag{6.1d}$$

$$\left(\frac{\partial}{\partial t} + U\frac{\partial}{\partial x}\right)(T + DBb_x) = -\beta w, \tag{6.1e}$$

where $\nabla_\perp^2 = \partial_{zz} + \partial_{yy}$. These equations can be solved subject to either no-slip $u = v = w = 0$, or stress-free $u' = v' = w = 0$ boundary conditions. As shown in appendix C, it is possible to manipulate equations (6.1) down to a single sixth order ordinary differential equation for the vertical component of velocity w,

$$\alpha_{\nu 1}w^{(6)} + \alpha_{\nu 2}w^{(4)} + \alpha_{\nu 3}w''' + \alpha_{\nu 4}w'' + \alpha_{\nu 5}w = 0, \tag{6.2}$$

where the coefficients $\alpha_{\nu i}$ are given by

$$\alpha_{\nu 1} = -\frac{\gamma(\omega + kU)}{kB^2 Re^2}, \tag{6.3a}$$

$$\alpha_{\nu 2} = \frac{\gamma}{kB^2 Re}\left((\omega + kU)a_1 + ia_2\right) - \frac{\gamma}{kRe^2}\left(\frac{\omega + kU}{B^2}\right)'', \tag{6.3b}$$

$$\alpha_{\nu 3} = -\frac{1}{Re}\left(\frac{2k^3 B^2 U'}{\omega + kU} - 2k^2 BB'\right), \tag{6.3c}$$

$$\alpha_{\nu 4} = \frac{i\gamma}{kB^2}\left[\frac{1}{Re}\left(\left(\frac{a_2}{B^2}\right)'' + a_4\right) - \frac{a_3 l^2}{Re} - a_1 a_2\right], \tag{6.3d}$$

$$\alpha_{\nu 5} = \left(\frac{2a_1 k^3 B^2 U'}{\omega + kU} - 2k^2 BB'\right) - \frac{1}{Re}\left(\frac{2k^3 B^2 U'}{\omega + kU} - 2k^2 BB'\right)''$$

$$+ \frac{i\gamma}{k}\left(\frac{l^2 a_1 a_3}{B^2} - \frac{l^2}{Re}\left(\frac{a_3}{B^2}\right)'' - \frac{a_1 a_4}{B^2} + \frac{1}{Re}\left(\frac{a_4}{B^2}\right)'' + \frac{il^2 k}{\gamma}\left(\frac{k^2 B^2 U'}{\omega + kU} - U'\right)\right), \tag{6.3e}$$

with

$$a_1 = i(\omega + kU) - \frac{ik^2 B^2}{(\omega + kU)} + \frac{l^2}{Re}, \tag{6.4a}$$

$$a_2 = (\omega + kU)^2 - k^2 B^2 - \frac{2il^2(\omega + kU)}{Re}, \tag{6.4b}$$

$$a_3 = (\omega + kU)^2 - F + \frac{kB^2U'}{\gamma(\omega + kU)} - \frac{il^2(\omega + kU)}{Re}, \tag{6.4c}$$

$$a_4 = -kU''(\omega + kU) + \frac{2k^3BB'U'}{\omega + kU} + \frac{k^3B^2U''}{\omega + kU} - \frac{2k^4B^2U'^2}{(\omega + kU)^2}. \tag{6.4d}$$

Guided by our work in the previous chapter, we expect that in the short-wavelength limit the eigenfunction will be localised around a point in the layer dictated by basic state quantities. As such, we will again tackle this problem by a boundary layer analysis and introduce a boundary layer variable similar to that seen in the previous chapter,

$$\xi_i = \frac{z - z_\nu}{\delta_i}. \tag{6.5}$$

At this stage, we would normally expand the eigenvalue ω in powers of δ_i, expand variables of z in a Taylor series around the point z_ν and then balance leading order coefficients in the governing equations in order to arrive at an expression for the leading order eigenvalue ω_0. However before we can take this approach, we have to comment on the magnitude of Re and, more importantly, its magnitude in relation to the wavenumber l. As we can see from the $\alpha_{\nu i}$ coefficients, the size of Re will play a crucial role in determining which terms will appear in the leading order equations of the boundary layer analysis.

To approach this problem, we split our analysis into three main subsections, $l^2/Re \sim 1$, $l^2/Re \sim \delta_i$ and $l^2/Re \sim \delta_i^2$. For smaller values of ν such that $l^2/Re < \delta_i^2$ we revert to the problem set out in the Chapter 5, in which viscosity plays no role. Alternatively for large ν, such that $l^2/Re \gg 1$, the instability is killed by viscosity.

In this section we shall follow the work laid out in the previous chapter in order to arrive at an asymptotic approximation for the eigenvalue and corresponding eigenvector. We shall then compare the asymptotic results to the solutions of the full boundary layer problem.

6.2.1 $l^2/Re \sim 1$

In this subsection we shall assume that the kinematic viscosity coefficient ν is sufficiently small that $l^2/Re \sim 1$. When introducing the boundary layer variable ξ_i, defined by (6.5),

expanding basic states variables of z about z_ν and expanding the eigenvalue as $\omega = \omega_0 + \delta_i \omega_1 + \delta_i^2 \omega_2 + o(\delta_i^2)$, the governing ODE (6.2) becomes

$$b_1 \frac{\mathrm{d}^6 w}{\mathrm{d}\xi_i^6} + Re\, \delta_i^2\, b_2 \frac{\mathrm{d}^4 w}{\mathrm{d}\xi_i^4} + Re^2\, \delta_i^4\, b_3 \frac{\mathrm{d}^2 w}{\mathrm{d}\xi_i^2} - Re^2\, l^2\, \delta_i^6\, b_4 w + o\,(1) = 0, \qquad (6.6)$$

where all b_i coefficients are $O(1)$ and given in appendix F to avoid unnecessary clutter. Considering a boundary layer associated with $i = 0$, we see that all terms in equation (6.6) balance when $\delta_0 = l^{-1}$. The only continuous non-trivial solution to this equation that obeys the boundary conditions is for a constant w, with $b_4 = 0$. This leads to an equation for the leading order growth rate ω_0 that is dependent on the basic state variables evaluated at z_ν. With the introduction of viscosity, the leading order growth rate equation is now a fourth order polynomial in ω_0, given as

$$\bar{\omega}_0^4 - \frac{2il^2}{Re}\bar{\omega}_0^3 - \left(F + k^2 B^2 + \frac{l^4}{Re^2} \right) \bar{\omega}_0^2$$

$$+ \frac{il^2}{Re}(F + k^2 B^2)\bar{\omega}_0 + k^2 B^2 F - \frac{ikB^2 U' l^2}{\gamma Re} = 0, \qquad (6.7)$$

where $\bar{\omega}_0 = \omega_0 + kU$. Having found the leading order growth rate, we are now in a position to introduce further boundary layers into the expansion. As in the previous chapter we shall split our analysis into two sections: the wall mode, in which z_ν is defined on either boundary, and the body mode, in which z_ν takes a possibly complex value with $0 < \Re(z_\nu) < 1$.

The wall mode

In the absence of any diffusion, an analytic expression for the wall mode was achieved by introducing a second boundary layer ξ_1 and then balancing the largest order derivative term with the next order correction to the w coefficient. Now the problem is a little more complex as there are more derivatives contributing to the leading order ODE and hence several different possible orderings for δ_1. As usual we expand our eigenvalue as $\omega = \omega_0 + \delta_1 \omega_1 + o(\delta_1)$. To ensure we take a δ_1 that has the greatest influence on the growth rate, we require a balance between terms that results in the largest possible value of δ_1. Upon introducing a second boundary layer the largest contributing terms from the

governing ODE yield the equation

$$b_1 \frac{d^6 w}{d\xi_1^6} + Re\, \delta_1^2\, b_2 \frac{d^4 w}{d\xi_1^4} + Re^2\, \delta_1^4\, b_3 \frac{d^2 w}{d\xi_1^2} - Re^2\, l^2\, \delta_1^7 \left(\omega_1 b_5 + \xi_1 b_6 \right) w = 0. \qquad (6.8)$$

As mentioned, there exist several possible balances between terms proportional to w and its derivatives, each resulting in a different value of δ_1. Balancing the sixth derivative and w terms results in $\delta_1 = l^{-6/7}$; similarly balancing the fourth derivative and w terms results in $\delta_1 = l^{-4/5}$. The largest δ_1 comes from balancing the terms in w and in its second derivative, leading to $\delta_1 = l^{-2/3}$. With this ordering for δ_1, the sixth order ordinary differential equation (6.8) reduces to the following second order equation,

$$b_3 \frac{d^2 w}{d\xi_1^2} - \left(\omega_1 b_5 + \xi_1 b_6 \right) w = 0. \qquad (6.9)$$

Interestingly, we have lost four derivatives from our governing equation and hence only require two boundary conditions, $w = 0$ at both boundaries, in order to solve the problem to this order. This is addressed further in §6.2.4 when we compare the asymptotic results to the full solution of the boundary value problem. We now have a problem that is directly analogous to that in §5.3.2 and writing equation (6.9) in the familiar form

$$\frac{d^2 w}{d\xi_1^2} - \left(\omega_1 b_7 - \xi_1 \Sigma \right) w = 0, \qquad (6.10)$$

where $b_7 = b_5/b_3$ and $\Sigma = -b_6/b_3$, allows us to use results already obtained in Chapter 5. Hence the eigenfunction solution can be expressed as an Airy function of the form

$$w(z) = C_1 \text{Ai} \left[\chi - l^{2/3}(z - z_\nu) \Sigma^{1/3} \right], \qquad (6.11)$$

with corresponding eigenvalue

$$\omega = \omega_0 \left(1 + l^{-2/3} \frac{\chi \Sigma^{2/3}}{b_7 \omega_0} \right) + o\left(l^{-2/3} \right), \qquad (6.12)$$

where $\chi \approx -2.338$. We have seen in Figure 5.8 how the Airy function of this form with a complex Σ behaves for large l.

The body mode

In the absence of diffusivity we saw how it was possible to manipulate the governing equation into the form of a parabolic cylinder equation required to produce an asymptotic

solution for the body mode. The process involved solving two simultaneous equations for the two unknowns ω_0 and z_u. Only after solving these equations could we say which of the acceptable z_u values corresponds to the eigenvalue with the largest growth rate, and therefore deduce the location in the layer at which the most unstable mode will be localised. Upon solving the two simultaneous equations we introduced a second boundary layer ξ_2 and looked for eigenvalue solutions of the form $\omega = \omega_0 + \delta_2^2 \omega_2 + o(\delta_2^2)$, with $\delta_2 = l^{-1/2}$. We shall adopt the same process in order to solve the problem with viscosity.

The first of the two simultaneous equations in this case is (6.7), the second, as we shall see, comes from the fact that an Airy mode can not satisfy both boundary conditions when the solution is localised in the layer. We know from the previous subsection that equation (6.9) leads to an Airy mode solution, which can not satisfy the impermeability boundary conditions for a mode peaked in the layer. Thus, following §5.3.3, we take $b_6 = 0$, $\omega_1 = 0$ and introduce a second boundary layer ξ_2 in order to reduce our equation to that of a parabolic cylinder. On fixing $b_6 = 0$, the second simultaneous equation to solve (along with (6.7)) is

$$4kU'\bar{\omega}_0^3 - \bar{\omega}_0^2(F' + 2kBB') - 2kU'\bar{\omega}_0(F + k^2 B^2) + k^2 B^2 F'$$
$$+ 2FBB'k^2 - \frac{il^2}{Re}\left[6kU'\bar{\omega}_0^2 - \left(F' + 2kBB' + \frac{2ikU'l^2}{Re}\right)\bar{\omega}_0\right.$$
$$\left. - kU'(F + k^2 B^2) + \frac{k}{\gamma}(2BB'U' + U''B^2)\right] = 0. \qquad (6.13)$$

Keeping only the largest possible terms, with (6.7), (6.13) and $\omega_1 = 0$ satisfied, the governing equation (6.2) becomes

$$b_1 \frac{\mathrm{d}^6 w}{\mathrm{d}\xi_2^6} + Re\,\delta_2^2\, b_2 \frac{\mathrm{d}^4 w}{\mathrm{d}\xi_2^4} + Re^2\,\delta_2^4\, b_3 \frac{\mathrm{d}^2 w}{\mathrm{d}\xi_2^2} - Re^2\, l^2\, \delta_2^8 \left(\omega_2 b_7 + \xi_2^2 b_8\right) w = 0. \qquad (6.14)$$

As was the case with the wall mode the governing equation is sixth order; therefore there exist several balances between terms, which all relate to a different ordering of δ_2. Again we seek a balance between the terms in w and its derivatives that leads to the largest value of δ_2. This is achieved by balancing the second order derivative term to that in w, resulting in the same ordering as in the previous chapter, namely $\delta_2 = l^{-1/2}$. With this scaling the governing equation at leading order becomes

$$b_3 \frac{\mathrm{d}^2 w}{\mathrm{d}\xi_2^2} - \left(\omega_2 b_7 + \xi_2^2 b_8\right) w = 0. \qquad (6.15)$$

On introducing the new variable $\Upsilon = -2b_8/b_3$, equation (6.15) can be rewritten in the more familiar form

$$\frac{\mathrm{d}^2 w}{\mathrm{d}\xi_2^2} - \left(\frac{\omega_2 b_7}{b_3} - \frac{\xi_2^2}{2}\Upsilon \right) w = 0. \tag{6.16}$$

Transforming this into a parabolic cylinder equation as in §5.3.3, we can derive asymptotic results for the body mode when $l^2 \sim Re$. The eigenvalue for this system becomes

$$\omega = \omega_0 \left(1 - l^{-1}\frac{b_3}{\omega_0 b_7}\sqrt{-\frac{\Upsilon}{2}} \right) + o\left(l^{-1} \right), \tag{6.17}$$

with w eigenmode

$$w = C_1 e^{-l\left(\frac{-\Upsilon}{8}\right)^{1/2}(z-z_\nu)^2}, \tag{6.18}$$

An example of how an eigenmode of this form behaves for large l was shown in Figure 5.9.

6.2.2 $\quad l^2/Re \sim \delta_i$

Now suppose we consider different regime in l such that $l^2/Re \sim \delta_i$. In this limit, the analogue equation to (6.6) becomes

$$\left[\bar\omega_0^2 - k^2 B^2 \right]^2 \frac{\mathrm{d}^2 w}{\mathrm{d}\xi_i^2} - \delta_i^2 l^2 \left[\left(\bar\omega_0^2 - F \right)\left(\bar\omega_0^2 - k^2 B^2 \right) \right] w + o(1) = 0. \tag{6.19}$$

This simplifies the problem greatly as we are now working with a second order equation and no longer have to worry about balancing higher order derivatives in order to obtain the desired δ_i. At leading order ($i = 0$) the two terms in (6.19) balance when $\delta_0 = l^{-1}$; the above equation can then be reduced to equation (5.56)

$$\left[\bar\omega_0^2 - k^2 B^2 \right] \frac{\mathrm{d}^2 w}{\mathrm{d}\xi_0^2} - \left[\bar\omega_0^2 - F \right] w = 0. \tag{6.20}$$

Thus the only continuous non-trivial solution exists when,

$$\omega_0 = -\sqrt{F(z_\nu)} - kU(z_\nu). \tag{6.21}$$

Notice here that the viscous terms do not enter this expression for the leading order eigenvalue. Therefore, for purely real z_ν, as is the case for the wall modes, viscosity plays no role in the leading order solution when $l^2/Re \sim \delta_i$. We cannot come to the same conclusion just yet for the body mode. Since it is possible that z_ν is dependent on the Reynolds number and therefore could influence ω_0.

The wall mode

Since the leading order terms of the full sixth order system reduce to a second order ODE when $l^2/Re \sim \delta_i$, it is fairly straightforward to proceed in a similar fashion to that previously laid out to arrive at the asymptotic results. When equation (6.21) is satisfied, we can introduce a second boundary layer ξ_1; thus, to leading order the governing equation becomes

$$c_1 \frac{\mathrm{d}^2 w}{\mathrm{d}\xi_1^2} - \delta_1^3 l^2 \left[c_2 \omega_1 - c_3 \frac{il^2}{\delta_1 Re} + \xi_1 c_4 \right] w = 0, \tag{6.22}$$

where the c_i coefficients are order unity and are given in appendix F. The terms in equation (6.22) balance provided that $\delta_1 = l^{-2/3}$; therefore we expect the asymptotics to be valid when $l^2/Re \sim l^{-2/3}$ or, equivalently, $l \sim Re^{3/8}$. With the previous work as our guide, we can proceed in a familiar fashion and introduce a new variable $\Sigma = -c_4/c_1$. With this, the asymptotic eigenvalue solution for the wall mode when $l \sim Re^{3/8}$ becomes

$$\omega = \omega_0 \left(1 + \frac{l^{-2/3}}{\omega_0} \left(\frac{\chi c_1 \Sigma^{2/3}}{c_2} + \frac{ic_3 l^{8/3}}{c_2 Re} \right) \right) + o(l^{-2/3}), \tag{6.23}$$

with corresponding w eigenvector

$$w = C_1 \mathrm{Ai} \left[\chi - l^{2/3}(z - z_\nu)\Sigma^{1/3} \right]. \tag{6.24}$$

The body mode

As with all the previous work on the body mode analysis, the aim is to try to reduce the governing equation down to the form of a parabolic cylinder equation. This is done by assuming that the $\mathrm{O}(\delta_i)$ coefficients of w are zero and the balancing the $\mathrm{O}(\delta_i^2)$ coefficients

of w with the leading order coefficients of the second derivative w''. In the current case, when $l^2/Re \sim \delta_i$, the $O(\delta_i)$ coefficients from (6.22) are

$$c_2\omega_1 - c_3\frac{il^2}{\delta_i Re} - \xi_i c_4. \tag{6.25}$$

For expression (6.25) to equal zero for all z we require that both $\omega_1 = ic_3l^2/c_2\delta_i Re$ and $c_4 = 0$. The first of these conditions is unusual in comparison to all our previous work, in which $\omega_1 = 0$. The second condition just leads to an equation that when solved simultaneously with (6.21) gives the values of ω_0 and z_ν. By using (6.21) and (F.2d), this second simultaneous equation becomes

$$F'(z_\nu) - 2kU'(z_\nu)(\omega_0 + kU(z_\nu)) = 0. \tag{6.26}$$

Equation (6.26) together with (6.21), are the same two equations seen in §5.3.3 where we were just considering a body mode under the influence of a velocity shear. Therefore in the region of l, such that $l^2/Re \sim \delta_i$, the leading order growth rate is independent of the viscosity.

Since ω_1 no longer equals zero we require an extra step in order to reduce the governing equation to the parabolic cylinder equation we require. Introducing a further boundary layer ξ_2 and expanding the eigenvalue as $\omega = \omega_0 + \delta_2\omega_1 + \delta_2^2\omega_2 + o(\delta_2^2)$, the leading order equation can we written in the form

$$c_1\frac{d^2w}{d\xi_2^2} - \delta_2^4 l^2 \left[c_5\omega_2 + c_6 + c_7\xi_2 + c_8\xi_2^2 \right] w = 0, \tag{6.27}$$

where the c_i coefficients are again provided in appendix F. When written in this form we can complete the square and introduce the new variable $\bar{\xi}_2 = \xi_2 + c_7/2c_8$. On balancing terms by taking $\delta_2 = l^{-1/2}$, the leading order equation becomes

$$\frac{d^2w}{d\bar{\xi}_2^2} - \left[\frac{c_5\omega_2 + c_9}{c_1} - \frac{\bar{\xi}_2^2}{2}\Upsilon \right] w = 0, \tag{6.28}$$

where $\Upsilon = -2c_8/c_1$ and $c_9 = c_6 - c_7^2/4c_8$. To this order we expect the asymptotics to be accurate when $l^2/Re \sim l^{-1/2}$ or equivalently when $l \sim Re^{2/5}$. Now in a familiar form we can transform equation (6.28) into a parabolic cylinder equation and proceed as usual. On

doing so, the asymptotic expression for the eigenvalue for a body mode when $Re \sim l^{5/2}$ becomes

$$\omega = \omega_0 \left(1 + \frac{ic_3 l^2}{\omega_0 c_2 Re} - \frac{l^{-1}}{\omega_0} \left(\frac{c_1}{c_5} \sqrt{-\frac{\Upsilon}{2}} + \frac{c_9}{c_5} \right) \right) + o(l^{-1}), \qquad (6.29)$$

with corresponding w eigenvector

$$w = C_1 e^{-l \left(\frac{-\Upsilon}{8} \right)^{1/2} \left(z - z_\nu + \frac{c_7}{2c_8 l^{1/2}} \right)^2}. \qquad (6.30)$$

Here we notice an extra term $c_7/2c_8 l^{1/2}$ in the exponential, that is not normally present and is introduced here as a result of $\omega_1 \neq 0$. Therefore, instead of the mode being peaked at $\Re(z_\nu)$, it is instead peaked at $\Re\left(z_\nu - c_7/2c_8 l^{1/2}\right)$, which for large l is merely a small correction. Even with this correction term, the structure of the mode still looks the same as what we observed in Figure 5.9.

6.2.3 $l^2/Re \sim \delta_i^2$

For completeness we include the asymptotic analysis for the regime when $l^2/Re \sim \delta_i^2$. After introducing a boundary layer ξ_i given by (6.5), the governing equation (6.2) reduces exactly to (6.19),

$$\left[(\omega_0 + kU)^2 - k^2 B^2 \right]^2 \frac{d^2 w}{d\xi_i^2}$$
$$- \delta_i^2 l^2 \left[\left((\omega_0 + kU)^2 - F \right) \left((\omega_0 + kU)^2 - k^2 B^2 \right) \right] w + o(1) = 0. \qquad (6.31)$$

Following §6.2.2, the leading order growth rate is therefore

$$\omega_0 = -\sqrt{F(z_\nu)} - kU(z_\nu). \qquad (6.32)$$

We proceed in the usual fashion, by first considering the wall modes. When $l^2/Re \sim \delta_i^2$, the analogue to equation (6.22) becomes

$$c_1 \frac{d^2 w}{d\xi_1^2} - \delta_1^3 l^2 \left[c_2 \omega_1 + \xi_1 c_4 \right] w = 0, \qquad (6.33)$$

where again all coefficients are given in appendix F. Although not obvious when written in this form, this equation is exactly the same as (5.59) as that found in §5.3.2. Consequently, the analysis for the wall mode follows the work in §5.3.2 and to O $\left(l^{-2/3}\right)$, viscosity never enters the problem.

The viscosity does however play a role in the next order correction to the growth rate for the body mode. To manipulate equation (6.33) into the form of a parabolic cylinder equation, we set both $\omega_1 = 0$ and $c_4 = 0$. This gives a second equation involving ω_0 and z_ν that can be solved simultaneously with (6.32),

$$F'(z_\nu) - 2kU'(z_\nu)(\omega_0 + kU(z_\nu)) = 0. \tag{6.34}$$

Equations (6.32) and (6.34) are precisely equations (6.21) and (6.26), in which viscosity plays no role in determining the leading order growth rate. This is not a surprising result; if viscosity does not influence ω_0 and z_ν when $l^2/Re \sim \delta_i$, we would not expect it to when $l^2/Re \sim \delta_i^2$. Introducing a second boundary layer ξ_2 and expanding the eigenvalue as $\omega = \omega_0 + \delta_2^2 \omega_2 + o(\delta_2^2)$, the leading order equation can we written as

$$c_1 \frac{\mathrm{d}^2 w}{\mathrm{d}\xi_2^2} - \delta_2^4 l^2 \left[c_5\omega_2 - c_3 \frac{il^2}{\delta_2^2 Re} + c_8\xi_2^2 \right] w = 0. \tag{6.35}$$

Balancing terms in this equation requires $\delta_2 = l^{-1/2}$. Therefore we expect our analysis in this subsection to be accurate when $l^2/Re \sim l^{-1}$, or $l \sim Re^{1/3}$. With this ordering in place, we transform equation (6.35) into the form of a parabolic cylinder equation by introducing the familiar variable $\Upsilon = -2c_8/c_1$. Following the procedure laid out in §5.3.3 we can express the eigenvalue as

$$\omega = \omega_0 \left(1 - \frac{l^{-1}}{\omega_0} \left(\frac{c_1}{c_5} \sqrt{-\frac{\Upsilon}{2}} - \frac{c_3 i l^3}{c_5 Re} \right) \right) + o(l^{-1}), \tag{6.36}$$

with corresponding w eigenvector

$$w = C_1 e^{-l\left(\frac{-\Upsilon}{8}\right)^{1/2}(z-z_\nu)^2}. \tag{6.37}$$

For $l^2/Re < \mathrm{O}\left(\delta_i^2\right)$, the analysis of both the wall and body mode reverts to that in Chapter 5, where up to the order of δ_i considered, viscosity has no influence on the instability.

6.2.4   Boundary value problem

This subsection aims to confirm the validity of the asymptotic analysis by comparing the derived results to numerical solutions of the full boundary value problem. To solve the full boundary value problem numerically we use both the inverse iteration method (appendix B) on the full set of governing equations (6.1) and the inbuilt MATLAB boundary value problem solver BVP4C. To solve the problem with MATLAB's boundary value problem solver, we express the 6th order system as

$$\bar{A}_1 u'' + \bar{A}_2 w + \bar{A}_3 u = 0, \tag{6.38a}$$

$$\bar{A}_4 w'''' + \bar{A}_5 w'' + \bar{A}_6 w' + \bar{A}_7 w + \bar{A}_8 u = 0, \tag{6.38b}$$

with boundary conditions at $z = 0$ and $z = 1$ corresponding to $w = 0, w'' = 0, u' = 0$ for stress-free, and $w = 0, w' = 0, u = 0$ for no-slip. These are the same as equations (C.19) found in appendix C and are used instead of (6.2), as it is easier to implement the boundary conditions.

One issue that arises from the asymptotic analysis is that when considering a δ_i that has the largest influence on the growth rate, the 6th order ordinary differential equation (6.2) is reduced to a 2nd order ODE. Consequently, to arrive at our final solution we only have to impose two boundary conditions, specifically the impermeability condition on w at both boundaries. Thus our asymptotic solutions do not depend on, or necessarily satisfy, the other two boundary conditions on u and v. Using our asymptotically derived expression for the eigenvector w, we can solve (6.38a) as a boundary value problem with two boundary conditions on u and arrive at an approximated value for u. However, through our analysis we can not satisfy the two remain boundary conditions, as we do not have a similar differential equation for v. Instead, once we have found w and u, we have to use the incompressibility condition to get an approximation for v, such that

$$v = \frac{-k}{l}u + \frac{i}{l}w'. \tag{6.39}$$

As we have not used the two remaining boundary conditions on v, we do not expect this approximation for v to necessarily satisfy the boundary conditions. This will not be a problem for the body mode, since the bulk of the eigenvectors is in the layer and both w

and u decay exponentially to zero as they approach the boundary. However, for a wall mode, where the bulk is located near the boundary, this is not the case; the boundary conditions must play a role in determining the structure of the mode. The knock-on effect of not fully satisfying the boundary conditions is examined further in the following subsection.

The wall mode

We will first compare the asymptotic results for the wall mode to those found from solving the full boundary value problem. Here we fix the Reynolds number at $Re = 10^4$, and take a linear velocity shear profile $U = 10(1 - z)$. For this value of Re we expect the asymptotics in §6.2.1 to be valid for $l \approx 100$ and the asymptotics in §6.2.2 to be valid for $l \approx 30$. Defining the magnetic field B and temperature gradient β as in Chapter 5,

$$B = 1 + \zeta(1 - z), \tag{6.40a}$$

$$\beta = \hat{\beta} + \alpha - \frac{\zeta(\gamma - 1)}{\gamma}(1 + \zeta(1 - z)), \tag{6.40b}$$

we introduce two new sets of parameter values

$$P_{\nu 1} : \quad \alpha = 0.5, \ \hat{\beta} = 0.1, \ \zeta = 1.5, \ k = 0, \tag{6.41a}$$

$$P_{\nu 2} : \quad \alpha = 0.5, \ \hat{\beta} = 0.1, \ \zeta = 1.5, \ k = 0.3. \tag{6.41b}$$

Figure 6.1 shows plots of the growth rate for a range of wavenumber l values. These figures include the full solution for both the stress-free and no-slip boundary conditions, as well as the asymptotic results (6.12), obtained when $l^2/Re \sim 1$, and (6.23) obtained when $l^2/Re \sim \delta_i$. The first thing to note from these results is the similarity between the stress-free and no-slip solutions, which suggests that the resulting growth rate is somewhat independent of the choice of boundary conditions used. This ties in well with our asymptotic results, in that, to the order of δ considered, the boundary conditions on u and v have no influence on the growth rate. Even for the relatively low values of l, the asymptotics provide a good approximation to the growth rate. As expected, (6.12) provides an accurate representation of the growth rate for $l \approx 30$, and becomes less precise as the ratio l^2/Re increases. A somewhat unexpected result is just how well

equation (6.12) estimates the growth rate for the entire range of l. This can be explained by considering the equation for the leading order growth rate (6.7) obtained when $l^2/Re \sim 1$. If we take $l^2/Re = o(1)$ this equation becomes

$$\left(\bar{\omega}_0^2 - k^2 B^2\right)\left(\bar{\omega}_0^2 - F\right) = 0. \tag{6.42}$$

Since we are looking for unstable modes ($\bar{\omega}_0^2 < 0$), we can assume that $\bar{\omega}_0^2 \neq k^2 B^2$ and thus equation (6.42) is satisfied when $\bar{\omega}_0^2 = F$. This is exactly the same as the equation for the leading order growth rate (6.21) obtained when $l^2/Re \sim \delta_i$. Therefore when $l^2/Re = o(1)$, the leading order growth rate predicted by (6.7) is the same as that in §6.2.2.

To examine the effect of the boundary conditions on the eigenfunctions we solved the full boundary value problem (6.38) using the inverse iteration method. Figure 6.2 shows the eigenfunction solutions of $|u|$, $|v|$ and $|w|$ for both the stress-free and no-slip boundary conditions, taken with parameter values $P_{\nu 1}$ at $l = 33$. This value of l was selected as it corresponds to the mode of maximum growth rate for parameter values $P_{\nu 1}$. The absolute difference between the two solutions for each eigenfunction is given in Figure 6.3. Throughout this thesis all eigenfunctions are normalised such that the maximum value of the real part of w is one. In these figures we notice that for both boundary conditions, the bulk of the mode is very similar. The eigenfunction profiles are almost identical, apart from a thin region close to the bottom boundary, where for the u and v eigenfunctions, the solutions do differ. This thin layer is just a consequence of the system satisfying the required boundary conditions. This is an important result and suggests that independent of the boundary conditions chosen, the bulk of the flow remains relatively similar.

As discussed, our asymptotic result for the eigenfunction w is derived using only two of the necessary six boundary conditions. Using the analytic approximation for w, we can solve (6.38a) as a boundary value problem to obtain u, and thus incorporate two extra boundary conditions into the solution. However, we have not found a way to successfully incorporate the final two boundary conditions required to fully determine v, and instead have to approximate v using the incompressibility condition (6.39). Figure 6.4 shows the approximated eigenfunctions derived in this fashion (black dashed lines), together with the eigenfunctions obtained from solving the full problem for the stress-free boundary

conditions (red lines). Again we have taken parameter values $P_{\nu 1}$ at $l = 33$, and have used (6.11) for our approximation to w. Even for this relatively low value of l, the asymptotics provide a very good estimate for all the eigenfunctions. Despite not actually enforcing the boundary conditions on v, the approximated method has done a very good job of satisfying them. Figure 6.5 shows similar plots, this time obtained using no-slip boundary conditions. As before, the approximated method provides a good estimate for the u and w eigenfunctions. However, this time we see the knock-on effect of not explicitly satisfying the v boundary conditions. Since $k = 0$ in our set-up, from (6.39), we have v proportional to w'. As we are approximating w with an Airy function of the form (6.11), we can never have $w' = 0$ at the bottom boundary. Therefore we can not fully satisfy the v no-slip boundary conditions using this approximated method. In future work it would be nice to investigate this further, in an attempt to fully incorporate the two remaining boundary conditions into our asymptotic analysis. Despite that, the impact of changing the boundary conditions seems to have minimal influence on the eigenvalue and bulk structure of the mode, and ultimately these asymptotic solutions do provide a good approximation to the full problem.
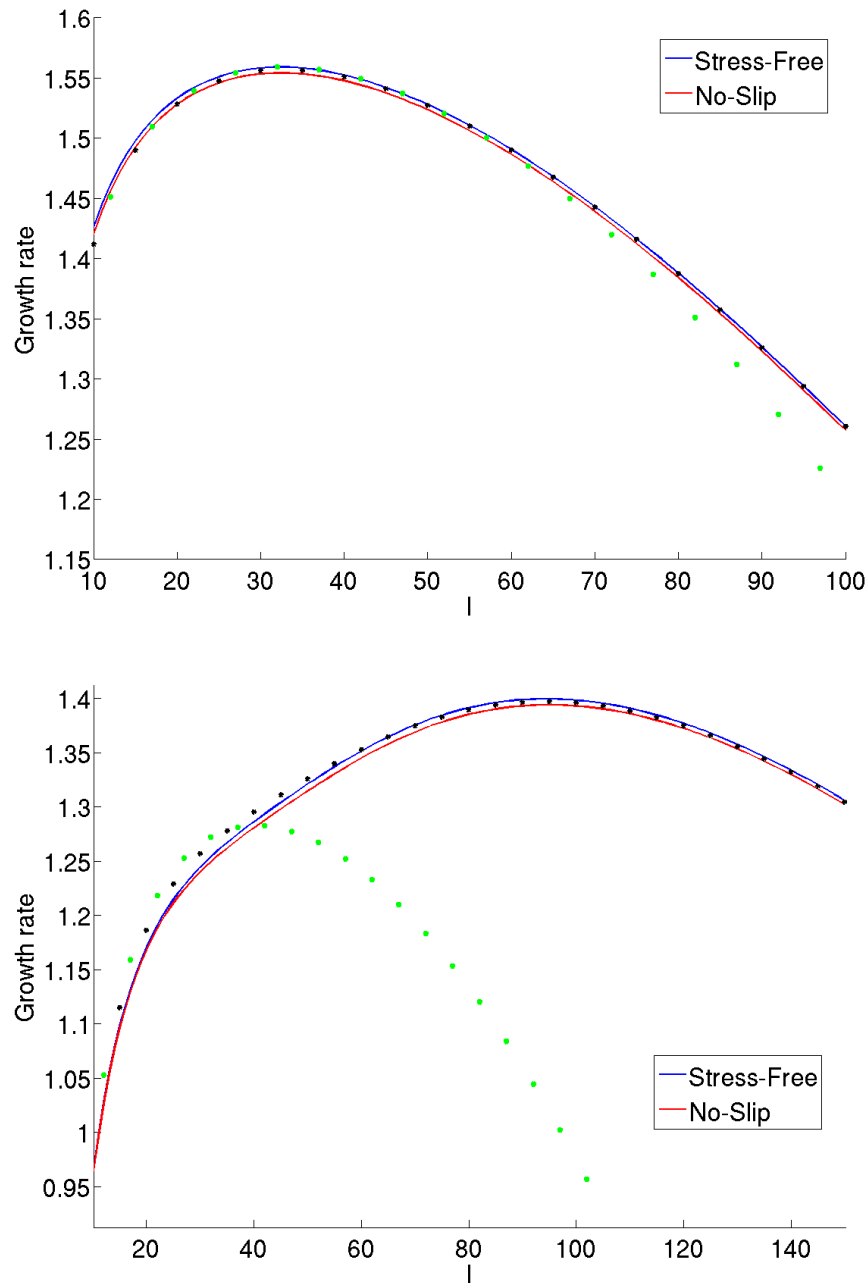
Figure 6.1: Growth rate versus wavenumber l for parameter values $P_{\nu 1}$ (top) and $P_{\nu 2}$ (bottom) defined in (6.41). In each figure the coloured lines represent the growth rate obtained from the boundary value problem (6.38), the black dots represent the asymptotic growth rate from (6.12) derived when $l^2/Re \sim 1$, and the green dots the asymptotic growth rate from (6.23) derived when $l^2/Re \sim \delta_i$.
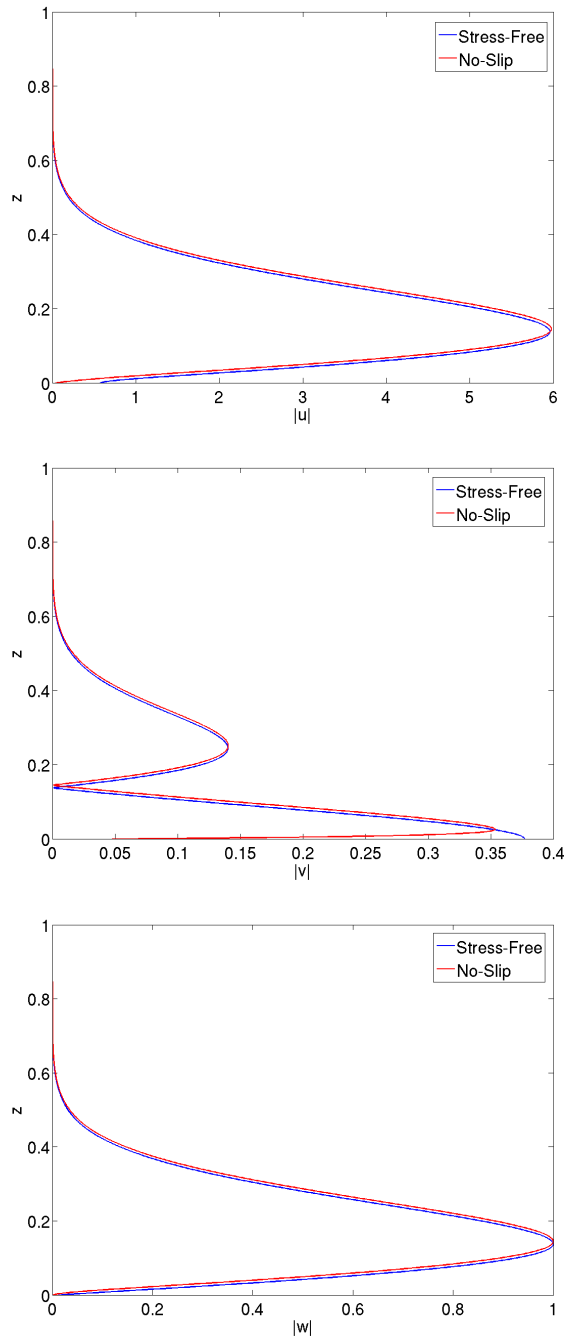
Figure 6.2: Eigenfunctions $|u|$, $|v|$ and $|w|$ for both the stress-free and no-slip boundary conditions derived by solving the full boundary value problem (6.38), for parameter values $P_{\nu 1}$, with wavenumber $l = 33$.
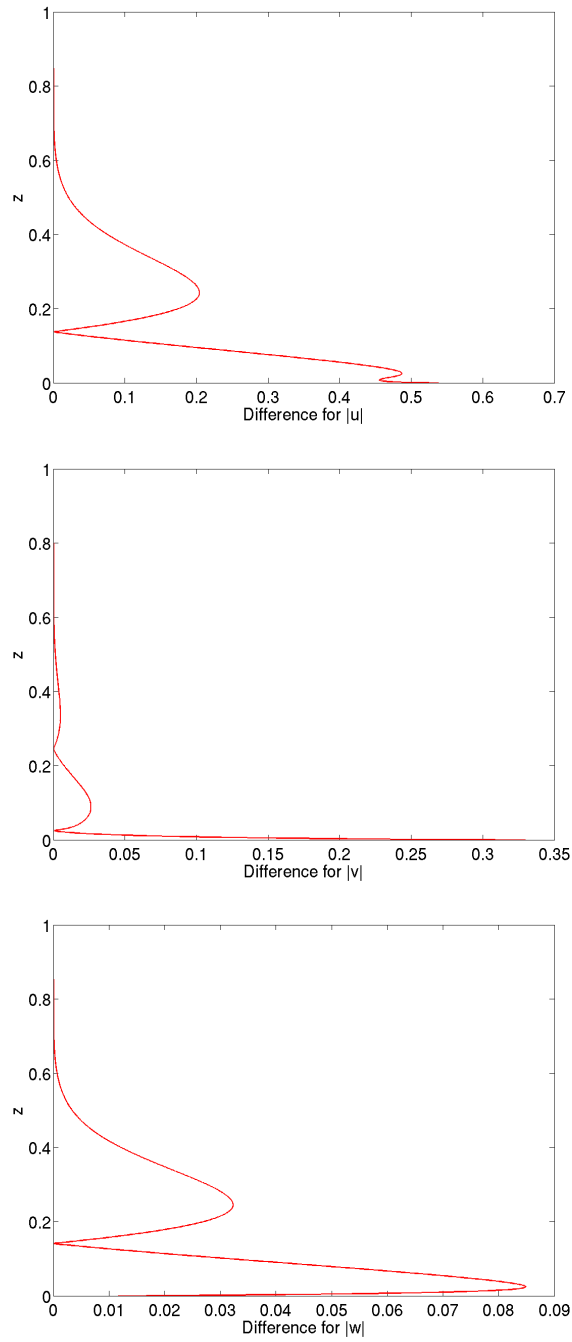
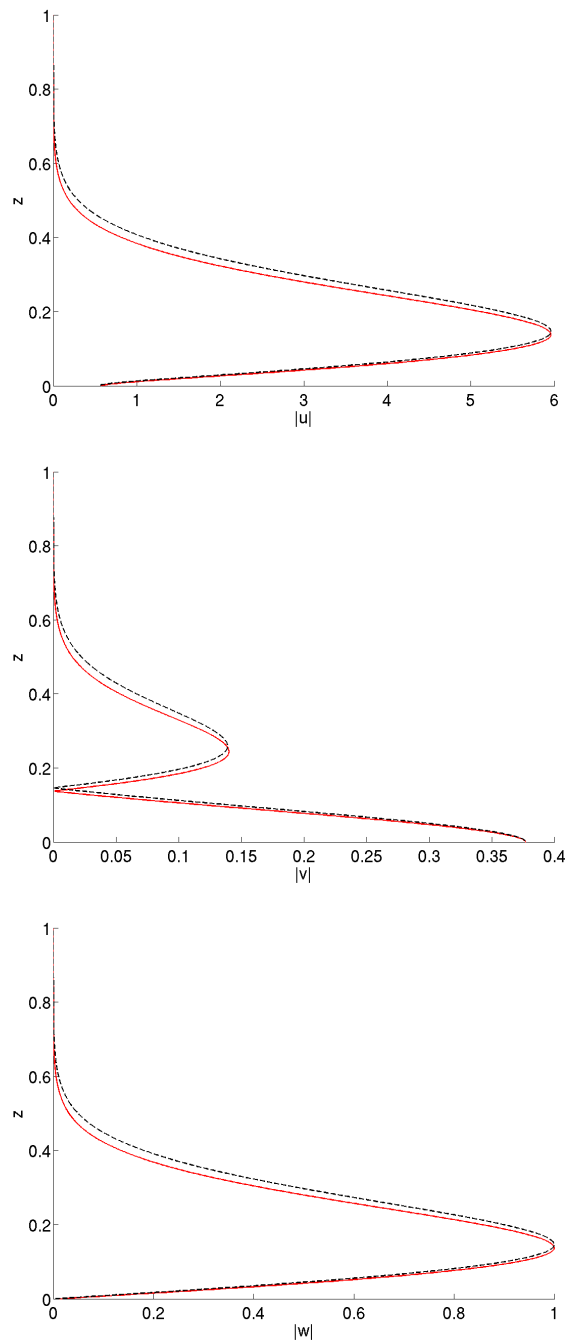Figure 6.3: The absolute difference between the stress-free and no-slip solutions found in Figure 6.2.

Figure 6.4: Eigenfunctions $|u|$, $|v|$ and $|w|$ obtained using stress-free boundary conditions, taken with parameter values $P_{\nu 1}$ at $l = 33$. In all cases the red solid line represents the solutions to the full boundary value problem (6.38), and the black dashed line represents the approximated solution using the asymptotics.
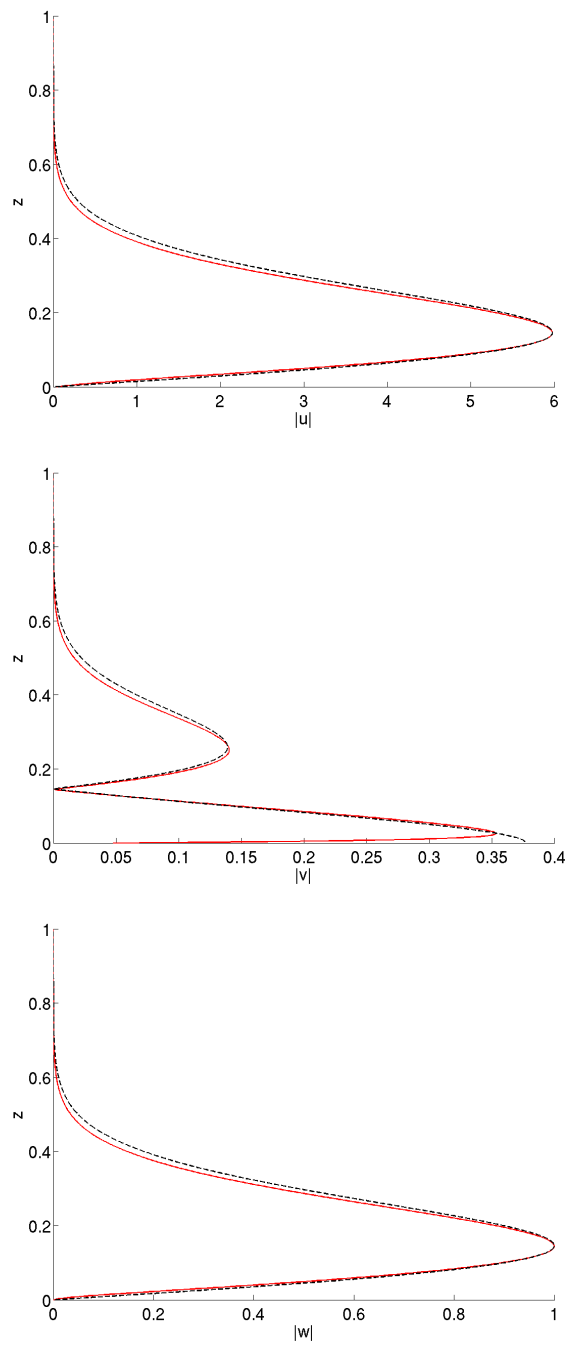
Figure 6.5: The same as Figure 6.4, obtained using no-slip boundary conditions.

The body mode

As in the previous subsection studying the wall mode, we will introduce a set of parameter values to validate our asymptotic results against the solutions to the full boundary value problem. In Chapter 5 we provided examples of eigenfunction solutions for a body mode, for which the bulk of the eigenfunction existed within an envelope peaked in the layer, and outside the envelope the eigenfunction was effectively zero. As a result both, w and its derivative are essentially zero at the boundary. Numerically this was not difficult to solve, as we only had to satisfy the impermeability condition on w. By considering viscosity we have introduced second order derivatives into the governing equations (6.1). Now the problem becomes very difficult to solve numerically, as both the inverse iteration method and the MATLAB solvers struggle to find the body modes. Since the only non-zero part of the eigenfunction is contained in an envelope peaked away from the boundary, the issue regarding the boundary conditions does not effect this problem; solving the full solution for stress-free and no-slip gives the same result. Therefore unlike the wall mode, our approximation for v using the incompressibility conditions (6.39) will fully satisfy the required boundary conditions. To validate the asymptotic analysis of the body mode we pick a quadratic shear profile $U = 10(z^2 - z + 1)$, which is maximised in the layer, and fix the Reynolds number at $Re = 10^5$. For this value of Re we expect the analysis of §6.2.1 to be valid for $l \approx 316$, the asymptotics in §6.2.2 to be valid when $l \approx 100$ and finally the asymptotics in §6.2.3 to be valid when $l \approx 46$. To ensure that we find a mode that is peaked in the layer we use parameter values

$$P_{\nu 3} : \quad \alpha = 0.1,\ \hat{\beta} = 0.1,\ \zeta = 1.5,\ k = 0.6. \tag{6.43}$$

Figure 6.6 plots the growth rate of the full boundary value solution versus wavenumber l for these parameter values. Included on the plot are the asymptotic results for the growth rates from (6.17) (black), (6.29) (green), (6.36) (blue). Even for these relatively low values of l, the asymptotic analysis provides a very good approximation to the full growth rate. As was the case for the wall mode, the asymptotics derived in §6.2.1 for when $l^2/Re \sim 1$ are found to hold when $l^2/Re \ll 1$.

Figure 6.7 plots the moduli of u, v and w obtained from solving the full boundary value problem at $l = 55$ (red). Also on these plots (black dashes) are the asymptotically derived
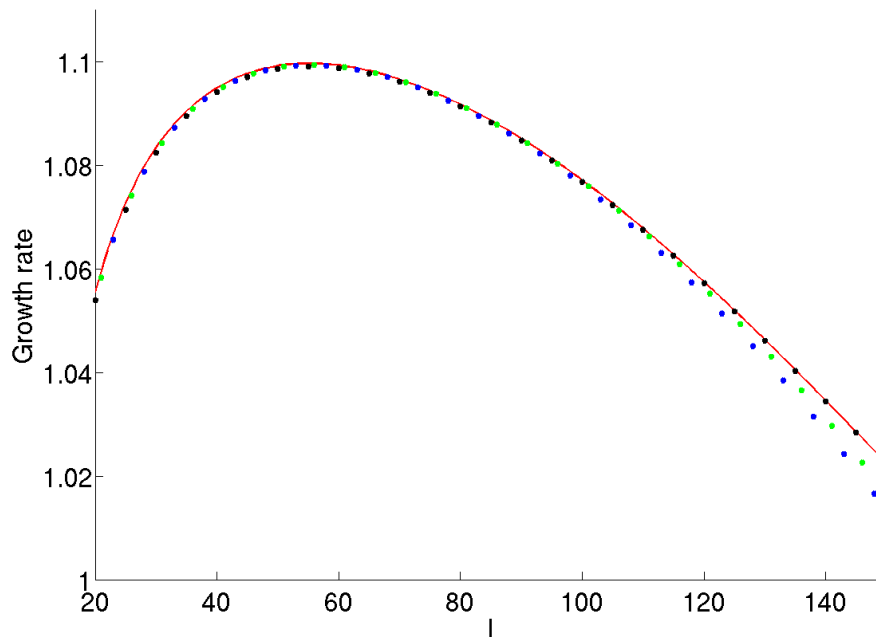
Figure 6.6: Growth rate versus wavenumber l for parameter values $P_{\nu 3}$ (6.43). The growth rate from the full boundary value problem (6.38) is given in solid red. The dots represent solutions to the asymptotics results: Equation (6.17) black, equation (6.29) green and equation (6.36) blue.

eigenfunctions — w is obtained from (6.37), u is derived from (6.38a) and v from (6.39). Here we note the excellent agreement between the full boundary value problem and the approximated solution. As mentioned the choice of boundary conditions does not effect the structure of the body mode and therefore our approximations are valid for both stress-free and no-slip.
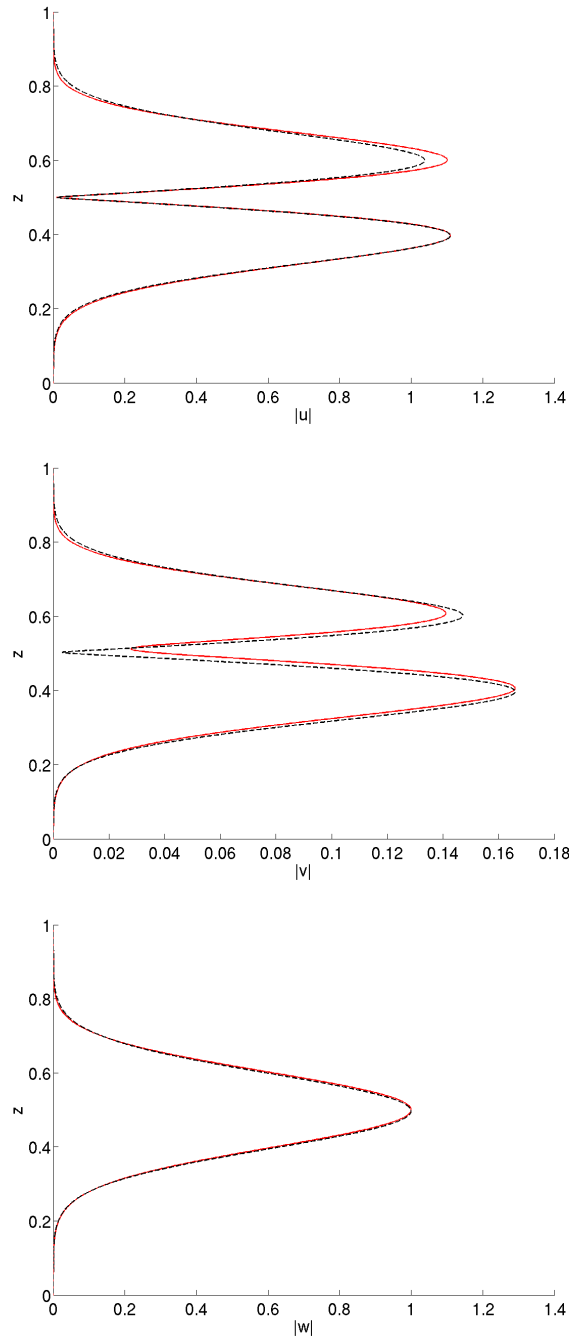
Figure 6.7: Plots of $|u|,|v|$ and $|w|$ for the body mode at $l = 55$ with parameter values $P_{\nu 3}$ given by (6.43). The solid red line represents the solution to the full boundary value problem (6.38), the black dashes the approximated solutions from the asymptotics.

6.2.5   Preferred mode of instability: viscosity

In the absence of both shear and diffusion it is fairly straight forward to determine which branch of the asymptotic solutions to follow in order to find an approximate eigenvalue and corresponding eigenvector. The most unstable mode in this case is the mode localised about the point z_c at which the function F, given by (5.2), is minimised. In §5.3.5 we discussed why, with the introduction of a velocity shear, this simple concept is no longer valid. Instead, the localisation of the most unstable mode can only be determined by considering the asymptotic growth rate for both the wall and body mode, and seeing which corresponded to the most unstable mode. This means that for a given set of parameter values it is possible that, by increasing the magnitude of the shear, the most unstable mode switches from a wall mode to a body mode, or *vice versa*. This unpredictable nature carries through to our analysis in this chapter.

In §5.3.1 we derived equation (5.57) for the leading order eigenvalue ω_0 in the presence of velocity shear, given by

$$\omega_0 = -\sqrt{F(z_u)} - kU(z_u). \tag{6.44}$$

For a wall mode, z_u is located on the boundary and therefore takes a real value, either $z_u = 0$ or $z_u = 1$. As discussed in §5.4, the shear plays no role in influencing the leading order growth rate, and instead only affects the frequency of the mode. The only influencing factor on the leading order growth rate is the function F, which is minimised when $k = 0$. Therefore the most unstable wall mode in the absence of any diffusion is always the interchange mode.

To study the effects of viscosity on the wall mode we split our analysis into two distinct sections, depending on the relative size of the Reynolds number Re to wavenumber l. In §6.2.2, we derived asymptotic results for the wall mode valid when $l \sim Re^{3/8}$. Under this assumption, the leading order eigenvalue ω_0 is given by equation (6.21), which is precisely equation (6.44). Therefore, for values of l such that $l \sim Re^{3/8}$, the most unstable wall mode will again be an interchange mode. Section 6.2.1 contains results valid for values of l, such that $l \sim Re^{1/2}$. The leading order eigenvalue for this case in now given by a

fourth order polynomial in ω_0 containing the effects of viscosity,

$$\bar{\omega}_0^4 - \frac{2il^2}{Re}\bar{\omega}_0^3 - \left(F + k^2B^2 + \frac{l^4}{Re^2}\right)\bar{\omega}_0^2$$
$$+ \frac{il^2}{Re}(F + k^2B^2)\bar{\omega}_0 + k^2B^2F - \frac{ikB^2U'l^2}{\gamma Re} = 0, \tag{6.45}$$

where $\bar{\omega}_0 = \omega_0 + kU$. As such, the growth rate in this limit is no longer dependent solely on F, but, instead, is also influenced by both the velocity shear gradient and the viscosity. Let us first consider the interchange mode present in this limit. Taking $k = 0$, equation (6.45) becomes

$$\omega_0 \left(\omega_0^2 - \frac{il^2}{Re}\omega_0 - F_0\right)\left(\omega_0 - \frac{il^2}{Re}\right) = 0, \tag{6.46}$$

where $F_0 = F|_{k=0} < 0$. Focusing on instability, i.e. $\Im(\omega_0) < 0$, we can reduce the above equation to

$$\omega_0^2 - \frac{il^2}{Re}\omega_0 - F_0 = 0, \tag{6.47}$$

the imaginary part of which gives

$$\Im(\omega_0) = \frac{l^2}{2Re} \pm \sqrt{\frac{l^4}{4Re^2} - F_0}. \tag{6.48}$$

Equation (6.48) takes its most negative value, and therefore corresponds to the mode of highest growth rate, for the negative root. Let us compare this result to what we obtain when taking the imaginary part of (6.21) with $k = 0$, valid when $l \sim Re^{3/8}$, namely

$$\Im(\omega_0) = -\sqrt{-F_0}. \tag{6.49}$$

For all l^2/Re, the resulting growth rate from equation (6.49) will be larger than that from (6.48). Therefore the most unstable interchange mode of the system will always exist for values of l in the region where $l \sim Re^{3/8}$.

As can be seen from (6.45), when $l \sim Re^{1/2}$ the growth rate of the system is no longer dependent only on F. Thus there may exist an undular mode in this limit that is more unstable than the interchange mode. To study this further, we fix $l^2/Re = 1$ and take a

linear shear profile $U = \lambda(1 - z)$. Figure 6.8 is a plot of the leading order growth rate from (6.45) versus shear strength λ, for parameter values

$$P_{\nu 4} : \quad \alpha = 0.1,\ \hat{\beta} = 0.1,\ \zeta = 1.5. \tag{6.50}$$

This figure includes several results for different wavenumber k values, with the interchange mode represented by the solid black line. Here we observe that for a critical value of λ, the mode with the largest growth rate and therefore the most unstable mode for these parameter values, switches from the interchange mode to an undular mode. Thus, by introducing viscosity, it becomes possible for an undular mode to be the most unstable mode. Interestingly the exact form of the shear profile is somewhat irrelevant when it comes to its influence on the growth rate. Under closer inspection, the growth rate obtained from (6.45) is only influenced by the value of the shear gradient U' evaluated at the boundary. Therefore the exact structure of the shear away from the boundary does not play a role on the leading order growth rate, and the undular mode is only destabilised when $U' \neq 0$ at the boundary. Numerically one can show that changing the sign of U' at the boundary will only alter the frequency of the mode. Thus, when considering a shear profile of the form $U = \lambda(1 + z)$, the growth rate will be precisely what we found in Figure 6.8 for when $U = \lambda(1 - z)$. Hence, it is the magnitude of the shear gradient U' evaluated at the boundary that impacts the instability.

To tie the interchange and undular mode results together, we fix the Reynolds number at $Re = 10^4$ and examine how the shear (combined with the viscosity) plays a role in the location of the most unstable mode. Again we take a linear shear profile $U = \lambda(1 - z)$ and parameter values $P_{\nu 4}$. To determine the growth rate of the wall mode we use equation (6.12), which includes the next order correction to the leading order growth rate. Figure 6.9 contains three separate plots of how the growth rate varies with l, each plot showing a different value of λ. When $\lambda = 0$ the most unstable mode is an interchange mode at $l \approx 32$. By increasing the shear gradient to $\lambda = 10$, the interchange mode at $l \approx 32$ is still the most unstable wall mode. However, for values of l such that $l \sim Re^{1/2}$, an undular mode is more unstable than the interchange mode. Finally, when $\lambda = 25$ the undular wall mode with $k = 0.5$, at $l = 145$, is the most unstable mode of system. This result ties in nicely with what we have seen in the asymptotic analysis. When $Re = 10^4$,
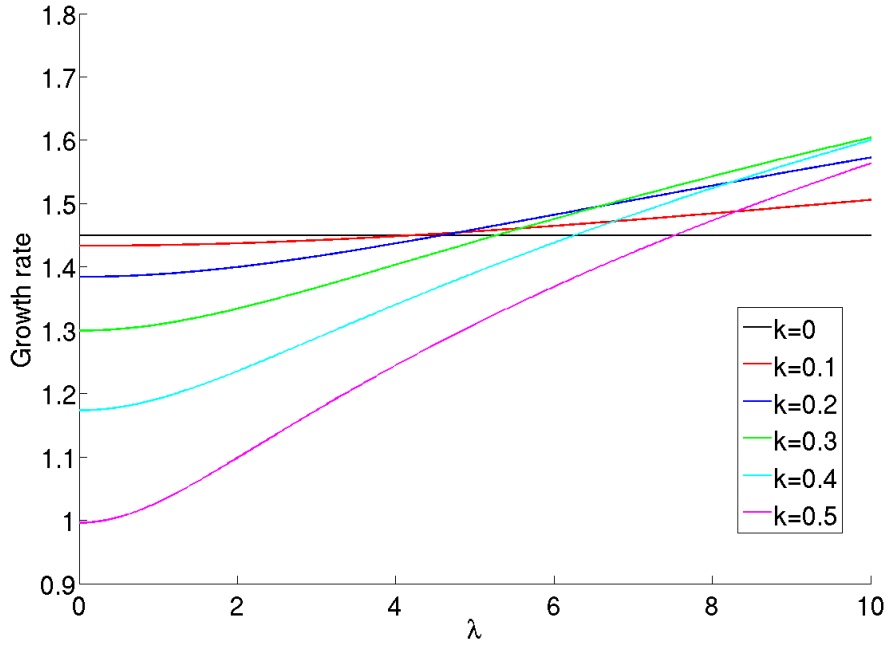
Figure 6.8: The leading order growth rate ω_0 from (6.45) versus shear strength λ obtained by fixing $l^2/Re = 1$, with linear shear profile $U = \lambda(1 - z)$ and parameter values $P_{\nu 4}$ (6.50).

we expect the asymptotic analysis for the wall mode in §6.2.2 to be accurate when $l^2/Re \sim \delta_i$, or specifically $l \approx 32$. As described above, independent of the profile or magnitude of the shear flow, the most unstable wall mode in the region where $l^2/Re \sim \delta_i$, will always be an interchange mode. This is precisely what we observe in Figure 6.9; no matter what the strength of the shear, the most unstable mode when $l^2/Re \sim \delta_i$ is the interchange mode. By increasing the shear gradient to $\lambda = 25$, the most unstable mode of the system switches from being the interchange mode at $l = 32$ to an undular mode at $l = 145$. For $l = 145$, $l^2/Re \approx 2$. It is therefore reasonable to use the analysis of §6.2.1, which assumes $l^2/Re \sim 1$, to describe what is happening here. As previously discussed, when considering wall modes in the region where $l^2/Re \sim 1$, the Reynolds number appears in the calculations for the leading order growth rate. Therefore it is possible that for a sufficiently large shear gradient, the undular mode becomes the most dominant mode. This is seen in Figure 6.9; the most unstable mode when $l^2/Re \sim 1$ has

changed from an interchange mode to an undular mode as the shear strength is increased.

To conclude, we can build a picture of how the wall mode behaves under the influences of velocity shear and viscosity. For 'low' shear gradients the most unstable wall mode will be an interchange mode with wavenumber l given by $l \sim Re^{3/8}$. By increasing the shear gradient past a certain critical value, it is possible that the most unstable mode switches from an interchange mode to an undular mode, with wavenumber $l \sim Re^{1/2}$. Due to the complex nature of the problem, we can not derive the critical value of λ for a general shear flow. However, through the introduction of viscosity we now know that it is possible that an undular mode, and hence a mode affected by velocity shear, can be the most unstable mode of the system.

Unfortunately due to the added complexity, it is not possible to provide a similar analysis for the body mode. For a body mode to exist two simultaneous equations must be satisfied, subject to the constraint that $0 < \Re(z_\nu) < 1$. These two simultaneous equations are heavily dependent on the profile and magnitude of the shear flow. It is possible that for a specific shear profile a body mode exists for certain values of λ but not for others. Therefore finding the body mode has to be done on a case by case basis, and solving for a range of λ values is not feasible. It would appear however (as seen in Figure 6.6) that the most unstable body mode appears around $l \approx Re^{1/3}$. This would suggest that the work in §6.2.3 holds the most significance and that the viscosity has no influence on the leading order growth rate.
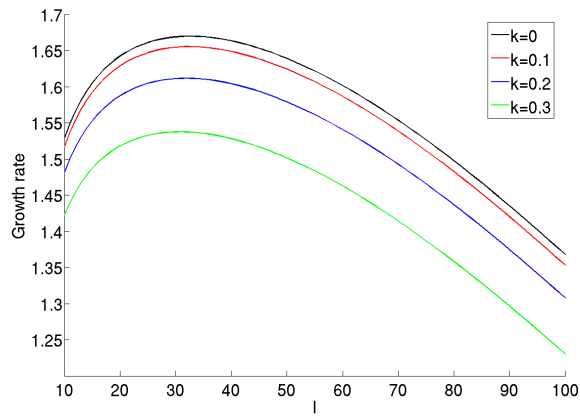
(a)
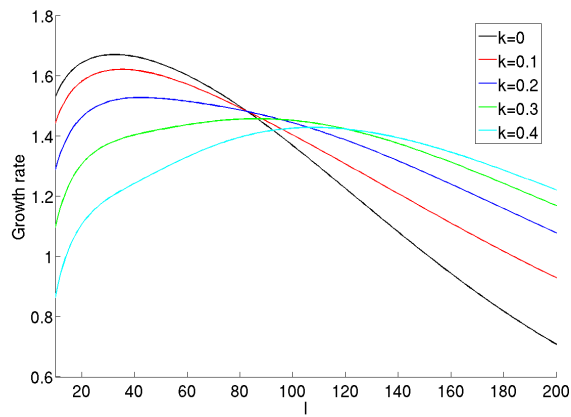
(b)
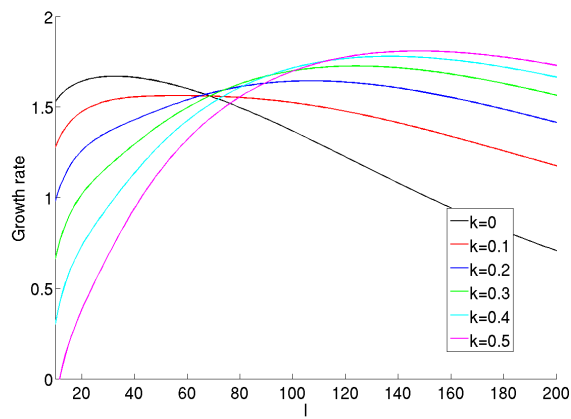
(c)

Figure 6.9: Growth rate obtained from (6.12) versus wavenumber l for shear strengths: (a) $\lambda = 0$, (b) $\lambda = 10$ and (c) $\lambda = 25$. Each figure uses parameter values $P_{\nu 4}$ (6.50), $Re = 10^4$ and shear profile $U = \lambda(1 - z)$.

6.3   Thermal diffusion

When considering only the effects of thermal diffusivity on the system, the linear set of governing equations from (3.61) are;

$$\nabla \cdot \boldsymbol{u} = 0, \tag{6.51a}$$

$$\nabla \cdot \boldsymbol{b} = 0, \tag{6.51b}$$

$$\left(\frac{\partial}{\partial t} + U\frac{\partial}{\partial x}\right)\boldsymbol{u} + \boldsymbol{U}'w = -\nabla_{\perp}\Pi + (T + Bb_x)\,\hat{\boldsymbol{z}} + B\frac{\partial \boldsymbol{b}}{\partial x} + \boldsymbol{B}'b_z, \tag{6.51c}$$

$$\left(\frac{\partial}{\partial t} + U\frac{\partial}{\partial x}\right)\boldsymbol{b} + \boldsymbol{B}'w = B\frac{\partial \boldsymbol{u}}{\partial x} + \boldsymbol{U}'b_z, \tag{6.51d}$$

$$\left(\frac{\partial}{\partial t} + U\frac{\partial}{\partial x}\right)(T + DBb_x) = -\beta w + \frac{1}{Pe}\nabla_{\perp}^2 T, \tag{6.51e}$$

where $\nabla_{\perp}^2 = \partial_{zz} + \partial_{yy}$. This set of equations can be solved subject to impermeable boundary conditions on top and bottom boundaries (i.e. $w = 0$), and two boundary conditions on the temperature T. Following the work laid out in appendix D, equations (6.51) can be reduced to a 4$^{\text{th}}$ order ordinary differential equation for $\psi = (\omega_0 + kU)^{-1}w$,

$$\alpha_{\kappa1}\psi'''' + \alpha_{\kappa2}\psi''' + \alpha_{\kappa3}\psi'' + \alpha_{\kappa4}\psi' + \alpha_{\kappa5}\psi = 0, \tag{6.52}$$

where the coefficients $\alpha_{\kappa i}$ are given by

$$\alpha_{\kappa1} = \frac{iP}{(\omega + kU)Pe}, \tag{6.53a}$$

$$\alpha_{\kappa2} = \frac{3iP'}{(\omega + kU)Pe}, \tag{6.53b}$$

$$\alpha_{\kappa3} = P + \frac{3iP''}{(\omega + kU)Pe} - \frac{i(a_{\kappa1} + P)}{l^2}(\omega + kU)Pe, \tag{6.53c}$$

$$\alpha_{\kappa4} = P' + \frac{iP'''}{(\omega + kU)Pe} - \frac{i(2a'_{\kappa1} + P)}{l^2}(\omega + kU)Pe, \tag{6.53d}$$

$$\alpha_{\kappa5} = -l^2 a_{\kappa2} - \frac{ia''_{\kappa1}l^2}{(\omega + kU)Pe} + \frac{ia_{\kappa1}l^4}{(\omega + kU)Pe}, \tag{6.53e}$$

with

$$P = (\omega + kU)^2 - k^2 B^2, \tag{6.54a}$$

$$a_{\kappa 1} = (\omega + kU)^2 - G, \tag{6.54b}$$

$$a_{\kappa 2} = (\omega + kU)^2 - F, \tag{6.54c}$$

where $G = k^2 B^2 + BB'$. Proceeding as in §6.2 we will perform a boundary layer analysis on equation (6.52), studying different limits depending on the relative size of the Péclet number Pe to the wavenumber l. With the benefit of hindsight we will focus on three relative orderings: $l^2/Pe \ll 1$, $l^2/Pe \sim 1$ and $l^2/Pe \gg 1$. We shall again introduce a boundary layer variable, analogous to that seen in the previous section,

$$\xi_i = \frac{z - z_\kappa}{\delta_i}. \tag{6.55}$$

We shall then expand the eigenvalue in orders of δ_i and expand all basic state variables of z in a Taylor series about z_κ.

6.3.1 $\quad l^2/Pe \ll 1$

Let us first consider the case where the wavenumber l satisfies the inequality $l^2/Pe \ll 1$. Proceeding in familiar fashion, at leading order, the governing 4$^{\text{th}}$ order ODE reduces down to the second order ODE,

$$\left((\omega_0 + kU)^2 - k^2 B^2\right) \frac{\mathrm{d}^2\psi}{\mathrm{d}\xi_i^2} - \delta_i^2 l^2 \left((\omega_0 + kU)^2 - F\right) \psi + o\,(1) = 0. \tag{6.56}$$

Considering the boundary layer associated with $i = 0$, and balancing terms in the equation by taking $\delta_i = l^{-1}$, equation (6.56) becomes equation (5.56). Therefore we can follow the work laid out in §5.3 to arrive at the asymptotic approximations, and conclude that for wavenumbers such that $l^2/Pe \ll 1$, the thermal diffusion has no impact on the instability. For future reference we include the leading order growth rate for the case of $l^2/Pe \ll 1$; from (5.57) we have

$$\omega_0 = -\sqrt{F(z_\kappa)} - kU(z_\kappa). \tag{6.57}$$

6.3.2 $l^2/Pe \sim 1$

Let us now consider the regime $l^2/Pe \sim 1$. In this case the governing leading order equation involves the thermal diffusivity, and can be written as

$$d_1 \frac{\mathrm{d}^4\psi}{\mathrm{d}\xi_i^4} + \left(d_2 Pe + d_3 l^2\right) \delta_i^2 \frac{\mathrm{d}^2\psi}{\mathrm{d}\xi_i^2} - l^2 \left(d_4 Pe + d_5 l^2\right) \delta_i^4 \psi + o\left(1\right) = 0, \tag{6.58}$$

where all d_i coefficients are $O\left(1\right)$ and given in appendix F. When considering a boundary layer associated with $i = 0$, all terms in the above equation balance when $\delta_0 = l^{-1}$. There is only a continuous, non-trivial solution that satisfies this equation when $d_4 Pe + d_5 l^2 = 0$. This corresponds to an equation for the leading order growth rate, given by

$$\bar\omega_0^3 - \frac{il^2}{Pe}\bar\omega_0^2 - F\bar\omega_0 + \frac{iGl^2}{Pe} = 0. \tag{6.59}$$

As in §6.2, we will provide asymptotic results for the wall and body mode individually.

The wall mode

When equation (6.59) is satisfied, the governing equation (6.52) in the presence of a boundary layer ξ_1, keeping only the highest order terms, becomes

$$d_1 \frac{\mathrm{d}^4\psi}{\mathrm{d}\xi_1^4} + \left(d_2 Pe + d_3 l^2\right) \delta_1^2 \frac{\mathrm{d}^2\psi}{\mathrm{d}\xi_1^2} - Pe\, l^2 \left(\omega_1 d_6 + d_7 \xi_1\right) \delta_1^5 \psi + o\left(1\right) = 0. \tag{6.60}$$

As we saw in §6.2, there exist different values of δ_1 that can be used to balance terms in an equation of this form. We will again pick the value of δ_1 that has the largest influence on the growth rate; therefore, as with all previous cases, $\delta_1 = l^{-2/3}$. On striking this balance, the fourth order equation (6.60) reduces down to a second order ODE

$$\left(d_2 + d_3 \frac{l^2}{Pe}\right) \frac{\mathrm{d}^2\psi}{\mathrm{d}\xi_1^2} - \left(\omega_1 d_6 + d_7 \xi_1\right) \psi = 0. \tag{6.61}$$

Following earlier work on the wall mode analysis (see §5.2.3), we introduce the variable $\Sigma = -d_7/(d_2 + d_3 l^2/Pe)$ and transform the equation (6.61) into an Airy equation. This allows us to derive an approximation to the eigenvalue

$$\omega = \omega_0 \left(1 + l^{-2/3} \frac{\chi \left(d_2 + d_3 l^2/Pe\right) \Sigma^{2/3}}{\omega_0 d_6}\right) + o\left(l^{-2/3}\right), \tag{6.62}$$

with ψ eigenmode

$$\psi = C_1 \mathrm{Ai} \left[\chi - l^{2/3}(z - z_\kappa) \Sigma^{1/3} \right]. \tag{6.63}$$

The body mode

To derive an asymptotic approximation for the body mode we need to transform the governing equation into the form of a parabolic cylinder equation. To do this we first take $\omega_1 = 0$ and $d_7 = 0$ in equation (6.60). The condition that $d_7 = 0$ gives

$$\bar{\omega}_0 \left(-F' + 2kU'\bar{\omega}_0 \right) + kU' \left(\bar{\omega}_0^2 - F \right) - \frac{il^2}{Pe} \left(2kU'\bar{\omega}_0 - G' \right) = 0, \tag{6.64}$$

which along with (6.59), can be solved simultaneously for ω_0 and z_κ. With these equations satisfied the leading order governing equation associated with the boundary layer ξ_2, becomes

$$d_1 \frac{\mathrm{d}^4\psi}{\mathrm{d}\xi_2^4} + \left(d_2 Pe + d_3 l^2 \right) \delta_2^2 \frac{\mathrm{d}^2\psi}{\mathrm{d}\xi_2^2} - Pe\, l^2 \left(\omega_2 d_8 + d_9 \xi_2^2 \right) \delta_2^5 \psi + o\left(1 \right) = 0. \tag{6.65}$$

Again we choose $\delta_2 = l^{-1/2}$, so that ω_2 has the largest influence on the growth rate. With this choice, equation (6.65) becomes a second order differential equation for ψ, which at leading order is

$$\left(d_2 + d_3 \frac{l^2}{Pe} \right) \frac{\mathrm{d}^2\psi}{\mathrm{d}\xi_2^2} - \left(\omega_2 d_8 + d_9 \xi_2^2 \right) \psi = 0. \tag{6.66}$$

In familiar fashion, we introduce the variable $\Upsilon = -2d_9/\left(d_2 Pe + d_3 l^2 \right)$ and transform the second order ODE (6.66) into a parabolic cylinder equation. With this in place we can derive an approximation to the most unstable body mode eigenvalue,

$$\omega = \omega_0 \left(1 - l^{-1} \frac{d_2 + d_3 l^2/Pe}{d_8 \omega_0} \sqrt{-\frac{\Upsilon}{2}} \right) + o\left(l^{-1} \right), \tag{6.67}$$

and eigenfunction for ψ,

$$\psi = C_1 e^{-l\left(\frac{-\Upsilon}{8} \right)^{1/2} (z - z_\nu)^2}. \tag{6.68}$$

6.3.3 $l^2/Pe \gg 1$

In this limit the leading order governing equation again reduces to a second order differential equation,

$$\left((\omega_0 + kU)^2 - k^2 B^2\right) \frac{\mathrm{d}^2\psi}{\mathrm{d}\xi_i^2} - \delta_i^2 l^2 \left((\omega_0 + kU)^2 - G\right)\psi + o\left(1\right) = 0. \tag{6.69}$$

Balancing terms in this equation by taking $\delta_0 = l^{-1}$, we arrive at a non-trivial, continuous solution when

$$\omega_0 = -\sqrt{G(z_\kappa)} - kU(z_\kappa). \tag{6.70}$$

This is very similar to what we saw in §6.3.1, in that the thermal diffusivity has no direct influence on the instability. Equation (6.69) is almost identical to equation (6.56), the only difference being the function G instead of F. Therefore, the appropriate results for the wall and body modes are precisely those of §5.3, with F replaced with G.

6.3.4   Preferred mode of instability: thermal diffusion

When considering the limit $l^2/Pe \ll 1$, the system reverts to that studied in §5.3. Thus, for a wall mode, the instability is governed solely by the function F, and the velocity shear has no influence on the instability. Furthermore, the most unstable wall mode in this case is the interchange mode. For wavenumbers such that $l^2/Pe \gg 1$, we obtain a very similar result. This time, however, the growth rate for a wall mode is dictated solely by the function G, with the most unstable wall mode appearing when G is most negative, which again corresponds to an interchange mode. By comparing the magnitudes of the functions F and G we can therefore determine which limit the system prefers when in the presence of just thermal diffusion. From Chapter 5, F is defined as

$$F = k^2 B^2 + \beta + \frac{BB'}{\gamma}. \tag{6.71}$$

In §3.3.1 we rewrite the temperature gradient as

$$\beta = \hat{\beta} + \frac{\partial T}{\partial z} + \left(1 - \frac{1}{\gamma}\right) BB', \tag{6.72}$$

where for a convectively stable atmosphere, $\hat{\beta} > 0$ and $\partial_z T > 0$. Substituting this expression into (6.71) gives

$$F = k^2 B^2 + \hat{\beta} + \frac{\partial T}{\partial z} + BB'. \tag{6.73}$$

In §6.3.2 we introduced a new variable G as

$$G = k^2 B^2 + BB'. \tag{6.74}$$

Comparing (6.73) and (6.74) we notice that for a convectively stable atmosphere, such as in the tachocline, $G < F$ everywhere in the layer. Therefore, wall modes in the region where $l^2/Pe \gg 1$ are guaranteed to be more unstable than those where $l^2/Pe \ll 1$. The transition period when $l^2/Pe \sim 1$ offers little information that aids us analytically. It would appear from all our numerical experiments, that the most unstable wall mode for a convectively stable atmosphere, with a linear basic state magnetic field, is the interchange mode appearing in the $l^2/Pe \gg 1$ limit.

As before, the analysis for the body mode is very limited due to the added complexity in finding both ω_0 and z_κ for a general shear. The preferred mode of instability seems to exist in the limit where $l^2/Pe \gg 1$, and in this limit we revert to the similar problem found in Chapter 5, the only difference being that the function F in Chapter 5 is replaced by the new function G. Since, in Chapter 5, we did not find an example of a body mode begin the most unstable mode, there is no reason to assume that the body mode will be the most unstable mode for this system. However we can not rule this out for a general shear profile, only the ones we have tested.

In §5.2 we commented on the difference between our diffusionless system, which ignores diffusive effects, and the system of equations found in Gilman (1970), the main difference being how we treated the variation of temperature. Gilman assumed the atmosphere was isothermal and thus neglected the energy equation in his analysis. We did not make this assumption and instead just ignored the contribution of thermal diffusion in the energy equation, whilst still including the variations in temperature. Upon taking Gilman's isothermal limit, our leading order equation in the absence of shear becomes equation (5.3), which is an exact analogue to (6.69) with $U = 0$. Since (at least for the wall mode) this limit produces the most unstable mode of the system, it appears the system

naturally wants to reduce to an isothermal state. This is not entirely surprising, especially when considering what we know about magnetic buoyancy in the presence of diffusion from §2.1.2. From equations (2.14) and (2.15) we see that for a given atmosphere, instability is more readily achieved as $\kappa \to \infty$, or, in terms of the Péclet number $Pe \to 0$. Therefore the most unstable wall mode in the presence only of thermal diffusion is one in which the temperature perturbation is constant, resulting in any contribution of thermal diffusion being neglected.

To arrive at the asymptotic results for both the wall and body modes we only satisfied two of the required four boundary conditions, these being the impermeability conditions on ψ (and therefore w). In appendix D we derive equation (D.6), which links the temperature perturbation T to the vertical velocity ψ,

$$\left(1 - \frac{il^2}{(\omega + kU)\,Pe} + \frac{i}{(\omega + kU)\,Pe}\frac{\partial^2}{\partial z^2}\right)T = -i\left(\left(1 - \frac{1}{\gamma}\right)BB' - \beta\right)\psi. \quad (6.75)$$

Using our derived approximations for ψ, we can solve (6.75) as a boundary value problem for T, subject to the two unused boundary conditions, i.e. either fixed temperature at both boundaries, or fixed temperature at one boundary and fixed flux at the other. Since the system prefers to be isothermal, we expect the temperature of the most unstable mode to be constant throughout the layer, with the constant temperature value given by the value of to T prescribed on the boundary.

To validate our asymptotic results we solve the full system of equations subject to boundary conditions $w = 0$ and $T = 0$ at the bottom boundary, and $w = 0$ and $T' = 0$ at the top boundary. Figure 6.10 plots the growth rate versus l obtained from solving the full boundary value problem together with the asymptotic results, for both the wall and body modes. The parameter values used are

$$P_{\kappa 1} : \quad \alpha = 0.1,\ \hat{\beta} = 0.1,\ \zeta = 1.5,\ k = 0,\ Pe = 1; \quad (6.76\text{a})$$

$$P_{\kappa 2} : \quad \alpha = 0.1,\ \hat{\beta} = 0.1,\ \zeta = 1.5,\ k = 0.6,\ Pe = 1, \quad (6.76\text{b})$$

with the wall mode associated with parameter values $P_{\kappa 1}$ and velocity shear $U = 10(1 - z)$, and the body mode with parameter values $P_{\kappa 2}$ and velocity shear $U = 10(z^2 - z + 1)$. As expected the systems prefers the $l^2/Pe \gg 1$ limit with $l \to \infty$.

The asymptotically derived growth rate for both $l^2/Pe \sim 1$ and $l^2/Pe \gg 1$ provide a good approximation to the full solution.
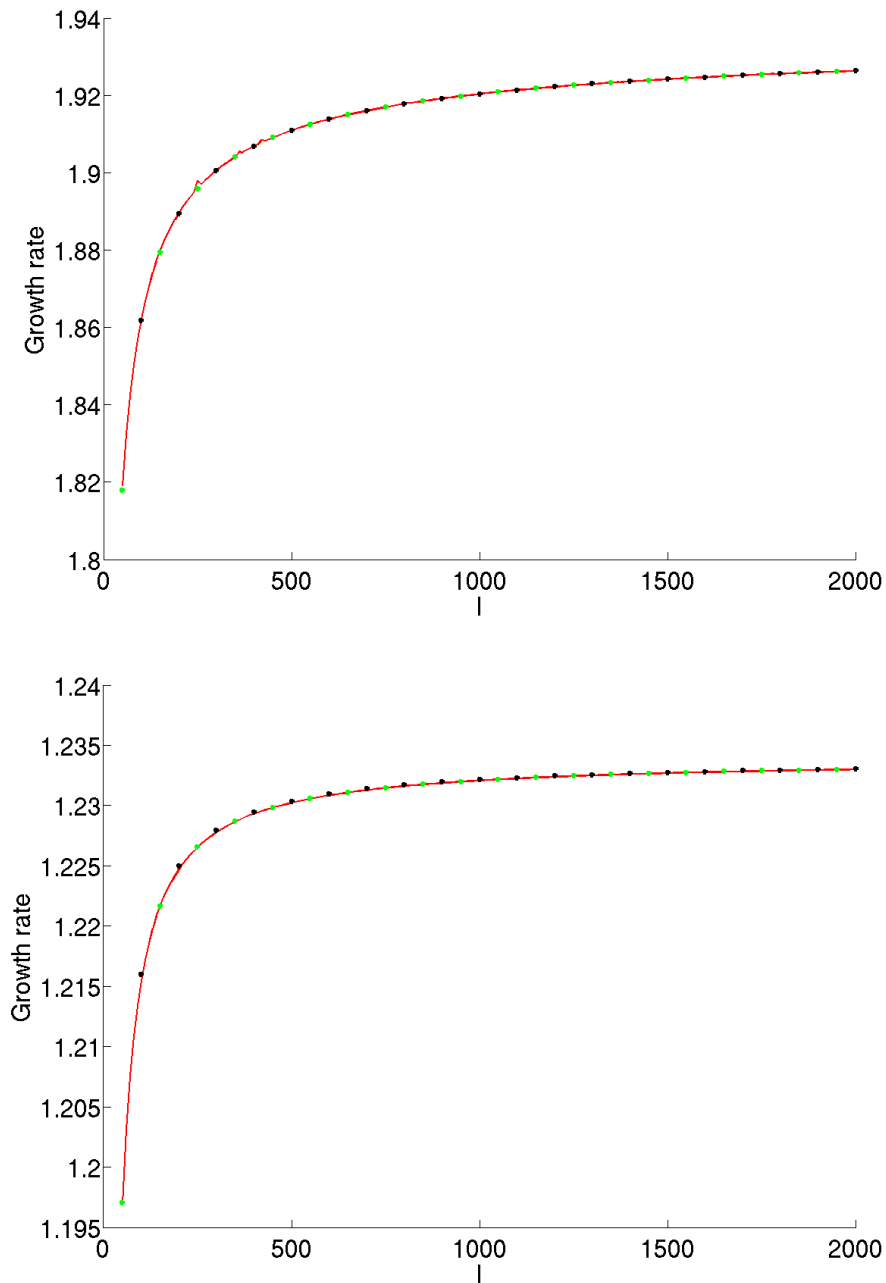
Figure 6.10: Growth rate versus wavenumber l for the wall mode (top) and body mode (bottom). In each plot the solid red line represents the solution to the full boundary value problem (6.52), the black dots represent the asymptotic growth rate obtained when $l^2/Pe \sim 1$, and the green dots represent the asymptotic growth rate obtained when $l^2/Pe \gg 1$.

6.4   Magnetic diffusion

In the presence of only magnetic diffusion, the linear set of governing equations from (3.61) are;

$$\boldsymbol{\nabla} \cdot \boldsymbol{u} = 0, \tag{6.77a}$$

$$\boldsymbol{\nabla} \cdot \boldsymbol{b} = 0, \tag{6.77b}$$

$$\left(\frac{\partial}{\partial t} + U \frac{\partial}{\partial x} \right) \boldsymbol{u} + \boldsymbol{U}' w = -\boldsymbol{\nabla}_\perp \Pi + \left(T + B b_x \right) \hat{\boldsymbol{z}}$$

$$+ B \frac{\partial \boldsymbol{b}}{\partial x} + \boldsymbol{B}' b_z, \tag{6.77c}$$

$$\left(\frac{\partial}{\partial t} + U \frac{\partial}{\partial x} \right) \boldsymbol{b} + \boldsymbol{B}' w = B \frac{\partial \boldsymbol{u}}{\partial x} + \boldsymbol{U}' b_z + \frac{1}{Rm} \nabla_\perp^2 \boldsymbol{b}, \tag{6.77d}$$

$$\left(\frac{\partial}{\partial t} + U \frac{\partial}{\partial x} \right) \left(T + DB b_x \right) = -\beta w. \tag{6.77e}$$

where $\nabla_\perp^2 = \partial_{zz} + \partial_{yy}$. As shown in the appendix E, we can reduce our system of equations (6.77) to four second order ordinary differential equations

$$\alpha_{\eta 1} w'' + \alpha_{\eta 2} w + \alpha_{\eta 3} b_y + \alpha_{\eta 4} b_y' + \alpha_{\eta 5} b_x + \alpha_{\eta 6} b_x' + \alpha_{\eta 7} b_z + \alpha_{\eta 8} b_z' = 0, \tag{6.78a}$$

$$\frac{1}{Rm} b_x'' + \alpha_{\eta 9} b_x + \alpha_{\eta 10} b_z + \alpha_{\eta 11} w = 0, \tag{6.78b}$$

$$\frac{1}{Rm} b_y'' + \alpha_{\eta 12} b_y + \alpha_{\eta 13} b_x + \alpha_{\eta 14} b_z + \alpha_{\eta 15} w + \alpha_{\eta 16} w' = 0, \tag{6.78c}$$

$$\frac{1}{Rm} b_z'' + \alpha_{\eta 17} b_z + \alpha_{\eta 18} w = 0, \tag{6.78d}$$

where the $\alpha_{\eta i}$ coefficients are also given in appendix E. These equations can be solved subject to the impermeable boundary condition on the vertical velocity w at both boundaries, and six other boundary conditions, two for each component of the magnetic field b. Unfortunately, equations (6.78) are too complicated to reduce to a single differential equation. Therefore, unlike in the previous two sections in this chapter, which focused on viscous and thermal diffusion individually, we are not able to progress very far analytically. We can however comment on the leading order growth rate for the wall modes. In all our previous work on short-wavelength instability, an equation for the leading order eigenvalue is obtained by assuming l is large and ignoring

all z derivatives on perturbed quantities. Suppose we apply this logic to our system of governing equations (6.78) for two different magnitudes of l^2/Rm: $l^2/Rm \sim 1$ and $l^2/Rm \ll 1$. Writing the eigenvalue as $\omega = \omega_0 + o(1)$ and expanding basic state quantities about a point z_η, the leading order eigenvalue for $l^2/Rm \sim 1$ becomes

$$\bar{\omega}_0^5 - \frac{2il^2}{Rm}\bar{\omega}_0^4 - \left(F + k^2 B^2 + \frac{l^4}{Rm^2}\right)\bar{\omega}_0^3 + \frac{il^2}{Rm}\left(2F - \frac{BB'}{\gamma}\right)\bar{\omega}_0^2$$

$$+ \left(k^2 B^2 F + \frac{ikB^2 U'l^2}{\gamma Rm} + \frac{\beta l^4}{Rm^2}\right)\bar{\omega}_0 - \frac{ik^2 \beta B^2 l^2}{Rm} = 0. \qquad (6.79)$$

Similarly, when $l^2/Rm \ll 1$ we obtain

$$\left(\bar{\omega}_0^2 - F\right)\left(\bar{\omega}_0^2 - k^2 B^2\right) = 0. \qquad (6.80)$$

As we are only interested in instability ($\bar{\omega}_0^2 \neq k^2 B^2$), (6.80) reduces to

$$\bar{\omega}_0^2 = F. \qquad (6.81)$$

As previously discussed, these equations can only give the leading order growth rate for a wall mode; we would require an extra equation for z_η in order to determine the growth rate of the body mode. Equations (6.79) and (6.81) are analogous to (6.7) and (6.21), in the sense that when $l^2/Rm \sim 1$, the magnetic diffusivity influences the leading order growth rate and when $l^2/Rm \ll 1$, magnetic diffusion has no influence. Because of this we can derive similar results to those seen in §6.2. Suppose we first look at the interchange wall mode. For an unstable mode, equation (6.79) becomes

$$\omega^4 - \frac{2il^2}{Rm}\omega^3 - \left(F_0 + \frac{l^4}{Rm^2}\right)\omega^2 + \frac{il^2}{Rm}\left(2F_0 - \frac{BB'}{\gamma}\right)\omega + \frac{\beta l^4}{Rm^2} = 0, \qquad (6.82)$$

where $F_0 = F|_{k=0}$, and (6.81) becomes

$$\omega^2 = F_0. \qquad (6.83)$$

For all values of l^2/Rm the growth rate obtained from (6.82) will be smaller than that from (6.83). Therefore we know that the interchange wall modes that exist for values of l such that $l^2/Rm \ll 1$ will be more unstable than those with wavenumbers such that $l^2/Rm \sim 1$. This is exactly what we found in §6.2.5; the most unstable wall interchange mode was present for wavenumbers where $l^2/Re \ll 1$, or, more specifically, $l \sim Re^{3/8}$.
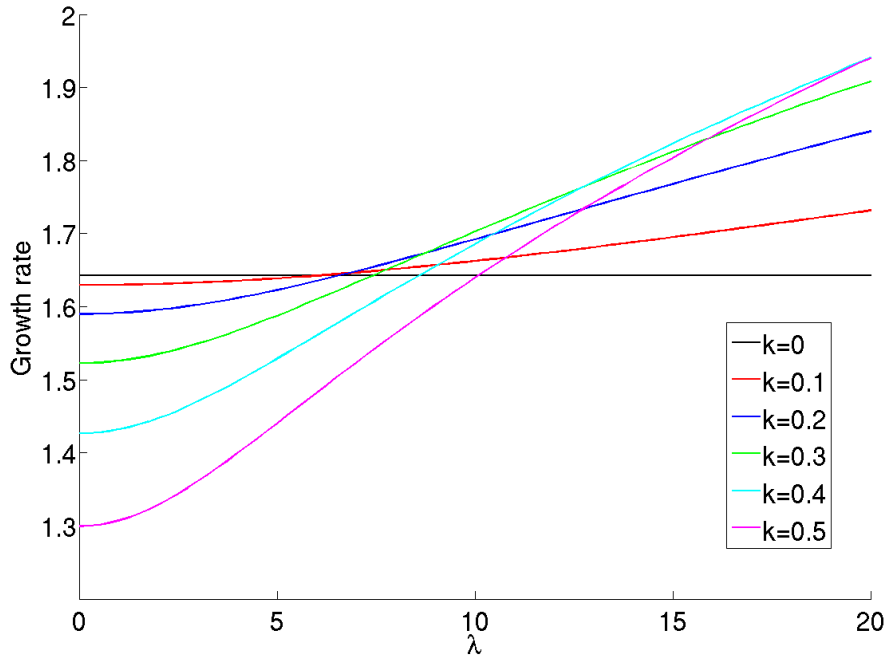
Figure 6.11: Leading order growth rate from (6.79) versus shear gradient λ. This plot is obtained using parameter values $P_{\eta 1}$ (6.84), fixing $l^2/Rm = 1$ and using a linear shear profile $U = \lambda(1 - z)$.

Equations (6.79) and (6.81) also provide us with some insight into the undular wall mode. We have seen before how the leading order growth rate from (6.81) is unaffected by the shear flow for a real value of z_η, and that the most unstable mode is the interchange mode. However, when $l^2/Rm \sim 1$, the magnetic diffusion and velocity shear can now play a role in destabilising the undular mode. Figure 6.11 plots the leading order growth rate obtained from (6.79) versus the shear gradient λ, for velocity shear $U = \lambda(1 - z)$, $l^2/Rm = 1$ and parameter values

$$P_{\eta 1} : \quad \alpha = 0.1, \ \hat{\beta} = 0.1, \ \zeta = 1.5. \tag{6.84}$$

Here we find the same result as found in §6.2.5; for a velocity shear of sufficient gradient, the undular mode becomes more unstable than the interchange for values of l such that $l^2/Rm \sim 1$. To test our analytic prediction we proceed by solving the system of equations (6.78) numerically.

6.4.1   Numerical results

To study the effects of magnetic diffusion on the instability we use the inverse iteration method to solve equations (6.78) subject to perfectly conducting boundary conditions on the magnetic field perturbations, i.e. $b'_x = b'_y = b_z = 0$, and the impermeability condition on the vertical velocity $w = 0$ at both boundaries. Fixing the magnetic Reynolds number at $Rm = 10^4$, we look for wall modes by taking a linear velocity shear $U = \lambda \left(1 - z\right)$ and $P_{\eta 1}$ from (6.84). This shear profile, the parameter values and the magnitude of the magnetic Reynolds number are directly analogous to those used to obtain the numerical results in §6.2.5. Figure 6.12 shows the growth rate versus l for these parameter values, at different values of λ. This figure confirms what we previously discussed; the most unstable wall mode in the absence of shear is the interchange mode and this mode appears around $l \approx 30$. For this value of l and magnetic Reynolds number we have $l^2/Rm \approx 0.09$, which is definitely less than 1, and furthermore when $Rm = 10^4$, $Rm^{3/8} \approx 0.09$. Therefore, with the knowledge gained from §6.2, this result suggests that the most unstable interchange wall mode will exist for a value of l around $l \sim Rm^{3/8}$. As the gradient of the shear is increased to $\lambda = 10$, the interchange mode is no longer the most unstable mode of the system. There now exists a more unstable undular mode, which appears for values of l around $l^2/Rm \sim 1$. This is what we expected to find from the analysis and suggests that both magnetic diffusion and viscosity play similar roles in the instability.

It appears that the body mode in the presence of only magnetic diffusion behaves similarly to the case when only viscous diffusion is present. For certain shear profiles there does exist a body mode, however we have yet to find a case where the body mode is more unstable than the wall mode.
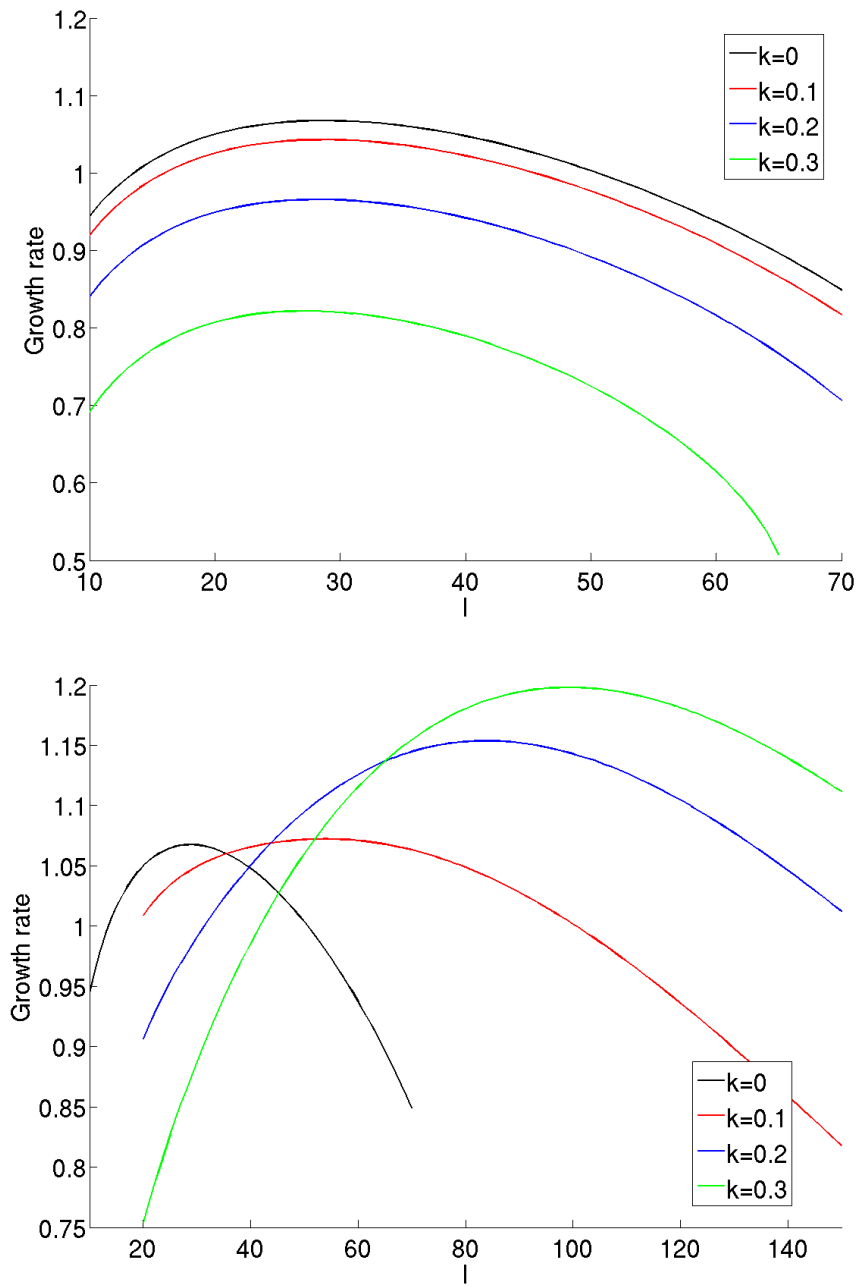
Figure 6.12: Growth rate versus wavenumber l obtained from (6.78) for shear strengths $\lambda = 0$ (top) and $\lambda = 10$ (bottom). Each figure uses parameter values $P_{\eta 1}$ (6.84), $Rm = 10^4$ and shear profile $U = \lambda(1 - z)$.

6.5 Discussion

The aim of this chapter is to bridge the gap between Chapter 5, which studies the effects of velocity shear on the short-wavelength magnetic buoyancy instability in the absence of diffusion, and Chapter 7, which contains results to the full system of equations (3.61) including all diffusive effects. In Chapter 5 it was shown that the shear has a big influence on the undular modes. An undular mode in the absence of shear that was localised at the bottom of the layer, could in fact be changed to a body mode for a shear profile maximised in the layer. Unfortunately, the addition of shear always had a stabilising effect and we could not find a shear profile in which these undular modes were more unstable than the interchange wall mode. Therefore, at least in the absence of diffusion, it appeared that the velocity shear would have no influence on the preferred mode of instability.

When considering only the effects of viscosity we split our analysis into two distinct parts depending on the relative size of l to the kinematic viscosity, $l^2/Re \sim 1$ and $l^2/Re = o(1)$. The most unstable wall mode in the absence of a velocity shear is indeed still an interchange mode and always appears in the region where $l \sim Re^{3/8}$. However, the addition of viscosity allows the velocity shear to have a destabilising effect on the growth rate in the region where $l \sim Re^{1/2}$. Therefore for a sufficiently large velocity shear the most unstable wall mode can be an undular mode. Thus shear certainly plays an influential role on the instability. We were not able to find a velocity shear profile in which the most unstable mode of the system was the body mode, however that does not necessarily mean it is not possible.

The role of magnetic diffusion on the system acts in a similar manner to that of viscosity, in that it allows the velocity shear to have a destabilising effect on the wall mode. Thermal diffusion on the other hand does not have this effect. As we have mentioned, for a given atmosphere the instability is more readily achieved as $\kappa \to \infty$. Therefore the system in the presence of just thermal diffusion wants to be in a state such that $l^2/Pe \gg 1$, in order to enhance thermal diffusion. In this limit we revert to a similar system of equations found in Chapter 5, in which viscosity plays no role in the preferred mode of instability.

This chapter has shown a contrast between the preferred mode of instability when just

viscosity (or magnetic diffusion) is present, to when just thermal diffusion is present. When considering viscosity the shear can have a destabilising role, whereas the shear is always stabilizing when we only consider thermal diffusion. In the next chapter we will solve the full system of equations (3.61) numerically and investigate how the instability acts when all diffusive effects are considered simultaneously.

Chapter 7

Linear solutions to the magneto-Boussinesq equations with velocity shear

7.1 Introduction

In Chapter 3 we derived a set of equations that consistently incorporate the effects of a velocity shear into the magneto-Boussinesq equations. These equations were derived with the intent of being used to study the magnetic buoyancy instability, the mechanism likely responsible for the break up of a strong toroidal magnetic field stored in the tachocline. Up to this point we have solved 'incomplete' versions of these equations, in order to gain a better insight into the problem. When neglecting all diffusive terms in the equations, the preferred mode of instability is always an interchange mode, with a large wavenumber l perpendicular to the imposed field. For a linear basic state magnetic field that decreases with height, the bulk structure of this mode will be located near the boundary and the velocity shear does not contribute to the growth rate. In the previous chapter we introduced the effects of diffusion individually, whilst still adopting the large l limit. When considering only the effects of thermal diffusion the system preferred to be in an isothermal state, with the temperature perturbation taking a constant value across

the layer. In this case, the thermal diffusion never plays a role in the instability, resulting in a system very similar to that considered in Chapter 5, with the interchange wall mode always being the most dominant and with the velocity shear altering only the frequency of the mode. However, by introducing the effects of either viscosity or magnetic diffusion we found a regime of l in which the velocity shear gradient can have a destabilising effect on the buoyancy instability. Specifically, for values of l such that $l \sim Re^{1/2}$ or $l \sim Rm^{1/2}$, the velocity shear gradient U', evaluated at the boundary, could destabilise the mode to the point where an undular mode becomes the dominant mode of the system. Again, the bulk structure of this mode is located at the bottom boundary. It is possible that for certain shear configurations a body mode could be the most unstable mode of the system. However, for the shear profiles and parameter values tested, we have never found this to be the case.

Of course, as we saw in §6.4, there is only so far one can go analytically. This chapter aims to solve the newly derived equations numerically, whilst including all the diffusive parameters. This gives us the chance to gain an insight into the whole picture, in which all diffusive terms play a role in the instability. The chapter will be split into two main sections. In §7.2 we focus on the numerical results to equations (3.61) in the absence of velocity shear. Guided from our previous results we expect the most unstable mode of this system always to be the interchange wall mode, with increasing field gradient destabilising the mode. In §7.3 we will introduce the velocity shear back into our equations; we will consider different shear profiles, and how the relative magnitude of the field gradient to the velocity shear affects the instability. Throughout both sections we will comment on the role of the diffusive parameters and investigate how varying them influences the instability.

Physically speaking, it would be ideal to solve the governing equations with diffusive parameter values that mirror those found in the tachocline. However, using (3.63) with estimated values $U_* = 30\text{ms}^{-1}$, $d = 2 \times 10^7\text{m}$ and parameter values given in Table 1.1, approximations for the non-dimensional parameters in the tachocline become

$$Re \approx 1 \times 10^{11}, \quad Rm \approx 7 \times 10^9, \quad Pe \approx 2 \times 10^5. \tag{7.1}$$

Due to computational limitations, we can never reach such extremely large parameter

values in our solutions. Instead, throughout this chapter we enforce an ordering such that $Re \gtrsim Rm$ and $Re, Rm \gg Pe$. This ensures that for whatever diffusive values we choice, we still remain somewhat physically relevant, since $\eta/\kappa \ll 1$, $\nu/\kappa \ll 1$ and $\nu \lesssim \eta$.

When including the effects of diffusion we are forced to satisfy equations 3.32b and 3.32c for our basic state magnetic field and temperature. After following the non-dimensional process described in §3.2.4, these equations become

$$\frac{\mathrm{d}^2 B_0}{\mathrm{d}z^2} = 0, \tag{7.2a}$$

$$\frac{\mathrm{d}^2 T_0}{\mathrm{d}z^2} = -D\,Pe \left[\frac{1}{Rm} \left(\frac{\mathrm{d}B_0}{\mathrm{d}z} \right)^2 + \frac{1}{Re} \left(\frac{\mathrm{d}U_0}{\mathrm{d}z} \right)^2 \right]. \tag{7.2b}$$

Equation (7.2a) is satisfied for a linear magnetic field, for which we keep the same field as used in previous chapters,

$$B_0 = 1 + \zeta\,(1 - z). \tag{7.3}$$

Throughout this chapter we will introduce several different velocity shear profiles in order to show their impact on the instability. Therefore the basic state temperature T_0 must be derived on a case by case basis, depending on the shear profile used. Due to the extreme parameter values of the tachocline, we can assume the right hand side of (7.2b) is small. Therefore we expect the basic state temperature to be almost linear. Since the basic state temperature enters into our definition of the subadiabatic temperature gradient β (equation (3.69)), we also must re-evaluate this for every shear profile used. The impact of these changes on β are minimal, since the temperature gradient T_0' is always $\mathrm{O}\,(Pe/Rm)$, which in all cases considered is small.

To solve the system of governing equations we use the inverse iteration method (appendix B) subject to a set of boundary conditions on the perturbations. Throughout this chapter we assume the boundaries are perfectly conducting, thus the boundary conditions for the magnetic field perturbations become $b_x' = b_y' = b_z = 0$ at $z = 0$ and $z = 1$. We will also fix the perturbation of temperature at the bottom boundary and fix the flux at the top, therefore taking $T = 0$ at $z = 0$ and $T' = 0$ at $z = 1$. Applying these same boundary conditions to the basic state temperature ensures that the background

atmosphere is stable to convection. Regarding the velocity perturbations, we will address both stress-free and no-slip boundary conditions and comment on the influence of each on the instability.

7.2 Magnetic buoyancy with an $O\left(1/d\right)$ field gradient, in the absence of velocity shear

As discussed throughout this thesis, equations (3.61) can be used to study magnetic buoyancy instability with an $O\left(1/d\right)$ magnetic field gradient, in the absence of velocity shear; the linearised governing equations used in this section are:

$$\boldsymbol{\nabla} \cdot \boldsymbol{u} = 0, \tag{7.4a}$$

$$\boldsymbol{\nabla} \cdot \boldsymbol{b} = 0, \tag{7.4b}$$

$$\frac{\partial \boldsymbol{u}}{\partial t} = -\boldsymbol{\nabla}_{\perp}\Pi + \left(T + B_0 b_x\right)\hat{\boldsymbol{z}}$$
$$+ B_0\frac{\partial \boldsymbol{b}}{\partial x} + \boldsymbol{B}'_0 b_z + \frac{1}{Re}\nabla_{\perp}^2 \boldsymbol{u}, \tag{7.4c}$$

$$\frac{\partial \boldsymbol{b}}{\partial t} + \boldsymbol{B}'_0 w = B_0\frac{\partial \boldsymbol{u}}{\partial x} + \frac{1}{Rm}\nabla_{\perp}^2 \boldsymbol{b}, \tag{7.4d}$$

$$\frac{\partial}{\partial t}\left(T + DB_0 b_x\right) = -w\beta + \frac{1}{Pe}\nabla_{\perp}^2 T$$
$$+ D\frac{1}{Rm}\left(2B'_0\frac{\partial b_x}{\partial z}\right), \tag{7.4e}$$

where $\beta = \hat{\beta} + \beta_0$ and $\nabla_{\perp}^2 = \partial_{zz} + \partial_{yy}$. We have seen in Chapter 5, that when neglecting the effects of diffusion the most unstable mode of this system will always be an interchange wall mode. By including the effects of viscosity and magnetic diffusion individually, as done in Chapter 6, it appears that the most unstable interchange mode is located for values of l such that $l \sim Re^{3/8}$ and $l \sim Rm^{3/8}$ respectively. At this point it is not clear exactly what form the most unstable mode will take when all diffusive parameters are competing with each other to act on the instability. To investigate this question, we split this section into three parts. In §7.2.1 we focus on the role of the magnetic field gradient ζ on the system, for fixed diffusion parameter values. This will

give us an idea of the structure of most unstable mode and how the field gradient impacts the instability. In §7.2.2 we vary the diffusive parameters so as to gain an understanding of how each affects the instability. Finally in §7.2.3 we expand upon what we found in §7.2.2 and look at the preferred mode of instability for the astrophysically relevant system.

7.2.1   The role of the field gradient

In §5.2 we derived an instability criteria for the diffusionless system in the large l limit, given by equation (5.8). This criteria states that for a given atmospheric configuration, instability is achieved when the magnetic field decreases sufficiently with height. We also note that in this limit, the instability is governed by the function made up of basic state quantities, $F = k^2 B_0^2 + \beta + B_0 B_0'/\gamma$, in which the magnitude of the growth rate corresponds to the most negative value of F. Specifically, the growth rate increases as we decrease the minimum value of F. For a linear magnetic field of the form (7.3), the function F becomes smaller for increasing values of ζ, and is minimised when $k = 0$. Thus by increasing the field gradient term ζ, we know that in the large l limit all modes become more unstable, and that the most unstable mode is always the interchange mode. When introducing only the effects of thermal diffusion in §6.3, we saw how the system wanted to revert to a case similar to that of §5.2, where the growth rate is governed by the function G, which behaves similar to F. Therefore, increasing ζ would also destabilise the mode. When considering the effects of introducing only viscosity in §6.2, the most unstable mode in the absence of shear occurs for values of l such that $l \sim Re^{3/8}$. In this limit, the leading order growth rate is unaffected by viscosity, and is in fact exactly the same as derived in §5.2. Therefore, increasing ζ would again only destabilise the mode, with the most unstable mode remaining the interchange mode. Since the same result holds in §6.4, there is no reason to expect ζ to play a different role in the instability when all diffusive parameters are present.

To determine the role of the magnetic field gradient on the instability we introduce the set of parameter values

$$P_3 : \quad \hat{\beta} = 0.2, \quad Re = 10^4, \quad Rm = 10^3 \quad Pe = 10^{-2}, \tag{7.5}$$

and solve the governing equations (7.4) subject to stress-free boundary conditions on the velocity perturbations, $u' = v' = w = 0$ at $z = 0$ and $z = 1$. Figure 7.1 plots the growth rate versus wave number l for different values of k. Here we can confirm that increasing the field gradient ζ does indeed destabilise the mode, and that the most unstable mode in all cases is the interchange mode. The field gradient also plays a role in determining the location in l of the dominant mode; increasing ζ moves the most unstable mode to a higher value of l. Figure 7.2 shows a plot of the eigenfunctions for the most unstable mode for $\zeta = 1.5$, found for wavenumbers $l = 13$, $k = 0$ and eigenvalue $\omega \approx -1.55i$. As in previous sections, all eigenvectors have been normalised such that the maximum value of the real part of w is one. The first thing to notice about this mode is that the magnitude of the temperature perturbation is essentially zero (10^{-6}). This implies that thermal diffusion plays no role in the instability. The structure of the other eigenfunctions suggests that this mode is what we would refer to as a wall mode. However, for such a small value of l it is very difficult to distinguish between the wall and body modes. In §7.2.2 we will consider larger Reynolds and magnetic Reynolds numbers, which force the most unstable mode to higher values of l. Thus we will continue the discussion of the structure of the most unstable mode when we address larger values of l.

In Chapter 6 we noticed that the choice of boundary conditions had little impact on the growth rate for both the wall and body modes. Figure 7.3 shows the eigenvectors of the system solved under no-slip boundary conditions, for the same parameter values used in Figure 7.2. Comparing these two figures we can see that the bulk of the mode is nearly identical; however, there exists an extremely sharp boundary layer for v in Figure 7.3. To ensure the inverse iteration method has satisfied the boundary conditions correctly we include Figure 7.4, which shows an enlarged version of the visible boundary layer for v and includes the points used by the solver. The boundary layer seen here is exactly what we witnessed in Chapter 6 when satisfying the no-slip boundary conditions for the wall mode. The eigenvalue for this mode is $\omega \approx -1.55i$, the same value as obtained when solving for the stress-free boundary conditions. Therefore the choice of boundary conditions has little impact on the growth rate and overall structure of the mode.
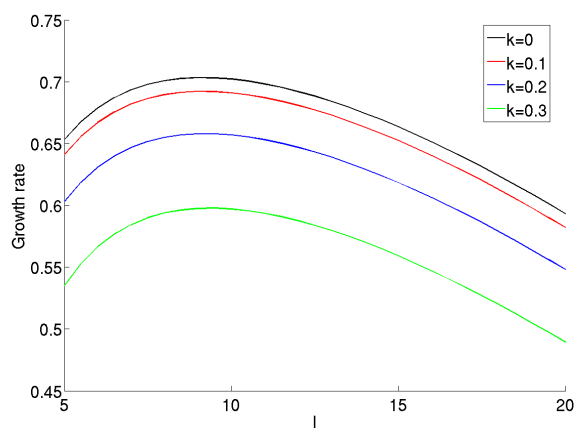
(a)
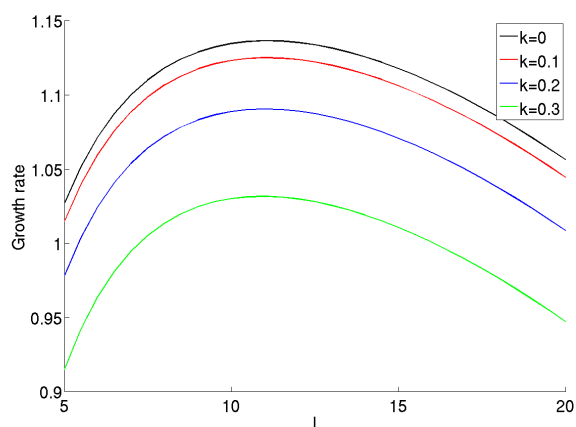
(b)
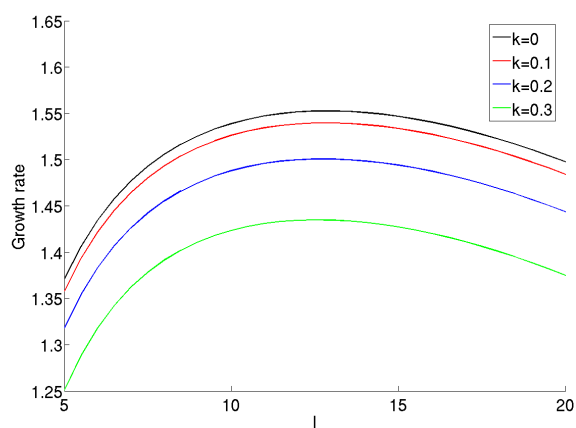
(c)

Figure 7.1: Growth rate obtained from solving (7.4) versus wavenumber l, for magnetic field gradients (a) $\zeta = 0.5$, (b) $\zeta = 1$ and (c) $\zeta = 1.5$. Each figure uses parameter values P_3 defined in (7.5).
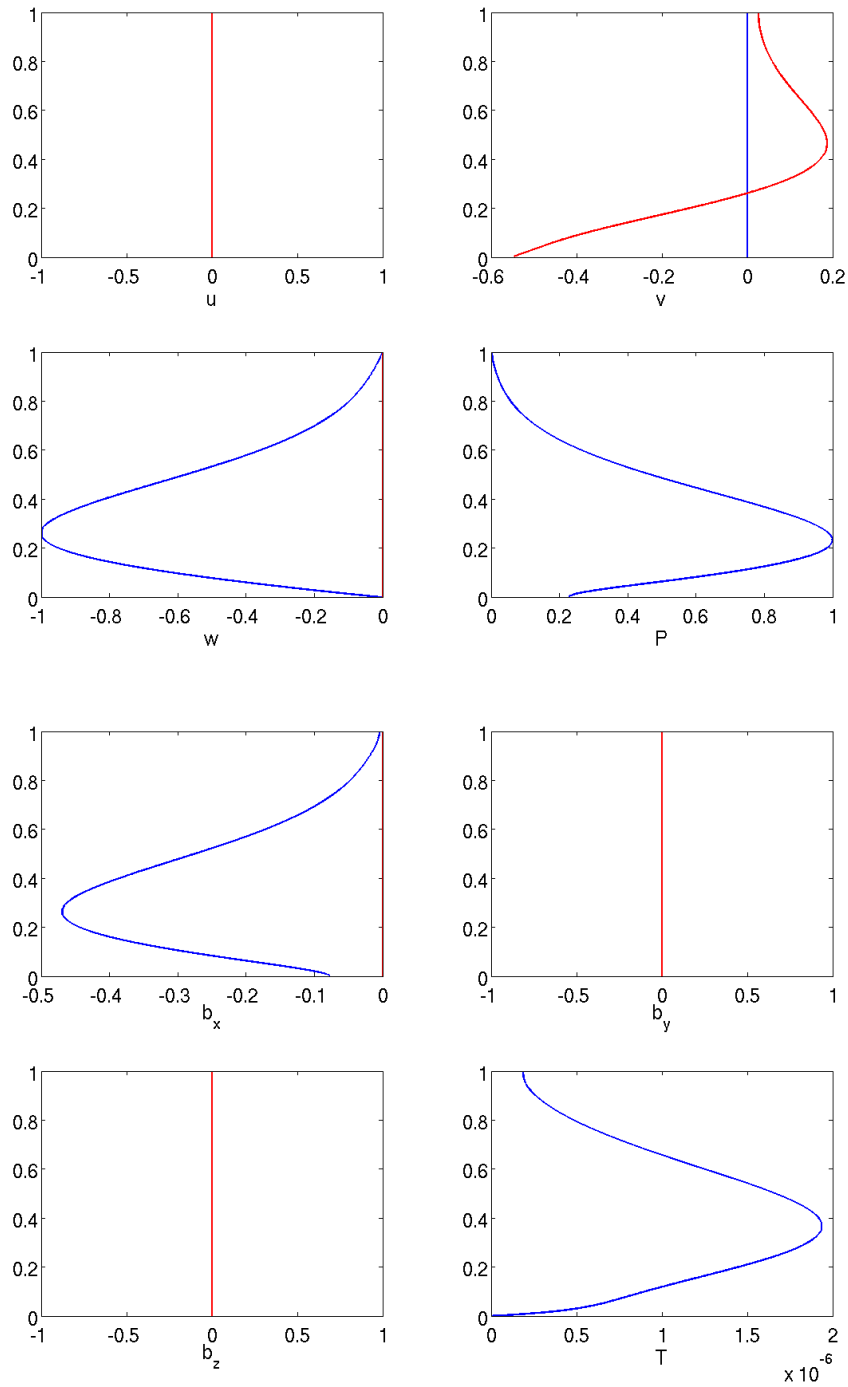
Figure 7.2: Eigenfunctions obtained with stress-free boundary conditions for the interchange mode taken at $l = 13$, with $\zeta = 1.5$ and parameter values P_3 (7.5). The blue line represents the real part of the eigenfunction, and the red the imaginary part.
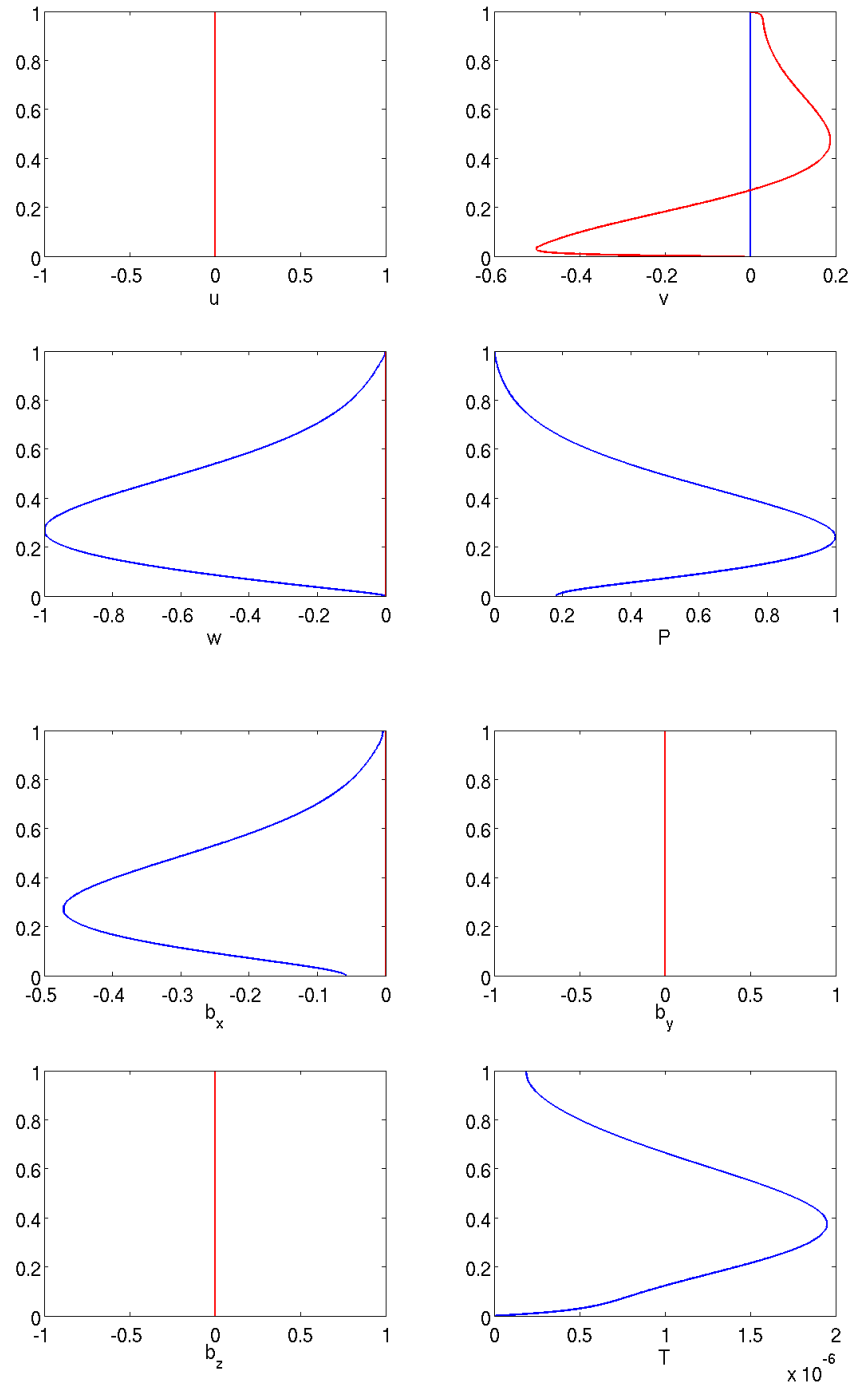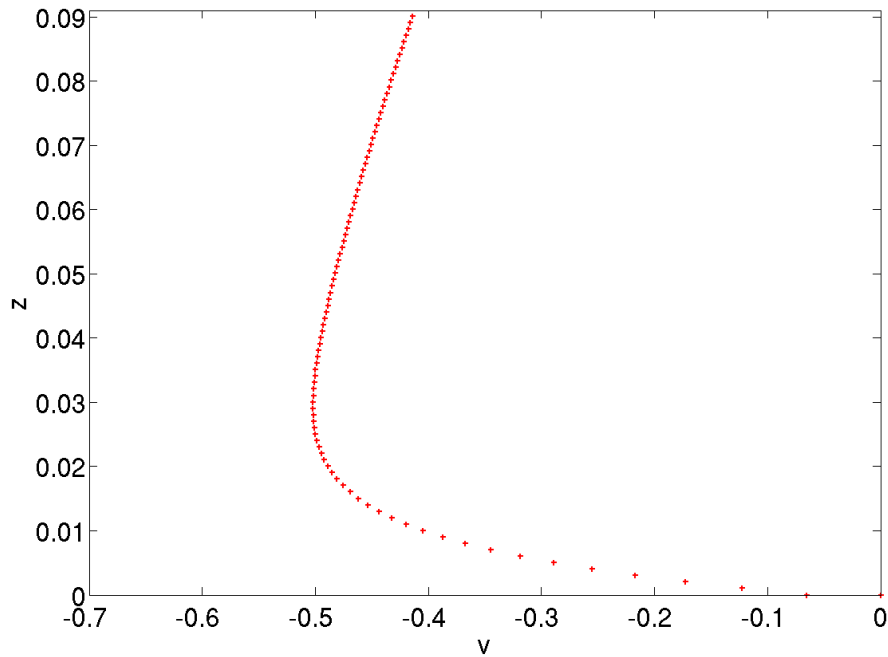
Figure 7.3: Eigenfunctions obtained with no-slip boundary conditions for the interchange mode taken at $l = 13$, with $\zeta = 1.5$ and parameter values P_3 (7.5).

Figure 7.4: Close up picture of the boundary layer seen in Figure 7.3 for eigenfunction v. The red crosses represent the points used by the inverse iteration solver (appendix B).

7.2.2   The impact of diffusion

By varying each of the diffusive terms individually we aim to gain some insight into which of the diffusive parameters has the largest influence on the instability. All numerical results in this subsection have $\zeta = 1.5$, $\hat{\beta} = 0.2$ and $U = 0$.

Thermal diffusion

Retaining the same values for the Reynolds numbers as in §7.2.1, namely $Re = 10^4$ and $Rm = 10^3$, we look to vary Pe in order to understand its influence on the instability. Figure 7.5 shows a plot of the growth rate for the interchange mode at different magnitudes of Pe. Here we see that the Péclet number essentially plays no role in the instability. In Chapter 6 when looking at only the effects of just thermal diffusion, the
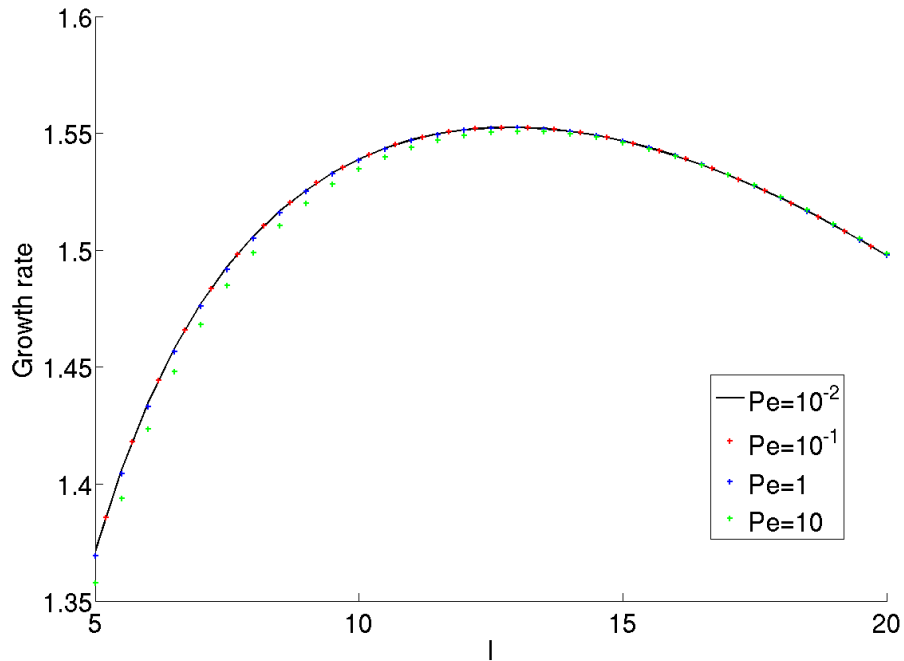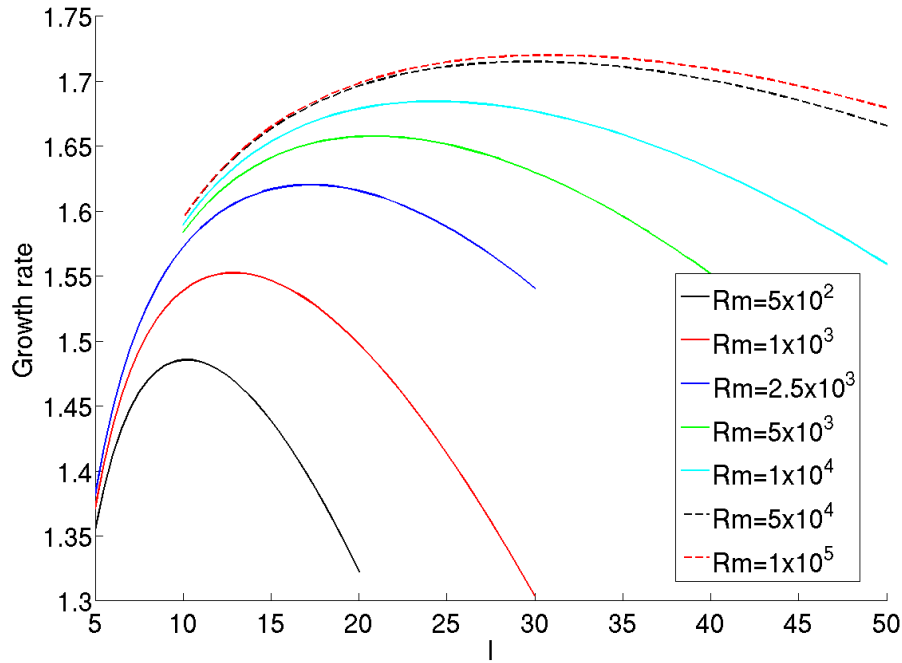
Figure 7.5: Growth rate of the interchange mode versus l for different magnitudes of Pélect number Pe. For this figure we fix $Re = 10^4$ and $Rm = 10^3$.

system prefers to be in the isothermal limit, with constant T throughout the layer. We also found that the most unstable mode in §7.2.1 has $T \approx 0$ everywhere. Therefore, the fact that Pe does not influence the instability is not entirely surprising. In §2.1.2 we presented instability criteria (equations (2.14) and (2.15)) for the magnetic buoyancy instability in the presence of an $O(1/H_P)$ magnetic field gradient, with thermal and magnetic diffusion. In these equations a crucial ratio that dictates the instability is η/κ, with a small η/κ favouring the instability. Since our criteria for stability of the diffusionless system derived in Chapter 4 is so similar to those found in Chapter 2, it is possible that a similar ratio of diffusive terms could play a role in our instability. In all cases considered we have $\eta/\kappa \ll 1$; if we take a larger κ such that $\eta/\kappa \sim 1$, we would expect the effects of thermal diffusion to influence the instability. However, this limit is not astrophysically relevant and therefore has not been considered.
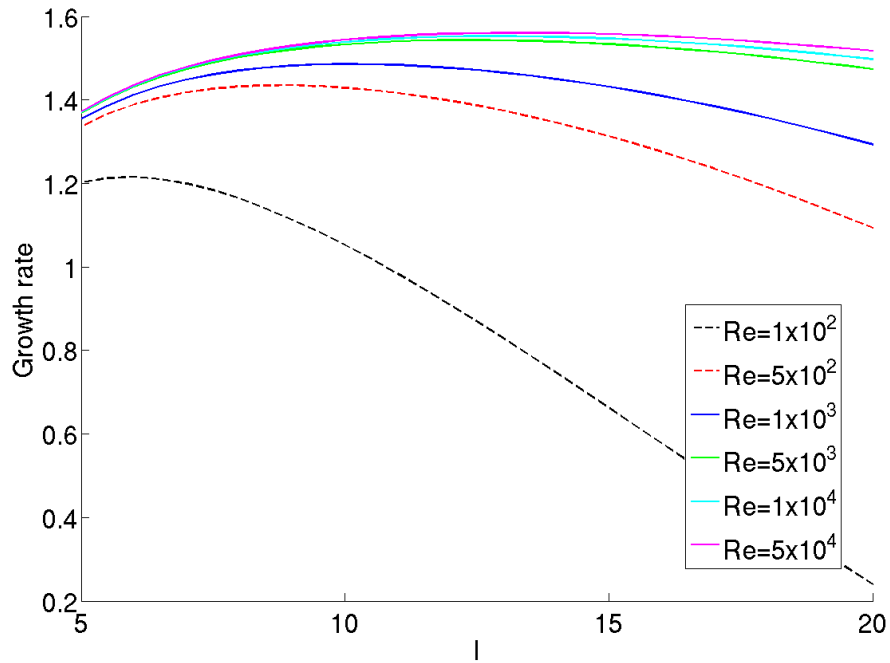
Figure 7.6: Growth rate of the interchange mode versus l for different magnitudes of magnetic Reynolds number Rm. For this figure we fix $Re = 10^4$ and $Pe = 10^{-2}$.

Magnetic diffusion

Let us now fix the Reynolds number at $Re = 10^4$ and the Péclet number at $Pe = 10^{-2}$ and vary the magnetic diffusivity η by considering different magnitudes of the magnetic Reynolds number. Figure 7.6 is a similar plot to Figure 7.5, this time for different values of Rm. Unlike the case of varying the thermal diffusion, the magnetic Reynolds number seems to play a big role in dictating the growth rate and the value of l associated with the most unstable mode. Increasing Rm past the point where $Rm = Re$ (displayed as dashed lines on the figure) has little effect on either the growth rate or the value of l. The reason for this is discussed in the following subsection on viscosity. However, since in stellar interiors we require $Rm \lesssim Re$, this is not too much of an issue astrophysically. Increasing the magnetic Reynolds number corresponds to a decrease in the magnetic diffusivity η. Therefore with our previous argument, that the ratio η/κ may play a significant role on the instability, it is not surprising that increasing the magnetic Reynolds

Figure 7.7: Growth rate of the interchange mode versus l for different magnitudes of Reynolds number Re. For this figure we fix $Rm = 10^3$ and $Pe = 10^{-2}$.

number leads to the mode becoming more unstable.

Viscosity

Finally we focus on the influence of viscosity, by fixing $Rm = 10^3$ and $Pe = 10^{-2}$, and varying the Reynolds number. Figure 7.7 shows a familiar figure of the growth rate of the interchange mode versus l, this time for different magnitudes of Re. Here we notice that when $Re \lesssim Rm$, the growth rate and the location of the most unstable mode is indeed influenced by viscosity, whereas for values of Re such that $Re > Rm$, changing the viscosity has little effect on the instability. This is somewhat of a reverse scenario from what we observed in Figure 7.6, when varying the magnetic diffusion. It would appear that the smallest of the two quantities, Re or Rm, essentially governs the instability. Hence when $Re > Rm$, changing the value of Re has little affect on the instability, and the instability is mainly influenced by the magnetic Reynolds number Rm. Similarly,

when $Rm > Re$, varying the magnetic Reynolds number has no affect on the instability and everything is governed by the Reynolds number Re. For the tachocline, $Re > Rm$, therefore the growth rate and the value of l at which the most unstable mode appears are mainly determined by the magnitude of Rm.

7.2.3   The dominant mode

In Chapter 6 we saw how the value of the wavenumber l associated with the most unstable mode is determined by the diffusion parameters. Specifically, when considering the effects of either viscosity or magnetic diffusion, the most unstable mode in the absence of a velocity shear is an interchange wall mode, appearing for values of l such that $l \sim Re^{3/8}$ or $l \sim Rm^{3/8}$ respectively. In §7.2.2 we observed that provided the orderings $Re \gtrsim Rm$ and $Re, Rm \gg Pe$ are maintained, the instability is essentially governed by the magnetic Reynolds number Rm. By keeping these orderings intact we will increase the magnetic Reynolds number and investigate its impact on the instability. For the numerical results in this subsection we take $\zeta = 1.5$, $\hat{\beta} = 0.2$ and consider three different relative magnitudes of the ratio Re/Rm, whilst fixing the Péclet number at $Pe = 10^{-2}$. This ratio of Re/Rm is otherwise known as the inverse magnetic Prandtl number, $Pm^{-1} = \eta/\nu$. Figure 7.8 contains three plots for when the ratio is $Re/Rm = 100$. This first of these shows the growth rate of the most unstable mode versus Rm. Here we see that the growth rate seems to be monotonically increasing as we increase Rm. The second figure plots the value of l corresponding to the most unstable mode versus Rm. As previously discussed, it appears that increasing the magnetic Reynolds number pushes the most unstable mode to a higher value of l. The final figure plots $\ln(l)$ versus $\ln(Rm)$ and provides us information on how the wavenumber of the most unstable mode scales with the Rm. Included on this plot is a red line with gradient $3/8$. It appears that when $Re/Rm = 100$, the preferred mode behaves in a similar fashion to that seen in Chapter 6: the most unstable mode in the absence of shear resides for values of l such that $l \sim Rm^{3/8}$. Figures 7.9 and 7.10 show similar pictures for different ratios, $Re/Rm = 10$ and $Re/Rm = 1$ respectively. Decreasing this ratio does not noticeably change the magnitude of the growth rate, certainly for larger values of Rm. It does however have a slight impact on the value

of l corresponding to the most unstable mode. However this is not enough to alter our conclusion that the most unstable mode appears when $l \sim Rm^{3/8}$.

In §7.2.1 we provided plots of the eigenfunctions for the most unstable mode of the system. However, since those results were derived using a relatively small magnetic Reynolds number, the resulting value of l was low. As a result we could not confidently conclude whether or not the most unstable mode of the system was a wall or a body mode. Figure 7.11 shows plots of the eigenfunctions of the most unstable mode for much larger diffusion parameter values, $Re = 10^6$, $Rm = 10^5$ and $Pe = 10^{-2}$, which using Figure 7.9b, corresponds to the mode with $l = 74$. Although still not a particularly large value of l, it is clear from this figure, that the mode is indeed a wall mode.
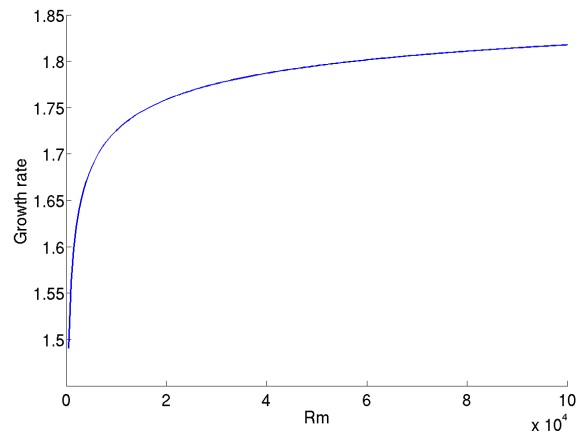
(a)
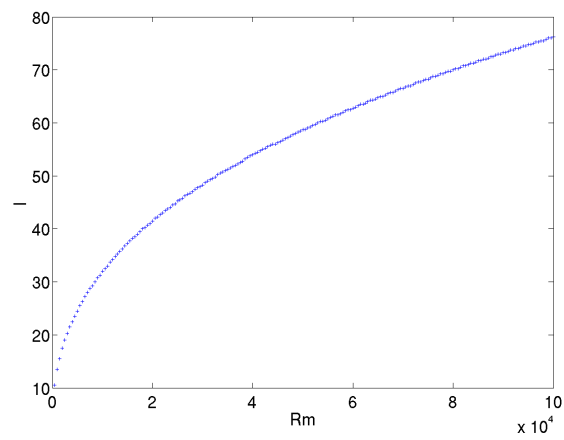
(b)
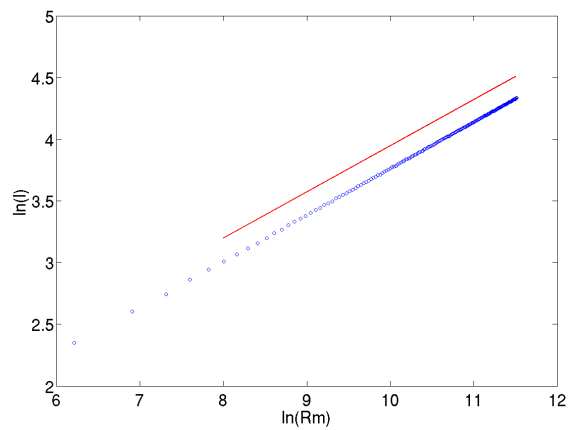
(c)

Figure 7.8: Plots of the most unstable mode for a given magnetic Reynolds number, with $Re/Rm = 100$, $Pe = 10^{-2}$, $\zeta = 1.5$ and $\hat{\beta} = 0.2$. (a) plots the growth rate versus Rm, (b) the value of l for the most unstable mode at a given Rm and (c) $\ln(l)$ versus $\ln(Rm)$. The red line in (c) is a line with gradient $3/8$.
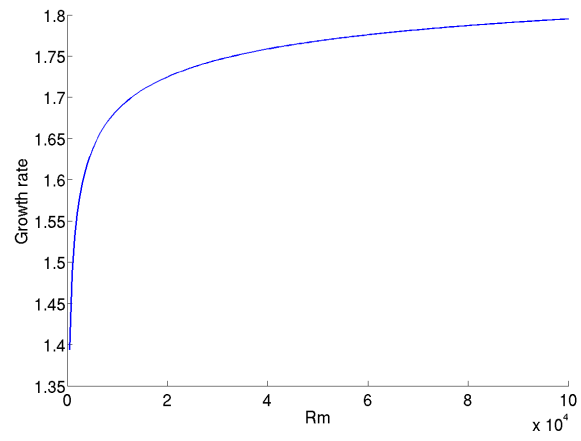
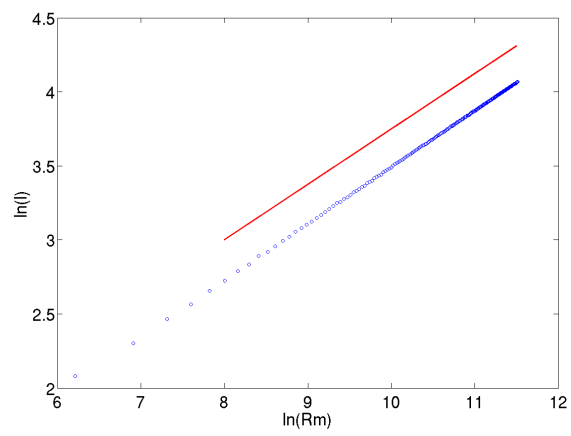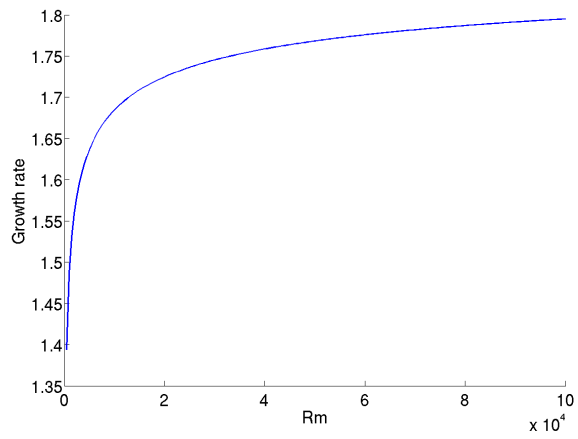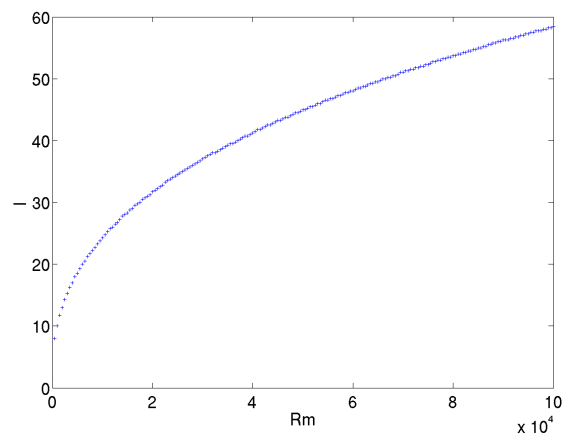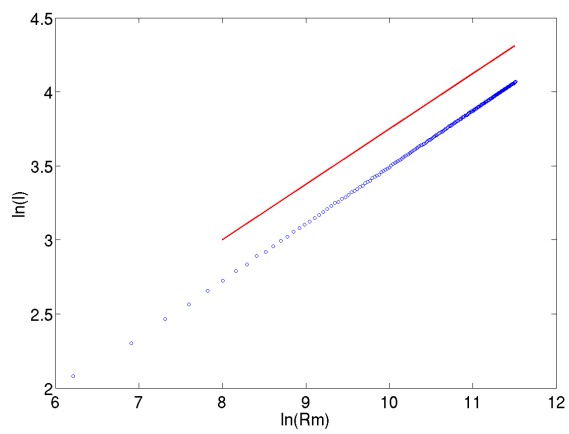(a)
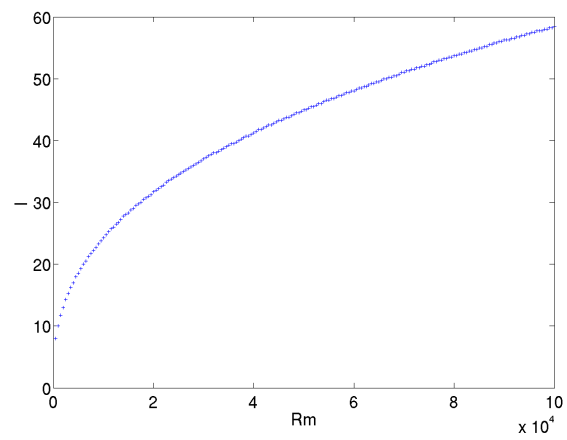
(b)

(c)

Figure 7.9: As Figure 7.8, with $Re/Rm = 10$.

(a)

(b)

(c)

Figure 7.10: As Figure 7.8, with $Re/Rm = 1$.
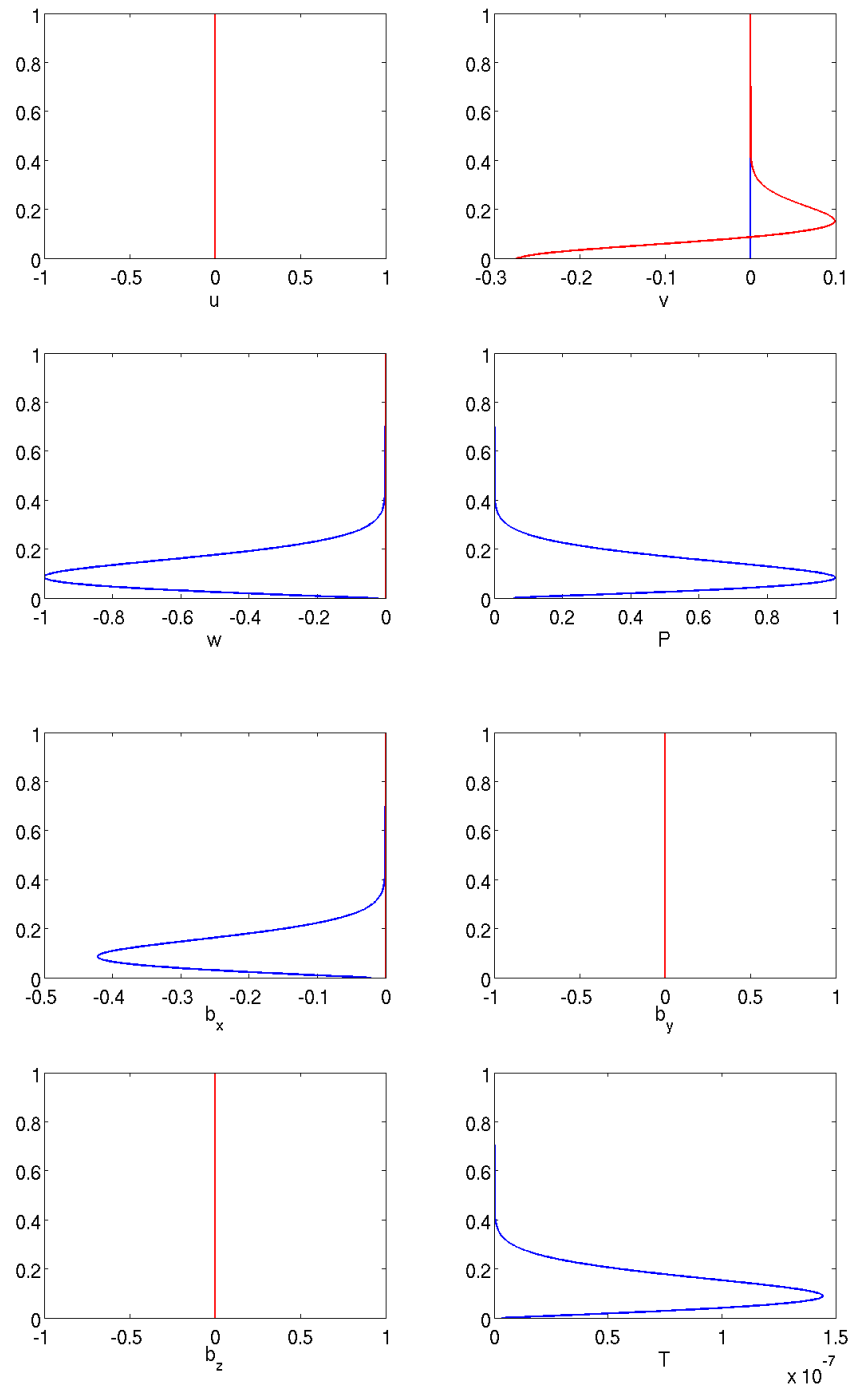
Figure 7.11: Eigenfunctions for the interchange mode taken at $l = 74$, with $\zeta = 1.5$, $\hat{\beta} = 0.2$ and diffusive parameter values $Re = 10^6$, $Rm = 10^5$ and $Pe = 10^{-2}$.

7.3   Velocity shear

In Chapter 6 we found that with the addition of either viscosity or magnetic diffusion, a wall mode for non-zero k can be destabilised by the introduction of velocity shear. The instability in this case is governed by the magnitude of the velocity shear gradient, evaluated at the same boundary at which the mode is localised. Furthermore, this undular mode can be destabilised sufficiently to the point at which it is more unstable than the interchange mode, and hence becomes the preferred mode of instability. Aided by the asymptotics we found that this undular mode could only be present for wavenumbers such that $l \sim Re^{1/2}$ and $l \sim Rm^{1/2}$, for viscosity and magnetic diffusion respectively. On top of this, the instability is only influenced by the value of U' at the boundary; therefore the exact form of the shear away from the boundary is irrelevant in determining the leading order growth rate. The boundary conditions of the system also have little influence on the instability. Building on the work in §7.2, we will re-introduce the effects of a velocity shear back into equations (3.61) in order to see if the above features are still present when all diffusive terms are competing against each other. Thus the linearised governing equations used in this section are:

$$\boldsymbol{\nabla} \cdot \boldsymbol{u} = 0, \tag{7.6a}$$

$$\boldsymbol{\nabla} \cdot \boldsymbol{b} = 0, \tag{7.6b}$$

$$\left(\frac{\partial}{\partial t} + U_0 \frac{\partial}{\partial x}\right) \boldsymbol{u} + \boldsymbol{U}_0' w = -\boldsymbol{\nabla}_\perp \Pi + (T + B_0 b_x)\, \hat{\boldsymbol{z}}$$
$$+ B_0 \frac{\partial \boldsymbol{b}}{\partial x} + \boldsymbol{B}_0' b_z + \frac{1}{Re} \nabla_\perp^2 \boldsymbol{u}, \tag{7.6c}$$

$$\left(\frac{\partial}{\partial t} + U_0 \frac{\partial}{\partial x}\right) \boldsymbol{b} + \boldsymbol{B}_0' w = B_0 \frac{\partial \boldsymbol{u}}{\partial x} + \boldsymbol{U}_0' b_z + \frac{1}{Rm} \nabla_\perp^2 \boldsymbol{b}, \tag{7.6d}$$

$$\left(\frac{\partial}{\partial t} + U_0 \frac{\partial}{\partial x}\right) (T + D B_0 b_x) = -w\beta + \frac{1}{Pe} \nabla_\perp^2 T$$
$$+ D \frac{1}{Rm} \left(2 B_0' \frac{\partial b_x}{\partial z}\right)$$
$$+ D \frac{1}{Re} \left(2 U_0' \frac{\partial u}{\partial z}\right), \tag{7.6e}$$

where $\beta = \hat{\beta} + \beta_0$ and $\nabla_\perp^2 = \partial_{zz} + \partial_{yy}$.

This section is split into three main parts. In §7.3.1 we fix the diffusive parameters to examine how changing the magnitude and profile of the shear affects the instability. We will also comment upon the role of the field gradient, as well as the impact of boundary conditions. In §7.3.2 we look at how varying the diffusive parameters alters instability. Finally, in §7.3.3, we look at the preferred mode of instability of the system.

7.3.1 The effects of a velocity shear

To study the effects of the velocity shear on the system we reuse parameter values (7.5) found in §7.2,

$$P_3 : \quad \hat{\beta} = 0.2, \quad Re = 10^4, \quad Rm = 10^3 \quad Pe = 10^{-2}. \tag{7.7}$$

At this stage we also fix the magnetic field gradient to $\zeta = 1.5$ and reintroduce the quadratic velocity shear

$$U_1 = \lambda_1 \left(z^2 - z + 1 \right). \tag{7.8}$$

Unless stated otherwise, all numerical solutions in this subsection are obtained by solving equations (7.6) with stress-free boundary conditions on the velocity perturbations, using the inverse iteration method. Figure 7.12 shows a familiar picture of growth rate versus l, plotted using different values of k. Here we see the same result as found in Chapter 6, namely that for a large enough value of λ_1 the undular mode becomes the dominant unstable mode. When $\lambda_1 = 20$, the most unstable mode has wavenumbers $l = 36$ and $k = 0.4$, with eigenvalue $\omega \approx -6.57 - 1.61i$; the eigenfunctions for this mode are shown in Figure 7.13. As with the most unstable mode in §7.2, the temperature perturbation is again essentially zero $(O\left(10^{-6}\right))$ and even for this relatively low value of l we would describe this mode as a wall mode, with the bulk of the eigenfunctions oscillating, contained within a peaked envelope.

Figure 7.14 is analogous to Figure 7.12c, but obtained using no-slip boundary conditions. As we concluded in Chapter 6, it appears that the choice of boundary conditions used to solve the problem has little influence on the growth rate of the mode. Figure 7.15 shows the eigenfunctions for the mode associated with $l = 36$, $k = 0.4$ and $\lambda_1 = 20$, solved

again using the no-slip boundary conditions. Comparing the eigenfunctions in Figure 7.15 to those in Figure 7.13, we observe that the bulk of the flow is nearly identical. As we have previously seen, there exists a thin, visible boundary layer on the bottom boundary, differentiating the two figures. The eigenvalue for this mode is $\omega = -6.50 - 1.59i$; thus both the bulk of the mode and the eigenvalue are almost unaffected by the choice of boundary conditions.

In Chapter 6 we derived expressions (6.7) and (6.79) for the leading order eigenvalue of the wall mode in the presence of either viscosity or magnetic diffusion respectively. The only term associated with the velocity shear that influences the growth rate in these expressions is U' evaluated at the same boundary at which the mode is peaked. It can be shown numerically that the sign of U' only alters the frequency of the mode. Hence the growth rate of the undular mode seen in Chapter 6 is dependent only on the magnitude of U' at the boundary. It may also be possible to derive this result straight from equations (6.7) and (6.79), however this is not attempted in this thesis. So far we have considered the velocity shear profile U_1 given in (7.8), and have found that the most unstable mode is located at the bottom boundary. Therefore we have $|U_1'(0)| = \lambda_1$, and by increasing λ_1 sufficiently the dominant mode switches from an interchange mode to an undular mode. However, increasing λ_1 not only changes the gradient at the bottom boundary, but also the magnitude of the shear. Thus it is not clear that when all diffusive terms are in play, whether it is again the gradient at the boundary, or instead the magnitude of the shear that is bringing out the undular mode. To examine this further we introduce a velocity shear of the form

$$U_2 = \lambda_2 \left(z^2 + 1 \right). \tag{7.9}$$

Here the gradient at the bottom boundary is always zero, and the magnitude of the shear is determined by λ_2. Figure 7.16 shows that increasing the magnitude of the shear has very little influence on the instability, and the most unstable mode of the system remains the interchange mode. These results have been obtained solving the full system subject to stress-free boundary conditions on the velocity perturbations. Comparing Figure 7.16b to Figure 7.16c, we see that increasing λ_2 does have a slight destabilising effect on the undular mode at $l \approx 40$, and it suggests that increasing λ_2 further would destabilise the

undular mode to the point that it is more unstable than the interchange mode. However, this is not the case; the slight destabilization of the undular mode is what we would refer to in Chapter 6 as the contribution from the next order correction (ω_1) to the leading order growth rate. Therefore, for more realistic, larger values of l this next order correction will never be large enough to dominate, and the undular mode will not become more unstable than the interchange mode. We have produced similar figures for shear magnitudes up to $\lambda_2 = 200$, and in all cases the interchange mode remains the most unstable mode. Therefore, as in Chapter 6, the wall mode in the full system is destabilised only by the shear gradient evaluated at the same boundary at which the mode is localised.

In §7.2.1 we studied the impact of the field gradient on the instability in the absence of a velocity shear. Increasing the field gradient ζ destabilises all the modes, and moves the most unstable mode to a slightly higher value of l. In all cases, it is the interchange mode that remains the most unstable mode without shear. By introducing the velocity shear U_1 with $\lambda_1 = 20$, as in Figure 7.12c, we now have a case where the most unstable mode of the system is an undular mode. Therefore it is of interest to see how changing the field gradient ζ affects the overall instability when this undular mode is present. Figure 7.17 contains three plots of growth rate versus l, for different magnitudes of ζ and λ_1, solved using stress-free boundary conditions. The first is exactly the same as Figure 7.12c, put here to aid the reader, where the undular mode is the preferred mode. The second is for an increased field gradient $\zeta = 3$, keeping $\lambda_1 = 20$. As one would expect, increasing the field strength destabilised all the modes. However, interestingly, the interchange mode is now the most unstable mode of the system. Finally, if we keep $\zeta = 3$ and increase the velocity shear gradient to $\lambda_1 = 40$, as in Figure 7.17c, the undular mode is once again the most unstable mode. This suggests there exists a trade off between the magnitude of the velocity gradient λ_1 and the field gradient ζ, which dictates whether an interchange or undular mode will be the preferred mode of instability.

Throughout our two chapters focusing on the short-wavelength magnetic buoyancy instability, we derived asymptotic results for the body mode. Unfortunately, due to the unpredictability involved in finding the point of the localisation and the leading order growth rate, we could not produce any further detailed analytic work on these modes. Therefore all results regarding the body modes had to be found numerically. In Chapter 5

we saw that by increasing the shear gradient λ for a specific undular mode, it was possible to switch from a wall mode, into a body mode peaked at the point where $U' = 0$. However, this specific mode was never more unstable than the interchange wall mode. With the inclusion of individual diffusivities in Chapter 6, we were able to introduce a shear such that the undular mode was more unstable than the interchange mode. Yet, in all cases we considered, the dominant undular mode of the system was always the wall mode. This still seems to be the case in this chapter, when all diffusion terms are included together. As we see in Figure 7.18, obtained using shear profile U_1 with $\lambda_1 = 20$, body modes do exist in the system. However, the eigenvalue of this mode is $\omega \approx -6.66 - 0.69i$, and therefore has a lower growth rate than the wall mode for the same wavenumbers, found in Figure 7.13. Although we can not possibly test every shear profile, for the ones we have considered the most unstable mode of the system is always a wall mode peaked at the bottom boundary.
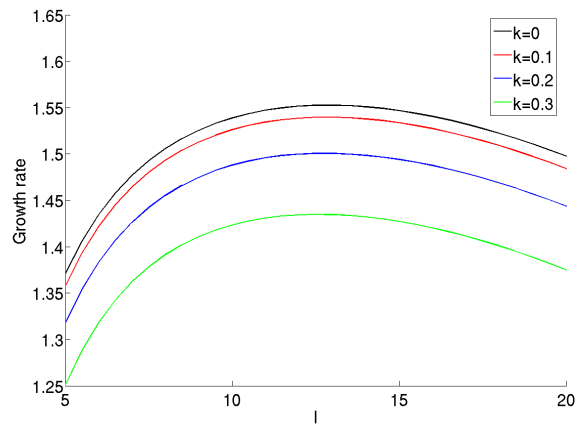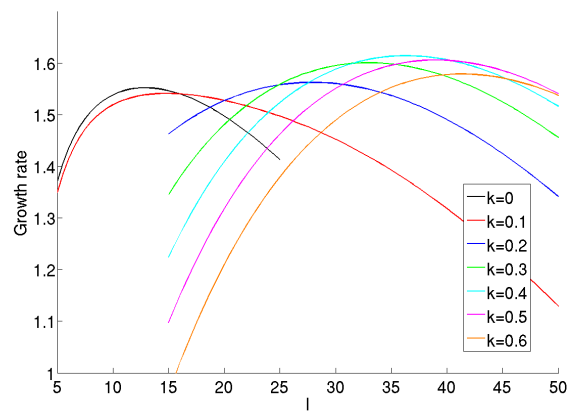
(a)
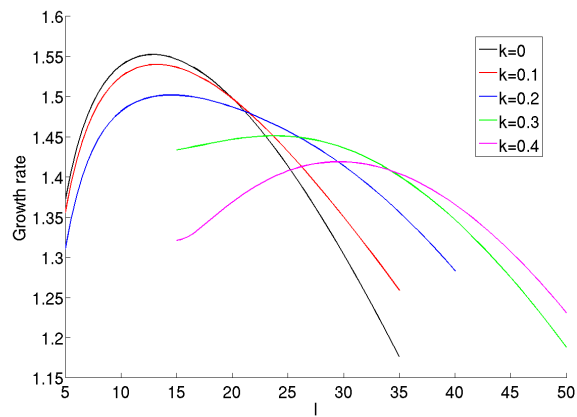
(b)

(c)

Figure 7.12: Growth rate versus wavenumber l, solved with parameter values P_3 (7.7) and velocity shear U_1 (7.8) for three different values of λ_1: (a) $\lambda_1 = 0$, (b) $\lambda_1 = 10$ and (c) $\lambda_1 = 20$.
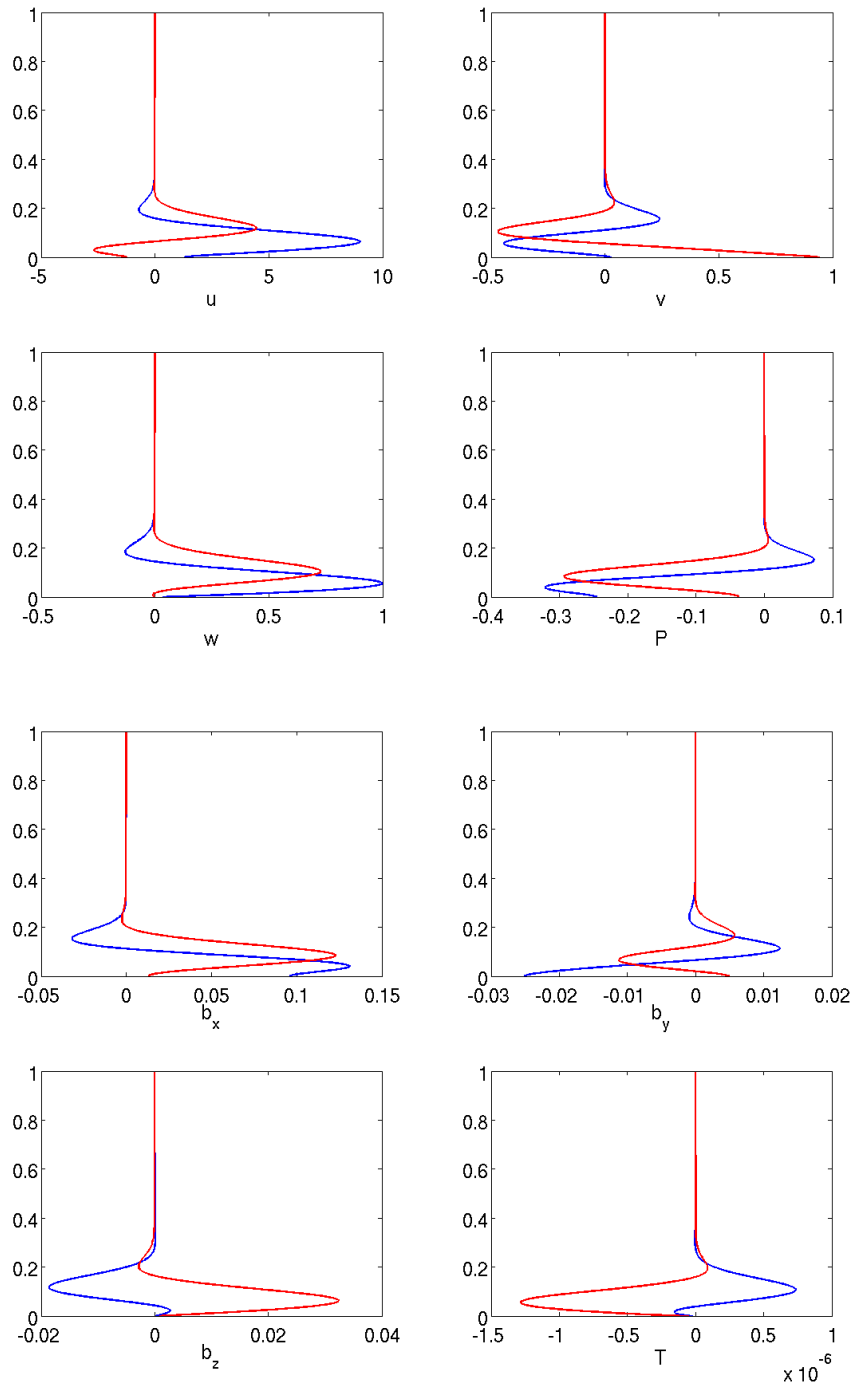
Figure 7.13: Eigenfunctions associated with the most unstable mode in Figure 7.12c, with $l = 36$, $k = 0.4$. The blue line represents the real part of the eigenfunction, and the red the imaginary part.
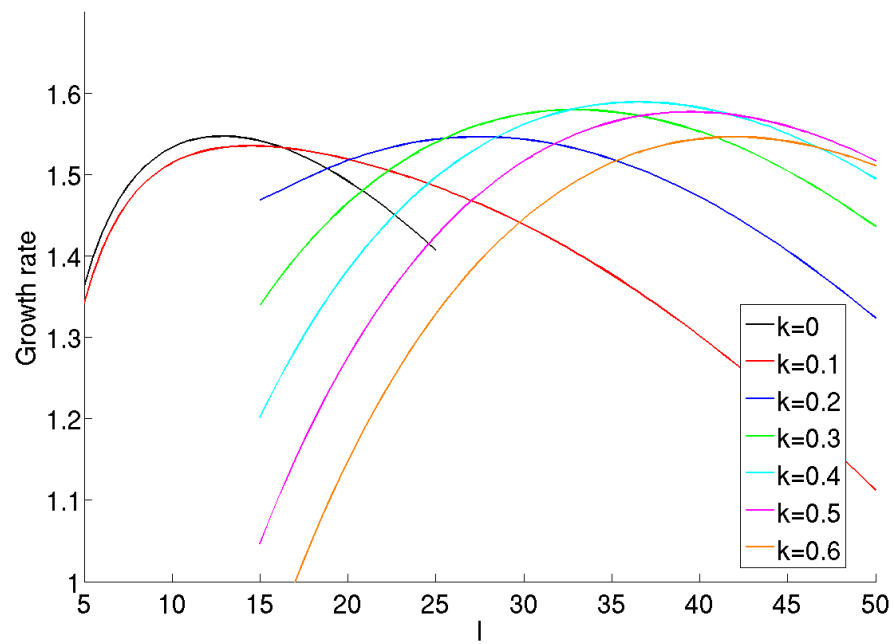
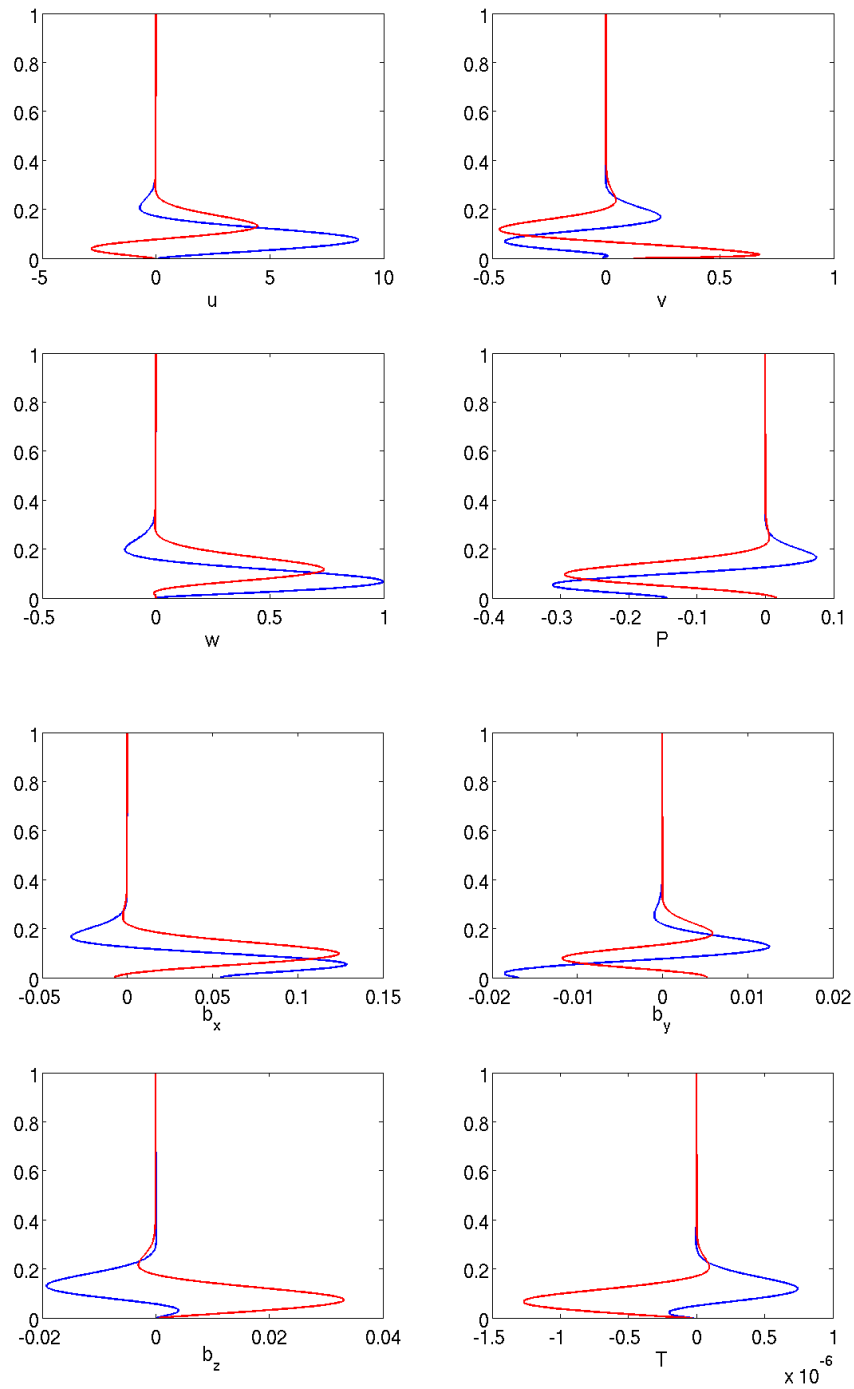Figure 7.14: As Figure 7.12c, obtained using no-slip boundary conditions.
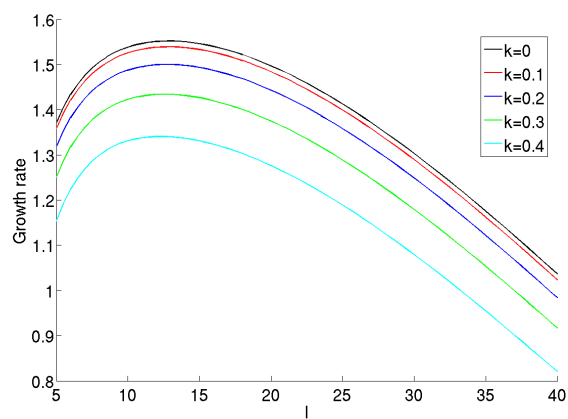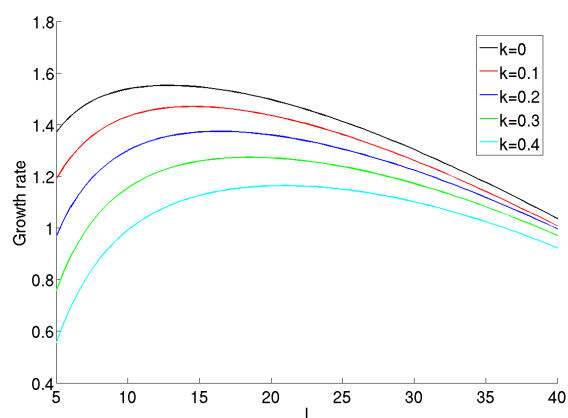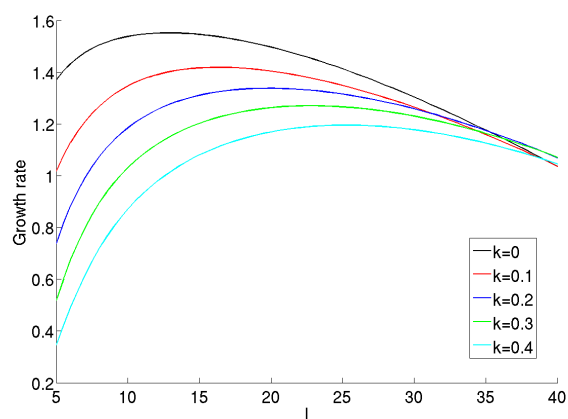
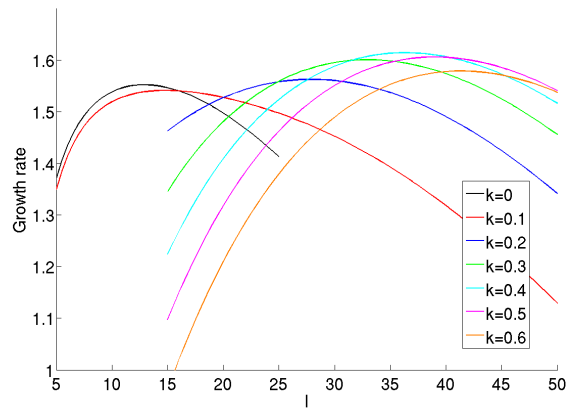Figure 7.15: As Figure 7.13, for no-slip boundary conditions on the velocity perturbations.
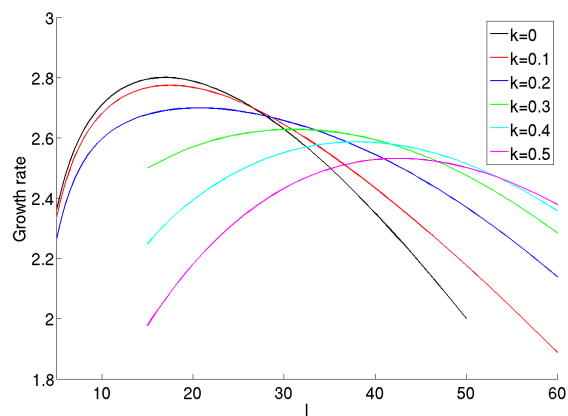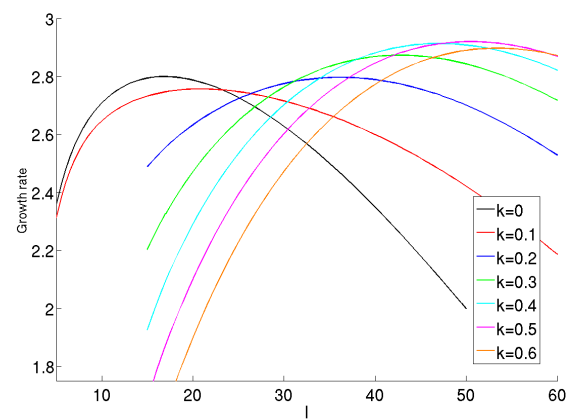
(a)

(b)

(c)

Figure 7.16: Growth rate versus wavenumber l, solved with parameter values P_3 (7.7) and velocity shear U_2 (7.9) for three different values of λ_2: (a) $\lambda_2 = 0$, (b) $\lambda_2 = 20$ and (c) $\lambda_2 = 40$.

(a)

(b)

(c)

Figure 7.17: Growth rate versus wavenumber l, solved with parameter values P_3 (7.7) and velocity shear U_1 (7.8) for different values of ζ and λ_1: (a) $\zeta = 1.5$, $\lambda_1 = 20$, (b) $\zeta = 3$, $\lambda_1 = 20$ and (c) $\zeta = 3$, $\lambda_1 = 40$.
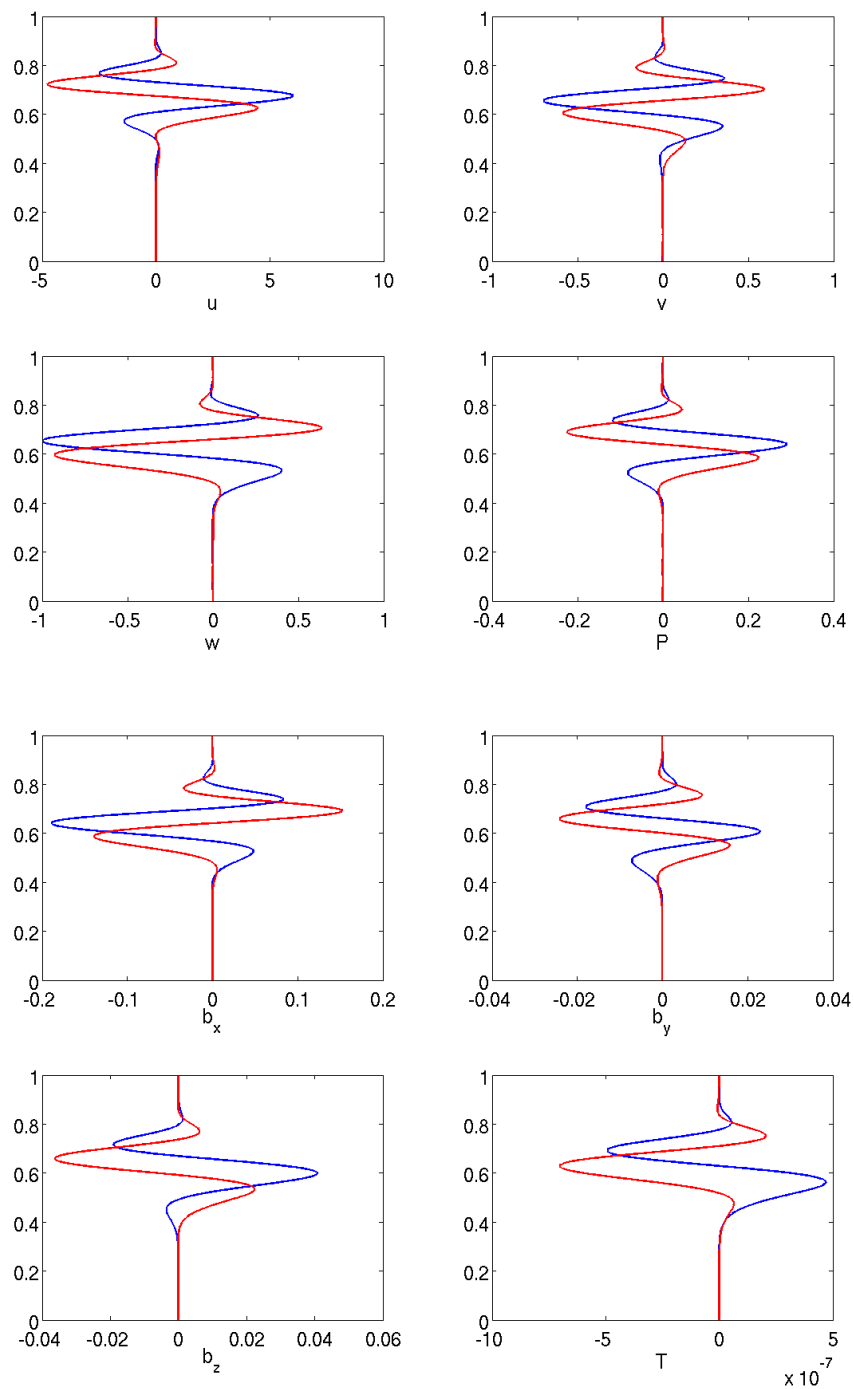
Figure 7.18: Eigenfunctions of a body mode for wavenumbers $l = 36$, $k = 0.4$ and parameter values P_3 (7.7). Here we have taken shear profile U_1 (7.8), with $\lambda_1 = 20.$, and have used stress-free boundary conditions.

7.3.2 Impact of diffusion: velocity shear

In §7.2.2 we showed that varying the Péclet number has little influence on the instability in the absence of velocity shear. This is due to the fact that the temperature perturbation of the most unstable mode of the system is essentially zero everywhere in the layer. The addition of a velocity shear does not change this fact; as can be seen from Figure 7.13, the temperature perturbation is $O\left(10^{-6}\right)$. Hence, thermal diffusion will not have an impact on the instability of the full system. The influence of viscosity and magnetic diffusion on the instability is however a lot more significant. Decreasing the magnetic diffusion (i.e. increasing Rm) destabilises the interchange mode and moves the most unstable mode to a higher l. Interestingly, this behaviour does not continue in the same fashion for Rm greater than Re. When $Rm \gtrsim Re$, increasing Rm further has minimal effect on the instability. The roles are reversed if Re is smaller than Rm; in this case, it is Re that has the greatest influence on the growth rate and the wavenumber l. Similarly, when $Re \gtrsim Rm$, increasing Re does not greatly affect the instability. Thus the ratio of Re/Rm, otherwise known as the inverse magnetic Prandtl number, $Pm^{-1} = \eta/\nu$, is very important in determining the role of instability, certainly for the interchange mode in the absence of shear.

The introduction of a velocity shear with the full set of diffusive parameters allows the system to have an undular mode as the most unstable mode. In this subsection we examine the effects of viscosity and magnetic diffusion on the undular mode, by considering several different magnitudes of Re/Rm. All numerical results in this subsection are obtained by solving the governing equations (7.6) subject to stress-free boundary conditions, with shear profile U_1 given by (7.8) and parameter values $\zeta = 1.5$, $Pe = 10^{-2}$ and $\hat{\beta} = 0.2$.

Figure 7.19 shows plots of growth rate versus l for three different values of Rm, with $\lambda_1 = 20$. For each plot in this figure we have simultaneously changed the magnitude of the Reynolds number, such that they all satisfy $Re/Rm = 100$. Here we see that increasing Rm has a destabilising effect on all modes, and has pushed the dominant mode to a higher l. The most unstable mode of the system remains the undular mode, taking the wavenumber values $l = 29$ and $k = 0.4$ in Figure 7.19a, and $l = 102$ and $k = 0.6$ in

Figure 7.19c. Therefore, by increasing Rm whilst keeping the ratio $Re/Rm = 100$, the most unstable mode has not only moved to a higher value of l, but also a slightly higher k.

Figure 7.20 shows the same plots found in Figure 7.19, but for a smaller inverse magnetic Prandtl number, $Re/Rm = 10$. Here the system displays nearly identical behaviour as before; increasing Rm moves the most unstable mode to higher values of l and k. Again, similar plots can be seen in Figure 7.21 for when $Re/Rm = 1$. In this case the undular mode is no longer the most unstable mode. Increasing Rm still has a destabilising effect; however, the interchange mode remains the dominant mode. Increasing the magnitude of the shear gradient λ_1 in an attempt to recover the undular mode, only has a stabilising effect on the undular modes. The interchange mode that is dominant in all the plots shown in Figure 7.21 is still the wall mode, similar to those shown in Figure 7.2. It is not clear why the undular mode is suppressed when $Re/Rm = 1$.

One might expect that if we keep decreasing Re/Rm, the system will remain in the same regime found in Figure 7.21, where the undular mode is always suppressed. Figure 7.22 shows the familiar plots of growth rate versus l, this time for $Re/Rm = 0.1$. Here we see the above assumption is incorrect; although we require a slightly larger λ_1 value ($\lambda_1 = 30$), the undular mode can be the preferred mode of instability. That suggests that there is something unique with the ratio $Re/Rm = 1$. However, due to time constraints coupled with the fact that for the tachocline, the ratio Re/Rm is greater than unity, we have not investigated this further.
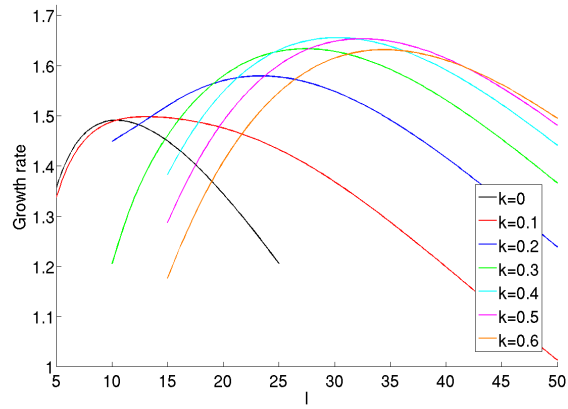
(a)
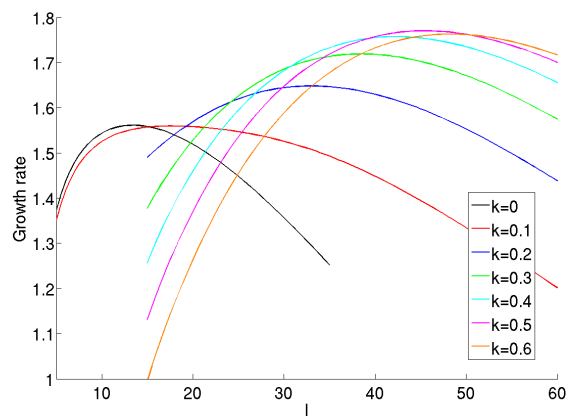
(b)
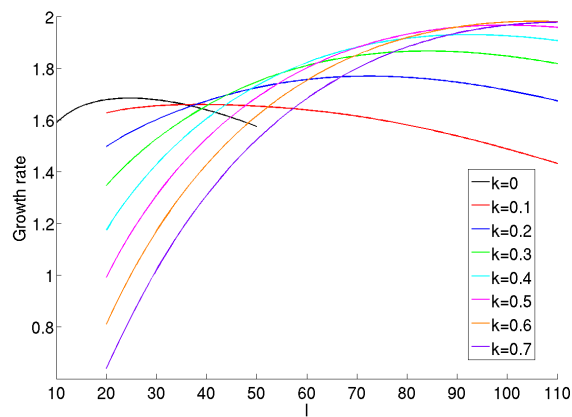
(c)

Figure 7.19: Growth rate versus wavenumber l for shear profile U_1 (7.8), with $\lambda_1 = 20$ and $Re/Rm = 100$: (a) $Rm = 500$, (b) $Rm = 1000$ and (c) $Rm = 5000$.
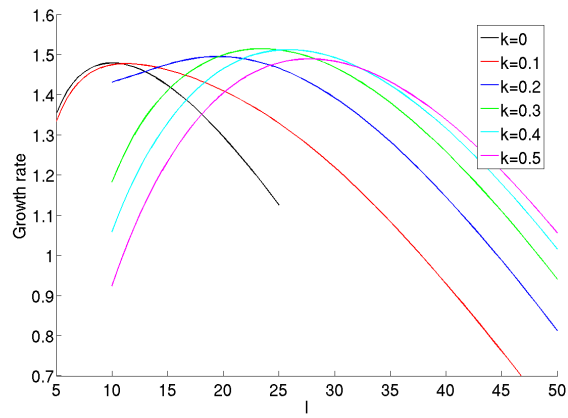
(a)
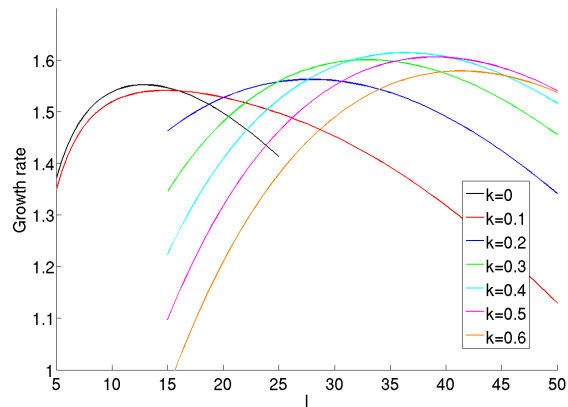
(b)
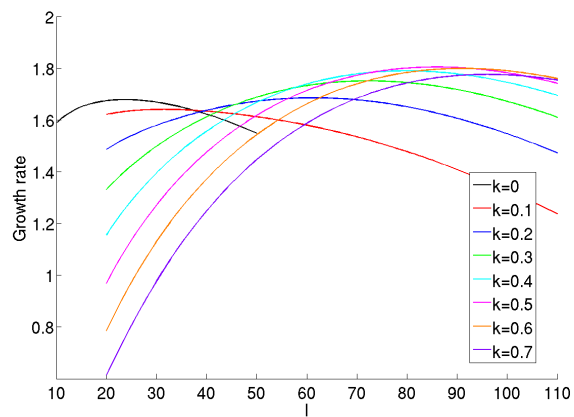
(c)

Figure 7.20: As Figure 7.19, with $Re/Rm = 10$: (a) $Rm = 500$, (b) $Rm = 1000$ and (c) $Rm = 5000$.
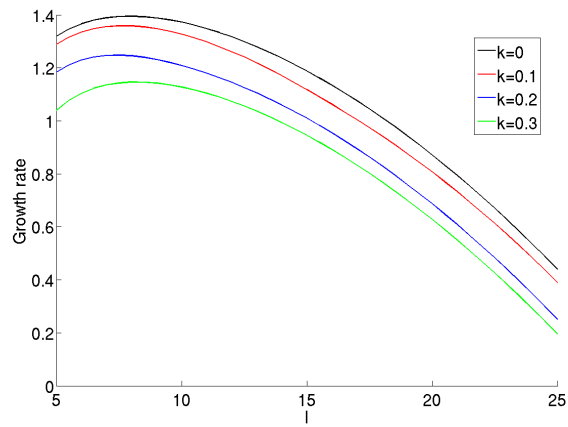
(a)
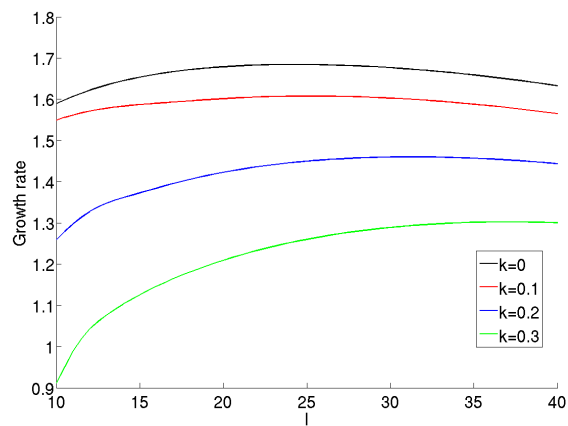
(b)
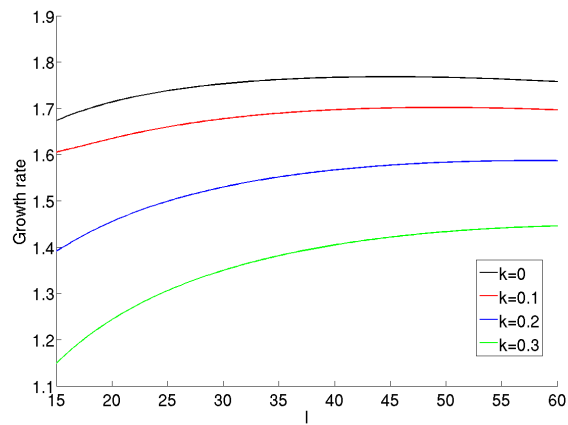
(c)

Figure 7.21: As Figure 7.19, with $Re/Rm = 1$: (a) $Rm = 500$, (b) $Rm = 1000$ and (c) $Rm = 5000$.
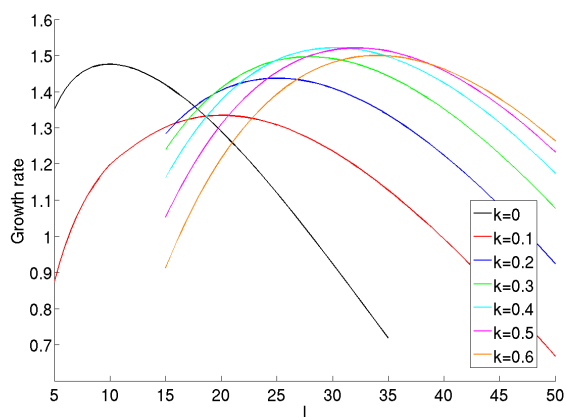
(a)
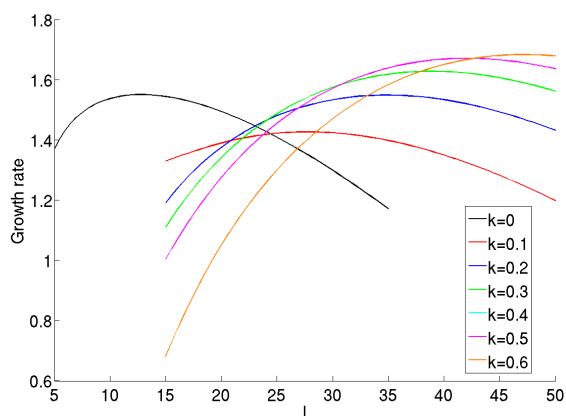
(b)
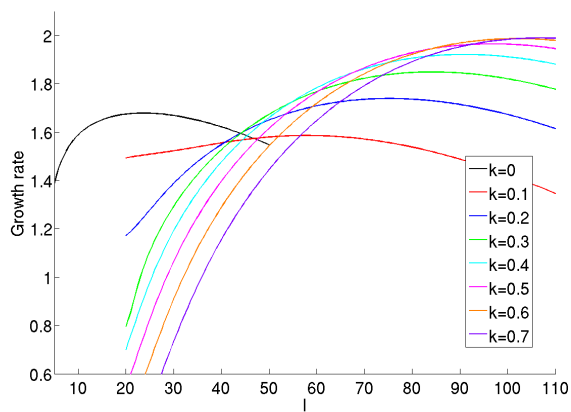
(c)

Figure 7.22: As Figure 7.19, with $Re/Rm = 0.1$ and $\lambda_1 = 30$: (a) $Rm = 5000$, (b) $Rm = 10000$ and (c) $Rm = 50000$.

7.3.3   The dominant mode: velocity shear

In §7.2.3 we concluded that most unstable mode in the absence of shear was the interchange mode, and since we focused on the case where $Rm < Re$, this mode appears for values of l such that $l \sim Rm^{3/8}$. As one would expect, the velocity shear has no influence on the interchange mode and therefore for the interchange mode this scaling still applies. This can be observed in Figure 7.19, where for $Rm = 500$, $Rm = 1000$ and $Rm = 5000$, the values of $Rm^{3/8}$ are approximately 10, 13 and 24 respectively. In all cases the interchange mode is maximised around these values of l and therefore the ordering $l \sim Rm^{3/8}$ does indeed hold. When $Rm > Re$, as in Figure 7.22, the interchange instability is now governed by the Reynolds number Re and the most unstable interchange mode appears for values of l such that $l \sim Re^{3/8}$.

The velocity shear, or more specifically $|U'|$ evaluated at the same boundary at which the eigenfunctions are localised, can however have a destabilising effect on the undular modes. By sufficiently increasing the shear gradient, it is possible to destabilise the undular mode to the point that it becomes the most unstable mode of the system. This seems to be the case provided that Re is not of the same order of magnitude as Rm, or, in other words the Prandtl number is not $\mathrm{O}\,(1)$. Unfortunately we have no clear explanation for why this is, and due to time constraints we have not investigated this further. Based on the typical parameter values of the tachocline (7.1), $Re/Rm \approx 14$, which is certainly within the regimes in which we expect to find undular modes. Thus, for the rest of this discussion, we shall focus on the astrophysically relevant limit, and assume $Re > Rm$.

The value of the wavenumber k at which the most unstable undular mode appears is very hard to predict, as it depends on a number of factors. To demonstrate this, suppose we fix all parameter values such that the undular mode for a particular k is the most unstable mode of the system. Clearly the size of the shear gradient at the boundary (which we will denote as λ_c) plays a large role in determining the value of k; if λ_c is decreased sufficiently, the most unstable mode switches from an undular mode, with finite k, to the interchange mode, with $k = 0$. A similar effect can be seen in Figure 7.17b, where increasing the magnetic field gradient ζ results in the most unstable mode switching from an undular mode to an interchange. Finally, the value of k seems somewhat dependent on Rm; as

seen in Figures 7.19, 7.20 and 7.22, increasing Rm pushes the most unstable mode to a slightly higher k . With all these variables in play, it is very difficult to predict an exact value of k corresponding to the most unstable mode. However, in all cases considered the undular mode appears for values of k such that $k = \text{O}\left(10^{-1}\right)$. On increasing Rm to more realistic values we might expect the dominant undular mode to have an increased value of k, but certainly do not expect it to exceed $k = \text{O}\left(1\right)$. This gives a rough idea of the value of k associated with the undular mode instability in the tachocline. In a similar vein, we can not easily predict the critical value of λ_c required to bring out the undular mode, which is very dependent on both the field gradient ζ and Rm. However, provided $Re > Rm$, there always seems to exist a value of λ_c such that when large enough, the undular mode will dominate.

We have previously discussed that when increasing Rm with the ratio Re/Rm fixed, the most unstable interchange mode appears for values of l such that $l \sim Re^{3/8}$. In §6.4 we showed that when the undular wall mode was the most unstable mode of the system, it would take a value of l such that $l \sim Rm^{1/2}$. By considering all the diffusive effects together, we can still produce a system in which the undular wall mode dominates. Therefore, it is of interest to see how the value of l, corresponding to the most unstable undular wall mode, varies in the full system. Fixing the ratio $Re/Rm = 10$, with $Pe = 10^{-2}$ we can increase Rm and find the dominant mode for a given k. All numerical results in this subsection are obtained by solving the governing equations (7.6) subject to stress-free boundary conditions, with shear profile U_1 given by (7.8) and parameter values $\zeta = 1.5$ and $\hat{\beta} = 0.2$. Figure 7.23 shows plots corresponding to the most unstable mode for a given value of Re, at wavenumber $k = 0.4$. As we have previously witnessed, increasing Rm has a destabilising effect on the undular mode and moves the most unstable mode to a higher value of l. Figure 7.23c plots $\ln(l)$ versus $\ln(Rm)$, alongside a red line gradient 0.5. Using this graph we can conclude that the value of l at which the most unstable undular mode appears scales as $l \sim Rm^{1/2}$. One drawback of this technique is that we can keep track of the most unstable mode only for a specific value of k; as we have seen, increasing Rm moves the dominant mode to a slightly higher value of k. Thus, the mode with $k = 0.4$ may not necessarily correspond to the most unstable mode of the whole system for all values of Rm. To address this we include Figure 7.24, which is

analogue to Figure 7.23 with $k = 0.7$. Again it can be seen that the same scaling for l is present for this value of k. Therefore, provided the value of λ_c is sufficiently large, the most unstable mode of the system will be an undular mode with wavenumbers $k \sim \mathrm{O}(1)$ and $l \sim Rm^{1/2}$.
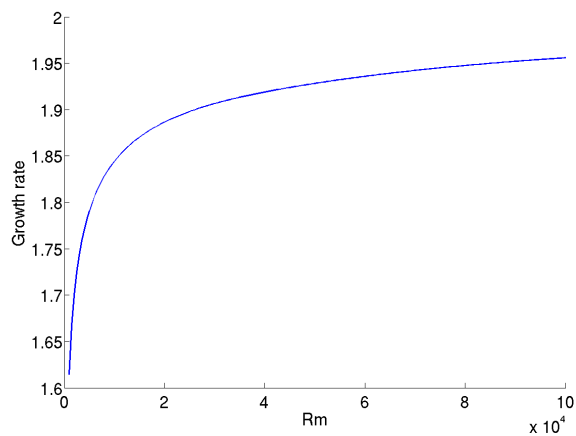
(a)
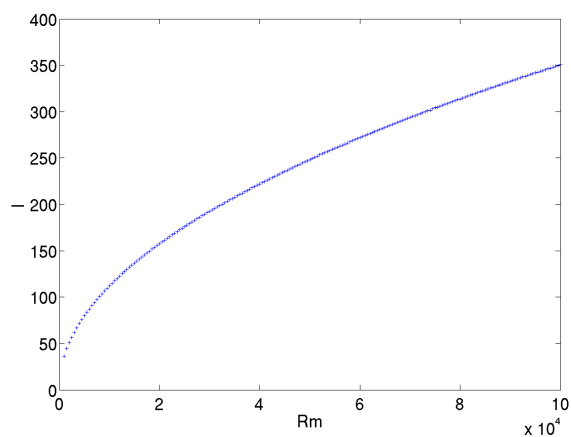
(b)
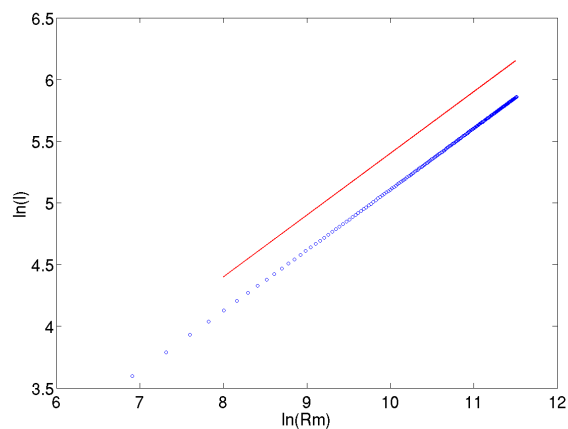
(c)

Figure 7.23: Plots of the most unstable mode for a given magnetic Reynolds number, taken for shear profile U_1 (7.8), with $\lambda = 20$, $k = 0.4$ and $Re/Rm = 10$. (a) plots the growth rate versus Rm, (b) the value of l for the most unstable mode at a given Rm and (c) $\ln(l)$ versus $\ln(Rm)$. The red line in (c) is a line with gradient 0.5.
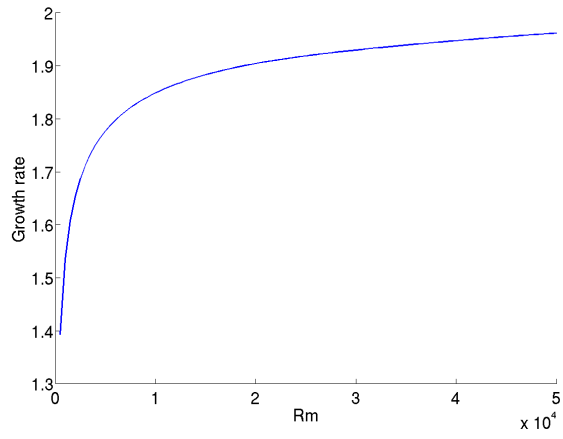
(a)
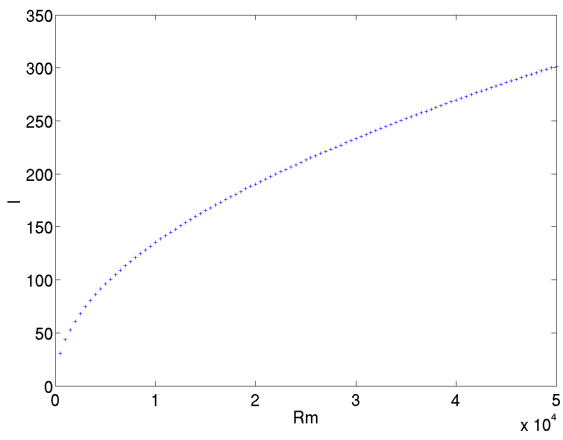
(b)
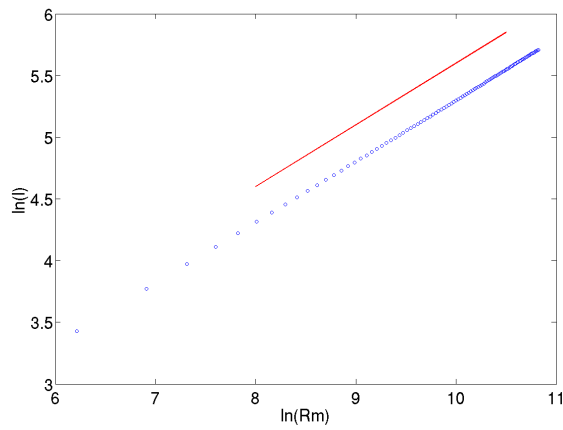
(c)

Figure 7.24: As Figure 7.23, with $k = 0.7$.

Chapter 8

Conclusions and Future Work

8.1 Summary and conclusions

The presence of a magnetic field in the Sun is well documented and can be observed indirectly through surface features such as sun spots and solar flares. However, the exact process by which the solar magnetic field is continually self generated is very much up for debate. Several contradicting dynamo models, discussed in §1.2.2, attempt to explain how this process works. Despite their differences, a common feature of these models is that the bulk of the field exists as strong toroidal field, located in the solar interior. It is likely that the tachocline, a thin region of strong velocity shear separating the radiative and convection zones, is an ideal location for this stored toroidal field. Conditions of the tachocline are such that a mechanism known as magnetic buoyancy instability is thought to be responsible for the break up of the toroidal field, sending it to the surface.

A lot of work has been carried out on magnetic buoyancy instability since Parker (1955), with an overview contained in Chapter 2, and that of particular relevance to this thesis is the derivation of the magneto-Boussinesq equations (Spiegel & Weiss, 1982). With the assumption that the magnetic field scale H_B is of the same order of magnitude as the pressure scale height H_p, Spiegel & Weiss derived a set of non-linear equations that have been used to model the magnetic buoyancy instability. Motivated by the strong velocity gradient that naturally exists in the tachocline, we here incorporate the effects of

a velocity shear in the magneto-Boussinesq equations. In Chapter 3 we initially attempt to add the velocity shear into the equations of Spiegel & Weiss, in what one might assume as the obvious fashion, by adding a basic state velocity shear that is of the same magnitude as the resulting velocity perturbations. Doing so results in a set of equations that appear to have all the necessary shear terms. However, as shown in §3.2.1, when performing a linear stability analysis on the ideal equations, the shear terms 'drop out', leaving the growth rate of the system unaffected by the velocity shear. To incorporate an 'influential' velocity shear fully, we had to return to the fundamental orderings underlying the magneto-Boussinesq equations. In a similar style to Corfield (1984), we re-derived the magneto-Boussinesq equations without fixing the magnitude of the magnetic field scale height *a priori*. This, in turn, gives us the appropriate orderings needed to derive the set of equations ((3.81) with $q = 1$ and $r = 0$) containing the effects of magnetic buoyancy instability with an $O\left(1/d\right)$ field gradient. As noted by Hughes (1985a), this is not possible straight from the equations of Spiegel & Weiss. Without specifying a particular magnetic scale height we then introduce a basic state velocity shear into the scaling analysis. In order that the velocity shear has an influential impact on the instability we require that two orderings are satisfied. The first is that the magnitude of the shear U_* is of the same order as the Alfvén velocity c_A. The second is that the velocity shear scale height H_u, and consequently the magnetic field scale height H_B, is of the same order as the height of the layer d.

With these orderings in place, §3.2.4 provides the derivation of a new set of equations that consistently incorporate the effect of an influential velocity shear into the magneto-Boussinesq equations. As discussed in §3.4, based on estimates of the magnetic field magnitude, these equations form an appropriate system for the study of magnetic buoyancy instability in the tachocline. It is these newly derived equations that are used throughout the remainder of the thesis.

Naturally we first consider the linear stability of the ideal ($\nu = \eta = \kappa = 0$) system. We do this in the usual manner, by looking at the temporal evolution of normal mode solutions and transforming the problem into an eigenvalue problem for the growth rate. Since our new equations are derived with an $O(1/d)$ field gradient, steeper than the $O(1/H_p)$ field gradient used in previous studies, the results in Chapter 4 differ from those in §2.1.1. We

found that when neglecting the velocity shear, it is not possible to have an unstable undular mode with a stable interchange mode for the same atmospheric background. Motivated by Howard (1961) and Hughes & Tobias (2001), we derive a set of semi-circle bounds for the eigenvalue, and ultimately stability criteria for the system with a velocity shear.

As part of our work in Chapter 4, we manipulate the system of equations to produce a single second order ODE, which can be solved as a boundary value problem subject to appropriate boundary conditions. As addressed by Mizerski et al. (2013) in a similar context, considering the strict large-wavenumber limit of this ODE reduces the equation to an algebraic 'depth-dependent' dispersion relation analogous to that of Gilman (1970), thus removing all derivatives from the system. This prompts the questions as to how the boundary conditions play a role on the instability. In Chapter 5 we follow the work of Mizerski et al. (2013) and perform a boundary layer analysis on our new system of equations, linking the idea of the large-wavenumber limit to the boundary value problem. In the absence of velocity shear we confirm the results found in Chapter 4 and also conclude that the most unstable mode for a linear magnetic field is an interchange wall mode, localised at the bottom boundary. When considering the influence of a velocity shear it appears at first glance (equation (5.53)) to play no role in determining the growth rate, contributing only to the frequency of the mode. However, this is not the case; the velocity shear can have a strong influence not only on the growth rate, but also the structure of a given mode. Despite this, in all the cases we considered the shear only had a stabilising effect on the undular mode. Thus, the overall dominant mode of the diffusionless system with shear, is an interchange wall mode.

In Chapter 5 we study the ideal system and despite introducing a velocity shear, an interchange mode is always dominant. In Chapter 7 we study the full system, including all diffusive effects, and find that under certain conditions an undular mode can dominate. Chapter 6 aims to bridge the gap between the opposing results found in Chapters 5 and 7. By individually reintroducing each diffusive parameter into the system, whilst sticking to the large-wavenumber limit, we find certain regimes where the velocity shear can have a destabilising effect on the instability. Specifically, when considering either viscosity or magnetic diffusion, the shear gradient term evaluated at the boundary can destabilise the undular wall modes for values of l such that $l \sim Re^{1/2}$ and $l \sim Rm^{1/2}$ respectively.

We also derive a similar scaling for the value of l corresponding to the most unstable interchange mode; the interchange wall mode takes values of l such that either $l \sim Re^{3/8}$ or $l \sim Rm^{3/8}$. Although we were able to derive analogous orderings for the body mode, we could never find a case where the body mode was more unstable than the wall mode. The addition of only thermal diffusion has little impact on the instability; in this case, the system is similar to that found in Chapter 5, where the shear does not play an influential role.

Chapter 7 contains numerical results of the linear system including all diffusive terms. In the absence of the velocity shear, we recover results obtained from our analysis of the ideal system: the most unstable mode is always the interchange wall mode, and increasing the field gradient has a destabilising effect on the instability. We also find that when the astrophysical ordering $Re > Rm$ and $Re, Rm \gg Pe$ is upheld, the dominant interchange mode has wavenumber l in the region $l \sim Rm^{3/8}$. Along with this, the choice of boundary conditions adopted for the velocity perturbations has minimal impact on the instability. When velocity shear is considered we can mimic the results found in Chapter 6; by increasing the shear gradient term at the boundary, the undular mode can be destabilised provided that $Re/Rm \neq \mathrm{O}(1)$. Again, this mode always appears to be a wall mode and the choice of boundary conditions is somewhat irrelevant. We also find that the location in l of the most unstable undular mode follows the ordering $l \sim Rm^{1/2}$, with the wavenumber k being no larger than $\mathrm{O}(1)$. We can not be certain if these wavenumbers provide a good approximation to the true values associated with the magnetic buoyancy instability at the tachocline. The field we observe at the surface has undergone so many unknown changes as it travels through the convection zone, that the true values are hard to predict.

8.2 Future work

We hope this thesis has provided the reader with an insight into the effects of a velocity shear on the magnetic buoyancy instability. As one might expect, arising from this thesis are several avenues that would be interesting to explore further, some of which

are discussed below.

All work in this thesis focuses first on the derivation of a new governing set of equations and then on the linear evolution of the instability. Due to the extremely small viscosity of the fluid in the tachocline, non-linear effects will play an important role on the instability and therefore studying the non-linear evolution is an obvious extension. Another feature of the tachocline that is likely to play an important role on the instability is rotation. Although not considered, it is possible to incorporate the effects of rotation into our new equations found in Chapter 3.

Returning to the linear study found in this thesis; §6.2 contains approximated results for the system with just viscosity in the large l limit. By focusing on a boundary layer that has the largest impact on the growth rate, we reduce our governing equation from a 6th order ODE to a 2nd order ODE. This equation can then be solved analytically to give an approximation for the vertical velocity w. Thus, we obtain a solution whilst only having satisfied two of the required six boundary conditions. By using this analytic solution for w, we numerically solved a separate boundary value problem for u, implementing two further boundary conditions. However, we could not find a way to fully satisfy the boundary conditions on v, and as a result our approximated numeral solution for v did not fully satisfy the bottom boundary condition. Fortunately the choice of boundary conditions had very little impact on the growth rate and the overall structure of eigenmode. Despite this, it would be a nice extension to look into a way of successfully implementing the remain two boundary conditions.

In §2.1.2 we presented an instability criteria for oscillatory interchange modes (2.16) driven by an $\mathrm{O}\left(1/H_p\right)$ magnetic field gradient. Hughes (1985a) identified a regime in which overstability can occur for a bottom heavy field gradient (B/ρ increasing with height). Throughout our analysis of equations (3.61) we have focused on a magnetic field that decreases with height. In future work it may be worth considering a field that increases with height to see if we can find an unstable mode in this regime. Equations for the leading order eigenvalue (6.7) and (6.79) in Chapter 6.2 may shed some light as to whether this is possible.

One drawback in our analysis is not having a direct relationship between the field gradient

ζ and the velocity shear gradient λ. We have shown that for a large enough λ, the most unstable mode of the system switches from an interchange mode to an undular mode. Similarly, we can increase ζ and destabilise the interchange mode to the point where it is again the dominant mode. Thus, there clearly is a balance between the magnitude of ζ and λ that dictates which mode is preferred. This would be a nice extension and aid with us putting our work into the context of the tachocline.

Appendices

A Derivation of equation (4.4)

In this appendix we provide a break down of the derivation of the 2nd order ordinary differential equation (4.4). The governing equations are;

$$iku + ilv + w' = 0, \tag{A.1a}$$

$$ikb_x + ilb_y + b'_z = 0, \tag{A.1b}$$

$$i\left(\omega + kU\right)u + U'w = ikBb_x + B'b_z, \tag{A.1c}$$

$$i\left(\omega + kU\right)v = -il\Pi + ikBb_y, \tag{A.1d}$$

$$i\left(\omega + kU\right)w = \Pi' + ikBb_z + T + Bb_x, \tag{A.1e}$$

$$i\left(\omega + kU\right)b_x + B'w = ikBu + U'b_z, \tag{A.1f}$$

$$i\left(\omega + kU\right)b_y = ikBv, \tag{A.1g}$$

$$i\left(\omega + kU\right)b_z = ikBw, \tag{A.1h}$$

$$i\left(\omega + kU\right)\left(T + DBb_x\right) = -\beta w. \tag{A.1i}$$

Equations (A.1c)–(A.1i) can be manipulated to give three equations for each component of velocity,

$$u = \frac{iU'}{\left(\omega + kU\right)}w, \tag{A.2a}$$

$$i\left(\omega + kU\right)v = -il\Pi + \frac{ik^2B^2}{\omega + kU}v, \tag{A.2b}$$

$$i\left(\omega + kU\right)w = \Pi' + \frac{kB^2}{\gamma\left(\omega + kU\right)}u - \frac{i}{\omega + kU}\left(\frac{kB^2U'}{\gamma\left(\omega + kU\right)} - k^2B^2 - \beta - \frac{BB'}{\gamma}\right)w. \tag{A.2c}$$

Taking the z derivative of (A.2b) and subtracting the y derivative of (A.2c) removes the total pressure Π from the equations. Doing so gives

$$i\left(\omega + kU\right)\left(v' - ilw\right) + ikU'v = \frac{ik^2B^2}{\omega + kU}v' + \left(\frac{ik^2B^2}{\omega + kU}\right)'v - \frac{ilkB^2}{\gamma\left(\omega + kU\right)}u$$
$$- \frac{l}{\omega + kU}\left(\frac{kB^2U'}{\gamma\left(\omega + kU\right)} - k^2B^2 - \beta - \frac{BB'}{\gamma}\right)w. \qquad \text{(A.3)}$$

Provided $l \neq 0$, we can substitute (A.2a) into the incompressibility condition to give and expression for v,

$$v = -\frac{kU'}{\left(\omega + kU\right)} + \frac{i}{l}w'. \qquad \text{(A.4)}$$

Finally, upon substituting equations (A.2a), (A.4) and the z derivative of (A.4) into (A.3), and rearranging terms we arrive at equation (4.4).

B   The inverse iteration method

In this appendix we give a overview of the inverse iteration method used throughout this thesis to numerically solve eigenvalue problems. A more in-depth review on the inverse iteration method, including examples can be found in Fearn (1991).

Let $\mathbf{A}$ be an $N \times N$ matrix with eigenvalues λ_n and corresponding eigenvectors $\mathbf{x}_n$, thus

$$\mathbf{A}\mathbf{x}_n = \lambda_n \mathbf{x}_n, \tag{B.5}$$

for $n = 1, \ldots, N$. Suppose we define estimates of the required eigenvalue and eigenvector as μ and $\mathbf{y}$ respectively. Expressing $\mathbf{y}$ in terms of $\mathbf{x}_n$,

$$\mathbf{y} = \sum_{n=1}^{N} \alpha_n \mathbf{x}_n, \tag{B.6}$$

we can write

$$(\mathbf{A} - \mu I)\,\mathbf{y} = \sum_{n=1}^{N} \alpha_n \left(\lambda_n - \mu\right) \mathbf{x}_n, \tag{B.7}$$

and therefore

$$(\mathbf{A} - \mu I)^{-m}\,\mathbf{y} = \sum_{n=1}^{N} \alpha_n \left(\lambda_n - \mu\right)^{-m} \mathbf{x}_n. \tag{B.8}$$

Let us now defined λ_i as the eigenvalue closest to the guess μ, that is to say

$$|\lambda_i - \mu| < |\lambda_j - \mu|, \tag{B.9}$$

for all $j = 1, \ldots, N$ when $j \neq i$. Provided $\alpha_i \neq 0$, the right hand side of (B.8) converges to

$$\alpha_i \left(\lambda_i - \mu\right)^{-m} \mathbf{x}_i, \tag{B.10}$$

as $m \to \infty$. Therefore, when provided the initial guesses for the eigenvalue μ and the eigenvector $\mathbf{y}$, the iterative scheme

$$\mathbf{y}_m = (\mathbf{A} - \mu I)^{-1}\,\mathbf{y}_{m-1}, \quad \mathbf{y}_0 = \mathbf{y}, \tag{B.11}$$

can be used to find the closest eigenvalue λ_i, to the guess μ, and corresponding eigenvector $\mathbf{x}_i$.

This method can be extended to solve generalised eigenvalue problems (such as we have in this thesis), of the form

$$\mathbf{A}\mathbf{x}_n = \lambda_n \mathbf{B}\mathbf{x}_n. \tag{B.12}$$

The analogue to (B.8) in this case becomes,

$$(\mathbf{A} - \mu\mathbf{B})^{-m}\,\mathbf{B}\,\mathbf{y} = \sum_{n=1}^{N} \alpha_n \left(\lambda_n - \mu\right)^{-m} \mathbf{x}_n. \tag{B.13}$$

This then alters the iterative scheme (B.11) required to find the eigenvalue to,

$$\mathbf{y}_m = (\mathbf{A} - \mu\mathbf{B})^{-1}\,\mathbf{B}\,\mathbf{y}_{m-1}, \quad \mathbf{y}_0 = \mathbf{y}. \tag{B.14}$$

The inverse iteration method is well suited to a matrices with a banded structure, as it can be coded in a manner that saves both allocated storage and thus computational time. One drawback of this method is that it only results in a single eigenvalue of the system, this eigenvalue being the one closest to the initial guess. This is of particular concern for our work, as it is possible to converge on an eigenvalue that are not the most unstable mode of the system, especially if two eigenvalues are close together in complex space. To ensure we have not included any of these 'false positive' results in our work, all numerical work is double checked using MATLAB's inbuilt boundary value problem solver BVP4c.

C   Derivation of equation (6.2)

In this appendix we provide a detailed break down of the derivation of the 6th order ordinary differential equation (6.2).   Seeking solutions of the form $\boldsymbol{f}(x, y, z, t) = \hat{\boldsymbol{f}}(z) \exp^{i(kx+ly+\omega t)}$, the governing set of equations (6.1) become

$$iku + ilv + w' = 0, \tag{C.15a}$$

$$ikb_x + ilb_y + b'_z = 0, \tag{C.15b}$$

$$i\left(\omega + kU\right)u + U'w = ikBb_x + B'b_z + \frac{1}{Re}\nabla^2_\perp u, \tag{C.15c}$$

$$i\left(\omega + kU\right)v = -il\Pi + ikBb_y + \frac{1}{Re}\nabla^2_\perp v, \tag{C.15d}$$

$$i\left(\omega + kU\right)w = \Pi' + ikBb_z + T + Bb_x + \frac{1}{Re}\nabla^2_\perp w, \tag{C.15e}$$

$$i\left(\omega + kU\right)b_x + B'w = ikBu + U'b_z, \tag{C.15f}$$

$$i\left(\omega + kU\right)b_y = ikBv, \tag{C.15g}$$

$$i\left(\omega + kU\right)b_z = ikBw, \tag{C.15h}$$

$$i\left(\omega + kU\right)\left(T + DBb_x\right) = -\beta w, \tag{C.15i}$$

where $\nabla^2_\perp = \partial_{zz} - l^2$.   Equations (C.15c)–(C.15i) can be manipulated to give three equations for each component of velocity,

$$i\left(\omega + kU\right)u = -U'w + \frac{ik^2B^2}{\omega + kU}u + \frac{k^2B^2U'}{\left(\omega + kU\right)^2}w + \frac{1}{Re}\nabla^2_\perp u, \tag{C.16a}$$

$$i\left(\omega + kU\right)v = -il\Pi + \frac{ik^2B^2}{\omega + kU}v + \frac{1}{Re}\nabla^2_\perp v, \tag{C.16b}$$

$$\begin{aligned} i\left(\omega + kU\right)w = \Pi' &+ \frac{kB^2}{\gamma\left(\omega + kU\right)}u \\ &- \frac{i}{\omega + kU}\left(\frac{kB^2U'}{\gamma\left(\omega + kU\right)} - F\right)w + \frac{1}{Re}\nabla^2_\perp w, \end{aligned} \tag{C.16c}$$

where F is defined in (5.2). Taking the z derivative of (C.16b) and subtracting the y derivative of (C.16c) removes the total pressure Π from the equations. Doing so gives

$$\begin{aligned} i\left(\omega + kU\right)\left(v' - ilw\right) + ikU'v = \frac{ik^2B^2}{\omega + kU}v' &+ \left(\frac{ik^2B^2}{\omega + kU}\right)'v - \frac{ilkB^2}{\gamma\left(\omega + kU\right)}u \\ &- \frac{l}{\omega + kU}\left(\frac{kB^2U'}{\gamma\left(\omega + kU\right)} - F\right)w + \frac{1}{Re}\nabla^2_\perp\left(v' - ilw\right). \end{aligned} \tag{C.17}$$

Making use of the incompressibility condition (C.15a) and its derivative, v and v' can be eliminated from the above equation to yield an equation of the form

$$A_{\nu1}w'''' + A_{\nu2}w'' + A_{\nu3}w' + A_{\nu4}w + A_{\nu5}u''' + A_{\nu6}u' + A_{\nu7}u = 0. \qquad \text{(C.18)}$$

Taking the derivative of equation (C.16a), it is possible to remove both the u''' and u' terms from the above equation. Therefore, together with (C.16a), the set of governing equations have been reduced to two equations for two unknowns, u and w,

$$\bar{A}_{\nu1}u'' + \bar{A}_{\nu2}w + \bar{A}_{\nu3}u = 0, \qquad \text{(C.19a)}$$

$$\bar{A}_{\nu4}w'''' + \bar{A}_{\nu5}w'' + \bar{A}_{\nu6}w' + \bar{A}_{\nu7}w + \bar{A}_{\nu8}u = 0, \qquad \text{(C.19b)}$$

where

$$\bar{A}_{\nu1} = -\frac{1}{Re}, \qquad \text{(C.20a)}$$

$$\bar{A}_{\nu2} = U' - \frac{k^2 B^2 U'}{(\omega + kU)^2}, \qquad \text{(C.20b)}$$

$$\bar{A}_{\nu3} = i(\omega + kU) - \frac{ik^2 B^2}{\omega + kU} + \frac{l^2}{Re}, \qquad \text{(C.20c)}$$

$$\bar{A}_{\nu4} = \frac{\gamma(\omega + kU)}{kB^2 Re}, \qquad \text{(C.20d)}$$

$$\bar{A}_{\nu5} = -\frac{i\gamma}{kB^2}\left((\omega + kU)^2 - k^2 B^2 - \frac{2il^2(\omega + kU)}{Re}\right), \qquad \text{(C.20e)}$$

$$\bar{A}_{\nu6} = -\frac{i\gamma}{kB^2}\left(\frac{2k^3 B^2 U'}{\omega + kU} - 2k^2 BB'\right), \qquad \text{(C.20f)}$$

$$\begin{aligned} \bar{A}_{\nu7} = {} & \frac{i\gamma l^2}{kB^2}\left((\omega + kU)^2 + \frac{kB^2 U'}{\gamma(\omega + kU)} - F - \frac{il^2(\omega + kU)}{Re}\right) \\ & - \frac{i\gamma}{kB^2}\left(-kU''(\omega + kU) + \frac{2k^3 BB'U'}{\omega + kU} + \frac{k^3 B^2 U''}{\omega + kU} - \frac{2k^4 B^2 U'^2}{(\omega + kU)^2}\right), \qquad \text{(C.20g)} \end{aligned}$$

$$\bar{A}_{\nu8} = -l^2. \qquad \text{(C.20h)}$$

On introducing the differential operator

$$\Gamma_\nu = i(\omega + kU) - \frac{ik^2 B^2}{\omega + kU} + \frac{l^2}{Re} - \frac{1}{Re}\frac{\partial^2}{\partial z^2}, \qquad \text{(C.21)}$$

equation (C.19a) can be written as $\Gamma_\nu u = -\bar{A}_{\nu2}w$. Applying this Γ operator to equation (C.19b) and rearranging terms yields the 6th order ordinary differential equation (6.2).

D   Derivation of equation (6.52)

This appendix contains a detailed breakdown on the derivation of the 4th order ordinary differential equation (6.52). Seeking solutions of the form $\boldsymbol{f}(x, y, z, t) = \hat{\boldsymbol{f}}(z) \exp^{i(kx+ly+\omega t)}$, the governing set of equations (6.51) become

$$iku + ilv + w' = 0, \tag{D.1a}$$

$$ikb_x + ilb_y + b'_z = 0, \tag{D.1b}$$

$$i(\omega + kU)u + U'w = ikBb_x + B'b_z, \tag{D.1c}$$

$$i(\omega + kU)v = -il\Pi + ikBb_y, \tag{D.1d}$$

$$i(\omega + kU)w = \Pi' + ikBb_z + T + Bb_x, \tag{D.1e}$$

$$i(\omega + kU)b_x + B'w = ikBu + U'b_z, \tag{D.1f}$$

$$i(\omega + kU)b_y = ikBv, \tag{D.1g}$$

$$i(\omega + kU)b_z = ikBw, \tag{D.1h}$$

$$i(\omega + kU)(T + DBb_x) = -\beta w + \frac{1}{Pe}\nabla_\perp^2 T, \tag{D.1i}$$

where $\nabla_\perp^2 = \partial_{zz} - l^2$. Equations (D.1c)–(D.1i) can be manipulated from six equations to three,

$$(\omega + kU)v = -l\Pi + \frac{k^2 B^2}{\omega + kU}v, \tag{D.2a}$$

$$(\omega + kU)w = -i\Pi' - iT + \frac{BB'}{\omega + kU}w + \frac{k^2 B^2}{\omega + kU}w, \tag{D.2b}$$

$$\left(i(\omega + kU) + \frac{l^2}{Pe} - \frac{1}{Pe}\frac{\partial^2}{\partial z^2}\right)T = \left(\left(1 - \frac{1}{\gamma}\right)BB' - \beta\right)w. \tag{D.2c}$$

Removing the total pressure by taking the z derivative of (D.2a) minus the y derivative of (D.2b), gives an equation of the form

$$A_{\kappa 1}w + A_{\kappa 2}v + A_{\kappa 3}v' + A_{\kappa 4}T = 0, \tag{D.3}$$

where

$$A_{\kappa 1} = il\left((\omega + kU)^2 - k^2B^2 - BB'\right), \tag{D.4a}$$

$$A_{\kappa 2} = \left(2k^2BB' - \frac{k^3B^2U'}{\omega + kU} - (\omega + kU)\,kU'\right), \tag{D.4b}$$

$$A_{\kappa 3} = \left((\omega + kU)^2 - k^2B^2\right), \tag{D.4c}$$

$$A_{\kappa 4} = -(\omega + kU)\,lT. \tag{D.4d}$$

Making use of the incompressibility condition (D.1a) and introducing the change of variable $w = (\omega + kU)\psi$, equation (D.3) becomes

$$P\psi'' + P'\psi' - l^2\left(P - BB'\right)w - il^2T = 0, \tag{D.5}$$

where $P = (\omega + kU)^2 - k^2B^2$. In terms of ψ equation (D.2c) becomes

$$\left(1 - \frac{il^2}{(\omega + kU)\,Pe} + \frac{i}{(\omega + kU)\,Pe}\frac{\partial^2}{\partial z^2}\right)T = -i\left(\left(1 - \frac{1}{\gamma}\right)BB' - \beta\right)\psi. \tag{D.6}$$

By introducing the differential operator

$$\Gamma_\kappa = 1 - \frac{il^2}{(\omega + kU)\,Pe} + \frac{i}{(\omega + kU)\,Pe}\frac{\partial^2}{\partial z^2}, \tag{D.7}$$

equation (D.6) can be rewritten as

$$\Gamma_\kappa T = -i\left(\left(1 - \frac{1}{\gamma}\right)BB' - \beta\right)\psi. \tag{D.8}$$

Applying the Γ_κ operator to equation (D.5) and making use of (D.8), yields a 4$^{\text{th}}$ order ODE for variable ψ,

$$(P\psi')' - l^2\left((\omega + kU)^2 - k^2B^2 - \beta - \frac{BB'}{\gamma}\right)w$$
$$+ \frac{i}{(\omega + kU)\,Pe}\left(\frac{\partial^2}{\partial z^2} - l^2\right)\left[(P\psi')' - l^2\left((\omega + kU)^2 - k^2B^2 - BB'\right)\right]w = 0. \tag{D.9}$$

This equation can then be expanded and rearranged to give equation (6.52).

E   Derivation of equations (6.78)

Seeking solutions of the form $\boldsymbol{f}(x,y,z,t) = \hat{\boldsymbol{f}}(z)\exp^{i(kx+ly+\omega t)}$, the governing set of equations (6.77) become

$$iku + ilv + w' = 0, \tag{E.1a}$$

$$ikb_x + ilb_y + b'_z = 0, \tag{E.1b}$$

$$i\left(\omega + kU\right)u + U'w = ikBb_x + B'b_z, \tag{E.1c}$$

$$i\left(\omega + kU\right)v = -il\Pi + ikBb_y, \tag{E.1d}$$

$$i\left(\omega + kU\right)w = \Pi' + ikBb_z + T + Bb_x, \tag{E.1e}$$

$$i\left(\omega + kU\right)b_x + B'w = ikBu + U'b_z + \frac{1}{Rm}\nabla^2_\perp b_x, \tag{E.1f}$$

$$i\left(\omega + kU\right)b_y = ikBv + \frac{1}{Rm}\nabla^2_\perp b_y, \tag{E.1g}$$

$$i\left(\omega + kU\right)b_z = ikBw + \frac{1}{Rm}\nabla^2_\perp b_z, \tag{E.1h}$$

$$i\left(\omega + kU\right)\left(T + DBb_x\right) = -\beta w, \tag{E.1i}$$

where again $\nabla^2_\perp = \partial_{zz} - l^2$. Substituting the energy equation (E.1i) into the z component of momentum eliminates the temperature T, giving

$$i\left(\omega + kU\right)w = \Pi' + \frac{B}{\gamma}b_x + \frac{i\beta}{\omega + kU}w + ikBb_z. \tag{E.2}$$

Taking the y derivative of (E.2) and subtracting the z derivative of (E.1d), removes the total pressure, giving

$$i\left(\omega + kU\right)\left(v' + lw\right) + ikU'v = ikBb'_y + ikB'b_y - \frac{ilB}{\gamma}b_x$$
$$+ \frac{l\beta}{\omega + kU}w + klBb_z. \tag{E.3}$$

The y component of velocity, v, can be eliminated from this equation using the incompressibility condition (E.1a), resulting in

$$\left(\omega + kU\right)\left(lw - \frac{1}{l}w'' - \frac{ik}{l}u'\right) - \frac{ik^2U'}{l}u - \frac{kU'}{l}w'$$
$$= ikBb'_y + ikB'b_y - \frac{ilB}{\gamma}b_x + \frac{l\beta}{\omega + kU}w + klBb_z. \tag{E.4}$$

From the x component of moment (E.1c) we can get an expression for u,

$$u = \frac{kB}{\omega + kU}b_x - \frac{iB'}{\omega + kU}b_z + \frac{iU'}{\omega + kU}w, \qquad \text{(E.5)}$$

and by differentiating equation (E.5) we get an expression for u',

$$u' = \left(\frac{kB}{\omega + kU}\right)' b_x + \frac{kB}{\omega + kU}b'_x - \left(\frac{iB'}{\omega + kU}\right)' b_z - \frac{iB'}{\omega + kU}b'_z$$
$$+ \left(\frac{iU'}{\omega + kU}\right)' w + \frac{iU'}{\omega + kU}w'. \qquad \text{(E.6)}$$

Substituting (E.5) and (E.6) into equation (E.4) gives, after some algebraic manipulation, an equation of the form

$$\alpha_{\eta 1}w'' + \alpha_{\eta 2}w + \alpha_{\eta 3}b_y + \alpha_{\eta 4}b'_y + \alpha_{\eta 5}b_x + \alpha_{\eta 6}b'_x + \alpha_{\eta 7}b_z + \alpha_{\eta 8}b'_z = 0, \qquad \text{(E.7)}$$

where

$$\alpha_{\eta 1} = (\omega + kU)^2, \qquad \text{(E.8a)}$$

$$\alpha_{\eta 2} = l^2\beta - l^2 (\omega + kU)^2 - kU'' (\omega + kU), \qquad \text{(E.8b)}$$

$$\alpha_{\eta 3} = iklB' (\omega + kU), \qquad \text{(E.8c)}$$

$$\alpha_{\eta 4} = -iklB (\omega + kU), \qquad \text{(E.8d)}$$

$$\alpha_{\eta 5} = ik^2B' (\omega + kU) - \frac{il^2 B (\omega + kU)}{\gamma}, \qquad \text{(E.8e)}$$

$$\alpha_{\eta 6} = ik^2B (\omega + kU), \qquad \text{(E.8f)}$$

$$\alpha_{\eta 7} = kB'' (\omega + kU) + kBl^2 (\omega + kU), \qquad \text{(E.8g)}$$

$$\alpha_{\eta 8} = kB' (\omega + kU). \qquad \text{(E.8h)}$$

Using the incompressibility conditions and equation (E.5), u and v can be eliminated from the induction equation to give three second order ordinary differential equations; equations (E.1f) to (E.1g) can be written in the form

$$\frac{1}{Rm}b''_x + \alpha_{\eta 9}b_x + \alpha_{\eta 10}b_z + \alpha_{\eta 11}w = 0, \qquad \text{(E.9a)}$$

$$\frac{1}{Rm}b''_y + \alpha_{\eta 12}b_y + \alpha_{\eta 13}b_x + \alpha_{\eta 14}b_z + \alpha_{\eta 15}w + \alpha_{\eta 16}w' = 0, \qquad \text{(E.9b)}$$

$$\frac{1}{Rm}b''_z + \alpha_{\eta 17}b_z + \alpha_{\eta 18}w = 0, \qquad \text{(E.9c)}$$

where

$$\alpha_{\eta9} = \frac{ik^2 B^2}{\omega + kU} - i\left(\omega + kU\right) - \frac{l^2}{Rm}, \tag{E.10a}$$

$$\alpha_{\eta10} = \frac{kBB'}{\omega + kU} + U', \tag{E.10b}$$

$$\alpha_{\eta11} = -\frac{kBU'}{\omega + kU} - B', \tag{E.10c}$$

$$\alpha_{\eta12} = -i\left(\omega + kU\right) - \frac{l^2}{Rm}, \tag{E.10d}$$

$$\alpha_{\eta13} = -\frac{ik^3 B^2}{l\left(\omega + kU\right)}, \tag{E.10e}$$

$$\alpha_{\eta14} = -\frac{k^2 BB'}{l\left(\omega + kU\right)}, \tag{E.10f}$$

$$\alpha_{\eta15} = \frac{k^2 BU'}{l\left(\omega + kU\right)}, \tag{E.10g}$$

$$\alpha_{\eta16} = -\frac{kB}{l}, \tag{E.10h}$$

$$\alpha_{\eta17} = -i\left(\omega + kU\right) - \frac{l^2}{Rm}, \tag{E.10i}$$

$$\alpha_{\eta18} = ikB. \tag{E.10j}$$

Equation (E.7) together with equations (E.9) form the set of equations (6.78), used in §6.4.

F Coefficients used in Chapter 6

To avoid unnecessary clutter, we have included the full coefficients found in Chapter 6 in this appendix. The b_i coefficients used in §6.2.1:

$$b_1 = -\frac{\gamma\bar{\omega}_0}{kB^2}, \tag{F.1a}$$

$$b_2 = \frac{\gamma}{kB^2}\left(\bar{\omega}_0 a_1 + ia_2\right), \tag{F.1b}$$

$$b_3 = \left(\bar{\omega}_0^2 - k^2 B^2\right)^2 - \frac{il^2}{Re}\left(4\bar{\omega}_0^3 - \bar{\omega}_0(3k^2 B^2 + F) + \frac{kBU'}{\gamma} - \frac{3i\bar{\omega}_0^2 l^2}{Re}\right), \tag{F.1c}$$

$$b_4 = \bar{\omega}_0^4 - \bar{\omega}_0^2(k^2 B^2 + F) + Fk^2 B^2$$
$$- \frac{il^2}{Re}\left(2\bar{\omega}_0^3 - \bar{\omega}_0(k^2 B^2 + F) + \frac{kB^2 U'}{\gamma} - \frac{i\bar{\omega}_0^2 l^2}{Re}\right), \tag{F.1d}$$

$$b_5 = 4\bar{\omega}_0^3 - 2\bar{\omega}_0(k^2 B^2 + F) - \frac{il^2}{Re}\left(6\bar{\omega}_0^2 - k^2 B^2 - F - \frac{2i\bar{\omega}_0 l^2}{Re}\right), \tag{F.1e}$$

$$b_6 = 4kU'\bar{\omega}_0^3 - \bar{\omega}_0^2(2k^2 BB' + F') - 2kU'\bar{\omega}_0(k^2 B^2 + F) + k^2 B^2 F'$$
$$+ 2k^2 FBB' - \frac{il^2}{Re}\left(kU'(6\bar{\omega}_0^2 - k^2 B^2 - F) - \bar{\omega}_0(2k^2 BB' + F')\right.$$
$$\left. + \frac{2kBB'U' + kB^2 U''}{\gamma} - \frac{2ikU'\bar{\omega}_0 l^2}{Re}\right), \tag{F.1f}$$

$$b_7 = 4\bar{\omega}_0^3 - 2\bar{\omega}_0(F + k^2 B^2) - \frac{il^2}{Re}\left(6\bar{\omega}_0^2 - k^2 B^2 - F - \frac{2i\bar{\omega}_0 l^2}{Re}\right), \tag{F.1g}$$

$$b_8 = \left(\bar{\omega}_0 kU'' + k^2 U'^2\right)\left(2\bar{\omega}_0^2 - F - k^2 B^2\right) + 4\bar{\omega}_0^2 k^2 U'^2$$
$$- 2\bar{\omega}_0 kU'(F' + 2k^2 BB') - \frac{F''}{2}\left(\bar{\omega}_0 - k^2 B^2\right)$$
$$+ k^2(BB'' + B'^2)(F - \bar{\omega}_0^2) + 2k^2 F' BB'$$
$$- \frac{il^2}{Re}\left[2\bar{\omega}_0(kU''\bar{\omega}_0 + k^2 U'^2) + 4k^2 U'^2\bar{\omega}_0 + kU''\bar{\omega}_0^2\right.$$
$$- \bar{\omega}_0\left(\frac{F''}{2} + k^2(BB'' + B'^2)\right) - kU'(2k^2 BB' + F') - \frac{1}{2}kU''(k^2 B^2 + F)$$
$$\left. + \frac{kB^2 U''' + 4kBB'U'' + 2k(BB'' + B'^2)U'}{2\gamma} - \frac{il^2}{Re}(\bar{\omega}_0 kU'' + k^2 U'^2)\right]. \tag{F.1h}$$

The c_i coefficients used in §6.2.2 and §6.2.3:

$$c_1 = \left(\bar{\omega}_0^2 - k^2 B^2\right)^2, \tag{F.2a}$$

$$c_2 = 4\bar{\omega}_0^3 - 2\bar{\omega}_0(F + k^2 B^2), \tag{F.2b}$$

$$c_3 = 2\bar{\omega}_0^3 - \bar{\omega}_0(F + k^2 B^2) + \frac{kB^2 U'}{\gamma} \tag{F.2c}$$

$$c_4 = 4kU'\bar{\omega}_0^3 - \bar{\omega}_0^2(F' + 2k^2 BB')$$
$$- 2kU'\bar{\omega}_0(F + k^2 B^2) + k^2 B^2 F' + 2k^2 FBB', \tag{F.2d}$$

$$c_5 = 4\bar{\omega}_0^3 - 2\bar{\omega}_0(F + k^2 B^2), \tag{F.2e}$$

$$c_6 = \omega_1^2 \left(6\bar{\omega}_0^2 - (F + k^2 B^2)\right)$$
$$- \frac{il^2}{\delta_2 Re} \left(\omega_1(6\bar{\omega}_0^2 - F - k^2 B^2) - \frac{i\bar{\omega}_0^2 l^2}{\delta_2 Re}\right), \tag{F.2f}$$

$$c_7 = \omega_1 \left(12kU'\bar{\omega}_0^2 - 2kU'(F + k^2 B^2) - 2\bar{\omega}_0(2k^2 BB' + F')\right)$$
$$- \frac{il^2}{\delta_2 Re} \left(kU'(6\bar{\omega}_0^2 - F - k^2 B^2) - \bar{\omega}_0(F' + 2k^2 BB') + \frac{kB^2 U'' + 2kBB'U'}{\gamma}\right), \tag{F.2g}$$

$$c_8 = \left(\bar{\omega}_0 kU'' + k^2 U'^2\right)\left(2\bar{\omega}_0^2 - F - k^2 B^2\right) + 4\bar{\omega}_0^2 k^2 U'^2$$
$$- 2\bar{\omega}_0 kU'(F' + 2k^2 BB') - \frac{F''}{2}\left(\bar{\omega}_0 - k^2 B^2\right)$$
$$+ k^2(BB'' + B'^2)(F - \bar{\omega}_0^2) + 2k^2 F' BB'. \tag{F.2h}$$

The d_i coefficients used in §6.3.2:

$$d_1 = i\left(\bar{\omega}_0^2 - k^2 B^2\right), \tag{F.3a}$$

$$d_2 = \bar{\omega}_0\left(\bar{\omega}_0^2 - k^2 B^2\right), \tag{F.3b}$$

$$d_3 = -i\left(2\bar{\omega}_0^2 - 2k^2 B^2 - BB'\right), \tag{F.3c}$$

$$d_4 = \bar{\omega}_0\left(\omega^2 - F\right), \tag{F.3d}$$

$$d_5 = -i\left(\bar{\omega}_0^2 - G\right), \tag{F.3e}$$

$$d_6 = 3\bar{\omega}_0^2 - F - \frac{2i\bar{\omega}_0 l^2}{Pe}, \tag{F.3f}$$

$$d_7 = \bar{\omega}_0\left(-F' + 2kU'\bar{\omega}_0\right) + kU'\left(\bar{\omega}_0^2 - F\right) - \frac{il^2}{Pe}\left(2kU'\bar{\omega}_0 - G'\right), \tag{F.3g}$$

$$d_8 = 3\bar{\omega}_0^2 - F - \frac{2i\bar{\omega}_0 l^2}{Pe}, \tag{F.3h}$$

$$d_9 = \bar{\omega}_0 \left(-\frac{F''}{2} + kU''\bar{\omega}_0 + k^2 U'^2 \right) + kU' \left(2kU'\bar{\omega}_0 - F' \right) + \frac{kU''}{2} \left(\bar{\omega}_0^2 - F \right)$$

$$- \frac{il^2}{Pe} \left(kU''\bar{\omega}_0 + k^2 U'^2 - \frac{G''}{2} \right). \tag{F.3i}$$

Bibliography

Abramowitz, M. & Stegun, I. A. (1972). *Handbook of mathematical functions*, New York: Dover.

Acheson, D. J. (1978). On the instability of toroidal magnetic fields and differential rotation in stars, *Phil. Trans. R. Soc. B* **289**: 459–500.

Acheson, D. J. (1979). Instability by magnetic buoyancy, *Sol. Phys.* **62**: 23–50.

Adam, J. A. (1978). Stability of aligned magnetoatmospheric flow, *J. Plasma Phys.* **19**: 77–86.

Babcock, H. W. (1961). The Topology of the Sun's Magnetic Field and the 22-Year Cycle., *Astrophys. J.* **133**: 572.

Bender, C. M. & Orszag, S. A. (1978). *Advanced mathematical methods for scientists and engineers*, Springer.

Bernstein, I. B., Frieman, E. A., Kruskal, M. D. & Kulsrud, R. M. (1958). An energy principle for hydromagnetic stability problems, *Proc. R. Soc. Lond.* **244**: 17–40.

Bowker, J. A., Hughes, D. W. & Kersalé, E. (2014). Incorporating velocity shear into the magneto-Boussinesq approximation, *Geophys. Astrophys. Fluid Dyn.* **108**: 553–567.

Cattaneo, F., Chiueh, T. & Hughes, D. W. (1990). Buoyancy-driven instabilities and the nonlinear breakup of a sheared magnetic layer, *J. Fluid Mech.* **219**: 1–23.

Cattaneo, F. & Hughes, D. W. (1988). The nonlinear breakup of a magnetic layer - Instability to interchange modes, *J. Fluid Mech.* **196**: 323–344.

Corfield, C. N. (1984). The magneto-Boussinesq approximation by scale analysis, *Geophys. Astrophys. Fluid Dyn.* **29**: 19–28.

Fearn, D. R. (1991). Eigensolutions of boundary value problems using inverse iteration, *J. Comput. Appl. Math.* **34**(2): 201–209.

Gilman, P. A. (1970). Instability of magnetohydrostatic stellar interiors from magnetic buoyancy. I., *Astrophys. J.* **162**: 1019.

Gough, D. (2007). An introduction to the solar tachocline, *in* D. W. Hughes, R. Rosner & N. O. Weiss (eds), *The Solar Tachocline*, Cambridge University Press, p. 3.

Griffiths, S. D. (2008). The limiting form of inertial instability in geophysical flows, *J. Fluid Mech.* **605**: 115–143.

Hale, G. E. (1908). On the probable existence of a magnetic field in sun-spots, *Astrophys. J.* **28**: 315.

Howard, L. N. (1961). Note on a paper of John W. Miles, *J. Fluid Mech.* **10**: 509–512.

Howard, R. & Labonte, B. J. (1980). The sun is observed to be a torsional oscillator with a period of 11 years, *Astrophys. J., Lett.* **239**: L33–L36.

Howe, R., Christensen-Dalsgaard, J., Hill, F., Komm, R. W., Larsen, R. M., Schou, J., Thompson, M. J. & Toomre, J. (2000). Deeply penetrating banded zonal flows in the solar convection zone, *Astrophys. J., Lett.* **533**: L163–L166.

Hughes, D. W. (1985a). Magnetic buoyancy instabilities for a static plane layer, *Geophys. Astrophys. Fluid Dyn.* **32**: 273–316.

Hughes, D. W. (1985b). Magnetic buoyancy instabilities incorporating rotation, *Geophys. Astrophys. Fluid Dyn.* **34**: 99–142.

Hughes, D. W. (2007). Magnetic buoyancy instabilities in the tachocline, *in* D. W. Hughes, R. Rosner & N. O. Weiss (eds), *The Solar Tachocline*, Cambridge University Press, p. 275.

Hughes, D. W. & Cattaneo, F. (1987). A new look at the instability of a stratified horizontal magnetic field, *Geophys. Astrophys. Fluid Dyn.* **39**: 65–81.

Hughes, D. W. & Proctor, M. R. E. (1988). Magnetic fields in the solar convection zone - Magnetoconvection and magnetic buoyancy, *Ann. Rev. Fluid Mech.* **20**: 187–223.

Hughes, D. W. & Tobias, S. M. (2001). On the instability of magnetohydrodynamic shear flows, *Proc. R. Soc. Lond.* **457**: 1365.

Jensen, E. (1955). On tubes of magnetic forces embedded in stellar material, *Annales d'Astrophysique* **18**: 127.

Jones, C. A., Soward, A. M. & Mussa, A. I. (2000). The onset of thermal convection in a rapidly rotating sphere, *J. Fluid Mech.* **405**: 157–179.

Matthews, P. C., Hughes, D. W. & Proctor, M. R. E. (1995). Magnetic buoyancy, vorticity, and three-dimensional flux-tube formation, *Astrophys. J.* **448**: 938.

Miesch, M. S. (2005). Large-scale dynamics of the convection zone and tachocline, *Living Reviews in Solar Physics* **2**(1).
URL: *http://www.livingreviews.org/lrsp-2005-1*

Mizerski, K. A., Davies, C. R. & Hughes, D. W. (2013). Short-wavelength magnetic buoyancy instability, *Astrophys. J., Suppl. Ser.* **205**: 16.

Newcomb, W. A. (1961). Convective instability induced by gravity in a plasma with a frozen-in magnetic field, *Physics of Fluids* **4**: 391–396.

Olver, F. W. J. (1974). *Asymptotics and special functions*, Academic Press, New York-London.

Ossendrijver, M. (2003). The solar dynamo, *Astron. Astrophys. Rev.* **11**: 287–367.

Parker, E. N. (1955). The formation of sunspots from the solar toroidal field., *Astrophys. J.* **121**: 491.

Parker, E. N. (1975). The generation of magnetic fields in astrophysical bodies. X - Magnetic buoyancy and the solar dynamo, *Astrophys. J.* **198**: 205–209.

Parker, E. N. (1993). A solar dynamo surface wave at the interface between convection and nonuniform rotation, *Astrophys. J.* **408**: 707–719.

Proctor, M. R. E. & Weiss, N. O. (1982). Magnetoconvection, *Rep. Prog. Phys.* **45**: 1317–1379.

Schmitt, J. H. M. M. & Rosner, R. (1983). Doubly diffusive magnetic buoyancy instability in the solar interior, *Astrophys. J.* **265**: 901–924.

Schou, J., Antia, H. M., Basu, S., Bogart, R. S., Bush, R. I., Chitre, S. M., Christensen-Dalsgaard, J., Di Mauro, M. P., Dziembowski, W. A., Eff-Darwich, A., Gough, D. O., Haber, D. A., Hoeksema, J. T., Howe, R., Korzennik, S. G., Kosovichev, A. G., Larsen, R. M., Pijpers, F. P., Scherrer, P. H., Sekii, T., Tarbell, T. D., Title, A. M., Thompson, M. J. & Toomre, J. (1998). Helioseismic studies of differential rotation in the solar envelope by the solar oscillations investigation using the michelson doppler imager, *Astrophys. J.* **505**: 390–417.

Spiegel, E. A. & Veronis, G. (1960). On the Boussinesq approximation for a compressible fluid., *Astrophys. J.* **131**: 442.

Spiegel, E. A. & Weiss, N. O. (1982). Magnetic buoyancy and the Boussinesq approximation, *Geophys. Astrophys. Fluid Dyn.* **22**: 219–234.

Spiegel, E. A. & Zahn, J.-P. (1992). The solar tachocline, *Astron. Astrophys.* **265**: 106–114.

Spruit, H. C. & van Ballegooijen, A. A. (1982). Stability of toroidal flux tubes in stars, *Astron. Astrophys.* **106**: 58–66.

Squire, H. B. (1933). On the stability for three-dimensional disturbances of viscous fluid flow between parallel walls, *Proc. R. Soc. Lond.* **142**: 621–628.

Synge, J. L. (1933). The stability of heterongeneous liquids, *Trans. R. Soc. Can.* **27**: 1–18.

Thomas, J. H. & Nye, A. H. (1975). Convective instability in the presence of a nonuniform horizontal magnetic field, *Physics of Fluids* **18**: 490.

Tobias, S. M. & Hughes, D. W. (2004). The influence of velocity shear on magnetic buoyancy instability in the solar tachocline, *Astrophys. J.* **603**: 785–802.

Tobias, S. & Weiss, N. (2007). The solar dynamo and the tachocline, *in* D. W. Hughes, R. Rosner & N. O. Weiss (eds), *The Solar Tachocline*, Cambridge University Press, p. 319.

Turner, J. S. (1973). *Buoyancy Effects in Fluids*, Cambridge Monographs on Mechanics, Cambridge University Press.

Vorontsov, S. V., Christensen-Dalsgaard, J., Schou, J., Strakhov, V. N. & Thompson, M. J. (2002). Helioseismic measurement of solar torsional oscillations, *Science* **296**: 101–103.

Yano, J.-I. (1992). Asymptotic theory of thermal convection in rapidly rotating systems, *J. Fluid Mech.* **243**: 103–131.